Universidad de Oviedo

Programa de Doctorado en Materiales

ESTIMACIÓN DE TENSIONES PARA LA MONITORIZACIÓN DEL DAÑO POR FATIGA: DETERMINACIÓN MEDIANTE MODELOS NUMÉRICOS Y ANÁLISIS MODAL OPERACIONAL

STRESS ESTIMATION FOR FATIGUE MONITORING: DETERMINATION THROUGH NUMERICAL MODELS AND OPERATIONAL MODAL ANALYSIS.

Doctorando:

Natalia García Fernández

Oviedo, noviembre 2024

Universidad de Oviedo

Departamento de Construcción e Ingeniería de Fabricación

Programa de Doctorado en Materiales

ESTIMACIÓN DE TENSIONES PARA LA MONITORIZACIÓN DEL DAÑO POR FATIGA: DETERMINACIÓN MEDIANTE MODELOS NUMÉRICOS Y ANÁLISIS MODAL OPERACIONAL

STRESS ESTIMATION FOR FATIGUE MONITORING: DETERMINATION THROUGH NUMERICAL MODELS AND OPERATIONAL MODAL ANALYSIS.

Doctorando:

Natalia García Fernández

Directores:

Dr. Manuel Aenlle López

Dr. Pelayo Fernández Fernández

Oviedo, noviembre 2024

Universidad de Oviedo

RESUMEN DEL CONTENIDO DE TESIS DOCTORAL

1.- Título de la Tesis	
Español: Estimación de tensiones para la monitorización del daño por fatiga: determinación mediante modelos numéricos y análisis modal operacional.	Inglés: Stress estimation for fatigue monitoring: determination through numerical models and operational modal analysis.

2.- Autora	
Nombre: Natalia García Fernández	
Programa de Doctorado: Materiales	
Órgano responsable: Centro Internacional de Postgrado	

FOR-MAT-VOA-010 (Reg.2018)

RESUMEN (en español)

Muchas estructuras están sometidas a cargas dinámicas que generan tensiones de amplitud variable, las cuales pueden provocar fallos por fatiga. Dado el gran número de estructuras, como puentes, chimeneas, torres, turbinas eólicas, paneles solares, etc., que son susceptibles de sufrir este fenómeno, las técnicas de monitorización de la salud estructural (SHM) son herramientas muy útiles para evitar las consecuencias catastróficas de este tipo de fallos. Aunque se han desarrollado numerosos métodos para la detección de daño mediante técnicas de monitorización, las técnicas de evaluación y predicción de daño acumulado en tiempo real siguen estando poco exploradas. Por lo tanto, para comprender y evaluar el daño por fatiga en las estructuras y, en consecuencia, poder determinar su vida útil remanente, es esencial implementar técnicas de monitorización a fatiga en tiempo real.

La monitorización a fatiga en continuo consiste en determinar el daño acumulado por fatiga, en tiempo real, durante el período de operación de la estructura. Se propone un enfoque de monitorización a fatiga que se puede dividir en cinco fases: (i) identificación de los componentes y ubicaciones críticas más probables de sufrir daño por fatiga, (ii) implementación de una estrategia de montaje de sensores, (iii) medición o estimación de deformaciones/tensiones en las ubicaciones de interés en tiempo real, (iv) cálculo del espectro de tensiones mediante técnicas de conteo de ciclos y evaluación del daño total por fatiga, y (v) cálculo de vida remanente a fatiga.

Para obtener el historial temporal de tensiones en los puntos de interés, existen dos metodologías comúnmente aplicadas: (a) medición directa con sensores de deformación instalados en las ubicaciones de interés, o (b) estimación de tensiones a partir de las respuestas estructurales mediante la medición continua de desplazamientos, velocidades, aceleraciones o deformaciones experimentales en puntos discretos de la estructura. Esta tesis se centra en la estimación de tensiones, concretamente utilizando superposición modal y la expansión de modos de vibración.

Estas técnicas de estimación de tensiones requieren, generalmente, modos de vibración un modelo numérico, que debe estar bien correlacionado con la estructura experimental, ya que la precisión de las tensiones estimadas depende del nivel de correlación. En esta tesis se proponen varias técnicas de correlación, basadas en la matriz de transformación ***T***, para detectar el origen de las discrepancias entre dos modelos (masa, rigidez o ambas). Además, se introduce una versión novedosa del MAC (Modal Assurance Criterion) para abordar los problemas que aparecen en modelos con modos cercanos o repetidos, donde el MAC puede arrojar valores bajos, incluso cuando existe una buena correlación. Todas las técnicas de correlación propuestas se validan mediante simulaciones numéricas y ensayos experimentales.
Una vez que el modelo numérico está adecuadamente calibrado, se pueden aplicar técnicas de estimación de tensiones basadas en expansión modal. Esta tesis presenta varios enfoques para estimar las coordenadas modales y expandir los modos de vibración, proponiendo ocho métodos para la estimación de tensiones. Se abordan las hipótesis de partida, los datos necesarios para su aplicación, así como la incertidumbre asociada a estos métodos y sus

limitaciones. Los métodos propuestos se validan mediante simulaciones numéricas, y ensayos experimentales en modelos estructurales a escala.

En definitiva, esta tesis propone una metodología para la monitorización a fatiga de estructuras en servicio. Para ello, se presentan ocho métodos de estimación de tensiones, los cuales requieren la utilización de un modelo numérico bien correlacionado con el modelo experimental. Además, se desarrollan nuevas técnicas de correlación para detectar discrepancias en masa y rigidez, así como una nueva versión del MAC. Finalmente, las metodologías presentadas se validan mediante simulaciones numéricas y ensayos experimentales.

RESUMEN (en Inglés)

Structures are often subjected to dynamic loads that generate variable stresses, potentially leading to fatigue failure. Given the vast number of structures, such as bridges, chimneys, towers, wind turbines, solar panels, etc., that are susceptible to this phenomenon, Structural Health Monitoring (SHM) techniques play a crucial role in preventing the potentially catastrophic consequences of such failures. While numerous SHM techniques have been developed for damage detection purposes, real-time assessment and prediction techniques for accumulated damage remain quite underexplored. Therefore, to understand and assess fatigue damage in structures and, consequently, determine their remaining life, it is essential to implement continuous fatigue monitoring techniques.

Continuous fatigue monitoring refers to the calculation of accumulated fatigue damage in real time during the period that the structure is in operation. A fatigue monitoring approach is proposed, which can be divided into five steps: (i) identification of the most likely critical components and locations to suffer fatigue damage, (ii) sensor location strategy, (iii) real time measurement or estimation of strains/stresses at the locations of interest, (iv) calculation of the stress spectrum using cycle counting techniques and evaluation of the total fatigue damage, and (v) calculation of the remaining fatigue life.

To obtain the stress time history response at the relevant locations, two commonly applied methodologies exist: (a) strain measurement with strain sensors installed at the locations of interest, or (b) stress estimation from the displacement, velocity, acceleration or strain structural responses, measured at discrete points of the structure. This thesis focuses on stress estimation, specifically using modal superposition and based on modal expansion.

These techniques typically require mode shapes from a numerical model which must be well correlated with the experimental structure, as the quality of the estimated stresses depends on the level of correlation. In this thesis, several correlation techniques based on the transformation matrix ***T***, are proposed to detect if the discrepancies between models can be attributed to mass, stiffness or both. Additionally, a novel version of the Modal Assurance Criterion (MAC) is introduced to address challenges in models with closely spaced or repeated modes, where the original MAC may yield low values even when strong correlation exists. All proposed techniques are validated through numerical simulations and experimental examples.

Once the numerical model is adequately correlated, stress estimation techniques based on modal expansion can be applied. This thesis presents various approaches to estimate modal coordinates and to expand mode shapes, proposing eight methods for stress estimation. The initial assumptions, the data required for their application, as well as the uncertainty associated with these methods and their limitations, are addressed. The proposed methods are validated through numerical simulations and experimental tests carried out on scaled structural models.

In summary, this thesis proposes a methodology for fatigue monitoring of structures in operation. To this end, eight stress estimation methods are presented, which require a numerical model well-correlated with the experimental model. New correlation techniques are developed to detect discrepancies in terms of mass and stiffness, along with a new version of the MAC. Finally, all the proposed methodologies are validated by numerical simulations and experimental tests.

SR. PRESIDENTE DE LA COMISIÓN ACADÉMICA DEL PROGRAMA DE DOCTORADO EN MATERIALES

A mis padres,

y a Álvaro

Acknowledgements

I would like to take this opportunity to express my gratitude to those who have made the completion of this doctoral thesis possible.

Como muchos se podrían imaginar, este apartado es el último que escribo, pero lo que la mayoría no sabe es que es aquí, en los agradecimientos, donde se encuentra lo más importante de estos años.

En primer lugar, quiero expresar mi agradecimiento a mis directores de tesis: Manuel Aenlle y Pelayo Fernández, por transmitirme sus conocimientos y su pasión por la temática. Gracias por darme la libertad de profundizar en los temas que realmente me interesaban y brindarme innumerables oportunidades para crecer, tanto académica como personalmente. A Manolo, por estar siempre disponible para resolver mis dudas y por esas correcciones en papel llenas de rojo que son únicas. Y, sobre todo, gracias por enseñarme que con el trabajo diario y sin atracones (excepto para escribir una tesis) se pueden conseguir grandes cosas. A Pelayo, por estar siempre dispuesto a ayudar cuando surgen problemas y por hacer que los desafíos no parezcan tan grandes como son. Porque la humildad permite aprender más que la arrogancia.

Thanks to Professor Gentile for opening the doors of the Politecnico di Milano for me during three months, and to all those who, in one way or another, shared their insights on bridge monitoring. I would also like to express my gratitude to Sergio Pereira (from FEUP) for transforming what initially seemed very complex into a straightforward learning experience. Thank you for guiding me. I also want to thank everyone I met during these two months in Porto, especially the AMRO residence group, who made those two months feel like being part of a new family.

Gracias a mis compañeros de Uniovi por dejarme ser como soy y por soportarme en estos últimos meses, cuando los altos niveles de estrés sacaban lo peor de mí. A quienes estaban cuando llegué (Guille, Adrián e Isma), gracias por compartir todo lo que sabíais sin esperar nada a cambio y por hacer que el inicio del doctorado fuese un camino más fácil. A Miguel y a Roberto por hacer de este laboratorio un lugar acogedor, donde hacer la tesis resulta mucho más fácil. A Víctor por todas las conversaciones y discusiones que nos planteas a menudo, porque, aunque no lo sabes, lo único que consiguen es unir lazos y que cada día este grupo de trabajo sea más un grupo de amigos (aunque a algunos nos cueste reconocerlo). Suerte en esta nueva etapa. A Paula, compañera de mesa, quien, aunque sabe que no me gustan los besos, insiste en despedirse cada vez que vamos a estar más de dos días sin vernos. Por enseñarnos a todos lo que significa ser una mujer, madre y trabajadora de verdad; Martín, Raquel y Luis todavía no saben la suerte que tienen. A Marcos, por invitarnos a la piscina. A Sara y a Lucas por descubrimos el pádel, ojalá podamos seguir compartiendo buenos momentos fuera del trabajo. Marquis… ¡que era broma! Gracias por escuchar (aunque a veces te resulta difícil de tanto hablar), por animar en los días malos y por hacer que cada día de trabajo sea un buen día y, sobre todo, gracias por mejorar la gastronomía del grupo. A Diego, porque a pesar de hacerme perder la paciencia alguna que otra vez, probablemente seas el mejor *Minion* que podría tener. Estoy segura de que te esperan grandes cosas. A Sofía por adaptarte al grupo de la mejor manera posible y por entretenernos durante las comidas con tus aventuras. Y a Borja, por hacer mi estancia en Milán más amena y por compartir consejos valiosos. Gracias a todas y cada una de las personas que pasaron por este laboratorio (TFGs, TFMs, IUTAs, estancias…) y a los profesores del área por su apoyo a las nuevas generaciones.

Gracias a Iván, Manuel y María, que, aunque el doctorado, el trabajo y la vida adulta nos separen, siempre que nos juntemos será como antes. Que nunca nos falte el brindis de Nochebuena.

Gracias a mis padres por inculcarme la constancia y el trabajo, por ser la base de todo lo que soy hoy, y por darme alas para ser libre. A toda mi familia, por estar más orgullosos de mí que nadie, especialmente *güeli*, y a los que ya no están, que seguro que también estarían orgullosos.

Álvaro, gracias por estar a la altura, por estar en los momentos buenos, por estar en los momentos malos, por estar cuando solo hacía falta estar, por estar, siempre. Gracias por dejarme compartir mi vida contigo (y con Anís). Pero es que, aunque esta tesis termina hoy, nosotros seguiremos escribiendo nuestra historia juntos.

Gracias a todos lo que de una manera u otra han hecho posible esta aventura.

Natalia García Fernández

Abstract

Structures are often subjected to dynamic loads that generate variable stresses, potentially leading to fatigue failure. Given the vast number of structures, such as bridges, chimneys, towers, wind turbines, solar panels, etc., that are susceptible to this phenomenon, Structural Health Monitoring (SHM) techniques play a crucial role in preventing the potentially catastrophic consequences of such failures. While numerous SHM techniques have been developed for damage detection purposes, real-time assessment and prediction techniques for accumulated damage remain quite underexplored. Therefore, to understand and assess fatigue damage in structures and, consequently, determine their remaining life, it is essential to implement continuous fatigue monitoring techniques.

Continuous fatigue monitoring refers to the calculation of accumulated fatigue damage in real time during the period that the structure is in operation. A fatigue monitoring approach is proposed, which can be divided into five steps: (i) identification of the most likely critical components and locations to suffer fatigue damage, (ii) sensor location strategy, (iii) real time measurement or estimation of strains/stresses at the locations of interest, (iv) calculation of the stress spectrum using cycle counting techniques and evaluation of the total fatigue damage, and (v) calculation of the remaining fatigue life.

To obtain the stress time history response at the relevant locations, two commonly applied methodologies exist: (a) strain measurement with strain sensors installed at the locations of interest, or (b) stress estimation from the displacement, velocity, acceleration or strain structural responses measured at discrete points of the structure. This thesis focuses on stress estimation, specifically using modal superposition and based on modal expansion.

These techniques typically require mode shapes from a numerical model which must be well correlated with the experimental structure, as the quality of the estimated stresses depends on the level of correlation. In this thesis, several correlation techniques based on the transformation matrix $\boldsymbol{T}$, are proposed to detect if the discrepancies between models can be attributed to mass, stiffness or both. Additionally, a novel version of the Modal Assurance Criterion (MAC) is introduced to address challenges in models with closely spaced or repeated modes, where the original MAC may yield low values even when good correlation exists. All proposed techniques are validated through numerical simulations and experimental examples.

Once the numerical model is adequately correlated, stress estimation techniques based on modal expansion can be applied. This thesis presents various approaches to estimate modal coordinates and to expand mode shapes, proposing eight methods for stress estimation. The initial assumptions, the data required for their application, as well as the uncertainty associated with these methods and their limitations, are addressed. The proposed methods are validated through numerical simulations and experimental tests carried out on scaled structural models.

In summary, this thesis proposes a methodology for fatigue monitoring of structures in operation. To this end, eight stress estimation methods are presented, which require a numerical model well-correlated with the experimental model. New correlation techniques are developed to detect discrepancies in terms of mass and stiffness, along with a new version of the MAC. Finally, all the proposed methodologies are validated by numerical simulations and experimental tests.

Resumen

Muchas estructuras están sometidas a cargas dinámicas que generan tensiones de amplitud variable, las cuales pueden provocar fallos por fatiga. Dado el gran número de estructuras, como puentes, chimeneas, torres, turbinas eólicas, paneles solares, etc., que son susceptibles de sufrir este fenómeno, las técnicas de monitorización de la salud estructural (SHM) son herramientas muy útiles para evitar las consecuencias catastróficas de este tipo de fallos. Aunque se han desarrollado numerosos métodos para la detección de daño mediante técnicas de monitorización, las técnicas de evaluación y predicción de daño acumulado en tiempo real siguen estando poco exploradas. Por lo tanto, para comprender y evaluar el daño por fatiga en las estructuras y, en consecuencia, poder determinar su vida útil remanente, es esencial implementar técnicas de monitorización a fatiga en tiempo real.

La monitorización a fatiga en continuo consiste en determinar el daño acumulado por fatiga, en tiempo real, durante el período de operación de la estructura. Se propone un enfoque de monitorización a fatiga que se puede dividir en cinco fases: (i) identificación de los componentes y ubicaciones críticas más probables de sufrir daño por fatiga, (ii) implementación de una estrategia de montaje de sensores, (iii) medición o estimación de deformaciones/tensiones en las ubicaciones de interés en tiempo real, (iv) cálculo del espectro de tensiones mediante técnicas de conteo de ciclos y evaluación del daño total por fatiga, y (v) cálculo de vida remanente a fatiga.

Para obtener el historial temporal de tensiones en los puntos de interés, existen dos metodologías comúnmente aplicadas: (a) medición directa con sensores de deformación instalados en las ubicaciones de interés, o (b) estimación de tensiones a partir de las respuestas estructurales mediante la medición continua de desplazamientos, velocidades, aceleraciones o deformaciones experimentales en puntos discretos de la estructura. Esta tesis se centra en la estimación de tensiones, concretamente utilizando superposición modal y la expansión de modos de vibración.

Estas técnicas de estimación de tensiones requieren, generalmente, modos de vibración un modelo numérico, que debe estar bien correlacionado con la estructura experimental, ya que la precisión de las tensiones estimadas depende del nivel de correlación. En esta tesis se proponen varias técnicas de correlación, basadas en la matriz de transformación $\boldsymbol{T}$, para detectar el origen de las discrepancias entre dos modelos (masa, rigidez o ambas). Además, se introduce una versión novedosa del MAC (Modal Assurance Criterion) para abordar los problemas que aparecen en modelos con modos

cercanos o repetidos, donde el MAC puede arrojar valores bajos, incluso cuando existe una buena correlación. Todas las técnicas de correlación propuestas se validan mediante simulaciones numéricas y ensayos experimentales.

Una vez que el modelo numérico está adecuadamente calibrado, se pueden aplicar técnicas de estimación de tensiones basadas en expansión modal. Esta tesis presenta varios enfoques para estimar las coordenadas modales y expandir los modos de vibración, proponiendo ocho métodos para la estimación de tensiones. Se abordan las hipótesis de partida, los datos necesarios para su aplicación, así como la incertidumbre asociada a estos métodos y sus limitaciones. Los métodos propuestos se validan mediante simulaciones numéricas, y ensayos experimentales en modelos estructurales a escala.

En definitiva, esta tesis propone una metodología para la monitorización a fatiga de estructuras en servicio. Para ello, se presentan ocho métodos de estimación de tensiones, los cuales requieren la utilización de un modelo numérico bien correlacionado con el modelo experimental. Además, se desarrollan nuevas técnicas de correlación para detectar discrepancias en masa y rigidez, así como una nueva versión del MAC. Finalmente, las metodologías presentadas se validan mediante simulaciones numéricas y ensayos experimentales.

Abbreviations

CDF	Curvature Damage Factor
COC	Cross-Orthogonality Check
COMAC	Co-Ordinate MAC
DOF	Degree Of Freedom
DOFs	Degrees Of Freedom
EMA	Experimental Modal Analysis
FBG	Fiber-Bragg Gratings
FDD	Frequency Domain Decomposition
FEM	Finite Element Model
FRAC	Frequency Response Assurance Criterion
LSCF	Least Squares Complex Frequency
MAC	Modal Assurance Criterion
MDOF	Multi-Degree of Freedom
NFCC	Natural Frequency Correlation Coefficient
NFD	Natural Frequency Difference
NRFD	Normalized Relative Frequency Difference
OMA	Operational Modal Analysis
OMAH	Operational Modal Analysis with Harmonic excitation
OMAX	Operational Modal Analysis with Exogenous input
p-LSCF	poly-reference Least Squares Complex Frequency
POC	Pseudo-Orthogonality Check
PP	Peak-Picking
PSD	Power Spectral Density
R^2	Coefficient of determination
ROTMAC	Rotated MAC
RVAC	Response Vector Assurance Criterion
SDOF	Single Degree of Freedom

SHM	Structural Health Monitoring
S-N	Stress - Number of cycles
SOBI	Second-Order Blind Identification
SSI	Stochastics Subspace Identification
SSI-COV	Covariance-Driven Stochastic Subspace Identification
SSI-DD	Data-Driven Stochastic Subspace Identification
STS	Statistical Time Series

Nomenclature

$\boldsymbol{I}$	Identity matrix
$\boldsymbol{D}$	Material constitutive matrix
$\boldsymbol{K_A}$	Stiffness matrix of system A
$\boldsymbol{K_B}$	Stiffness matrix of system B
$\boldsymbol{\Delta K}$	Stiffness change matrix
$\boldsymbol{M_A}$	Mass matrix of system A
$\boldsymbol{M_B}$	Mass matrix of system B
$\boldsymbol{\Delta M}$	Mass change matrix
$\boldsymbol{Q}$	Upper triangular matrix obtained from the QR decomposition
$\boldsymbol{R}$	Rotation matrix
$\boldsymbol{T}$	Transformation matrix
$\boldsymbol{T_U}$	Transformation matrix obtained with unscaled mode shapes
$\boldsymbol{T_{mm}}$	Transformation matrix of size *m* x *m* estimated with experimental mode shapes $\boldsymbol{\phi_{xam}}$ and numerical mode shapes $\boldsymbol{\phi_{FEam}}$
$\breve{\boldsymbol{T}}_{\boldsymbol{mm}}$	Estimation of the transformation matrix $\boldsymbol{T_{mm}}$
$\boldsymbol{T_{\varepsilon mm}}$	Transformation matrix of size *m* x *m* estimated with experimental strain mode shapes $\boldsymbol{\phi_{x\varepsilon am}}$ and numerical mode shapes $\boldsymbol{\phi_{FE\varepsilon am}}$
$\breve{\boldsymbol{T}}_{\boldsymbol{\varepsilon mm}}$	Estimation of the transformation matrix $\boldsymbol{T_{\varepsilon mm}}$
$\boldsymbol{T_{\sigma mm}}$	Transformation matrix of size *m* x *m* estimated with experimental stress mode shapes $\boldsymbol{\phi_{x\sigma am}}$ and numerical mode shapes $\boldsymbol{\phi_{FE\sigma am}}$
$\breve{\boldsymbol{T}}_{\boldsymbol{\sigma mm}}$	Estimation of the transformation matrix $\boldsymbol{T_{\sigma mm}}$
$\breve{\boldsymbol{T}}_{\boldsymbol{t\varepsilon mm}}$	Transformation matrix of size *m* x *m* estimated with experimental mode shapes and strain mode shapes $\begin{bmatrix}\boldsymbol{\phi_{x\varepsilon am}}\\ \boldsymbol{\phi_{xam}}\end{bmatrix}$ and numerical mode shapes $\begin{bmatrix}\boldsymbol{\phi_{FE\varepsilon am}}\\ \boldsymbol{\phi_{FEam}}\end{bmatrix}$
$\breve{\boldsymbol{T}}_{\boldsymbol{t\sigma mm}}$	Transformation matrix of size *m* x *m* estimated with experimental mode shapes and strain mode shapes $\begin{bmatrix}\boldsymbol{\phi_{x\varepsilon am}}\\ \boldsymbol{\phi_{xam}}\end{bmatrix}$ and numerical mode shapes $\begin{bmatrix}\boldsymbol{\phi_{FE\varepsilon am}}\\ \boldsymbol{\phi_{FEam}}\end{bmatrix}$
$\boldsymbol{T_{t\varepsilon mm}}$	Estimation of the transformation matrix $\breve{\boldsymbol{T}}_{\boldsymbol{t\varepsilon mm}}$
$\boldsymbol{T_{t\varepsilon mm}}$	Estimation of the transformation matrix $\breve{\boldsymbol{T}}_{\boldsymbol{t\sigma mm}}$
$\boldsymbol{T_{ch}}$	Matrix containing the effects of shear and scaling

$\boldsymbol{T}_{sc}$	Matrix containing the effects of scaling
$\boldsymbol{T}_{sh}$	Matrix containing the effects of shear
$\boldsymbol{Z}$	Positive semi-definite Hermitian matrix obtained from the polar decomposition
f_{Aj}	Natural frequency on mode j of system A
f_{Bj}	Natural frequency on mode j of system B
$\boldsymbol{m}_{A}$	Diagonal matrix containing the modal masses of system A
$\boldsymbol{n}_{xa}$	Noise in the response signals
$\boldsymbol{q}$	Modal coordinates $\boldsymbol{q}(\boldsymbol{t})$
$\boldsymbol{q}_{xm}$	'm' experimental modal coordinates
$\boldsymbol{q}_{xr}$	'r' experimental modal coordinates of the unmeasured modes
$\boldsymbol{q}_{xm}^{*}$	'm' complex experimental modal coordinates
$\boldsymbol{q}_{xr}^{*}$	'r' complex experimental modal coordinates of the unmeasured modes
$\widehat{\boldsymbol{q}}_{xm}$	'm' experimental modal coordinates (projecting into a subspace spanned by experimental mode shapes)
$\widetilde{\boldsymbol{q}}_{xm}$	'm' experimental modal coordinates (projecting into a subspace spanned by numerical mode shapes)
$\widehat{\boldsymbol{q}}_{\varepsilon xm}$	'm' experimental modal coordinates (projecting into a subspace spanned by experimental strain mode shapes)
$\widetilde{\boldsymbol{q}}_{\varepsilon xm}$	'm' experimental modal coordinates (projecting into a subspace spanned by numerical strain mode shapes)
$\widehat{\boldsymbol{q}}_{txm}$	'm' experimental modal coordinates (projecting into a subspace spanned by experimental mode shapes and strain mode shapes)
$\widetilde{\boldsymbol{q}}_{txm}$	'm' experimental modal coordinates (projecting into a subspace spanned by numerical mode shapes and strain mode shapes)
$\boldsymbol{q}_{\psi xm}$	'm' experimental modal coordinates obtained with unscaled mode shapes
$\widehat{\boldsymbol{q}}_{\psi xm}$	'm' experimental modal coordinates (projecting into a subspace spanned by experimental unscaled mode shapes)
$\boldsymbol{s}$	Diagonal matrix of ones or negative ones relating experimental mode shapes and numerical mode shapes
$\boldsymbol{s}_{\varepsilon}$	Diagonal matrix of ones or negative ones relating experimental strain mode shapes and numerical strain mode shapes
$\boldsymbol{u}$	Displacements $\boldsymbol{u}(\boldsymbol{t})$
$\boldsymbol{u}_{x}$	Experimental displacements

$\boldsymbol{u}_{\boldsymbol{xa}}$	Experimental displacements at 'a' DOFs
$\widehat{\boldsymbol{u}}$	Displacements projected in the experimental subspace
$\widetilde{\boldsymbol{u}}$	Displacements projected in the numerical subspace
y	Distance to the neutral axis
$\boldsymbol{\varepsilon}_{\boldsymbol{x}}$	Experimental strains
$\boldsymbol{\varepsilon}_{\boldsymbol{1}}$	Strains estimated with Method 1
$\boldsymbol{\varepsilon}_{\boldsymbol{2}}$	Strains estimated with Method 2
$\boldsymbol{\varepsilon}_{\boldsymbol{3}}$	Strains estimated with Method 3
$\boldsymbol{\varepsilon}_{\boldsymbol{4}}$	Strains estimated with Method 4
$\boldsymbol{\varepsilon}_{\boldsymbol{5}}$	Strains estimated with Method 5
$\boldsymbol{\varepsilon}_{\boldsymbol{6}}$	Strains estimated with Method 6
$\boldsymbol{\varepsilon}_{\boldsymbol{7}}$	Strains estimated with Method 7
$\boldsymbol{\varepsilon}_{\boldsymbol{8}}$	Strains estimated with Method 8
$\boldsymbol{\sigma}_{\boldsymbol{1}}$	Stress estimated with Method 1
$\boldsymbol{\sigma}_{\boldsymbol{2}}$	Stress estimated with Method 2
$\boldsymbol{\sigma}_{\boldsymbol{3}}$	Stress estimated with Method 3
$\boldsymbol{\sigma}_{\boldsymbol{4}}$	Stress estimated with Method 4
$\boldsymbol{\sigma}_{\boldsymbol{5}}$	Stress estimated with Method 5
$\boldsymbol{\sigma}_{\boldsymbol{6}}$	Stress estimated with Method 6
$\boldsymbol{\sigma}_{\boldsymbol{7}}$	Stress estimated with Method 7
$\boldsymbol{\sigma}_{\boldsymbol{8}}$	Stress estimated with Method 8
$\boldsymbol{\omega}_{\boldsymbol{B}}^{\boldsymbol{2}}$	Diagonal matrix containing the natural frequencies of systems B
$\boldsymbol{\omega}_{\boldsymbol{A}}^{\boldsymbol{2}}$	Diagonal matrix containing the natural frequencies of systems A
$\boldsymbol{\phi}$	Modal matrix
$\boldsymbol{\phi}_{\boldsymbol{A}}$	Modal matrix of system A (perturbed system)
$\boldsymbol{\psi}_{\boldsymbol{A}}$	Unscaled modal matrix of system A (perturbed system)
$\boldsymbol{\phi}_{\boldsymbol{Aj}}$	Mode shape j of system A (perturbed system)
$\boldsymbol{\phi}_{\boldsymbol{LAj}}$	Mode shape j of system A (perturbed system) normalized to the unit length
$\boldsymbol{\phi}_{\boldsymbol{B}}$	Modal matrix of system B (perturbed system)
$\boldsymbol{\phi}_{\boldsymbol{Bi}}$	Mode shape i of system B (perturbed system)
$\boldsymbol{\phi}_{\boldsymbol{LBi}}$	Mode shape i of system B (perturbed system) normalized to the unit length
$\boldsymbol{\phi}_{\boldsymbol{BR}}$	Rotated modal matrix of system B (perturbed system)

$\boldsymbol{\phi}_{x}$	Experimental modal matrix
$\boldsymbol{\phi}_{xa}$	Experimental modal matrix at ‘a’ DOFs
$\boldsymbol{\phi}_{xd}$	Experimental modal matrix at ‘d’ DOFs
$\boldsymbol{\phi}_{xdm}$	Experimental modal matrix at ‘d’ DOFs and ‘m’ modes
$\boldsymbol{\phi}_{xdr}$	Experimental modal matrix at ‘d’ DOFs and ‘r’ unmeasured modes
$\boldsymbol{\phi}_{xam}$	Experimental modal matrix at ‘a’ DOFs and ‘m’ modes
$\boldsymbol{\phi}_{xar}$	Experimental modal matrix at ‘a’ DOFs and ‘r’ unmeasured modes
$\boldsymbol{\phi}^{*}_{xam}$	Complex experimental modal matrix at ‘a’ DOFs and ‘m’ modes
$\boldsymbol{\phi}^{*}_{xar}$	Complex experimental modal matrix at ‘a’ DOFs and ‘r’ unmeasured modes
$\boldsymbol{\psi}_{xam}$	Experimental unscaled modal matrix at ‘a’ DOFs and ‘m’ modes
$\boldsymbol{\alpha}_{xm}$	Diagonal matrix containing the experimental scaling factors
$\widehat{\boldsymbol{\phi}}_{xam}$	Experimental modal matrix with errors in the mode shapes
$\boldsymbol{\phi}_{x\varepsilon}$	Experimental strain modal matrix
$\boldsymbol{\phi}_{x\varepsilon m}$	Experimental strain modal matrix with ‘m’ modes
$\boldsymbol{\phi}_{x\varepsilon am}$	Experimental strain modal matrix at ‘a’ DOFs and ‘m’ modes
$\boldsymbol{\phi}_{x\varepsilon ar}$	Experimental strain modal matrix at ‘a’ DOFs and ‘r’ unmeasured modes
$\boldsymbol{\psi}_{\varepsilon xam}$	Experimental unscaled strain modal matrix at ‘a’ DOFs and ‘m’ modes
$\boldsymbol{\alpha}_{\varepsilon xm}$	Diagonal matrix containing the experimental strain scaling factors
$\boldsymbol{\phi}_{x\sigma}$	Experimental stress modal matrix
$\boldsymbol{\phi}_{FE}$	Numerical modal matrix
$\boldsymbol{\phi}_{FEa}$	Numerical modal matrix at ‘a’ DOFs
$\boldsymbol{\phi}_{FEd}$	Numerical modal matrix at ‘d’ DOFs
$\boldsymbol{\phi}_{FEam}$	Numerical modal matrix at ‘a’ DOFs and ‘m’ modes
$\boldsymbol{\phi}_{FEdm}$	Numerical modal matrix at ‘d’ DOFs and ‘m’ mode
$\boldsymbol{\phi}_{FEar}$	Numerical modal matrix at ‘a’ DOFs and ‘r’ unmeasured modes
$\boldsymbol{\phi}_{FEdr}$	Numerical modal matrix at ‘d’ DOFs and ‘r’ unmeasured modes
$\boldsymbol{\phi}_{FE\varepsilon}$	Numerical strain modal matrix
$\boldsymbol{\phi}_{FE\varepsilon am}$	Numerical strain modal matrix at ‘a’ DOFs and ‘m’ modes
$\boldsymbol{\phi}_{FE\varepsilon ar}$	Numerical strain modal matrix at ‘a’ DOFs and ‘r’ unmeasured modes
$\boldsymbol{\phi}_{FE\sigma}$	Numerical stress modal matrix
$\widetilde{\boldsymbol{\phi}}_{xam}$	Expanded experimental mode shapes at ‘a’ DOFs and ‘m’ modes
$\widetilde{\boldsymbol{\phi}}_{xdm}$	Expanded experimental mode shapes at ‘d’ DOFs and ‘m’ modes

$\widetilde{\boldsymbol{\phi}}_{\boldsymbol{x\varepsilon}}$	Expanded experimental strain mode shapes
$\widetilde{\boldsymbol{\phi}}_{\boldsymbol{x\varepsilon am}}$	Expanded experimental strain mode shapes at ‘a’ DOFs and ‘m’ modes
$\widetilde{\boldsymbol{\phi}}_{\boldsymbol{x\varepsilon d}}$	Expanded experimental strain mode shapes at ‘d’ DOFs and ‘m’ modes
$\widetilde{\boldsymbol{\phi}}_{\boldsymbol{x\varepsilon m}}$	Expanded experimental strain mode shapes with ‘m’ modes
$\widetilde{\boldsymbol{\phi}}_{\boldsymbol{x\sigma}}$	Expanded experimental stress mode shapes
$\widetilde{\boldsymbol{\phi}}_{\boldsymbol{x\sigma am}}$	Expanded experimental stress mode shapes at ‘a’ DOFs and ‘m’ modes
$\widetilde{\boldsymbol{\phi}}_{\boldsymbol{x\sigma dm}}$	Expanded experimental stress mode shapes at ‘d’ DOFs and ‘m’ modes
$\widetilde{\boldsymbol{\phi}}_{\boldsymbol{x\sigma m}}$	Expanded experimental stress mode shapes with ‘m’ modes
$\boldsymbol{\Delta\phi_{xFE}}$	Error between experimental mode shapes $\boldsymbol{\phi_{xam}}$ and numerical mode shapes $\boldsymbol{\phi_{FEam}}$
$\boldsymbol{\Delta\phi_{xam}}$	Error between experimental $\boldsymbol{\phi_{xam}}$ and expanded $\widetilde{\boldsymbol{\phi}}_{\boldsymbol{xam}}$ mode shapes
$\boldsymbol{\Delta\phi_{x\varepsilon am}}$	Error between experimental $\boldsymbol{\phi_{x\varepsilon am}}$ and expanded $\widetilde{\boldsymbol{\phi}}_{\boldsymbol{x\varepsilon am}}$ strain mode shapes

“El comienzo de la sabiduría es el silencio.”

Pitágoras

Content

1

Introduction

1.1 Research context and problem statement

Structures and their components are subjected to dynamic loads, such as waves, wind, and traffic, among others. These time-dependent loadings generate strains and stresses with variable amplitudes, potentially leading to fatigue failure. Even when the maximum stress remains well below the material's yield strength it can still cause fatigue failures in the long-term.

Fatigue failure in concrete and metal structures involves the initiation and propagation of cracks due to repetitive or cyclic loading. These loads cause microscopic imperfections in the material to grow into macroscopic cracks. Subsequently, the crack can propagate until it reaches a critical size, leading to a fatigue failure of the structure. Fatigue failures in structures have caused numerous incidents and catastrophic accidents in recent decades, resulting in significant material, economic, and human losses.

Several types of structures are subjected to variable loading, making them prone to fatigue failure. Given the potential for severe consequences in the event of collapse, it is crucial to monitor their structural health. Some examples of such structures are presented below:

- ***Road bridges*** are one of the most essential, costly, and vulnerable elements of the transportation network. Moreover, the lack of maintenance and the aging of structures is affecting bridges worldwide. In the case of Europe, most transport bridges constructed after 1945 were designed with a lifespan of 50 to 100 years [1].

In the case of USA, according to a report issued in 2021 by the American Society of Civil Engineers (ASCE), 7.5% of the 600.000 highway bridges are in poor condition, and the estimated cost of their repair is $123 billion [2]. Additionally, 42% of the bridges are over 50 years old. In Europe, the BRIME project determined in 2001 that, road bridges in three different European countries - France, UK and Germany - had deficiencies in 39%, 30% and 37% of cases, respectively [3]. In Spain, according to a report published in 2018, the Spanish highway network (Red de Carreteras del Estado) includes nearly 23.000 bridges, of which 66 show potentially serious issues that could compromise their load capacity.

These issues, along with several bridge collapses in last decades (A-6 Castro viaducts 2022 and Morandi Bridge 2018), which resulted in severe consequences - human casualties, economic losses, and transport network disruptions - highlight the critical importance of assessing and monitoring the health of bridges and viaducts.

- ***Railway bridges*** play a crucial role in promoting sustainable mobility, especially within the context of the European Green Deal and the mobility strategy, which aims to double high-speed rail traffic by 2030 and triple it by 2050. This has raised concerns about vibrations induced by rail traffic, which can lead to loads exceeding design limits [4], [5]. Therefore, it is essential to assess the current structural health of these structures to make informed decisions about their future use and ensure their safety.

- Another type of structures significantly affected by dynamic loads, and prone to fatigue failure, are ***wind turbines***. Wind energy has proven to be a key energy source in the European Union's energy transition, growing rapidly and surpassing coal in installed capacity in 2016. In 2023, Europe had 272 GW of installed wind capacity, 87% onshore and 13% offshore. By 2030, the total capacity is expected to reach 420 GW [6]. However, wind energy faces several challenges, as many of the current wind turbines have a design life between 20 and 25 years and are nearing the end of their life. Additionally, limited technical knowledge, the increasing size of wind turbines, and their offshore installation present new challenges [7], [8]. Therefore, wind turbines monitoring aims to detect stiffness losses caused by damage, as well as assess the remaining fatigue life of these structures. This information is crucial for future decisions regarding maintenance, inspections, and extending their operational life.

- Solar energy is also crucial in the green transition, with photovoltaic energy being the most popular. In 2023, Europe had 260 GW of solar power capacity, and to reach the 2030 targets, it is projected to install an average of 45 GW per year [9]. Currently, to maximize energy production, single-axis ***solar trackers*** are commonly used in large photovoltaic installations [10]. Since they are located in open areas without barriers, these structures are exposed to significant wind loads [11]. Furthermore, due to the ongoing effort to reduce manufacturing costs, materials with higher strength are being used, decreasing the thickness of the structural elements. This reduction in thickness decreases their stiffness, making structures more vulnerable to the dynamic effects of wind.
- In addition to conventional photovoltaic systems, there are also ***floating solar panels***, which are used in both freshwater and marine environments. In the case of systems installed in freshwater, a regulatory framework has been published, which includes some design guidelines addressing aspects such as fatigue [12], [13]. However, marine solar panels face greater challenges due to harsh environmental conditions, such as extreme wind and wave loads. Moreover, the technical knowledge and specific regulations for these systems are limited, posing difficulties in both their design and long-term operation [12].
- There are also ***other*** types of structures that may also be subjected to dynamic loads, making it important to assess their health and remaining fatigue life. These include metal structures exposed to wind loads, such as antennas and transmission towers, as well as chimneys and buildings of significant heritage value.

The large number of structures subjected to dynamic loads and potentially susceptible to fatigue failure highlights the importance of this phenomenon, and consequently, the significance of fatigue design and monitoring.

Fatigue design refers to the calculation of accumulated fatigue damage over the design life of structures. Although there are approaches based on strain, energy, and fracture mechanics, the most established practice in fatigue design is stress-based and consists of the following steps: (i) determining the stress time series, (ii) calculating the stress spectrum (cycle counting techniques), and (iii) evaluating the total fatigue damage. The main sources of uncertainty are the fatigue material characterization and the real stress time histories. Regarding the fatigue material characterization, the S-N field and the Miner's Rule are widely accepted in both academia and industry. Regarding the real stress time histories, they are often unknown, so simplified load models are commonly employed. However, these models do not capture, with the necessary accuracy, the load characteristics (variable amplitude, random nature, frequency bandwidth, sequence effect, etc.). Therefore, the determination of the loading scenarios to which the structure will be subjected is crucial. To minimize errors from these and other assumptions during the design phase, the monitoring of structural health in service is a viable solution.

Structural Health Monitoring (SHM) generally refers to any type of damage detection procedure for civil, aerospace or mechanical engineering structures. Currently, there is a vast amount of literature related to vibration-based SHM [14]–[18], and there are several successful applications in real structures and companies specialised on implementing these systems. SHM techniques allow for damage detection, localization, assessment, and prediction [19], however, most of the applications and literature about SHM is focused on damage detection, whereas damage localization presents many challenges. SHM techniques for damage assessment allow for quantifying the damage of the structure, which could include fatigue damage, however, damage assessment and prediction in SHM are still being explored with almost no real applications. Therefore, predicting remaining life and making informed decisions based on real data is still not possible. For this reason, it is essential to continue researching in fatigue monitoring of structures to prevent future structural failures similar to those that have occurred in recent years.

Continuous fatigue monitoring refers to the calculation of accumulated fatigue damage in real time during the period that the structure is in operation, therefore, it can also be used for determining the remaining fatigue life of structures. Continuous fatigue monitoring of structures can be divided into five phases: (i) identification of the most likely critical components and locations to suffer fatigue damage, (ii) sensor location strategy, (iii) measurement or estimation of strains/stresses at the locations of interest in real-time, (iv) calculation of the stress spectrum using cycle counting techniques and evaluation of the total fatigue damage , and (v) calculation of the remaining life. The measurement or estimation of stresses is the most advantageous aspect of fatigue monitoring, as it avoids errors associated with simplified loading models. Stresses can be obtained measuring directly with strain sensors installed at the locations of interest, or they can be estimated from the experimental response of the structure using modal superposition techniques. The structure's response is usually known at a limited number of locations, so it must be expanded to the points of interest using modal expansion techniques. Modal expansion is commonly performed using the mode shapes extracted from a numerical model of the structure (Figure 1.1).

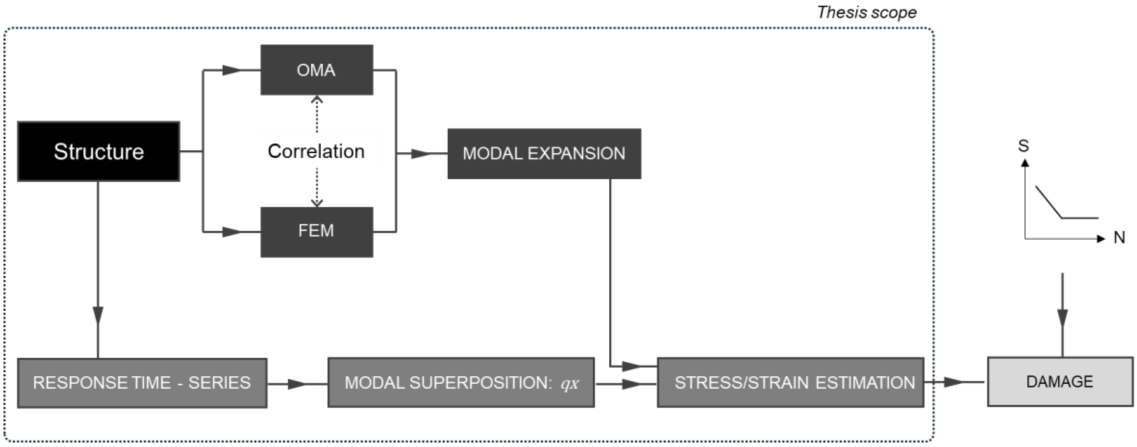

Figure 1.1 Fatigue monitoring phases and thesis scope.

Fatigue monitoring techniques can also be easily combined with other SHM techniques. Specifically, the experimental responses of the structure can be used simultaneously for fatigue assessment and for detecting damage through vibration-based SHM by tracking modal parameters.

Fatigue monitoring can enhance decision-making related to the maintenance, inspection, life extension, or demolition of structures. This optimizes the use of structures and resources, improving sustainability and reducing the carbon footprint. The reduction of fatigue failures in structures, also prevents the associated economic, material, and human losses. Moreover, the growing importance of fatigue monitoring is underscored by the rise of lightweight slender structures, which are more vulnerable to dynamic loads and fatigue. However, the literature on fatigue monitoring is limited, and real applications or companies offering these services are even rarer [8], [20], [21]. This lack of knowledge is largely attributed to existing challenges, the most significant being the difficulty in accurately determining the stresses acting on the structure of interest. Therefore, developing new methodologies for model correlation and updating, as well as improving existing ones, is crucial, since most stress estimation techniques require the use of updated numerical models to expand the measured responses.

1.2 Objectives

According to the previous ideas, the main objectives of this thesis are as follows:

1. **To develop a methodology for fatigue monitoring of structures, combining a numerical model and the experimental response of the structure measured at discrete points.** In order to achieve this objective, the following specific objectives have been set:

- To review the existing literature about structural health monitoring and fatigue monitoring of structures.
- To develop a general framework for monitoring the accumulated fatigue damage at critical points of structures in real time.

2. **To propose and validate novel indicators for correlation of numerical and experimental models.** Specific objectives:
   - To review the existing literature about model correlation.
   - To propose new model correlation indicators able to identify if the discrepancies between models can be attributed to mass, stiffness or both.
   - To propose a new version of the modal assurance criterion (MAC) that overcomes the inconveniences of MAC in the case of repeated or closely spaced modes.
   - To validate the proposed model indicators with numerical simulations and experimental examples.
3. **To propose, compare and validate real time stress estimation techniques based on modal superposition and on the expansion of experimental mode shapes and/or strain mode shapes.** Specific objectives:
   - To review the existing literature about mode shape expansion and stress estimation.
   - To propose real time stress estimation techniques based on the projection of the experimental responses on the subspace spanned by the experimental mode shapes.
   - To propose real time stress estimation techniques based on the projection of the experimental responses on the subspace spanned by the numerical mode shapes.
   - To study the sources of error in stress estimation.
   - To compare and validate the proposed methods with numerical simulations and experimental tests.

1.3 Thesis outline

Accordingly, this thesis is organized in the following chapters:

- Chapter 1: Introduction

  This chapter provides an overview of the topic addressed in the thesis. First, the context of fatigue design in structures is introduced, followed by a statement of the associated problems. The importance of structural monitoring is emphasized, while the limitations of SHM are presented. In response to these limitations the advantages of fatigue monitoring are presented. Then, the main objectives of the thesis are outlined to finish with the organization of the text.

- Chapter 2: Structural Health Monitoring

  The state of the art of SHM techniques is presented, focusing on vibration-based SHM techniques, thus, modal analysis and operational modal analysis are introduced. Moreover, a fatigue damage methodology is proposed, and its main phases are explained.

- Chapter 3: Model Correlation

  Chapter 3 outlines various applications of correlation techniques, highlighting their relevance in the engineering field and the most commonly used correlation techniques are presented and classified. New correlation indicators based on structural dynamic modification are proposed to detect discrepancies in mass, stiffness or both. Additionally, insights into mode shape rotation, shear, and scaling are provided. Finally, three case studies are presented to validate the proposed indicators, assess their limitations, and explore their implications for future applications.

- Chapter 4: Stress estimation

  This chapter presents the state of the art in stress estimation techniques using structural response measurements, with a focus on methods employing modal superposition and modal expansion. The theory underlying stress estimation techniques is presented, including the exact solution, various modal expansion approaches, and methods for obtaining modal coordinates. With this foundation, eight methods for estimating stresses and strains are proposed. Finally, considerations regarding errors in modal coordinates and estimated results are presented, along with comments on scaling.

- Chapter 5: Application cases

  Three application cases are presented in this section to validate the methods proposed in Chapter 4, along with the correlation indicators introduced in Chapter 3. A numerical case involving a cantilever beam is considered to avoid potential error sources from the experimental measurements or signal processing. Additionally, an experimental case of a monolithic glass beam and an experimental case of a cantilever beam are employed to validate the methods under real conditions.

- Chapter 6: Conclusions and future work.

  The main conclusions of this PhD thesis are presented in this chapter, organized according to the proposed objectives. The main possible research activities for continuing the advancements achieved in this thesis are described.

2

Structural Health Monitoring

The purpose of this chapter is to review the existing literature on SHM techniques, with a focus on modal-based SHM methods due to their relevance and ease of integration with fatigue monitoring. Additionally, a fatigue monitoring method is developed, and the main phases are outlined in detail.

This chapter provides a comprehensive understanding of the overall fatigue monitoring methodology, serving as a framework for the subsequent chapters, which will focus on specific phases of the fatigue monitoring process.

2.1 Introduction to SHM

Structural health monitoring generally refers to any type of damage detection procedure for civil, aerospace or mechanical engineering structures [22]. This process involves: (i) the observation of a system over time using periodically spaced measurements, (ii) the extraction of appropriate damage-sensitive features from these measurements and (iii) the subsequent analysis of these features to determine the current state of the system's health [23]. For this reason, SHM is considered an alternative to current local inspection methods, which are more expensive for large structures.

2.1.1 Classification of SHM techniques

Different possible classifications of SHM techniques can be done:

- *Continuous* or *intermittent* methods, based on the frequency of their application. Intermittent techniques measure responses for specific periods of time and no information is gathered the rest of the time. By contrast, in continuous monitoring, information must be transmitted in real time to the site where the measurements are processed [24].
- *Local* and *global* methods, based on the scope of the variables. This classification is usually based on the relation of the wave length of the test signals with respect to the defect size as well as the overall structural dimensions. An example of local methods is the use of high-frequency ultrasonic waves, whose wavelengths should be smaller than the size of the defect to be detected. By contrast, global methods typically use the lower modes of the structure [25].
- *Static* and *dynamic* methods. Static methods measure changes in static responses, whereas dynamic methods make use of the structure's vibration properties [26]. This is the most commonly used classification (Figure 2.1) and will be further developed in this document as follows.

Although static methods can be used for a wide range of applications and are a powerful tool in masonry heritage structures [27], they are rarely used in other civil and mechanical structures. Dynamic methods, which are commonly employed, use vibration responses to gather information about changes in a structure's dynamic properties, enabling the monitoring of its health [18]. Dynamic SHM methods can be classified into *model-based SHM* or *data-based SHM*.

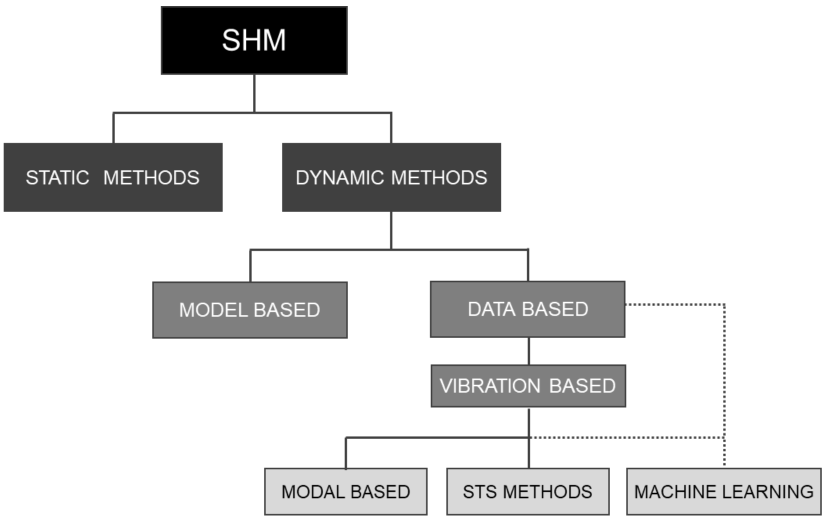

Figure 2.1: Classification of SHM methods.

- Model-based SHM consists of creating a finite element model, which is later used to identify and localize damage in either mass or stiffness [28], [29]. The accuracy provided by the finite element model depends on the level of correlation with the real structure.
- Data-based SHM uses real data of a structure obtained through experimental measurements. It involves the observation of a system over time using experimental responses measured through an array of sensors and the extraction and analysis of damage-sensitive parameters. The structure's undamaged state, which corresponds to the healthy structure, is used as a pattern. Then, data obtained from posterior measurements are compared with the healthy state. Data-based techniques which rely on the measurement of vibration signals are known as *vibration-based methods* [30]–[32].

Vibration-based SHM can be divided into *modal-based methods* and *statistical time series (STS) methods*:

- Modal-based methods use one or a set of the following modal parameters as damage-sensitive parameters: natural frequencies, mode shapes, strain mode shapes and/or other variables dependent on modal parameters (frequency response functions, change in flexibility, etc.). To obtain this modal parameters, modal analysis [33] is used, specifically operational modal analysis (OMA) is attractive in many situations because it does not require excitation to be measured, which is very practical for large structures as it is an output-only technique [34]. In modal-based SHM, automated modal analysis and automated damage detection techniques must be used to work in real time.
- STS methods combine random excitations and/or response signals with statistical and decision-making tools to infer the state of a structure [35]. Non-parametric STS methods are based on non-parametric time series representations, such as PSDs, frequency response functions and residual variances. Parametric STS methods are based on time series representations, such as autoregressive moving average models.

Additionally, *machine learning (ML) for SHM* consists of data-driven approaches (usually vibration-based) which have gained popularity in recent years due to technological advancements [36]. It refers to a set of algorithms that are capable of learning from available response data by automatically extracting hidden patterns from large datasets to make predictions. Several ML methods are based on identifying certain modal parameters from the structural system, and then, the trained ML system is utilised to identify the presence and location of structural damage.

2.1.2 Modal-based SHM

Among the SHM techniques previously presented, modal-based SHM is perhaps one of the most popular for the monitoring of civil structures due to recent developments in the field of OMA and the availability of several robust and automated OMA algorithms [37].

Modal-based SHM methods use modal parameters estimated by modal analysis techniques from the experimental responses of the structure. Changes observed in modal parameters with respect to a predefined reference condition are used as indicators of the formation, location and severity of damage.

Modal Analysis

Modal analysis is used to characterise a structure's dynamic behaviour by separating a structure's response into vibration modes which are defined by the following modal parameters: natural frequencies, mode shapes, damping ratios and modal masses. Modal analysis is termed theoretical modal analysis when modal parameters are determined using an analytical model or a numerical model (Figure 2.2). On the other hand, when modal parameters are determined using an experimental approach, modal analysis is known as experimental modal analysis (EMA) or OMA, depending on the type of excitation used in the experiments.

- EMA: Both, excitation forces and responses must be known to determine modal parameters [33]. The loading used to excite the structure is commonly artificial, and no other excitation loading is allowed when using this technique.
- OMA: It is used to determine modal parameters without knowledge of the input excitation. In short, the forces which are naturally present during the operation of the structure are used as excitation and not measured. A stochastic framework is used in OMA, assuming that the excitation is Gaussian white noise [38].
- When both artificial and operational forces are acting on a structure, OMA and EMA can be combined in the identification process. This technique is called operational modal analysis with exogenous input (OMAX) [39] or operational modal analysis with harmonic (OMAH) excitation [40].

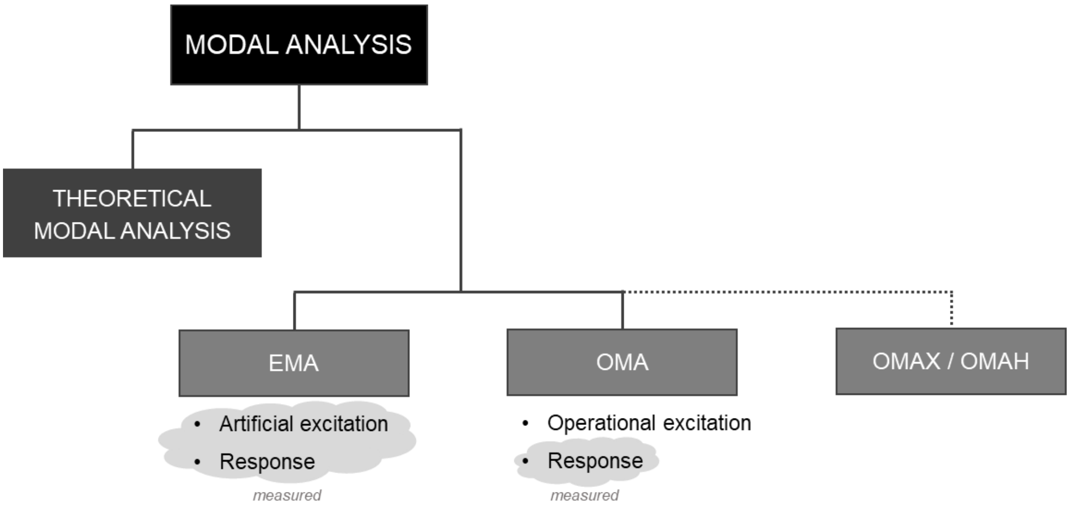

Figure 2.2: Classification of modal analysis techniques.

Due to the significant advantages of measuring only the system's responses (tests are cheap and fast and they do not interfere with the normal use of the structure), especially in large structures, OMA is more commonly employed.

Operational Modal Analysis (OMA)

In OMA, modal parameters can be estimated using different identification techniques, which can be classified as [37]:

- *Parametric* and *non-parametric* methods. In parametric methods a model is fitted to data whereas non-parametric methods work directly with the data. Parametric methods are more complex and present a higher computational cost, however they usually perform better. Non-parametric methods are faster and easier to use.
- *Single degree of freedom* (*SDOF*) and *multi-degree of freedom* (*MDOF*), depending on the number of modes in a given bandwidth. SDOF methods assume that only one mode is dominant in that frequency range. These methods are very fast, however, if repeated modes or closely spaced modes are present, MDOF techniques are required.
- *One-stage* methods and *two-stage* methods. In one-stage methods all modal parameters are estimated at the same time. In two-stage methods some parameters are estimated first, and the remaining parameters are estimated in a second step.
- *Time domain methods* and *frequency domain* methods. Time domain methods are based on the analysis of time histories or correlation functions, whereas frequency domain methods are based on spectral density functions.

The most common estimation techniques used in OMA are the following: in the frequency domain, the *peak-picking (PP)* and the *frequency domain decomposition* (*FDD*) are the most popular non-parametric techniques. The *least squares complex frequency* (*LSCF*) method and the *poly-reference least squares complex frequency* (*p-LSCF*) method are the most used parametric methods. In the time domain, the most popular techniques are those based on stochastics subspace identification (SSI), such as the *covariance-driven stochastic subspace identification* (*SSI-COV*) and the *data-driven stochastic subspace identification* (*SSI-DD*).

When OMA is used in SHM, automated modal analysis is required, i.e. estimation techniques must be automated.

Automated modal analysis

In SHM, considerable data must be processed in a short amount of time; thus, methodologies to automatically estimate modal parameters have gained attention in recent years. Specifically, numerous automated techniques for OMA have been reported in the literature in both the time and frequency domains, which can also be classified as parametric and non-parametric methods:

- *Non-parametric* frequency domain methods are based on selecting the peaks of variables derived from frequency response functions or PSDs [41], [42].
- Automated *parametric methods* are based on the automated interpretation of stabilisation diagrams, which involves tracking estimates of modal parameters as a function of model order [43], [44]. As the model order increases, the estimates of physical modal parameters stabilise. Poorly excited modes may not stabilise until a very high model order, whereas very active modes stabilise at a very low model order.
- A combination of *parametric* and *non-parametric* algorithms can also be used for automated modal analysis, such as the second-order blind identification (SOBI) and the popular covariance-driven stochastic subspace identification (SSI-COV) [45].

2.1.3 Damage detection and localisation

In this section, damage detection and localisation techniques based on modal analysis are commented. However, damage detection and localisation techniques are based on model correlation techniques, which are going to be detailed in Chapter 3.

The most common modal-based techniques used to ***detect damage*** are the eigenfrequency method, which is used to monitor changes in natural frequencies, and eigenvector-based criteria, which are used to monitor changes in mode shapes. However, other techniques could also be applied (Figure 2.3).

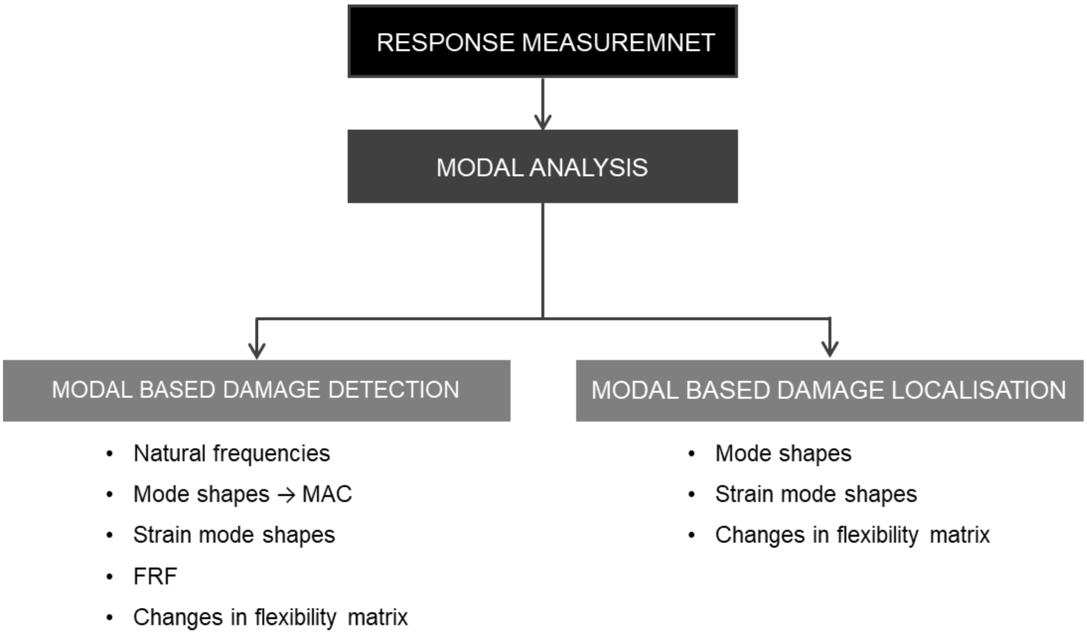

Figure 2.3: Damage detection and localisation method.

One of the advantages of *natural frequencies* is that they are very sensitive to damage. However, they are also sensitive to other mechanical and environmental effects. It is well-known that changes in temperature, wind velocity, wave height, wind direction, and wave directionality modify natural frequencies [46], [47].

The criteria based on eigenvectors compares a set of *mode shapes*. The best-known method is the modal assurance criterion (MAC) [48], [49], which compares the shapes of two eigenvectors based on the inner product of both vectors. Mode shapes are affected by damage, however, for low severity damage the method indicates damage only in higher-order modes, which are more sensitive to damage but also more difficult to identify in real-life situations. Moreover, the estimation of mode shapes is not as precise as the estimation of natural frequencies [50].

Techniques based on monitor *strain mode shapes* have also been proposed in the literature. They are based on the relationship between mode shape curvatures and flexural stiffness. The modal curvatures of the lower modes are generally more accurate than those of higher modes [50].

Changes in *frequency response functions* or *flexibility* [51] can be also used to detect damage. The computation of flexibility matrices from vibration data requires mass-normalized mode shapes. If

OMA is used to estimate modal parameters, an additional technique to scale the mode shapes is needed.

In the case on modal-based ***damage localisation*** methods (Figure 2.3), they are traditionally based on changes in mode shapes, mode shape derivatives or flexibility matrices assembled from available modes. Although mode shapes can be easily estimated using modal analysis, the localisation of damage based on the curvature of mode shapes has been shown to be more sensitive to damage than mode shapes [52], using for example the curvature damage factor (CDF) [50].

2.2 Fatigue design and fatigue monitoring

Different approaches for fatigue assessment exist, such as stress-based, strain-based, energy-based, and fracture mechanics methods [53]. Stress-based models are mainly used to predict fatigue life for high-cycle fatigue, whereas strain-based models are suitable for low-cycle fatigue in which plastic deformation is significant. Energy-based models can consider out-of-phase hardening behaviour because both the stress and strain terms are inherent in the energy expression [54]. Moreover, for welded details, a fatigue approach based on nominal or geometrical stress is preferred to local approaches based on continuum mechanics [55].

As previously commented, a well-established stress-based practice in fatigue design consists of three steps: (i) the determination of stress time histories (ii) the calculation of the fatigue stress spectrum, and (iii) the evaluation of total fatigue damage. Regarding the determination of stress time histories in fatigue design, simplified fatigue loading models from codes and standards are commonly used, as no information about the loads that will affect the structure is available.

In fatigue monitoring this assumption is avoided and the structure response is used to estimate the real stress time histories. In fatigue monitoring, the following steps are required:

1. The structure's hot spots must be known. Thus, the most probable locations and components of suffering fatigue damage must be identified as points of interest.
2. A sensor location strategy must be stablished.
3. Estimation (or measurement) of strains/stresses at the locations of interests. Although a brief introduction is done in section 2.2.1, different methods to estimate stresses will be proposed in Chapter 4.

4. Calculation of the fatigue stress spectrum and the total fatigue damage. The existing methodologies are explained in section 2.2.2.
5. Calculation of the remaining life.

2.2.1 Stress estimation or measurement

To obtain the stress time history response from all relevant locations, two commonly applied methodologies are used:

- The stress time histories at discrete points of interest can be obtained directly from strain gauge measurements located at the same discrete points. However, in many cases, it is not possible to make measurements at every position of interest due to economic constraints, inaccessibility, or harsh environment. Moreover, strain gauges are fragile, have a life expectancy of only a few years and often unreliable for long time measurements.
- Stress time histories can be estimated from structural responses by continuously measuring experimental displacements, velocities, accelerations or strain responses. Accelerometers are commonly used due to their reliability for long-term measurements. This approach allows for the estimation of stresses at any point of the structure using a limited number of installed sensors. There are different techniques for stress/strain estimation, with *modal expansion* and the *Kalman filter* techniques being the most used.

The core of modal expansion is the modal superposition principle; thus, strain mode shapes and modal coordinates are required. Moreover, to perform modal expansion, a numerical model of the structure is commonly used, usually a finite element model. For this reason, special attention should be given to model correlation, as the accuracy of the results depends on the similarity between the experimental and numerical models. If the correlation is not satisfactory, model updating techniques must be used to modify the finite element model.

Stress estimation techniques based on modal expansion techniques are thoroughly explored in Chapter 4, with various methods proposed based on the source of the strain mode shapes and the approach used to obtain the modal coordinates.

2.2.2 Accumulated fatigue damage

Methodologies applied in fatigue damage assessment were traditionally formulated in both time and frequency domains, being time domain methods firstly formulated, and more frequently applied

(Figure 2.4). However, frequency domain or spectral methods allow complex loading histories to be directly and rapidly computed as part of a more consistent statistical and analytical approach.

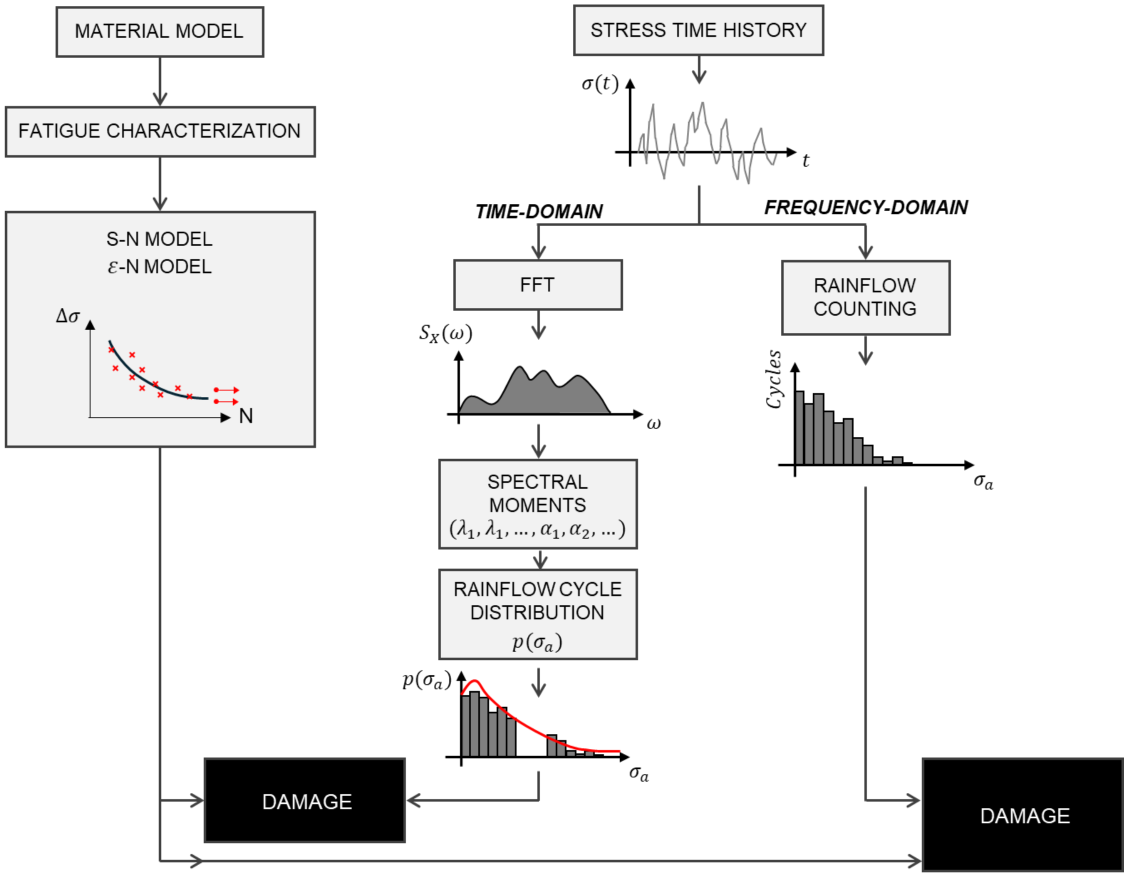

Figure 2.4 Fatigue damage assessment from both time-domain and frequency-domain approaches.

Time domain methods

The analysis of stress time histories is accomplished using different counting algorithms, such as the rainflow method [56], to obtain an equivalent set of counted cycles with constant amplitudes. Despite being widely used as a reference procedure, the rainflow method entails some important disadvantages, such as its dependence on the particular time window selected in the loading history and its time-consuming nature.

After that, numerous damage fatigue models can be applied. Five different categories can be distinguished:

- *Linear damage models*. Palmgren [57] was the first who proposed a linear fatigue damage rule and Miner [58] subsequently popularised it as one of the most widely applied approaches to calculating damage, due to its easy formulation, which is only based on the ratio between the applied cycles n_i and the total cycles to failure N_i for the i-th load level, i.e.:

$$D = \sum_{i=1}^{k} \frac{n_i}{N_i} \tag{2.1}$$

where D is a damage index ($0 \leq D \leq 1$) and k is the number of different stress levels considered in the analysis.

Linear accumulation models use the S-N curve from constant amplitude tests (Figure 2.5). Moreover, they assume no load sequence effects and no damage for stress repetitions below the fatigue limit [59].

Double linear models were also proposed in the literature by other authors such as: Manson and Halford, Langer and Grover [60]–[62] (Figure 2.5). Despite being widely applied, its main drawbacks are its independence with respect to both load level and load sequence.

In variable amplitude loading, stress repetitions below the fatigue limit also cause damage. Some models have been proposed by Haibach and Corten and Dolan to account for this effect.

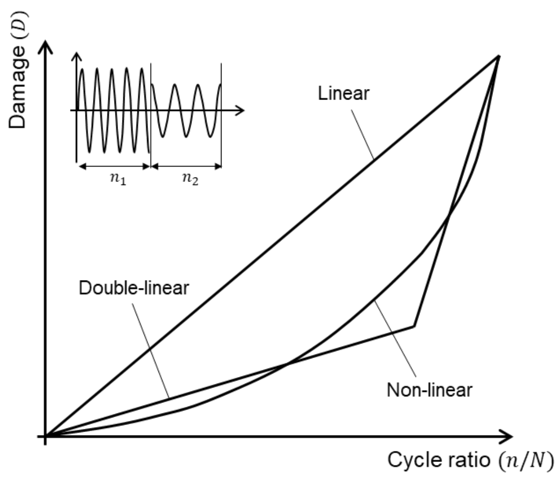

Figure 2.5: Illustration of fatigue damage rules, including linear, double-linear and non-linear models.

- *Non-linear damage models.* In an attempt to improve the incongruences of linear damage rules, non-linear damage rules have been proposed in the literature [63], [64] by Richart and Newmark and Marko and Starkey, such as those based on powering the cycle ratio n_i/N_i, i.e.:

$$D = \sum_{i=1}^{k} \left(\frac{n_i}{N_i}\right)^{x_i} \tag{2.2}$$

- *Energy-based damage models*. As an alternative to previous phenomenological approaches, different energy-based definitions of fatigue damage are available. Watson [65] proposed an energy-based model based on the Smith–Watson–Topper parameter given by:

$$D = \frac{4\sigma_f'}{E}(2N_N)^{2b_1} + 4\sigma_f'\varepsilon_f'(2N_N)^{b_1+c_1} \tag{2.3}$$

  where σ_f' and ε_f' are fatigue strength and ductility coefficients, respectively; N_N is the number of reversals to failure; and b_1 and c_1 are constants that depend on an instantaneous strain-hardening law.

- *Continuum-based damage models*. This approach addresses the continuum mechanical behaviour of a medium in degenerating conditions. The proposal by Chaboche and Lesne [66] is one of the most representative of these models and it has been popularised as a highly non-linear damage rule that takes into account the mean stress effect:

$$D = 1 - \left[1 - \left(\frac{n}{N_N}\right)^{1/1-\alpha}\right]^{1/\beta-1} \tag{2.4}$$

  where α is a function of the stress state and β is a material function.

- *Probabilistic damage models*. Probabilistic approaches propose to consider probability p $(0 < p < 1)$ as a random fatigue damage index. Castillo et al. [67] derived the following probabilistic fatigue model:

$$p = 1 - exp\left[-\left(\frac{(logN - B)(log\Delta\sigma - C) - \lambda}{\delta}\right)^{\beta}\right] \tag{2.5}$$

  where B and C are the horizontal and vertical asymptotes (that is, the cycle value below which failure does not occur and the fatigue endurance limit, respectively), while λ, β and δ are the location, shape and scale Weibull parameters, respectively.

Frequency domain methods

Frequency domain fatigue methods make use of the spectral density function of the stress time histories, which can be classified in narrow-band (NB) or broad-band (BB) [68]. The former leads to simpler and easier formulations about statistical properties, while the latter offers more complex identification of stress cycles.

The statistical information contained in the spectral density $S_X(\omega)$ of a random process X can be summarised by means of the m-th spectral moments λ_m as follows:

$$\lambda_m = \int_{-\infty}^{\infty} \omega^m S_X(\omega) d\omega \qquad m = 0,1,2, \dots \tag{2.6}$$

From a statistical perspective, the rainflow cycle distribution could be considered a bivariate distribution with maximum and minimum stresses, $p_{RFC}(\sigma_{max}, \sigma_{min})$, or, equivalently, with mean and amplitude stresses, $p_{RFC}(\sigma_a, \sigma_m)$ [69]. However, due to the inherent complexity of peak-to-valley pairing procedures in the rainflow algorithm, there is no explicit analytical solution for the bivariate rainflow cycle distribution. Thus, it is usually simplified by neglecting the mean stress effect and considering only the stress amplitude; as a result, different approximate proposals $p_{RFC}(\sigma_a)$ are defined in the literature, with the following being the most widely applied:

- *Narrow-band approximation* is based on the assumption that the random process is of NB type; that is, each peak and valley is coincident with each cycle. Thus, the stress amplitude can be considered to follow a Rayleigh distribution as:

$$p_{RFC}^{NB}(\sigma_a) = \frac{\sigma_a}{\sigma_X^2} exp\left[-\frac{1}{2}\left(\frac{\sigma_a}{\sigma_X}\right)^2\right] \tag{2.7}$$

- *The Dirlik model* [70], [71] approximates the cycle amplitude distribution by using a combination of one exponential and two Rayleigh probability densities, i.e.:

$$p_{RFC}^{DK}(\sigma_a) = \frac{1}{\sigma_X}\left[\frac{D_1}{Q} exp\left(-\frac{Z}{Q}\right) + \frac{D_2 Z}{R^2} exp\left(-\frac{Z^2}{2R^2}\right)\right] \tag{2.8}$$

  where $Z = \sigma_a/\sigma_X$ is the normalized amplitude and D_1, D_2, Q and R are constants that depend on the spectral moments.

- *The Zhao and Baker model* [72] proposes a linear combination of the Rayleigh and Weibull probability density functions, which is expressed as:

$$p_{RFC}^{ZB}(\sigma_a) = w\alpha\beta Z^{\beta-1} exp(-\alpha Z^{\beta}) + (1-w) Z exp\left(-\frac{Z^2}{2}\right) \tag{2.9}$$

  where w is a weighting factor $(0 \leq w \leq 1)$ as a function of the spectral parameters and α and β are the scale and shape Weibull parameters, respectively.

- Tovo-Benasciutti [71], [73] proposed that the amplitude–mean joint probability distribution of rainflow cycles lies between two limit distributions and can be estimated as their linear combination:

$$p_{RFC}^{TB}(\sigma_a) = w\, p_{LCC}(\sigma_a, m) + (1 - w) p_{RC}(\sigma_a, m) \qquad (2.10)$$

  where w is a weight factor that must be determined. The two functions $p_{LCC}(\sigma_a, m)$ and $p_{RC}(\sigma_a, m)$ represent the amplitude–mean distributions of the level-crossing counting (LCC) and of the simple-range counting (RC).

Once the rainflow cycle distribution for the stress amplitude has been defined, the fatigue damage assessment can be performed using an S-N rule and the Miner rule. If the S-N curve is defined with the Basquin law ($s^k N = C$), the damage rate $\overline{D}_{RFC}$ (i.e. damage/sec) can be calculated as follows [74]:

$$\overline{D}_{RFC} = \nu_a C^{-1} \int_0^\infty \sigma_a^k p_{RFC}(\sigma_a) d\,\sigma_a \qquad (2.11)$$

where ν_a is the rate of occurrence of counted cycles (that is, counted cycles per second) and $p_{RFC}(\sigma_a)$ can be defined according to the previously mentioned proposals. Finally, from Eq. (2.11), total expected damage D until failure can be directly obtained as follows:

$$D = \overline{D}_{RFC}\, T_f \qquad (2.12)$$

where T_f is the time (in seconds) to failure (that is, the fatigue lifetime). Moreover, it should be noted that, depending on the particular analytical definition of the rainflow cycle distribution in Eq. (2.11), the total expected damage in Eq. (2.12) could be different.

3

Model correlation

The purpose of this chapter is to enhance the understanding of correlation methods, enabling a more accurate identification of similarities and discrepancies between two models, as well as the sources of these differences. Therefore, novel indicators are proposed: ***T-Mass*** and ***T-Stiffness***, along with a novel version of the MAC, named the ROTMAC.

Within the overall framework of this thesis, this chapter is crucial for fatigue monitoring and stress estimation. As previously discussed, fatigue monitoring relies on the accurate estimation of stresses in the structure's hot spots, which in most cases requires mode shapes and strain mode shapes from a numerical model. For these models to provide reliable results, their correlation with the real structure must be precise.

3.1 Introduction

Model correlation techniques are methods used in structural dynamics to compare two different models:

- Two experimental models can be compared for purposes of damage detection and SHM, as well as for comparing modal parameters estimated using different modal identification techniques.

- Two numerical models can be compared for mesh convergence investigations or for comparing a full model with a reduced model.
- An experimental model and a numerical model are usually compared in model updating procedures, usually to update a finite element model (FEM).

Starting with the applications of correlation techniques to compare ***two experimental models***, the following comments can be done. Regarding OMA identification techniques, in the case of the FDD, the MAC is used to define the single degree of freedom (SDOF) spectral density function, comparing the reference vector (singular vector at the picked frequency) with the singular vectors estimated on both sides of the picked frequency from the FDD [75]. In the case of time-domain techniques such as the SSI-COV, once the modal parameters are estimated for each model order, the spurious modes and the physical modes are separated using different stabilization criteria, most of them being based on the variation of modal parameters corresponding to two consecutive increasing orders. Correlation techniques are also crucial in the clustering process, where the estimated modes that represent the same physical mode are grouped, usually based on natural frequencies and mode shapes [76]–[78].

Two experimental models are also compared in modal-based SHM, where correlation techniques play also a significant role. In this context, correlation techniques are used to observe changes in the modal parameters to detect variations relative to a predefined reference condition (undamaged condition). Over the past decades, numerous methods have been proposed for damage detection, with the most common techniques relying on natural frequencies, mode shapes, and their derivatives [50]. However, a significant challenge in modal monitoring is the sensitivity of modal properties to environmental variations. Changes in weather conditions can alter the experimental modal parameters of a structure, being temperature one of the environmental factors that induces the greatest variation in the case of concrete and steel structures [79].

Another popular application of correlation techniques is model updating, where ***an experimental model and a numerical model*** are compared [80], [81]. Model updating methods are used to improve the correlation between numerical and experimental models by updating a finite element model. Model updating techniques can be classified into <u>*direct methods*</u> (or matrix methods) and <u>*iterative methods*</u> (parameter updating methods) [80]–[82]. Direct methods update the entries of the stiffness and mass matrices in a one-step procedure; however, the updated mass and stiffness matrices have limited physical meaning and cannot be directly related to physical changes in the finite element model [83]. Iterative methods modify iteratively some parameters, and they allow a wide choice of parameters to be updated. This requires a sensitivity analysis, where the user must preselect the physical parameters to be included in the analysis, thus iterative methods require some engineering judgment and expertise. Iterative methods can, in turn, be subdivided into *sensitivity methods* and *optimization methods* [83]. Another possible classification is to divide iterative methods into *deterministic methods* and *stochastic methods* [84].

An experimental model and a numerical model are also compared in model-based SHM, where a finite element model is required to predict the dynamic responses and to detect and locate damage. This numerical model must be well correlated with the real structure, requiring the application of correlation and model updating techniques.

As previously discussed, the applications of correlation techniques are numerous, spanning fields such as civil engineering (bridges, dams, towers, buildings, etc.), aerospace, and mechanical structures. This widespread use underscores their importance in ensuring structural accuracy and reliability. However, the success of these applications largely depends on the proper use of correlation techniques. The main correlation techniques proposed in the literature are classified into four categories:

- ***Eigenvalue-based criteria***. They compare a set of natural frequencies of two models. The Normalized Relative Frequency Difference (NRFD) is the most used method [80], [85], [86]. The NRFD corresponding to the j-th mode is calculated with the expression:

$$NRFD_j = \frac{|f_{Bj} - f_{Aj}|}{f_{Bj}} \tag{3.1}$$

  where f_{Bj} and f_{Aj} indicate the j-th natural frequency of the two models B and A, respectively. Similar indexes are the Natural Frequency Difference (NFD), which compares the relative difference between all natural frequencies, and the Natural Frequency Correlation Coefficient (NFCC), which gives the standard deviation of corresponding natural frequencies [87].

- ***Eigenvector-based criteria***. They compare a set of mode shapes. The best-known method is the modal assurance criterion (MAC) which compares the shapes of two eigenvectors based on the inner product [48], [49], [88]–[90]. If two vectors $\boldsymbol{\phi}_{Bi}$ (model B) and $\boldsymbol{\phi}_{Aj}$ (model A) are compared, the MAC is given by:

$$MAC(\boldsymbol{\phi}_{Bi}, \boldsymbol{\phi}_{Aj}) = \frac{\left|\boldsymbol{\phi}_{Bi}^{T}\, \boldsymbol{\phi}_{Aj}\right|^2}{\left(\boldsymbol{\phi}_{Bi}^{T}\, \boldsymbol{\phi}_{Bi}\right)\left(\boldsymbol{\phi}_{Ai}^{T}\, \boldsymbol{\phi}_{Aj}\right)} \tag{3.2}$$

where the superscript ‘T’ indicates transpose. MAC is always a real value so that if the vectors are complex the MAC is calculated with the expression:

$$MAC(\boldsymbol{\phi_{Bi}}, \boldsymbol{\phi_{Aj}}) = \frac{\left|\boldsymbol{\phi_{Bi}^{H}}\,\boldsymbol{\phi_{Aj}}\right|^2}{\left(\boldsymbol{\phi_{Bi}^{H}}\,\boldsymbol{\phi_{Bi}}\right)\left(\boldsymbol{\phi_{Ai}^{H}}\,\boldsymbol{\phi_{Aj}}\right)} \tag{3.3}$$

where the subscript ‘H’ indicates complex conjugate.

The modal assurance criterion takes on values from zero (representing no consistent correspondence), to one (representing a consistent correspondence). If the vectors are normalized to the unit length (vectors $\boldsymbol{\phi_{LBi}}$ and $\boldsymbol{\phi_{LAj}}$, where subscript ‘L’ indicates mode shape normalized to the unit length), Eq. (3.2) simplifies to:

$$MAC(\boldsymbol{\phi_{Bi}}, \boldsymbol{\phi_{Aj}}) = \left|\boldsymbol{\phi_{LBi}^{T}}\boldsymbol{\phi_{LAj}}\right|^2 \tag{3.4}$$

Several modifications or variants of the MAC have also been proposed in the literature. The AUTOMAC (MAC of a model with itself) is commonly used to detect spatial aliasing [89]. COMAC (Co-Ordinate MAC) correlates two models for each individual degree of freedom (DOF) [91]. The Mass-weighed MAC and Stiffness-weighed MAC, which include the mass or stiffness matrices, have also been proposed [33]. The $S2MAC$ [92], [93] can be used to correlate an experimental mode shape $\boldsymbol{\phi_{Aj}}$ with two closely spaced modes of a FE model $\boldsymbol{\phi_{B1}}$ and $\boldsymbol{\phi_{B2}}$, as:

$$S2MAC = \max_{\alpha,\beta}\left(\frac{\left|\boldsymbol{\phi_{Aj}^{H}}(\alpha\boldsymbol{\phi_{B1}} + \beta\boldsymbol{\phi_{B2}})\right|^2}{\boldsymbol{\phi_{Aj}^{H}}\boldsymbol{\phi_{Aj}}(\alpha\boldsymbol{\phi_{B1}} + \beta\boldsymbol{\phi_{B2}})^{H}(\alpha\boldsymbol{\phi_{B1}} + \beta\boldsymbol{\phi_{B2}})}\right) \tag{3.5}$$

- ***Frequency-response-based criteria***. They compare frequency response functions (FRF). The frequency response assurance criterion (FRAC) compares the FRF’s at a particular DOF, whereas the response vector assurance criterion (RVAC) compares the FRF’s for all the DOFs at just one frequency.

- ***Orthogonality criteria***. They are based on the orthogonality of mode shapes with respect to the mass and the stiffness matrices. Based on these properties, several techniques have been proposed. The cross-orthogonality check (COC) is obtained as the inner product of the experimental mode shapes ($\boldsymbol{\phi_A}$) over the numerical mass matrix ($\boldsymbol{M_B}$):

$$\boldsymbol{COC_1} = \boldsymbol{\phi_A^{T}}\boldsymbol{M_B}\boldsymbol{\phi_A} \tag{3.6}$$

The COC can also be defined as the inner product of the numerical mode shapes ($\boldsymbol{\phi_B}$) over the experimental mass matrix ($\boldsymbol{M_A}$):

$$\boldsymbol{COC_2 = \phi_B^T M_A \phi_B} \tag{3.7}$$

Another way of assessing correlation is with the pseudo-orthogonality check (POC). The inner product of the numerical and experimental mode shapes over the numerical mass matrix is defined as:

$$\boldsymbol{POC_M = \phi_B^T M_B \phi_A} \tag{3.8}$$

The POC can also be defined as the inner product of the numerical and experimental mode shapes over the stiffness matrix as:

$$\boldsymbol{POC_K = \phi_B^T K_B \phi_A} \tag{3.9}$$

Although NRFD and MAC are the most used correlation techniques, numerous correlation methods can be found in the literature. However, each correlation method compares a certain characteristic, i.e., a single technique capable of comparing two models with respect to different dynamic characteristics does not exist, and multiple methods are commonly used. Therefore, the previously described methods do not allow for determining whether the differences are due to discrepancies resulting from a change in mass, stiffness, or both. Identifying these discrepancies would help improve correlation techniques.

In this chapter, it is proposed to use the transformation matrix $\boldsymbol{T}$ as a new model correlation technique, using the orthogonality properties of the mode shapes with respect to the mass and stiffness matrices. Different correlation criteria to detect mass and stiffness changes, derived from $\boldsymbol{T}$ matrix, are proposed.

3.2 Structural dynamic modification and proposed criteria

In this section, a model B (unperturbed), defined with the mass matrix $\boldsymbol{M_B}$ and the stiffness matrix $\boldsymbol{K_B}$, is considered and perturbed with the mass change matrix $\boldsymbol{\Delta M}$ and stiffness change matrix $\boldsymbol{\Delta K}$. According to the structural dynamic modification theory, the mass matrix of the modified (or perturbed) system $\boldsymbol{M_A}$ can be expressed as:

$$\boldsymbol{M_A} = \boldsymbol{M_B} + \boldsymbol{\Delta M} \tag{3.10}$$

and the stiffness matrix $\boldsymbol{K_A}$ as:

$$\boldsymbol{K_A} = \boldsymbol{K_B} + \boldsymbol{\Delta K} \tag{3.11}$$

From the eigenvalue problem of the unperturbed system B:

$$\left(\boldsymbol{K_B} - \boldsymbol{M_B}\boldsymbol{\omega_B^2}\right)\boldsymbol{\phi_B} = \boldsymbol{0} \tag{3.12}$$

where $\boldsymbol{\omega_B^2}$ is a diagonal matrix containing the squared numerical natural frequencies of system B. For the perturbed system:

$$\left(\boldsymbol{K_A} - \boldsymbol{M_A}\boldsymbol{\omega_A^2}\right)\boldsymbol{\phi_A} = \boldsymbol{0} \tag{3.13}$$

where $\boldsymbol{\omega_A^2}$ is a diagonal matrix containing the squared numerical natural frequencies of system A. According to the structural dynamic modification theory, it is derived that the modal matrix $\boldsymbol{\phi_A}$ of the perturbed structure (usually the experimental model) can be expressed as a linear combination of the modal shape matrix of system $\boldsymbol{\phi_B}$ (usually the numerical model), as:

$$\boldsymbol{\phi_A} = \boldsymbol{\phi_B}\,\boldsymbol{T} \tag{3.14}$$

where $\boldsymbol{T}$ is a transformation matrix.

Considering that the response of the structure is only measured in a few degrees of freedom (DOFs) and only the modal parameters in a certain frequency range are identified, an estimation of matrix $\boldsymbol{T}$ can be obtained by means of the expression:

$$\boldsymbol{T} \simeq \boldsymbol{\phi_B^+}\,\boldsymbol{\phi_A} \tag{3.15}$$

where superscript '$^+$' indicates pseudoinverse. Premultiplying of Equation (3.10) by $\boldsymbol{\phi_A^T}$, and post-multiplying by $\boldsymbol{\phi_A}$, gives:

$$\boldsymbol{\phi_A^T}\,\boldsymbol{M_A}\,\boldsymbol{\phi_A} = \boldsymbol{\phi_A^T}\,\boldsymbol{M_B}\,\boldsymbol{\phi_A} + \boldsymbol{\phi_A^T}\,\boldsymbol{\Delta M}\,\boldsymbol{\phi_A} \tag{3.16}$$

Considering that the product $\boldsymbol{\phi}_A^T\,\boldsymbol{M}_A\,\boldsymbol{\phi}_A$ is an identity matrix in the case of mass-normalized mode shapes, and that the product $\boldsymbol{\phi}_A^T\,\boldsymbol{M}_B\,\boldsymbol{\phi}_A$ can be expressed as:

$$\boldsymbol{\phi}_A^T\,\boldsymbol{M}_B\,\boldsymbol{\phi}_A = \boldsymbol{T}^T\boldsymbol{B}^T\boldsymbol{M}_B\boldsymbol{B}\,\boldsymbol{T} = \boldsymbol{T}^T\boldsymbol{T} \tag{3.17}$$

Equation (3.16) can be rewritten as:

$$\boldsymbol{I} = \boldsymbol{T}^T\boldsymbol{T} + \boldsymbol{\phi}_A^T\,\boldsymbol{\Delta M}\,\boldsymbol{\phi}_A \tag{3.18}$$

Following a similar approach with Eq. (3.11), premultiplying by $\boldsymbol{\phi}_A^T$ and post-multiplying by $\boldsymbol{\phi}_A$, gives:

$$\boldsymbol{\phi}_A^T\,\boldsymbol{K}_A\,\boldsymbol{\phi}_A = \boldsymbol{\phi}_A^T\,\boldsymbol{K}_B\,\boldsymbol{\phi}_A + \boldsymbol{\phi}_A^T\,\boldsymbol{\Delta K}\,\boldsymbol{\phi}_A \tag{3.19}$$

which, in the case of mass-normalized mode shapes, leads to:

$$\boldsymbol{\omega}_A^2 = \boldsymbol{T}^T\boldsymbol{\omega}_B^2\,\boldsymbol{T} + \boldsymbol{\phi}_A^T\,\boldsymbol{\Delta K}\boldsymbol{\phi}_A \tag{3.20}$$

where $\boldsymbol{\omega}_A^2$ and $\boldsymbol{\omega}_B^2$ are diagonal matrices containing the natural frequencies of systems A and B, respectively.

In the case of unscaled mode shapes for system A (denoted $\boldsymbol{\psi}_A$), a new transformation matrix ($\widehat{\boldsymbol{T}}_U$) is obtained with Eq. (3.15), i.e:

$$\boldsymbol{T}_U \simeq \boldsymbol{\phi}_B^+\,\boldsymbol{\psi}_A \tag{3.21}$$

Therefore Eq. (3.16) is now rewritten as:

$$\boldsymbol{\psi}_A^T\,\boldsymbol{M}_A\,\boldsymbol{\psi}_A = \boldsymbol{\psi}_A^T\,\boldsymbol{M}_B\,\boldsymbol{\psi}_A + \boldsymbol{\psi}_A^T\,\boldsymbol{\Delta M}\,\boldsymbol{\psi}_A \tag{3.22}$$

which leads to:

$$\boldsymbol{m}_A = \boldsymbol{T}_U^T\boldsymbol{T}_U + \boldsymbol{\psi}_A^T\,\boldsymbol{\Delta M}\,\boldsymbol{\psi}_A \tag{3.23}$$

where $\boldsymbol{m}_A$ is a diagonal matrix containing the modal masses. Similarly, Eq. (3.20) leads to:

$$\boldsymbol{m_A}\,\boldsymbol{\omega_A^2} = \boldsymbol{T_U^T}\boldsymbol{\omega_B^2}\,\boldsymbol{T_U} + \boldsymbol{\psi_A^T}\,\boldsymbol{\Delta K}\,\boldsymbol{\psi_A} \tag{3.24}$$

3.2.1 The T-Mass correlation indicator

Given that model B is only perturbed by a stiffness change ($\boldsymbol{\Delta K}$) and there are no mass discrepancies between models ($\boldsymbol{\Delta M} = \boldsymbol{0}$), Equation (3.18) can be expressed as:

$$\boldsymbol{I} = \boldsymbol{T^T T} \tag{3.25}$$

This means that, if there are no discrepancies in terms of mass between models B and A, the product $\boldsymbol{T^T T}$ is an identity matrix or, alternatively, the column vectors of matrix $\boldsymbol{T}$ are orthogonal to each other. Thus, there are mass discrepancies if:

- The diagonal terms of $\boldsymbol{T^T T}$ are lower than 1.
- The off diagonal terms of $\boldsymbol{T^T T}$ are different than zero.

When working with mass-normalized modal matrices $\boldsymbol{\phi_A}$ and $\boldsymbol{\phi_B}$, the inner product $\boldsymbol{T^T T}$ can be used as a mass correlation criterion, where values equal to 1 in the diagonal elements and equal to 0 for the off-diagonal elements, indicate perfect correlation in terms of mass (Figure 3.1).

In the case of unscaled experimental modes (denoted as $\boldsymbol{\psi_A}$) and no discrepancies in terms of mass, Eq. (3.23) results in:

$$\boldsymbol{m_A} = \boldsymbol{T_U^T T_U} \tag{3.26}$$

Which means that the product $\boldsymbol{T_U^T T_U}$ is a diagonal matrix and the column vectors of matrix $\boldsymbol{T_U}$ are orthogonal to each other. It the modal masses $\boldsymbol{m_A}$ are not known, the information contained in the diagonal of $\boldsymbol{T_U^T T_U}$ cannot be used for correlation.

Based on the orthogonality of the column vectors of matrices $\boldsymbol{T}$ and $\boldsymbol{T_U}$, the following indicators can also be proposed (Figure 3.1):

- ***T-Mass***: angles between the column vectors of matrix $\boldsymbol{T}$ (or $\boldsymbol{T_U}$). Angles equal to 90º in the off-diagonal elements indicate perfect correlation, meaning no discrepancies in mass.
- ***T-Mass-norm***: ***T-Mass*** divided by 90º. Off-diagonal elements equal to 1 indicate perfect correlation in terms of mass.

- AUTOMAC of $\boldsymbol{T}$ matrix (or $\boldsymbol{T_U}$): Off-diagonal elements equal to 0 indicate perfect correlation in terms of mass

3.2.2 The T-Stiffness correlation indicator

Considering that model B is only perturbed with a mass change ($\boldsymbol{\Delta M}$) and there are no discrepancies in terms of stiffness between models ($\boldsymbol{\Delta K} = \mathbf{0}$), Equation (3.20) can be expressed as:

$$\boldsymbol{\omega_A^2} = \boldsymbol{T^T} \boldsymbol{\omega_B^2} \, \boldsymbol{T} \tag{3.27}$$

This means that the inner product $\boldsymbol{T^T} \boldsymbol{\omega_B^2} \, \boldsymbol{T}$ is a diagonal matrix containing the natural frequencies $\boldsymbol{\omega_A^2}$ in the diagonal, or alternatively, the column vectors of the matrix $\boldsymbol{T}$ are orthogonal with respect to the eigenvalue matrix $\boldsymbol{\omega_B^2}$. Thus, there are stiffness discrepancies if:

- The diagonal terms of $\boldsymbol{T^T} \boldsymbol{\omega_B^2} \, \boldsymbol{T}$ are different than $\boldsymbol{\omega_A^2}$.
- The off-diagonal terms of $\boldsymbol{T^T} \boldsymbol{\omega_B^2} \, \boldsymbol{T}$ are different than zero.

When working with mass-normalized modal matrices $\boldsymbol{\phi_A}$ and $\boldsymbol{\phi_B}$, the inner product $\boldsymbol{T^T} \boldsymbol{\omega_B^2} \, \boldsymbol{T}$ can be used as a stiffness correlation criterion, where values equal to $\boldsymbol{\omega_A^2}$ in the diagonal elements and equal to 0 for the off-diagonal elements, indicate perfect correlation in terms of stiffness (Figure 3.1).

In the case of unscaled experimental mode ($\boldsymbol{\psi_A}$) and no discrepancies in term of stiffness, it is inferred from Eq. (3.24) that:

$$\boldsymbol{m_A} \, \boldsymbol{\omega_A^2} = \boldsymbol{T_U^T} \boldsymbol{\omega_B^2} \, \boldsymbol{T_U} \tag{3.28}$$

Which means that the inner product $\boldsymbol{T_U^T} \boldsymbol{\omega_B^2} \, \boldsymbol{T_U}$ is a diagonal matrix containing the product $\boldsymbol{m_A} \, \boldsymbol{\omega_A^2}$ in the diagonal, or alternatively, the column vectors of the matrix $\boldsymbol{T_U}$ are orthogonal with respect to the eigenvalue matrix $\boldsymbol{\omega_B^2 T_U}$.

Based on the orthogonality of the column vectors of matrix $\boldsymbol{T}$ with respect to $\boldsymbol{\omega_B^2 T}$ (and the column vectors of matrix $\boldsymbol{T_U}$ with respect to $\boldsymbol{\omega_B^2 T_U}$), the following indicators can be proposed (Figure 3.1):

- ***T-Stiffness***: angles between the vectors of matrix $\boldsymbol{T}$ and $\boldsymbol{\omega_B^2} \, \boldsymbol{T}$ (or $\boldsymbol{T_U}$ and $\boldsymbol{\omega_B^2} \, \boldsymbol{T_U}$). Angles equal to 90º in the off-diagonal elements indicate perfect correlation, meaning no discrepancies in stiffness.
- ***T-Stiffness-norm***: ***T-Stiffness*** divided by 90º. Off-diagonal elements equal to 1 indicate perfect correlation in terms of stiffness.

- MAC between $\boldsymbol{T}$ and $\boldsymbol{\omega_B^2}\ \boldsymbol{T}$ (or $\boldsymbol{T_U}$ and $\boldsymbol{\omega_B^2}\ \boldsymbol{T_U}$): Off-diagonal elements equal to 0 indicate perfect correlation in terms of stiffness.

It is also worth noting that in the case of closely spaced or repeated modes, the product $\boldsymbol{T^T T}$ is a diagonal matrix, therefore the angles of ***T-Mass*** are very close to 90º and ***T-Mass-norm*** very close to 1.

3.2.3 Rotmac

From Eq. (3.25) it is inferred that the inner product $\boldsymbol{T^T T}$ must be an identity matrix when there are only ***stiffness discrepancies*** ($\boldsymbol{\Delta K}$) between models B and A , i.e., matrix $\boldsymbol{T}$ (or $\boldsymbol{T^T}$) must be a rotation matrix. This implies that a pure rotation of the mode shapes does not modify the mass of the system. In case of a pure rotation, the modal matrices $\boldsymbol{\phi_B}$ and $\boldsymbol{\phi_A}$ are related as:

$$\boldsymbol{\phi_A^T} = \boldsymbol{R}\ \boldsymbol{\phi_B^T} \tag{3.29}$$

where $\boldsymbol{R}$ indicates rotation matrix. From Eq. (3.29) is inferred that:

$$\boldsymbol{T^T} = \boldsymbol{R} \tag{3.30}$$

and:

$$\boldsymbol{\phi_B} = \boldsymbol{\phi_A}\ \boldsymbol{R} \tag{3.31}$$

From the sensitivity equations, which are based on a Taylor expansion [94], it can be also deduced that ***a mass change*** induces a change in the scaling of the mode shapes and in the relative angle between the mode shapes (shear). From these considerations, when the system is perturbed with mass changes, it is proposed to express the matrix $\boldsymbol{T^T}$ as a linear combination of rotation ($\boldsymbol{R}$), shear ($\boldsymbol{T_{sh}}$) and scaling ($\boldsymbol{T_{sc}}$) (Figure 3.1), i.e.:

$$\boldsymbol{T^T} = \boldsymbol{R}\ \boldsymbol{T_{sh}} \boldsymbol{T_{sc}} \tag{3.32}$$

If the effects of shear and scaling are combined in only one matrix ($\boldsymbol{T_{ch}}$), Eq. (3.32) leads to:

$$\boldsymbol{T^T} = \boldsymbol{R}\ \boldsymbol{T_{ch}} \tag{3.33}$$

If two ***repeated modes*** ($\omega_{b1}^2 = \omega_{b1}^2 = \omega_b^2$) are considered, and there is a ***mass change*** between models B and A, Eq. (3.27) can be written as:

$$\begin{bmatrix} \omega_{a1}^2 & 0 \\ 0 & \omega_{a2}^2 \end{bmatrix} = \omega_b^2\, \boldsymbol{T}^{\boldsymbol{T}} \boldsymbol{T} \tag{3.34}$$

from which is inferred that matrix $\boldsymbol{T}$ must be a pure rotation matrix if $\omega_{a1}^2 = \omega_{a2}^2$. This demonstrates that if a system B with closely spaced or repeated modes is perturbed with a mass change matrix, the mode shapes will mainly rotate in the local subspace defined by the closely spaced or repeated modes. In this case, the submatrix of the inner product $\boldsymbol{T}^{\boldsymbol{T}}\boldsymbol{T}$ corresponding to the closely spaced modes will be close to an identity matrix in the case of mass scaled mode shapes and the angles in the ***T-Mass*** will be close to 90º (Figure 3.1). Due to the fact that $\boldsymbol{T}^{\boldsymbol{T}}\boldsymbol{T}$ is diagonal, from Eq. (3.18) is inferred that $\boldsymbol{\phi}_{\boldsymbol{A}}^{\boldsymbol{T}}\, \boldsymbol{\Delta M}\, \boldsymbol{\phi}_{\boldsymbol{A}}$ must be diagonal, i.e. there are only changes in the scaling of the mode shapes whereas the relative angle between mode shapes is not modified (Figure 3.1).

Considering that a rotation is always involved in matrix $\boldsymbol{T}$, the QR decomposition [95] can be used to factorize matrix $\boldsymbol{T}^{\boldsymbol{T}}$ as:

$$\boldsymbol{T}^{\boldsymbol{T}} = \boldsymbol{R}\, \boldsymbol{Q} \tag{3.35}$$

where $\boldsymbol{R}$ matrix is a rotation matrix and $\boldsymbol{Q}$ is an upper triangular matrix. And the following results are expected:

- If there are only stiffness discrepancies ($\boldsymbol{\Delta K}$), matrix $\boldsymbol{T}^{\boldsymbol{T}}$ is a pure rotation. Therefore, the $\boldsymbol{Q}$ matrix obtained with the QR decomposition will be an identity matrix in case of mass-normalized mode shapes, or a diagonal matrix in case of unscaled mode shapes.
- If there are only discrepancies in mass ($\boldsymbol{\Delta M}$), the QR decomposition gives a rotation matrix $\boldsymbol{R}$ and matrix $\boldsymbol{Q}$ containing information of shear and scaling.

The polar decomposition can also be used to factorize matrix $\boldsymbol{T}^{\boldsymbol{T}}$ as:

$$\boldsymbol{T}^{\boldsymbol{T}} = \boldsymbol{R}\, \boldsymbol{Z} \tag{3.36}$$

where $\boldsymbol{R}$ is a rotation matrix and $\boldsymbol{Z}$ is a positive semi-definite Hermitian matrix. Similarly, if there are only stiffness discrepancies ($\boldsymbol{\Delta K}$), matrix $\boldsymbol{Z}$ will be an identity matrix in case of mass-normalized mode shapes, or a diagonal matrix in case of unscaled mode shapes.

Considering that closely spaced modes are highly sensitive to small mass and stiffness perturbations of the system, they can rotate within their subspace. Therefore, two models can present good correlation in terms of mass and stiffness, but still low MAC values can be obtained due to this rotation.

Following these considerations, a new indicator is proposed in this section, denoted as ROTMAC. It is a novel version of the MAC, where the rotated mode shapes of system B ($\boldsymbol{\phi_{BR}}$) are used, i.e.:

$$ROTMAC(\boldsymbol{\phi_{BRi}}, \boldsymbol{\phi_{Aj}}) = \frac{\left|\boldsymbol{\phi_{BRi}^T}\, \boldsymbol{\phi_{Aj}}\right|^2}{(\boldsymbol{\phi_{BRi}^T}\, \boldsymbol{\phi_{BRi}})(\boldsymbol{\phi_{Aj}^T}\, \boldsymbol{\phi_{Aj}})} \tag{3.37}$$

where $\boldsymbol{\phi_{BRi}}$ is a column vector of matrix $\boldsymbol{\phi_{BR}}$, obtained rotating matrix $\boldsymbol{B}$ as:

$$\boldsymbol{\phi_{BR}} = \boldsymbol{\phi_B}\, \boldsymbol{R} \tag{3.38}$$

The mode shapes are scaled to unit length to calculate the modal assurance criterion, so no information about changes in scaling can be obtained with Eq. (3.37). Thus, the ROTMAC is an indicator of shear, and it must be an identity matrix in the following cases:

- System B is perturbed with a stiffness change only ($\boldsymbol{\Delta K}$). This occurs because the rotated mode shapes $\boldsymbol{\phi_{BR}}$ coincide with mode shapes $\boldsymbol{\phi_A}$, indicating no shear effect.
- System B, with repeated or closely spaced modes, is only perturbed with a mass change ($\boldsymbol{\Delta M}$). In this case, the effect of shear is negligible.

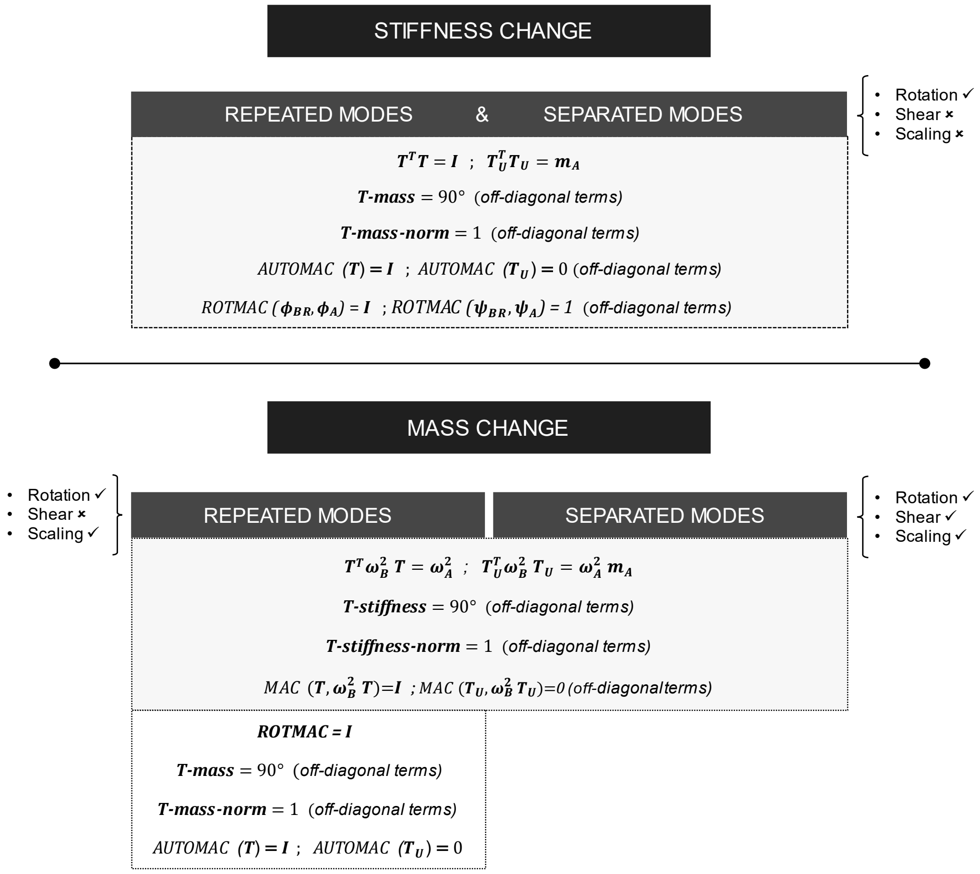

Figure 3.1: Summary of the proposed indicators to detect mass changes and stiffness changes. Expected results for repeated modes (and closely spaced) and separated modes.

3.3 Numerical example: a symmetric steel structure

In this section, an example of a symmetric numerical structure is considered to validate the proposed correlation indicators.

A steel structure composed of a vertical column 1500 mm high and four horizontal beams at the top with a length of 500 mm, all of them with a squared hollow section of 50 x 4 mm^2 was considered in the simulations (Figure 3.2). The structure was modelled in Abaqus CAE and meshed with shell elements (S4R). The steel was modelled as a linear elastic material with properties: $E = 210$ GPa, $\nu = 0.3$ and $\rho = 7850$ kg/m^3. This structure model is considered as the unperturbed model (system B). The perturbated model (system A), it is derived from system B introducing a local mass of 0.463 kg as show in Figure 3.2.

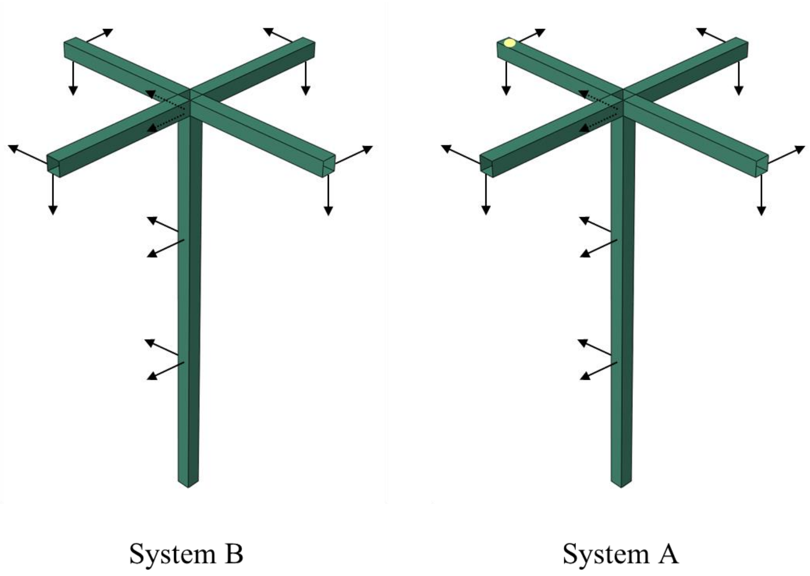

Figure 3.2 Unperturbed (System B) and perturbed (System A) Abaqus models. The lumped mass location is show in yellow.

The first ten natural frequencies obtained from both systems A and B are presented in Table 3.1 and the corresponding mode shapes are shown in Figure 3.3. Table 3.1 shows a classification of the mode shapes based on the relative frequency shift between a pair of modes $(\Delta\omega\backslash\omega)$ modes [96]. When the relative frequency shift is higher than 0.1, the modes are considered well separated; they are considered repeated modes when it is zero, and closely spaced modes when the relative frequency shift $(\Delta\omega\backslash\omega)$ is between 0 and 0.1. In this example, most of repeated modes in system B are closely spaced modes in system A.

Table 3.1 Natural frequencies [Hz] of systems A and B

<table>
<tr><th>Mode</th><th>Unperturbed
(System B)</th><th>Perturbed
(System A)</th><th colspan="2">Classification</th></tr>
<tr><td>1</td><td>10.30</td><td>10.10</td><td rowspan="2">Repeated / Closely spaced</td><td></td></tr>
<tr><td>2</td><td>10.30</td><td>10.14</td><td rowspan="2">Separated</td></tr>
<tr><td>3</td><td>24.13</td><td>22.97</td><td rowspan="2">Separated</td></tr>
<tr><td>4</td><td>70.39</td><td>65.02</td><td rowspan="2">Repeated / Closely spaced</td></tr>
<tr><td>5</td><td>70.39</td><td>70.39</td><td rowspan="2">Separated</td></tr>
<tr><td>6</td><td>81.21</td><td>77.19</td><td rowspan="2">Separated</td></tr>
<tr><td>7</td><td>173.74</td><td>157.57</td><td rowspan="2">Closely spaced</td></tr>
<tr><td>8</td><td>173.93</td><td>172.29</td><td rowspan="2">Repeated / Closely spaced</td></tr>
<tr><td>9</td><td>173.93</td><td>173.83</td><td rowspan="2">Separated</td></tr>
<tr><td>10</td><td>184.66</td><td>181.31</td><td></td></tr>
</table>

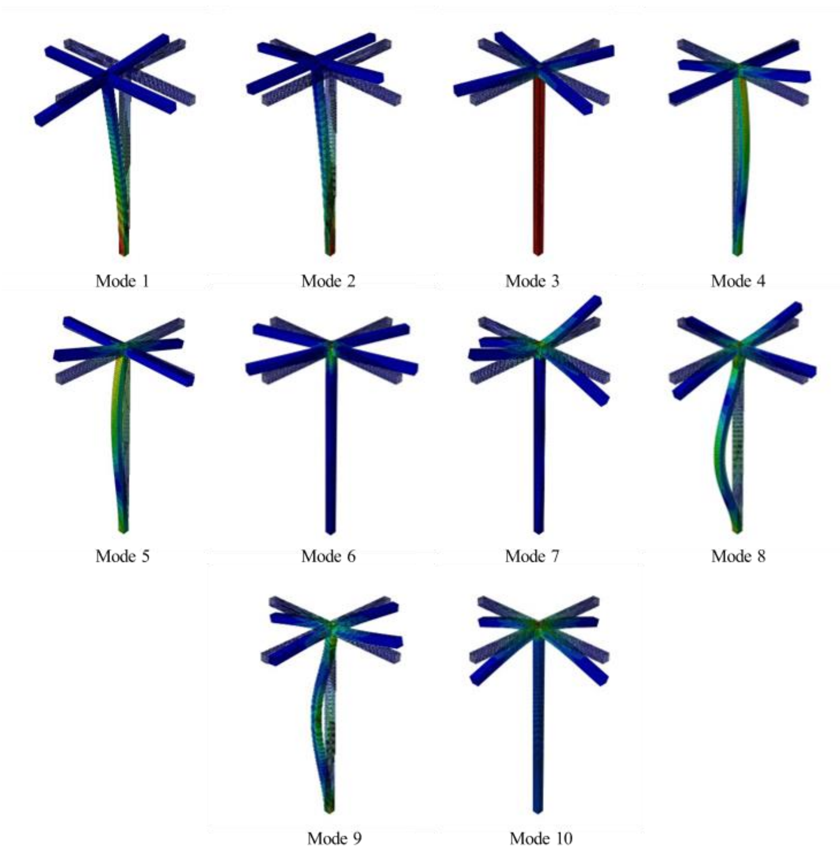

Figure 3.3: Mode shapes of system B.

Matrix $\widehat{\boldsymbol{T}}$ (hereafter denoted as $\boldsymbol{T}$) showed in Table 3.2, is estimated with Equation (3.15) using mass-normalized mode shapes for both systems. No errors are considered in the mode shapes. Moreover, in order to minimize truncation errors, matrix $\boldsymbol{T}$ is estimated with 12 modes, but only a matrix size 10 x 10 is considered in this study.

Table 3.2: Matrix $\widehat{\boldsymbol{T}}$

0.976	-0.092	-0.006	0.037	0.000	0.005	0.033	-0.002	-0.004	0.009
-0.091	-0.979	-0.067	-0.004	0.002	0.052	-0.005	-0.022	0.000	-0.001
0.000	-0.013	0.951	0.000	0.004	0.105	-0.003	-0.042	0.000	-0.001
0.000	0.000	0.000	0.092	-0.995	0.013	-0.020	-0.001	0.000	-0.004
-0.001	0.000	0.000	0.916	0.100	-0.001	-0.200	0.000	-0.001	-0.042
0.000	-0.001	0.009	0.000	-0.010	-0.949	-0.002	-0.057	0.000	-0.001
0.000	0.000	0.000	0.023	0.000	0.000	0.688	0.000	-0.517	-0.408
0.000	0.000	0.000	-0.014	0.000	0.001	-0.409	-0.134	-0.848	0.248
0.000	0.000	-0.001	0.002	0.000	0.010	0.057	-0.978	0.116	-0.034
0.000	0.000	0.000	-0.020	0.000	0.000	-0.390	0.000	-0.004	-0.873

Considering that mass-normalized modes are used, the products $\boldsymbol{T}^{\boldsymbol{T}}\boldsymbol{T}$ and $\boldsymbol{T}^{\boldsymbol{T}}\,\boldsymbol{\omega}_{\boldsymbol{B}}^{2}\,\boldsymbol{T}$ are calculated to study mass and stiffness discrepancies. Table 3.3 shows $\boldsymbol{T}^{\boldsymbol{T}}\boldsymbol{T}$ matrix, which detects mass discrepancies between models. Diagonal values quite bellow unit for modes 1, 2, 3, 4, 6, 7 and 8 indicate changes in scaling. Regarding off-diagonal terms, most of them are approximately zero because there cannot be shear in the mode shapes corresponding to repeated modes when system B is perturbed with a mass change matrix $\boldsymbol{\Delta M}$.

Table 3.3: $\boldsymbol{T^T T}$ matrix

0.961	0.000	0.000	0.036	0.000	0.000	0.033	0.000	-0.004	0.009
0.000	0.968	0.054	0.000	-0.002	-0.052	0.002	0.022	0.000	0.001
0.000	0.054	**0.909**	0.000	0.003	0.087	-0.002	-0.038	0.000	-0.001
0.036	0.000	0.000	**0.849**	0.000	0.000	-0.154	0.000	-0.001	-0.034
0.000	-0.002	0.003	0.000	1.000	-0.003	0.000	0.001	0.000	0.000
0.000	-0.052	0.087	0.000	-0.003	**0.915**	0.002	0.038	0.000	0.001
0.033	0.002	-0.002	-0.154	0.000	0.002	**0.838**	-0.001	-0.001	-0.034
0.000	0.022	-0.038	0.000	0.001	0.038	-0.001	0.983	0.000	0.000
-0.004	0.000	0.000	-0.001	0.000	0.000	-0.001	0.000	0.999	0.000
0.009	0.001	-0.001	-0.034	0.000	0.001	-0.034	0.000	0.000	0.993

Table 3.4 shows $\boldsymbol{T^T \omega_B^2 T}$ matrix, which detects stiffness discrepancies between models. In case of no changes in stiffness, it must be a diagonal matrix containing $\boldsymbol{\omega_A^2}$ in the diagonal. This comparison is done in Table 3.5, showing error values below 1% for all the diagonal terms, indicating almost perfect correlation in terms of stiffness.

Table 3.4: $\boldsymbol{T^T \omega_B^2 T}$ matrix

4026.2	0.0	0.1	-3.9	0.0	-0.6	-23.1	1.4	-0.3	-9.7
0.0	4056.0	-0.5	1.6	0.0	4.1	10.1	-8.6	0.1	3.0
0.1	-0.5	20836.1	-11.5	0.0	-32.5	-70.7	66.0	-0.5	-20.9
-3.9	1.6	-11.5	167080.3	-0.8	113.9	621.2	-240.3	39.5	536.2
0.0	0.0	0.0	-0.8	195580.7	-2.6	-5.0	5.3	0.0	-1.6
-0.6	4.1	-32.5	113.9	-2.6	235493.3	702.3	-507.9	5.3	207.2
-23.1	10.1	-70.7	621.2	-5.0	702.3	980900.8	-1481.5	215.8	2543.1
1.4	-8.6	66.0	-240.3	5.3	-507.9	-1481.5	1172764.2	-9.9	-436.6
-0.3	0.1	-0.5	39.5	0.0	5.3	215.8	-9.9	1192889.0	48.9
-9.7	3.0	-20.9	536.2	-1.6	207.2	2543.1	-436.6	48.9	1299248.6

Table 3.5: Comparison of diagonal elements $\sqrt{\boldsymbol{T^T \omega_B^2 T}}$ matrix and $\boldsymbol{\omega_A}$.

Mode	1	2	3	4	5	6	7	8	9	10
$\sqrt{\boldsymbol{T^T \omega_B^2 T}}$	63.5	63.7	144.3	408.8	442.2	485.3	990.4	1082.9	1092.2	1139.8
$\boldsymbol{\omega_A}$	63.5	63.7	144.3	408.5	442.2	485.0	990.0	1082.5	1092.2	1139.2
Error [%]	0.00	0.00	-0.01	-0.05	0.00	-0.06	-0.04	-0.04	0.00	-0.06

As previously mentioned, when working with unscaled mode shapes (which is not this case), other correlation techniques must be used. Regarding mass discrepancies, the ***T-mass***, ***T-mass-norm*** and the AUTOMAC of $\boldsymbol{T}$ matrix can be used. Regarding stiffness perturbations, the ***T-Stiffness***, ***T-Stiffness-norm*** and the MAC of $\boldsymbol{T}$ and $\boldsymbol{\omega_B^2}\ \boldsymbol{T}$.

T-mass and ***T-mass-norm*** are shown in Table 3.6 and Table 3.7. Off-diagonal elements of ***T-mass*** quite below 90° indicate mass discrepancies, being the minimum value around 80°. Similarly, ***T-mass-norm*** off diagonal values below 1, indicate mass discrepancies, being the minimum value 0.88. However, it must be noted that there is no shear in the mode shapes corresponding to repeated mode when system B is perturbed with a mass change $\boldsymbol{\Delta M}$. Therefore, the angles between the columns of matrix $\boldsymbol{T}$ relating both models (***T-mass***) must be 90° (1 for ***T-mass-norm*** and 0 for the AUTOMAC of $\boldsymbol{T}$). Thus, in case of repeated modes or closely spaced modes and no stiffness discrepancies, only the diagonal terms of $\boldsymbol{T^T T}$ matrix provide information of mass discrepancies.

Table 3.6: ***T-mass***

----	90.00	90.00	87.71	90.00	90.00	87.89	90.00	89.76	89.50
90.00	----	86.70	89.98	89.90	86.83	89.88	88.69	90.00	89.97
90.00	86.70	----	89.97	89.83	84.50	89.84	87.70	90.00	89.96
87.71	89.98	89.97	----	90.00	89.98	79.50	89.99	89.94	87.89
90.00	89.90	89.83	90.00	----	89.83	90.00	89.92	90.00	90.00
90.00	86.83	84.50	89.98	89.83	----	89.87	87.72	90.00	89.96
87.89	89.88	89.84	79.50	90.00	89.87	----	89.95	89.95	87.83
90.00	88.69	87.70	89.99	89.92	87.72	89.95	----	90.00	89.99
89.76	90.00	90.00	89.94	90.00	90.00	89.95	90.00	----	90.00
89.50	89.97	89.96	87.89	90.00	89.96	87.83	89.99	90.00	----

Table 3.7: ***T-mass-norm***

----	1.000	1.000	0.975	1.000	1.000	0.977	1.000	0.997	0.994
1.000	----	0.963	1.000	0.999	0.965	0.999	0.985	1.000	1.000
1.000	0.963	----	1.000	0.998	0.939	0.998	0.974	1.000	1.000
0.975	1.000	1.000	----	1.000	1.000	0.883	1.000	0.999	0.977
1.000	0.999	0.998	1.000	----	0.998	1.000	0.999	1.000	1.000
1.000	0.965	0.939	1.000	0.998	----	0.999	0.975	1.000	1.000
0.977	0.999	0.998	0.883	1.000	0.999	----	0.999	0.999	0.976
1.000	0.985	0.974	1.000	0.999	0.975	0.999	----	1.000	1.000
0.997	1.000	1.000	0.999	1.000	1.000	0.999	1.000	----	1.000
0.994	1.000	1.000	0.977	1.000	1.000	0.976	1.000	1.000	----

The same information can also be obtained with the AUTOMAC of ***T*** matrix, where off diagonal values are not equal to zero, indicating mass discrepancies (Table 3.8).

Table 3.8: AUTOMAC (***T***)

----	0.000	0.000	0.002	0.000	0.000	0.001	0.000	0.000	0.000
0.000	----	0.003	0.000	0.000	0.003	0.000	0.001	0.000	0.000
0.000	0.003	----	0.000	0.000	0.009	0.000	0.002	0.000	0.000
0.002	0.000	0.000	----	0.000	0.000	0.033	0.000	0.000	0.001
0.000	0.000	0.000	0.000	----	0.000	0.000	0.000	0.000	0.000
0.000	0.003	0.009	0.000	0.000	----	0.000	0.002	0.000	0.000
0.001	0.000	0.000	0.033	0.000	0.000	----	0.000	0.000	0.001
0.000	0.001	0.002	0.000	0.000	0.002	0.000	----	0.000	0.000
0.000	0.000	0.000	0.000	0.000	0.000	0.000	0.000	----	0.000
0.000	0.000	0.000	0.001	0.000	0.000	0.001	0.000	0.000	----

T-stiffness and ***T-stiffness-norm*** are shown in Table 3.9 and Table 3.10, respectively. Considering that there are no stiffness discrepancies, in the case of repeated modes $t_i^T t_j$ is equal zero for $i \neq j$, and the angles between t_i and t_j must be $90°$. Off-diagonal values of well separated modes are close to $90°$ denoting almost a perfect correlation between models in terms of stiffness, being the minimum value 89.8. The same observation is done with ***T-stiffness-norm*** where all off-diagonal are almost equal to one (minimum value equal to 0.998), indicating no stiffness discrepancies.

Table 3.9: ***T-Stiffness***

----	90.000	90.000	89.999	90.000	90.000	89.999	90.000	90.000	90.000
90.000	----	89.999	89.999	90.000	89.999	89.999	90.000	90.000	90.000
89.999	89.993	----	89.996	90.000	89.992	89.996	89.997	90.000	89.999
89.941	89.976	89.968	----	90.000	89.972	89.965	89.987	89.998	89.974
90.000	90.000	90.000	90.000	----	89.999	90.000	90.000	90.000	90.000
89.991	89.941	89.912	89.963	89.999	----	89.961	89.974	90.000	89.990
89.649	89.848	89.801	89.790	89.998	89.824	----	89.922	89.989	89.878
89.981	89.880	89.829	89.925	89.998	89.883	89.922	----	90.000	89.981
89.996	89.999	89.999	89.988	90.000	89.999	89.989	90.000	----	89.998
89.865	89.959	89.946	89.833	90.000	89.952	89.866	89.979	89.998	----

Table 3.10: ***T-Stiffness-norm***

----	1.000	1.000	1.000	1.000	1.000	1.000	1.000	1.000	1.000
1.000	----	1.000	1.000	1.000	1.000	1.000	1.000	1.000	1.000
1.000	1.000	----	1.000	1.000	1.000	1.000	1.000	1.000	1.000
0.999	1.000	1.000	----	1.000	1.000	1.000	1.000	1.000	1.000
1.000	1.000	1.000	1.000	----	1.000	1.000	1.000	1.000	1.000
1.000	0.999	0.999	1.000	1.000	----	1.000	1.000	1.000	1.000
0.996	0.998	0.998	0.998	1.000	0.998	----	0.999	1.000	0.999
1.000	0.999	0.998	0.999	1.000	0.999	0.999	----	1.000	1.000
1.000	1.000	1.000	1.000	1.000	1.000	1.000	1.000	----	1.000
0.998	1.000	0.999	0.998	1.000	0.999	0.999	1.000	1.000	----

Stiffness discrepancies between models can also be studied with the MAC between $\boldsymbol{T}$ matrix and the product $\boldsymbol{\omega_B^2 T}$. All off-diagonal values equal to zero indicate perfect correlation in terms of stiffness.

Table 3.11: MAC ($\boldsymbol{T}, \boldsymbol{\omega}_{\boldsymbol{B}}^{2}\boldsymbol{T}$)

----	0.000	0.000	0.000	0.000	0.000	0.000	0.000	0.000	0.000
0.000	----	0.000	0.000	0.000	0.000	0.000	0.000	0.000	0.000
0.000	0.000	----	0.000	0.000	0.000	0.000	0.000	0.000	0.000
0.000	0.000	0.000	----	0.000	0.000	0.000	0.000	0.000	0.000
0.000	0.000	0.000	0.000	----	0.000	0.000	0.000	0.000	0.000
0.000	0.000	0.000	0.000	0.000	----	0.000	0.000	0.000	0.000
0.000	0.000	0.000	0.000	0.000	0.000	----	0.000	0.000	0.000
0.000	0.000	0.000	0.000	0.000	0.000	0.000	----	0.000	0.000
0.000	0.000	0.000	0.000	0.000	0.000	0.000	0.000	----	0.000
0.000	0.000	0.000	0.000	0.000	0.000	0.000	0.000	0.000	----

Correlation between models can also be studied through the ROTMAC. Firstly, matrix $\boldsymbol{T}$ is decomposed using the QR decomposition:

$$\boldsymbol{T} = \boldsymbol{R}\,\boldsymbol{Q} \tag{3.39}$$

where $\boldsymbol{R}$ is the rotation matrix and $\boldsymbol{Q}$ contains the effects of scaling and shear.

Table 3.12: Matrix $\boldsymbol{R}$

-0.996	-0.093	0.001	-0.001	0.000	0.000	0.000	0.000	0.000	0.000
0.093	-0.996	0.013	0.000	0.000	0.001	0.000	0.000	0.000	0.000
0.000	-0.013	-1.000	0.000	0.000	0.010	0.000	-0.001	0.000	0.000
0.000	0.000	0.000	-0.100	0.995	0.010	0.004	0.000	0.000	-0.001
0.001	0.000	0.000	-0.994	-0.100	-0.001	0.036	0.000	0.000	-0.007
0.000	-0.001	-0.010	0.000	0.010	-1.000	0.000	-0.012	0.000	0.000
0.000	0.000	0.000	-0.025	0.000	0.000	-0.770	0.001	0.517	-0.374
0.000	0.000	0.000	0.015	0.000	0.002	0.458	-0.136	0.848	0.228
0.000	0.000	0.001	-0.002	0.000	0.011	-0.064	-0.989	-0.117	-0.031
0.000	0.000	0.000	0.022	0.000	0.000	0.438	-0.001	0.005	-0.899

From the rotation matrix (Table 3.12) is inferred that the first two modes are rotated in their local subspace an angle $\boldsymbol{\theta}$ equal to -5.3344°. Modes 4 and 5 also rotate an angle $\boldsymbol{\theta}$ of 5.7448°, although they are not well paired. Modes from 7 to 10 are a set of closely spaced and repeated modes mainly rotating on the subspace spanned by these four modes.

Table 3.13: Matrix $\boldsymbol{Q}$

-0.981	0.000	0.000	-0.037	0.000	0.000	-0.034	0.000	0.004	-0.009
0.000	0.984	0.055	0.000	-0.002	-0.053	0.002	0.023	0.000	0.001
0.000	0.000	-0.952	0.000	-0.003	-0.095	0.003	0.041	0.000	0.001
0.000	0.000	0.000	-0.921	0.000	0.000	0.168	0.000	0.001	0.037
0.000	0.000	0.000	0.000	-1.000	0.003	0.000	-0.001	0.000	0.000
0.000	0.000	0.000	0.000	0.000	0.950	0.003	0.045	0.000	0.001
0.000	0.000	0.000	0.000	0.000	0.000	-0.899	0.001	0.001	0.046
0.000	0.000	0.000	0.000	0.000	0.000	0.000	0.989	0.000	0.000
0.000	0.000	0.000	0.000	0.000	0.000	0.000	0.000	-1.000	0.000
0.000	0.000	0.000	0.000	0.000	0.000	0.000	0.000	0.000	0.995

From the $\boldsymbol{Q}$ matrix (Table 3.13) the effects of shear and scaling are studied. Changes in scaling due to mass changes appear in the diagonal terms, mainly in modes 3, 4, 6 and 7. The off-diagonal terms indicate changes in shear in some modes. As previously mentioned, in the case of repeated modes and no-stiffness perturbations, there is no shear and, consequently, off-diagonal elements related to repeated modes are very close to zero.

The MAC between modal matrices $\boldsymbol{\phi_A}$ and $\boldsymbol{\phi_B}$ is shown in Table 3.14. It can be observed that modes 4 and 5 are not well paired and low MAC values are obtained for modes 7, 8, 9 and 10.

Table 3.14: MAC

0.991	0.009	0.000	0.001	0.063	0.000	0.000	0.005	0.000	0.000
0.009	0.991	0.001	0.063	0.001	0.000	0.000	0.000	0.005	0.000
0.000	0.001	0.999	0.000	0.000	0.000	0.000	0.000	0.000	0.000
0.052	0.000	0.000	0.010	0.988	0.000	0.001	0.167	0.003	0.001
0.001	0.062	0.000	0.990	0.010	0.000	0.000	0.003	0.158	0.000
0.000	0.000	0.011	0.000	0.000	0.988	0.000	0.000	0.000	0.000
0.002	0.000	0.000	0.000	0.005	0.000	0.687	0.066	0.001	0.210
0.000	0.001	0.003	0.153	0.002	0.006	0.000	0.018	0.968	0.000
0.004	0.000	0.000	0.001	0.090	0.000	0.434	0.555	0.011	0.000
0.001	0.000	0.000	0.000	0.012	0.000	0.180	0.037	0.001	0.781

The ROTMAC (Table 3.15) is calculated using Eq. (3.37) and rotating the modes of system B with ***R*** matrix. As it is shown, diagonal elements are very close to unity (except mode 7), which indicates little shear effect (due to mass changes). In the off-diagonal elements, there are non-zero values, which indicate changes in mass.

Table 3.15: ROTMAC

1.000	0.000	0.000	0.064	0.000	0.000	0.000	0.000	0.003	0.000
0.000	1.000	0.000	0.000	0.063	0.000	0.000	0.000	0.000	0.000
0.000	0.000	0.999	0.000	0.000	0.000	0.000	0.000	0.000	0.000
0.053	0.000	0.000	1.000	0.000	0.000	0.021	0.000	0.085	0.004
0.000	0.063	0.000	0.000	1.000	0.000	0.000	0.152	0.000	0.000
0.000	0.000	0.009	0.000	0.000	0.990	0.000	0.000	0.000	0.000
0.002	0.000	0.000	0.001	0.000	0.000	0.970	0.000	0.121	0.003
0.000	0.001	0.003	0.000	0.155	0.004	0.000	0.993	0.000	0.000
0.004	0.000	0.000	0.084	0.000	0.000	0.087	0.000	1.000	0.018
0.001	0.000	0.000	0.010	0.000	0.000	0.000	0.000	0.019	0.996

3.4 Numerical example: a two-spanned steel beam

In this section a numerical two-span steel beam is perturbed with different levels of mass and stiffness changes to validate the proposed correlation indicators.

A two-span steel beam with a rectangular section of 12 x 6 cm^2 was modelled in ABAQUS. The unperturbed model (System B) was created with a fixed boundary condition at the left border and simply supported at the mid-point and the right border (Figure 3.4). The model was meshed with 200 quadratic beam elements (B22). The following mechanical properties were considered for the steel, modelled as a linear elastic material: $E = 210$ GPa, $\nu = 0.3$ and $\rho = 7850$ kg/m^3.

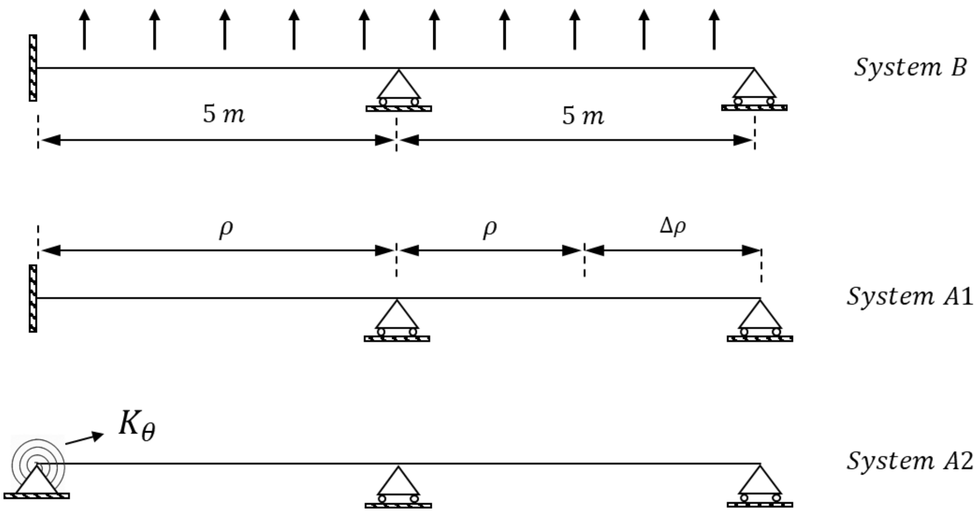

Figure 3.4: Unperturbed and perturbed models of the numerical steel beam.

As shown in Figure 3.4, system B was perturbed by mass modifications (System A1) and stiffness modifications (System A2). In System A1, a mass loss was introduced in a part of the right span. In System A2, stiffness loss was simulated by substituting the fixed support with a pinned support and a rotational spring (Figure 3.4).

To study the sensitivity of the correlation indicators to mass and stiffness perturbations, various levels of mass changes and stiffness changes were modelled. In system A1, the mass loss was modelled by altering the mass density of the location of interest. As shown in Table 3.16, mass density reductions ranging from 5% to 25% were simulated. In system A2, different levels of stiffness reduction were simulated by varying the spring stiffness (Table 3.16).

Table 3.16: Changes of mass and stiffness induced in systems A1 and A2, and their corresponding notation.

	Notation	Perturbation
System A1	$\Delta M1$	$\Delta\rho =$ -5%
	$\Delta M2$	$\Delta\rho =$ -10%
	$\Delta M3$	$\Delta\rho =$ -15%
	$\Delta M4$	$\Delta\rho =$ -20%
	$\Delta M5$	$\Delta\rho =$ -25%
System A2	$\Delta K1$	$K_\theta = 8\,x\,10^6$ N m
	$\Delta K2$	$K_\theta = 3\,x\,10^6$ N m
	$\Delta K3$	$K_\theta = 8\,x\,10^5$ N m
	$\Delta K4$	$K_\theta = 3\,x\,10^5$ N m
	$\Delta K5$	$K_\theta = 1\,x\,10^5$ N m

The natural frequencies of all systems are presented in Table 3.17, whereas the diagonal terms of the MAC are shown in Figure 3.5.

Table 3.17 Natural frequencies of systems B, A1 and A2

Natural frequencies [Hz]										
B	A1					A2				
	$\Delta M1$	$\Delta M2$	$\Delta M3$	$\Delta M4$	$\Delta M5$	$\Delta K1$	$\Delta K2$	$\Delta K3$	$\Delta K4$	$\Delta K5$
6.56	6.64	6.80	6.96	7.22	7.40	6.54	6.49	6.33	6.11	5.87
11.35	11.39	11.49	11.60	11.79	11.96	11.16	10.90	10.18	9.55	9.09
24.41	24.64	25.16	25.76	26.84	27.68	24.29	24.13	23.63	23.15	22.77
32.80	32.88	33.06	33.30	33.81	34.38	32.28	31.61	30.17	29.27	28.75
53.38	53.93	55.04	56.19	57.91	59.03	53.14	52.81	51.95	51.28	50.84
65.47	65.67	66.14	66.73	67.96	69.13	64.46	63.30	61.20	60.13	59.58
93.45	94.38	96.37	98.51	101.72	103.54	93.05	92.51	91.29	90.49	90.01
109.17	109.46	110.17	111.21	114.01	117.39	107.56	105.86	103.21	102.04	101.47

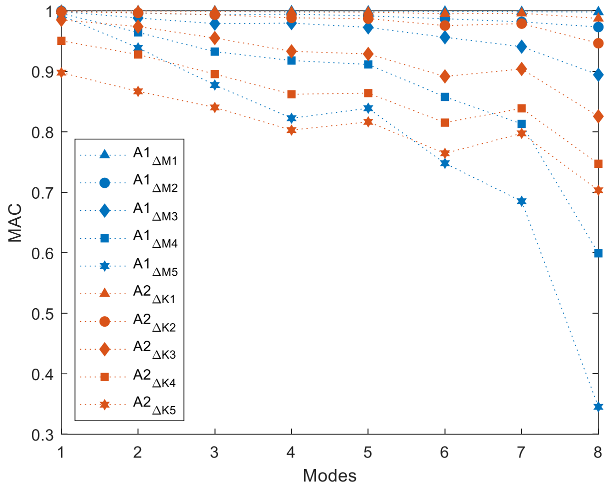

Figure 3.5: MAC diagonal values between systems A and system B.

It is worth noting that, since this is a numerical example, the mode shapes are mass-scaled. Therefore, the products $\boldsymbol{T}^{\boldsymbol{T}}\boldsymbol{T}$ and $\boldsymbol{T}^{\boldsymbol{T}}\boldsymbol{\omega}_{\boldsymbol{B}}^{\boldsymbol{2}}\ \boldsymbol{T}$ can be used as correlation indicators to detect discrepancies in mass or stiffness.

The product $\boldsymbol{T}^{\boldsymbol{T}}\boldsymbol{T}$, which serves as an indicator of mass discrepancies, should be an identity matrix in the absence of mass discrepancies, as it is the case for systems A2. In Figure 3.6 (a), the diagonal terms are plotted, showing values equal to one for systems A2, confirming no mass discrepancies. It can be seen that the last term of the diagonal is affected by modal truncation effects. In Figure 3.6 (b), the off-diagonal terms are plotted, showing values equal to zero for systems A2, further confirming no mass discrepancies between models B and A2.

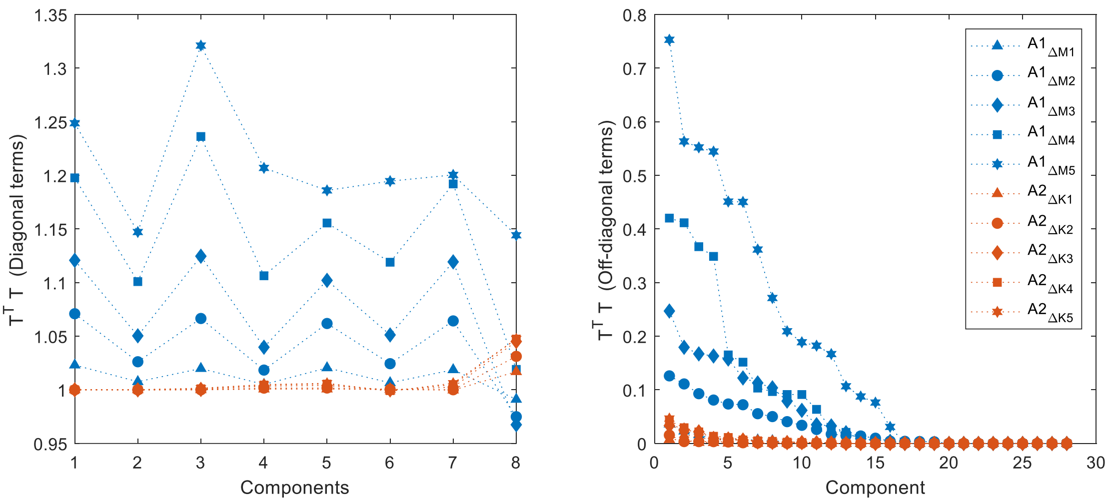

Figure 3.6: $\boldsymbol{T}^{\boldsymbol{T}}\boldsymbol{T}$ product: (a) diagonal values and (b) off-diagonal values.

Regarding the $\boldsymbol{T^T \omega_B^2 T}$ matrix, in case of no stiffness discrepancies, the diagonal terms should be equal to $\boldsymbol{\omega_A^2}$. Therefore, the relative error between the diagonal terms of $\boldsymbol{T^T \omega_B^2 T}$ and $\boldsymbol{\omega_A^2}$ for all systems is presented in Table 3.18. If the last mode is not considered due to modal truncation error, values close to zero are obtained for systems A1, whereas significantly higher values are observed for systems A2, indicating stiffness discrepancies between models B and A2. The diagonal terms of $\sqrt{\boldsymbol{T^T \omega_B^2 T}}$and $\boldsymbol{\omega_A^2}$ for systems A1 and A2 are showed in Appendix A, in Table A 1 and Table A 2, respectively.

Table 3.18: Relative error between $\boldsymbol{T^T \omega_B^2 T}$ and $\boldsymbol{\omega_A^2}$

Relative error between $T^T \omega_B^2 T$ and ω_A^2 [%]									
A1					A2				
$\Delta M1$	$\Delta M2$	$\Delta M3$	$\Delta M4$	$\Delta M5$	$\Delta K1$	$\Delta K2$	$\Delta K3$	$\Delta K4$	$\Delta K5$
0.00	0.00	0.00	0.00	0.00	0.54	1.80	9.98	28.20	54.71
0.00	0.00	0.00	0.00	0.00	1.99	5.82	21.51	39.55	53.22
0.00	0.00	0.00	0.00	0.00	0.55	1.71	7.21	14.59	21.15
0.00	0.00	0.00	0.00	0.01	1.86	4.80	12.63	17.62	19.95
0.00	0.01	0.03	0.10	0.15	0.56	1.57	5.11	8.36	10.58
0.01	0.03	0.03	0.03	0.16	1.67	3.82	7.66	9.13	9.59
0.07	0.02	0.38	1.55	2.07	0.47	1.23	3.29	4.68	5.47
0.73	2.43	4.60	8.84	11.83	2.27	4.31	6.41	6.73	6.70

The off-diagonal terms of $\boldsymbol{T^T \omega_B^2 T}$ are plotted in Figure 3.7, where values different from zero indicate stiffness discrepancies, as it is the case for systems A2.

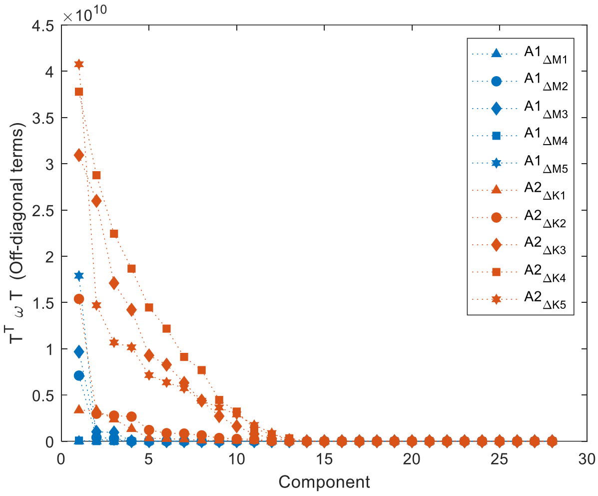

Figure 3.7: $\boldsymbol{T^T \omega_B^2 T}$ off diagonal terms.

Finally, the ***T-Mass*** and ***T-Stiffness*** indicators, which can also be used in the case of unscaled mode shapes, are plotted in Figure 3.8. ***T-Mass*** (Figure 3.8 (a)) successfully detects mass discrepancies in systems A1, with the angles decreasing as increasing the mass discrepancies. However, values close to 90° are obtained for system A1-ΔM1. In Figure 3.8 (b), ***T-Stiffness*** clearly detects stiffness discrepancies.

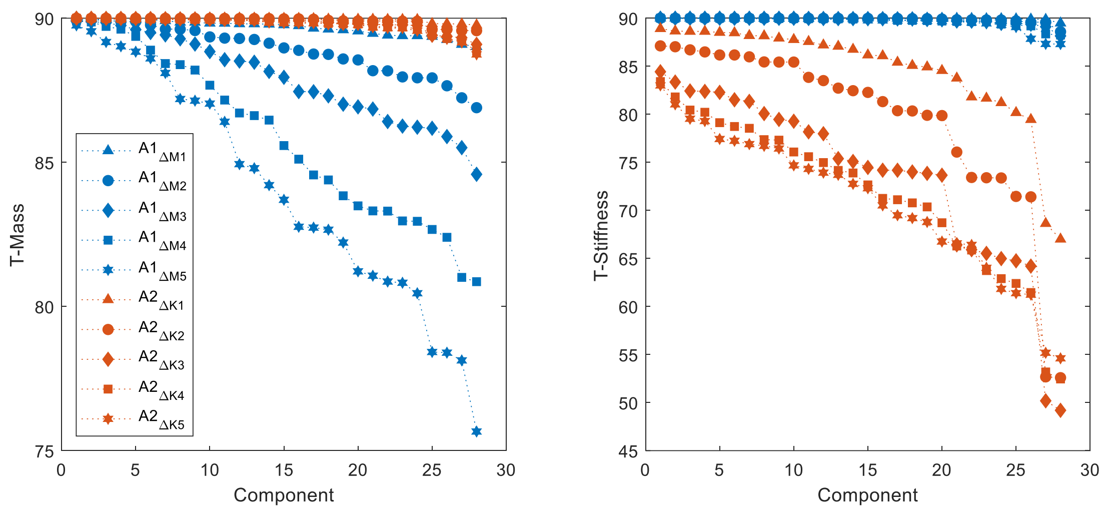

Figure 3.8: ***T-Mass*** and ***T-Stiffness*** indicators

To study the effect of errors in the mode shapes of system A (usually the experimental system) on the ***T-Mass*** and ***T-Stiffness*** indicators, different simulations have been performed considering errors in the mode shapes. Random errors of 2% are induced in the components of mode shapes of systems A, specifically in A1-ΔM2, A1-ΔM5, A2-ΔK2 and A2-ΔK5, by performing one thousand simulations for each case. It can be observed, in Figure 3.9, how the ***T-Stiffness*** is significantly affected by errors in the mode shapes, particularly when there are no changes in stiffness (systems A1).

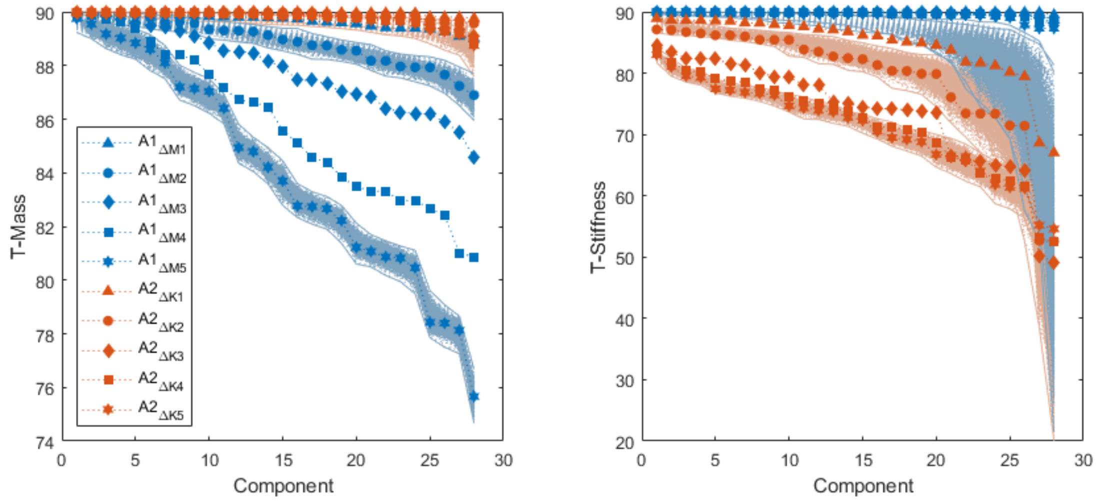

Figure 3.9. ***T-Mass*** and ***T-Stiffness*** considering errors in the mode shapes of systems A.

This effect can be explained by the effect of $\boldsymbol{\omega_B^2}$, which magnifies the inconsistencies in the mode shapes estimation (the contribution of the errors in the mode shapes increases as the natural frequencies increase). To avoid this effect, a variation of the ***T-Stiffness*** is proposed. Considering that $\boldsymbol{\omega_B} = \boldsymbol{\omega_B^T}$, the product $\boldsymbol{T^T \omega_B^2 \, T}$ can also be rewritten as:

$$\boldsymbol{T^T \omega_B^{2\,T} \omega_B^2 \, T = \left(\omega_B^2 \, T\right)^T \left(\omega_B^2 \, T\right)} \qquad (3.40)$$

Therefore, the angle between the columns of the matrix $\boldsymbol{\omega_B^2 \, T}$ (denoted ***T-Stiffness*** Variation) is also proposed to quantify the stiffness discrepancies. The obtained angles are shown in Figure 3.10.

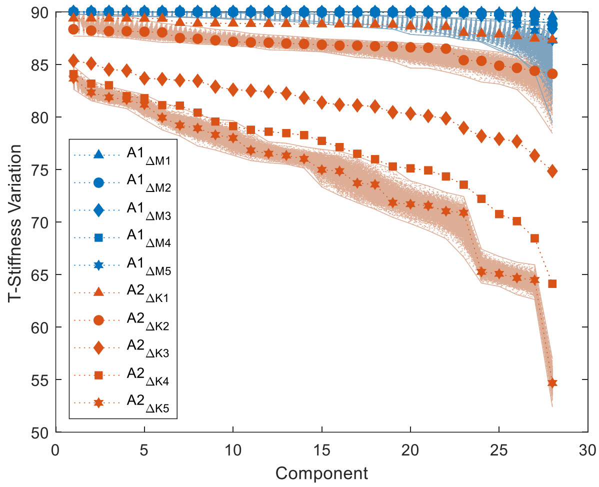

Figure 3.10. ***T-Stiffness*** variation angles with errors in the mode shapes.

3.5 Experimental example: a square glass plate

In this section, the ***T-Mass***, ***T-Stiffness,*** and ROTMAC concepts are applied to correlate a numerical model with an experimental model of a square laminated glass plate. The plate, measuring 1400 mm x 1400 mm, was composed of two 4 mm thick glass layers and a 1.14 mm polymer interlayer, and was pinned at all four corners (Figure 3.11).

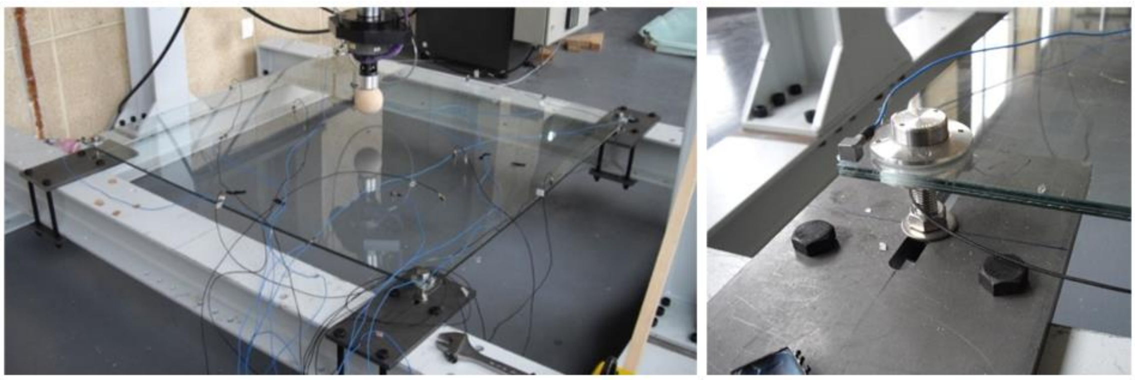

Figure 3.11: Square laminated glass plate. Experimental set up.

The experimental modal parameters were estimated through OMA. The structure was excited by randomly applying impacts to the plate using an impact hammer. The response was measured at 25 DOFs using 16 accelerometers with sensitivity of 100 mV/g. To cover the 25 DOFs, two data sets were collected using 7 reference sensors. A sampling rate of 2000 Hz and an acquisition time of 6 minutes were used. The modal parameters for the first five modes were estimated using the EFDD technique. The natural frequencies are shown in Table 3.19, where it can be observed that modes 2 and 3 are closely spaced. The experimental mode shapes normalized to the unit length are shown in Figure 3.12.

Table 3.19: Experimental and numerical natural frequencies.

Mode shape	Natural frequencies [Hz]		Error [%]
	Experimental (System A)	Numerical (System B)	
1	9.35	9.72	3.80
2	19.62	21.11	7.01
3	19.83	21.11	6.10
4	22.53	24.82	9.22
5	55.76	56.11	0.62

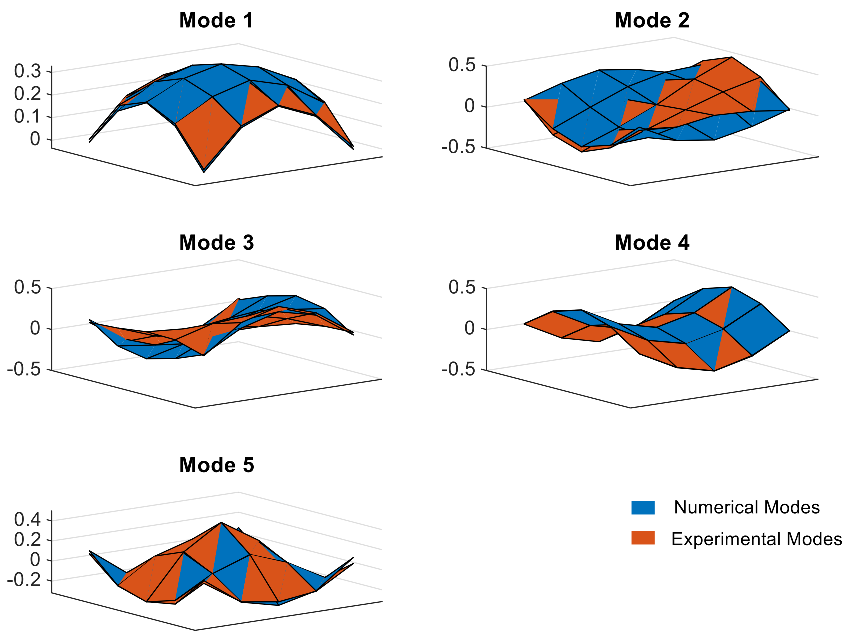

Figure 3.12: Experimental and numerical mode shapes normalized to the unit length.

A 3D finite element model of the structure was previously developed in ANSYS, using a mesh of 19200 3D solid elements with 20 nodes each. The numerical natural frequencies for the first five modes are presented in Table 3.19, where it can be observed that modes 2 and 3 are repeated.

The correlation between systems A and B is firstly studied with the MAC (Table 3.20). It can be observed that for modes 2 and 3 values far from 1 are obtained, which can be an indicator of poor correlation, whereas for modes 1, 4 and 5 very good correlation exits.

Table 3.20: MAC between systems A and B

0.9971	0.0000	0.0001	0.0000	0.0976
0.0000	0.5990	0.3965	0.0000	0.0001
0.0000	0.5088	0.4896	0.0002	0.0000
0.0000	0.0001	0.0000	0.9996	0.0000
0.0661	0.0002	0.0007	0.0000	0.9862

Considering that experimental mode shapes are unscaled, an estimation of $\widehat{\boldsymbol{T}}_{\boldsymbol{U}}$ is obtained with Eq. (3.21), using five numerical modes and five experimental modes, which is factorized using the QR decomposition. From the decomposition, matrices $\boldsymbol{R}$ and $\boldsymbol{Q}$ are obtained, where $\boldsymbol{R}$ is the rotation matrix and $\boldsymbol{Q}$ contains the effects of scaling and shear. However, as unscaled mode shapes are used, the changes in scaling cannot be detected.

Table 3.21: Matrix $\boldsymbol{R}$

-0.9992	0.0068	-0.0006	0.0008	0.0390
-0.0031	-0.6997	-0.7137	-0.0050	0.0330
0.0056	0.7141	-0.6998	0.0109	0.0084
0.0007	-0.0113	0.0040	0.9999	-0.0004
-0.0391	-0.0168	-0.0295	-0.0005	-0.9987

Table 3.22: Matrix $\boldsymbol{Q}$

-1.4819	0.0007	0.0168	-0.0001	-0.0249
0.0000	-1.1840	0.1345	-0.0011	-0.0482
0.0000	0.0000	-1.1992	-0.0009	-0.0060
0.0000	0.0000	0.0000	-0.9801	-0.0007
0.0000	0.0000	0.0000	0.0000	-1.0596

From the $\boldsymbol{R}$ matrix presented in Table 3.21, a rotation angle of -45.5890° is obtained for modes 2 and 3, with the mode shapes mainly rotating in the local subspace defined by vectors $\boldsymbol{b}_{\boldsymbol{2}}$ and $\boldsymbol{b}_{\boldsymbol{3}}$. The second and third rotated numerical mode shapes ($\boldsymbol{b}_{\boldsymbol{r2}}$ and $\boldsymbol{b}_{\boldsymbol{r3}}$) are shown in Figure 3.13, where a good correlation can be observed between the numerical and the experimental models. Moreover, the ROTMAC is presented in Table 3.23, showing a very good correlation for all modes. The off-diagonal terms are very low indicating that the effect of shear is very low.

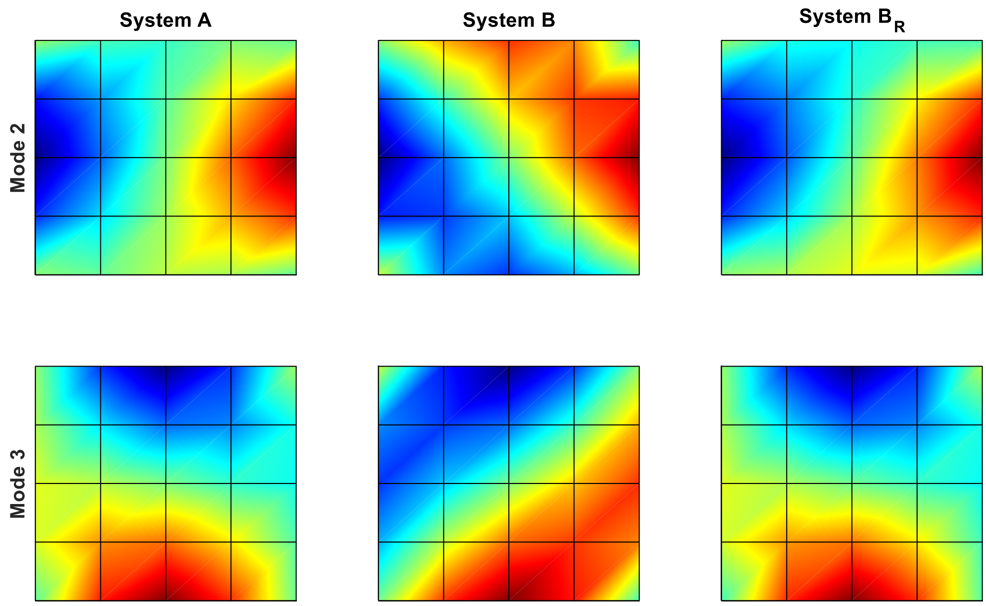

Figure 3.13: Mode shapes 2 and 3 of systems A, B and rotated B (B_R)

Table 3.23: ROTMAC: MAC between systems A and B_R

0.9974	0.0001	0.0001	0.0000	0.0822
0.0000	0.9810	0.0125	0.0000	0.0013
0.0000	0.0000	0.9986	0.0000	0.0000
0.0000	0.0000	0.0000	0.9997	0.0000
0.0938	0.0001	0.0000	0.0000	0.9879

The ***T-mass*** and ***T-stiffness*** matrices are shown in Table 3.24 and Table 3.25. The last row and column have been shaded as they can be affected by modal truncation when the number of numerical modes is not larger than the number of experimental modes (as it is this case).

Table 3.24: ***T-mass***

----	89.91	89.35	89.99	89.04
89.91	----	83.54	89.95	87.69
89.35	83.54	----	89.95	89.71
89.99	89.95	89.95	----	89.96
89.04	87.69	89.71	89.96	----

Table 3.25: ***T-stiffness***

----	89.78	89.63	89.97	88.80
89.17	----	83.53	89.96	89.25
88.57	83.54	----	89.78	89.87
89.84	89.94	89.70	----	89.94
55.90	84.74	89.12	89.68	----

From Table 3.24 it could be inferred that there are mass discrepancies, because although most components are close to 90°, the value in row three, column two is 83.54°. However, it must be emphasized that a low angle can also be obtained if the mode shapes ‑ closely spaced in this case ‑ are not estimated accurately. For instance, when using the FDD technique in the case of repeated or closely spaced modes, the mode shape associated with the higher singular value is sometimes estimated with accuracy whereas the uncertainty of the second one is higher.

Moreover, when two repeated modes are considered, the inner product $\widehat{\boldsymbol{T}}^{\boldsymbol{T}}\boldsymbol{\omega}_{\boldsymbol{b}}^{\boldsymbol{2}}\,\widehat{\boldsymbol{T}} = \boldsymbol{\omega}_{\boldsymbol{b}}^{\boldsymbol{2}}\,\widehat{\boldsymbol{T}}^{\boldsymbol{T}}\,\widehat{\boldsymbol{T}}$ is proportional to $\widehat{\boldsymbol{T}}^{\boldsymbol{T}}\,\widehat{\boldsymbol{T}}$, and the same angles are obtained with ***T-mass*** and ***T-stiffness***. This result does not depend on the accuracy achieved in the estimation of the mode shapes and holds for changes in stiffness, mass or both. This can be observed in Table 3.24 and Table 3.25 where the same angle is obtained in row three, column two.

Additionally, in the case of mass matrix $\boldsymbol{M_A}$ proportional to $\boldsymbol{M_B}$, the product $\boldsymbol{T^T T}$ is diagonal (there are changes in scaling and not shear). Therefore, when using unscaled mode shapes, no information of mass discrepancies can be obtained with inner product $\boldsymbol{T_U^T T_U}$.

4

Stress estimation

This chapter aims to develop different strain and stress estimation techniques base on modal decomposition, with the goal of estimating an accurate stress time history. A precisely estimated stress time history is crucial for fatigue assessment and fatigue monitoring. Moreover, the methods presented in this chapter rely on modal expansion, requiring a numerical model and highlighting the importance of correlation techniques, presented in Chapter 3, for accurate stress estimation.

An introduction to the main stress estimation techniques is presented, along with a review of the state of the art. Then, the structural dynamic modification theory is developed to provide a foundation for understanding the proposed methods. Additionally, the sources of error in the estimated stresses are analysed.

4.1 Introduction

Stresses (or strains) are considered the principal variable responsible for fatigue damage. Therefore, the stress time history is crucial for estimating the accumulated fatigue damage and assessing the remaining fatigue lifetime. To estimate the actual stress time history to which operating structures are subjected, different approaches are commonly used:

- The stress time histories at discrete points of interest can be obtained directly from strain gauge measurements located at those same points, which in many cases is not possible due to economic constraints, inaccessibility, or harsh environment.
- Stress/strain estimation, also known as full-field stress/strain estimation or virtual sensing techniques. In this case stress time histories can be estimated from structural responses by continuously measuring experimental displacements, velocities, accelerations or strain responses. Accelerometers are commonly used due to their reliability for long-term measurements. This approach allows for the estimation of stresses at any point of the structure using a limited number of installed sensors. There are different techniques for stress/strain estimation, with *modal expansion* and the *Kalman filter* techniques being the most used.

In applications where a good understanding of structural dynamics and modal parameters is desired, modal expansion techniques are chosen, allowing for their combination with other SHM techniques. The core of modal decomposition-based estimation techniques is the modal superposition principle; thus, strain mode shapes and modal coordinates are needed.

In 2003, R. Brincker et al. [97] introduced some of the possible applications of OMA, such as: monitoring, vibration level estimation, fatigue estimation and load estimation. Based on the reviewed literature, this conference paper was the first publication mentioning of stress history estimation from vibrations response. The first methodology to estimate stress time histories at any point of the structure was proposed by Henrik P. Hjelm [98]. In this methodology the displacements at any point of the structure are estimated through modal superposition using modal coordinates and numerical mode shapes (from an updated finite element model). Once the displacements are estimated at any point of the structure, stresses can be calculated by traditional finite element calculations. The methodology was validated by two experimental tests, carried out on a lab cantilever L-shaped beam and a 20 m high lattice tower. P. Fernández [99] propose to estimate stresses using modal superposition and expanding the experimental mode shapes to unmeasured locations using a numerical model, i.e. a transformation matrix is obtained assuming that the experimental modal matrix can be obtained as a linear combination of the numerical modal matrix. The methodology was validated on an experimental 1.875 meter long steel cantilever beam [99], a glass beam [100], a symmetric scale model of a two story building [101] and a glass plate [102]. Experimental strain mode shapes can also be expanded using numerical strain mode shapes [103], [104]. M. Tarpo [103] validated the methodology in an offshore structure. B. Nabuco [104] used also the same approach to estimated stresses with the objective of calculating fatigue damage in an offshore jacket structure.

Several techniques have been proposed to estimate the transformation matrix which relates experimental and numerical mode shapes, such as static condensation of stiffness and mass matrices [105], Dynamic Condensation [106], SEREP [107] and the Hybrid method [108], being SEREP one of the most widely used and studied for stress estimation [109], [110]. The results provided by these techniques can be improved using the local correspondence principle [111] or the methodology proposed by P. Avitabile [112]. Marius Tarpo [113] compared the following techniques: SEREP, the local correspondence principle and an enhanced version of the local correspondence principle (leave-p-out).

Many other authors, avoid the use of a transformation matrix in the modal expansion algorithm by directly relying on a well correlated finite element model [114]–[116]. In this approach mode shape expansion is not needed, and strain mode shapes at the locations of interest (virtual locations) are obtained from the numerical model.

Experimental modal coordinates can be calculated using mode shapes (numerical or experimental) and experimental displacements, among others. Henkel [115] stated that the use of numerical mode shapes is preferred, giving a set of continuous mode shapes over the entire structure, although the use of experimental mode shapes (data-driven approach) avoid any errors present in the numerical model. This approach was widely validated in offshore wind turbines. However, A. Iliopoulos [114] concluded that the quality of the method was directly related to the quality of the FE model.

Modal coordinates can also be estimated using strain responses. Although the responses are usually measured with accelerometers, the use of strain mode shapes for vibration-based monitoring is becoming more relevant due to numerous advantages they present, such as lower sensitivity to temperature, higher sensitivity to small-scale damage and high accuracy and precision. Moreover, when fiber-optic sensors are employed, modal strains can be obtained in a dense grid with a relatively low cost [117], [118]. For these reasons, the use of strain sensors (combined or not with accelerometers) to estimate strains at any point of the structure is also regarded as a promising technique.

Several authors have also applied modal expansion techniques with strain mode shapes [119]–[123]. In this case, modal coordinates are calculated with the experimental strain mode shapes and the measured strain responses, which are then expanded to the unmeasured locations using a numerical model. In this approach, a high-fidelity finite element model of the studied structure is needed [121], however the use of accelerometers is not required. Mora [122], compared different virtual sensing techniques based on strain mode shapes. In 2022, M. Tarpo [124] proposed a new a data-driven strain estimation technique using principal component analysis (PCA). In this case, temporary strain gauges at the locations of interest and accelerometers are required, but a finite element model is not necessary. The methodology was validated in an offshore wind turbine.

To validate the estimated strains or stresses by comparing them with the reference signals, different tools have been used in the literature. The Time Response Assurance Criterion (TRAC) [109] is an indicator similar to the MAC used to compare two time series such as the estimated strains and the expected strains at one single DOF. Values between zero and one are obtained, where values close to unity indicate perfect correlation. Similarly, the Frequency Response Assurance Criterion (FRAC) compares the estimated and expected strains in the frequency domain. Since the TRAC and FRAC values do not take into account amplitude differences, the coefficient of determination R^2 [125] was also used both in time domain and frequency domain [103], [113]. A coefficient of determination with a value of 1 indicates perfect correlation with the same amplitudes. [126]. The Mean Absolute Error (MAE) [127] is also an indicator of discrepancies between signals. Small values with respect to the actual magnitude indicate good correlation, thus, it is not normalized. The Root-Mean-Square Error (RMSE) it also a way of quantifying discrepancies, both in the time and frequency domains. Other indicators related to fatigue analysis were proposed in the literature, such as the Normalized Error of Fatigue Damage (NEFD) which calculates the normalized error between the cumulated fatigue damage with estimated stresses and expected stresses [103], [113].

A numerical model of the structure is commonly used to perform modal expansion, usually a finite element model. For this reason, special attention must be paid to model correlation (Chapter 3), as the accuracy of the results relies on the similarity of the experimental and numerical models, specifically on the mode shapes and strain mode shapes. If the correlation is not satisfactory, model updating techniques must be used to modify the finite element model according to the experimental modal parameters.

4.2 Theory

In this section the theory needed to estimate stresses using modal superposition and modal expansion techniques is presented.

4.2.1 Exact solution

In linear discrete un-damped dynamical systems, the response of a structure given by the vector of displacements $\boldsymbol{u}(\boldsymbol{t})$ (hereafter denoted as $\boldsymbol{u}$) can be decomposed in modal coordinates as [33]:

$$\boldsymbol{u} = \boldsymbol{\phi}\, \boldsymbol{q} \tag{4.1}$$

where $\boldsymbol{\phi}$ is the modal matrix (a matrix containing the mode shapes in column vectors) and $\boldsymbol{q}$ are the modal coordinates $\boldsymbol{q}(\boldsymbol{t})$ (hereafter denoted as $\boldsymbol{q}$).

In this chapter, the numerical model is considered the unperturbed system (or system B) and the experimental model the perturbed system (or system A). Particularizing Eq. (4.1) for an experimental system, denoted with subscript $'x'$, the modal coordinates can be estimated with:

$$\boldsymbol{q_x} = \boldsymbol{\phi}_{\boldsymbol{x}}^{-1}\, \boldsymbol{u_x} \tag{4.2}$$

where it has been assumed that $\boldsymbol{\phi_x}$ is a square matrix. Using modal superposition, strains can be estimated with the expression:

$$\boldsymbol{\varepsilon_x} = \boldsymbol{\phi_{x\varepsilon}}\, \boldsymbol{q_x} \tag{4.3}$$

where $\boldsymbol{\phi_{x\varepsilon}}$ is the experimental strain mode shape matrix, in this case also a square matrix. Similarly, stresses can be estimated with:

$$\boldsymbol{\sigma_x} = \boldsymbol{\phi_{x\sigma}}\, \boldsymbol{q_x} \tag{4.4}$$

where $\boldsymbol{\phi_{x\sigma}}$ is the stress mode shape matrix, which is related to the strain mode shape matrix by:

$$\boldsymbol{\phi_{x\sigma}} = \boldsymbol{D}\, \boldsymbol{\phi_{x\varepsilon}} \tag{4.5}$$

with matrix $\boldsymbol{D}$ being the constitutive matrix that depends on the material properties.

According to the structural dynamic modification theory [128], and particularizing Eq. (3.14) for experimental (System A) and numerical (System B) modes shapes, the experimental mode shapes can be expressed as a linear combination of the numerical ones:

$$\boldsymbol{\phi_x} = \boldsymbol{\phi_{FE}}\, \boldsymbol{T} \tag{4.6}$$

where $\boldsymbol{\phi_{FE}}$ is a matrix containing the numerical mode shapes. A similar relationship exists between the strain mode shape matrices:

$$\boldsymbol{\phi}_{x\varepsilon} = \boldsymbol{\phi}_{FE\varepsilon}\,\boldsymbol{T}_{\varepsilon} \tag{4.7}$$

where $\boldsymbol{\phi}_{x\varepsilon}$ and $\boldsymbol{\phi}_{FE\varepsilon}$ are the experimental and the numerical strain mode shape matrices, respectively. Regarding the stress mode shapes, a similar relationship exists:

$$\boldsymbol{\phi}_{x\sigma} = \boldsymbol{\phi}_{FE\sigma}\,\boldsymbol{T}_{\sigma} \tag{4.8}$$

Given that the components of the transformation matrix $\boldsymbol{T}$ are constant scalars and the strain mode shapes are derivatives of the mode shapes, from Equations (4.6), (4.7) and (4.8), it is derived that:

$$\boldsymbol{T}_{\sigma} = \boldsymbol{T}_{\varepsilon} = \boldsymbol{T} \tag{4.9}$$

4.2.2 Modal expansion

To estimate strain at the location of interest, experimental mode shapes and/or the experimental strain mode shapes must be expanded to the unmeasured DOFs using a numerical model, which must be well correlated with the experimental model.

To better understand the following explanations, two subspaces will be considered (Figure 4.1): a subspace spanned by the experimental mode shapes $(\boldsymbol{\phi}_x)$ and another one spanned by the numerical mode shapes $(\boldsymbol{\phi}_{FE})$. Any vector of experimental responses, such as displacements $(\boldsymbol{u})$, projected in the experimental subspace, will be denoted with circumflex accent $(\widehat{\boldsymbol{u}})$ (Figure 4.1 (a)) whereas tilde will be used when projecting onto the numerical subspace $(\widetilde{\boldsymbol{u}})$. If only the active DOFs are considered, subscript $'a'$ is used (Figure 4.1 (b)).

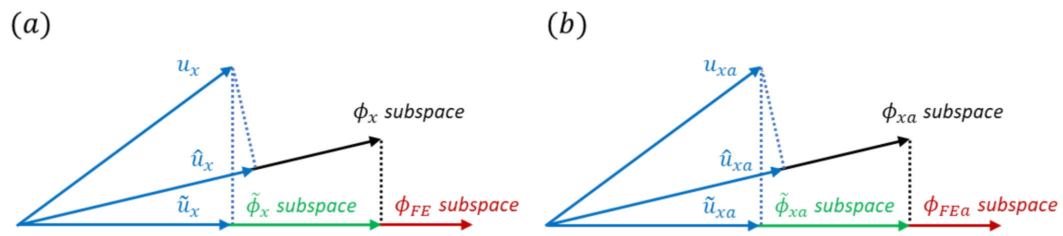

Figure 4.1 Nomenclature for experimental and numerical subspaces: (a) all DOFs and (b) only active DOFs.

In experimental modal analysis the responses are measured in reduced number of DOFs (active DOFs) and in a limited frequency range, so that only $'m'$ number of modes can be identified. The experimental modal matrix $\boldsymbol{\phi}_x$ can be partitioned as:

$$\boldsymbol{\phi}_x = \begin{bmatrix} \boldsymbol{\phi}_{xam} & \boldsymbol{\phi}_{xar} \\ \boldsymbol{\phi}_{xdm} & \boldsymbol{\phi}_{xdr} \end{bmatrix} \tag{4.10}$$

where subscripts $'m'$ and $'r'$ indicate measured and unmeasured modes, and $'a'$ and $'d'$ indicate active (measured) and deleted (not measured) DOFs, respectively. However, due to the effect of truncation, only the submatrix $\boldsymbol{\phi}_{xam}$ can be estimated. The linear combination given by Eq. (4.6) can now be expressed as:

$$\begin{bmatrix} \boldsymbol{\phi}_{xam} & \boldsymbol{\phi}_{xar} \\ \boldsymbol{\phi}_{xdm} & \boldsymbol{\phi}_{xdr} \end{bmatrix} = \begin{bmatrix} \boldsymbol{\phi}_{FEam} & \boldsymbol{\phi}_{FEar} \\ \boldsymbol{\phi}_{FEdm} & \boldsymbol{\phi}_{FEdr} \end{bmatrix} \begin{bmatrix} \boldsymbol{T}_{mm} & \boldsymbol{T}_{mr} \\ \boldsymbol{T}_{rm} & \boldsymbol{T}_{rr} \end{bmatrix} \tag{4.11}$$

Therefore, if a numerical model is assembled, an estimate of matrix $\boldsymbol{T}$, denoted hereafter $\breve{\boldsymbol{T}}_{mm}$, can be derived from Eq. (4.11) as:

$$\breve{\boldsymbol{T}}_{mm} = \boldsymbol{\phi}_{FEam}^{+} \, \boldsymbol{\phi}_{xam} \tag{4.12}$$

where superscript $'+'$ indicates pseudoinverse. In Eq. (4.12) the modal matrix $\boldsymbol{\phi}_{xam}$ is a matrix size (a, m), and $\breve{\boldsymbol{T}}_{mm}$ is size (m, m). The result obtained with Eq. (4.12) depends on the number of modes considered in the modal matrix $\boldsymbol{\phi}_{FEa}$, but it can be different than $'m'$ [111]. Thus, the size of $\breve{\boldsymbol{T}}_{mm}$ will depend on the size of matrices $\boldsymbol{\phi}_{xam}$ and $\boldsymbol{\phi}_{FEa}$. For simplicity, it is assumed the same number of modes $'m'$ in $\boldsymbol{\phi}_{FEam}$ and $\boldsymbol{\phi}_{xam}$.

From these equations, the numerical model can be used to expand the experimental mode shapes to the un-measured DOFs by:

$$\begin{bmatrix} \widetilde{\boldsymbol{\phi}}_{xam} \\ \widetilde{\boldsymbol{\phi}}_{xdm} \end{bmatrix} = \begin{bmatrix} \boldsymbol{\phi}_{FEam} \\ \boldsymbol{\phi}_{FEdm} \end{bmatrix} \breve{\boldsymbol{T}}_{mm} \tag{4.13}$$

where $\widetilde{\boldsymbol{\phi}}_{xam}$ is the projection of the experimental mode shapes $\boldsymbol{\phi}_{xam}$ on the subspace spanned by the numerical mode shapes $\boldsymbol{\phi}_{FEa}$ (Figure 4.1). Equation (4.13) can also be expressed as:

$$\begin{bmatrix} \widetilde{\boldsymbol{\phi}}_{xam} \\ \widetilde{\boldsymbol{\phi}}_{xdm} \end{bmatrix} = \begin{bmatrix} \boldsymbol{\phi}_{FEam} \\ \boldsymbol{\phi}_{FEdm} \end{bmatrix} \boldsymbol{\phi}_{FEam}^{+} \, \boldsymbol{\phi}_{xam} = \begin{bmatrix} \boldsymbol{I} \\ \boldsymbol{\phi}_{FEdm} \boldsymbol{\phi}_{FEam}^{+} \end{bmatrix} \boldsymbol{\phi}_{xam} \tag{4.14}$$

A similar relationship is obtained for strain mode shapes:

$$\begin{bmatrix} \boldsymbol{\phi}_{x\varepsilon gm} & \boldsymbol{\phi}_{x\varepsilon gr} \\ \boldsymbol{\phi}_{x\varepsilon gm} & \boldsymbol{\phi}_{x\varepsilon gr} \end{bmatrix} = \begin{bmatrix} \boldsymbol{\phi}_{FE\varepsilon gm} & \boldsymbol{\phi}_{FE\varepsilon gr} \\ \boldsymbol{\phi}_{FE\varepsilon gm} & \boldsymbol{\phi}_{FE\varepsilon gr} \end{bmatrix} \begin{bmatrix} \boldsymbol{T}_{\varepsilon mm} & \boldsymbol{T}_{\varepsilon mr} \\ \boldsymbol{T}_{\varepsilon rm} & \boldsymbol{T}_{\varepsilon rr} \end{bmatrix} \tag{4.15}$$

where subscript $'g'$ denotes the active points where strains are measured. The DOFs $'g'$ can coincide or not with the active DOFs $'a'$. Hereafter, it is assumed for simplicity, that the strains are measured at the active DOFs $'a'$. Therefore, a transformation matrix $\breve{\boldsymbol{T}}_{\boldsymbol{\varepsilon mm}}$ can be estimated with the equation:

$$\breve{\boldsymbol{T}}_{\boldsymbol{\varepsilon mm}} = \boldsymbol{\phi}_{\boldsymbol{FE\varepsilon am}}^{+}\, \boldsymbol{\phi}_{\boldsymbol{x\varepsilon am}} \tag{4.16}$$

It must be noticed that, in addition to the numerical mode shapes $\boldsymbol{\phi}_{\boldsymbol{FE}}$, both the strain mode shapes $\boldsymbol{\phi}_{\boldsymbol{FE\varepsilon}}$ and the stress mode shapes $\boldsymbol{\phi}_{\boldsymbol{FE\sigma}}$ can be extracted from a finite element software with a modal frequency analysis, at the required locations. Thus, the measured strain mode shapes can also be expanded to the un-measured DOFs by:

$$\widetilde{\boldsymbol{\phi}}_{\boldsymbol{x\varepsilon m}} = \begin{bmatrix} \widetilde{\boldsymbol{\phi}}_{\boldsymbol{x\varepsilon am}} \\ \widetilde{\boldsymbol{\phi}}_{\boldsymbol{x\varepsilon dm}} \end{bmatrix} = \begin{bmatrix} \boldsymbol{\phi}_{\boldsymbol{FE\varepsilon am}} \\ \boldsymbol{\phi}_{\boldsymbol{FE\varepsilon dm}} \end{bmatrix} \breve{\boldsymbol{T}}_{\boldsymbol{\varepsilon mm}} \tag{4.17}$$

The stress mode shapes can also be expanded with the expression:

$$\widetilde{\boldsymbol{\phi}}_{\boldsymbol{x\sigma m}} = \begin{bmatrix} \widetilde{\boldsymbol{\phi}}_{\boldsymbol{x\sigma am}} \\ \widetilde{\boldsymbol{\phi}}_{\boldsymbol{x\sigma dm}} \end{bmatrix} = \begin{bmatrix} \boldsymbol{\phi}_{\boldsymbol{FE\sigma am}} \\ \boldsymbol{\phi}_{\boldsymbol{FE\sigma dm}} \end{bmatrix} \breve{\boldsymbol{T}}_{\boldsymbol{\varepsilon mm}} \tag{4.18}$$

or as:

$$\widetilde{\boldsymbol{\phi}}_{\boldsymbol{x\sigma m}} = \boldsymbol{D}\, \widetilde{\boldsymbol{\phi}}_{\boldsymbol{x\varepsilon m}} \tag{4.19}$$

Therefore, to estimate strains by modal superposition with Eq. (4.3), the strain mode shapes at the locations of interest needed can be obtained from:

- Experimental strain mode shapes estimated by modal analysis: $\boldsymbol{\phi}_{\boldsymbol{x\varepsilon}}$
- Numerical strain mode shapes obtained from a numerical model: $\boldsymbol{\phi}_{\boldsymbol{\varepsilon FE}}$
- Experimental strain mode shapes expanded with a numerical model through a transformation matrix: $\widetilde{\boldsymbol{\phi}}_{\boldsymbol{x\varepsilon m}}$

4.2.3 Modal coordinates

In modal superposition, strain mode shapes and modal coordinates are required to estimate strains. Modal coordinates can be estimated by projecting the experimental responses onto an experimental subspace or onto a numerical subspace. Moreover, these subspaces can be spanned by mode shapes, strain mode shapes, or both.

If the experimental displacement response of the structure is measured at the $'a'$ active DOFs, Eq. (4.1) results in:

$$\boldsymbol{u}_{xa} = \boldsymbol{\phi}_{xam}\, \boldsymbol{q}_{xm} \tag{4.20}$$

An approximation of the experimental modal coordinates (denoted as $\widehat{\boldsymbol{q}}_{xm}$) can be obtained with:

$$\widehat{\boldsymbol{q}}_{xm} = \boldsymbol{\phi}_{xam}^{+}\, \boldsymbol{u}_{xa} \tag{4.21}$$

Alternatively, other equations can be proposed to obtain an estimation of the experimental modal coordinates. If the structure response ($\boldsymbol{u}_{xa}$), is projected onto the subspace spanned by the numerical mode shapes ($\boldsymbol{\phi}_{FEam}$), modal coordinates ($\widetilde{\boldsymbol{q}}_{xm}$) are estimated as:

$$\widetilde{\boldsymbol{q}}_{xm} = \boldsymbol{\phi}_{FEam}^{+}\, \boldsymbol{u}_{xa} \tag{4.22}$$

If strain sensors are installed in the structure, strain mode shapes and experimental strain time series ($\boldsymbol{\varepsilon}_{xa}$) are known. Therefore, an approximation of the experimental modal coordinates (denoted as $\widehat{\boldsymbol{q}}_{\varepsilon xm}$) can be obtained with:

$$\widehat{\boldsymbol{q}}_{\varepsilon xm} = \boldsymbol{\phi}_{x\varepsilon am}^{+}\, \boldsymbol{\varepsilon}_{xa} \tag{4.23}$$

If the experimental structural strain response ($\boldsymbol{\varepsilon}_{xa}$) is projected onto the subspace spanned by the numerical mode shapes ($\boldsymbol{\phi}_{FE\varepsilon am}$), the modal coordinates can also be obtained by the expression:

$$\widetilde{\boldsymbol{q}}_{\varepsilon xm} = \boldsymbol{\phi}_{FE\varepsilon am}^{+}\, \boldsymbol{\varepsilon}_{xa} \tag{4.24}$$

In the case that both strains and displacements are measured, and projected onto the subspace spanned by the experimental mode shapes and strain mode shapes, the modal coordinates ($\widehat{\boldsymbol{q}}_{txm}$) can be estimated by the expression:

$$\widehat{\boldsymbol{q}}_{txm} = \begin{bmatrix} \boldsymbol{\phi}_{x\varepsilon am} \\ \boldsymbol{\phi}_{xam} \end{bmatrix}^{+} \begin{bmatrix} \boldsymbol{\varepsilon}_{xa} \\ \boldsymbol{u}_{xa} \end{bmatrix} \tag{4.25}$$

In a similar way, strains and displacements can be projected onto the subspace spanned by the numerical mode shapes and strain mode shapes, obtaining the modal coordinates ($\widetilde{\boldsymbol{q}}_{txm}$) as:

$$\widetilde{\boldsymbol{q}}_{txm} = \begin{bmatrix} \boldsymbol{\phi}_{FE\varepsilon am} \\ \boldsymbol{\phi}_{FEam} \end{bmatrix}^{+} \begin{bmatrix} \boldsymbol{\varepsilon}_{xa} \\ \boldsymbol{u}_{xa} \end{bmatrix} \tag{4.26}$$

All the equations proposed to estimate modal coordinates have been summarized in Figure 4.2.

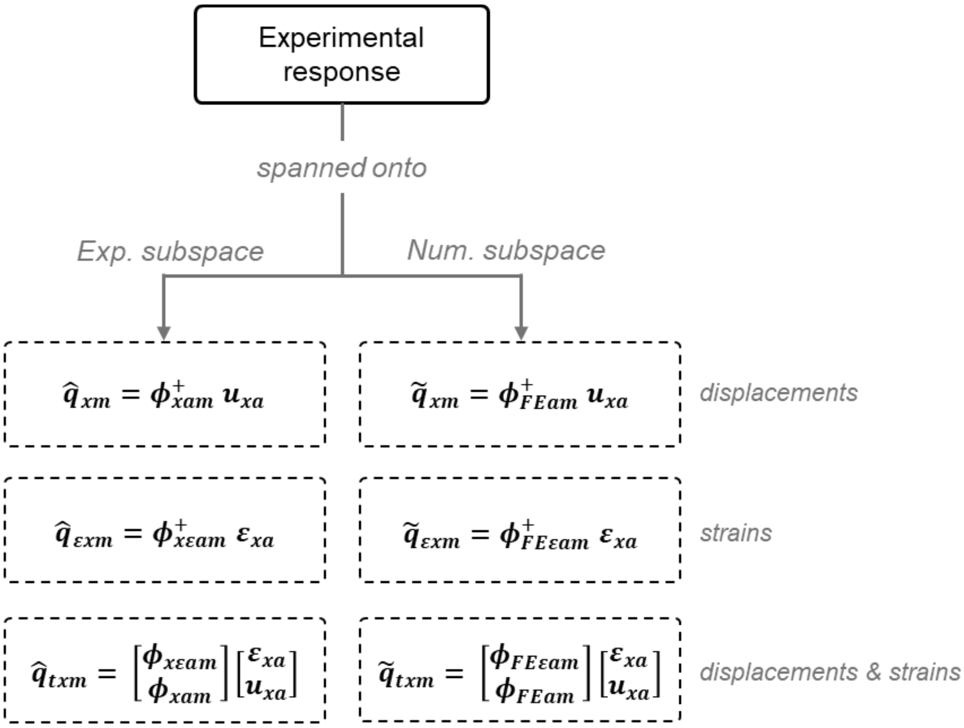

Figure 4.2: Summary of the proposed equations to obtain modal coordinates.

It is worth noting that if the displacements are not measured, it is assumed that they can be obtained by integration of velocities or through double integration of accelerations, in either time or frequency domains. If the experimental displacements are measured in real time, the strains and the stresses can also be estimated in real time.

4.3 Stress estimation methods

In this section, different methods for estimating stresses and strains based on modal superposition are proposed. Modal superposition enables the estimation of strains/stresses at the locations of interests using modal coordinates and strain/stress mode shapes. Depending on how mode shapes are expanded and how modal coordinates are estimated, eight methods are proposed in this thesis. *Methods 1* to *4* are based on projecting the experimental responses (displacements or strains) onto an experimental subspace, whereas in *Methods 5* to *8*, responses are projected onto a numerical subspace.

4.3.1 Method 1

In this section, a methodology to estimate strains and stresses in structures, denoted as *Method 1*, is described in detail. An updated numerical model is needed as well as the following information from the experimental structure:

- Mode shapes $\boldsymbol{\phi}_{xam}$ (estimated with modal analysis).
- Displacements $\boldsymbol{u}_{xa}$ (measured with displacement sensors or by double integration of accelerations).

In this method, modal coordinates $\widehat{\boldsymbol{q}}_{xm}$ are calculated with Eq. (4.21).

Since the experimental strain mode shapes are not known, the following approximation can be considered $\breve{\boldsymbol{T}}_{mm} = \breve{\boldsymbol{T}}_{\sigma mm} = \breve{\boldsymbol{T}}_{\varepsilon mm}$, and the strain mode shapes can be estimated with the following expression:

$$\widetilde{\boldsymbol{\phi}}_{x\varepsilon m_1} = \boldsymbol{\phi}_{FE\varepsilon m}\, \breve{\boldsymbol{T}}_{mm} \tag{4.27}$$

Therefore, strains estimated with *Method 1* (denoted as $\boldsymbol{\varepsilon_1}$) are expressed as:

$$\boldsymbol{\varepsilon_1} = \begin{bmatrix} \boldsymbol{\phi}_{FE\varepsilon am} \\ \boldsymbol{\phi}_{FE\varepsilon dm} \end{bmatrix} \breve{\boldsymbol{T}}_{mm}\, \widehat{\boldsymbol{q}}_{xm} = \begin{bmatrix} \boldsymbol{\phi}_{FE\varepsilon am} \\ \boldsymbol{\phi}_{FE\varepsilon dm} \end{bmatrix} \breve{\boldsymbol{T}}_{mm}\, \boldsymbol{\phi}^{+}_{xam} \boldsymbol{u}_{xa} \tag{4.28}$$

or alternatively,

$$\boldsymbol{\varepsilon_1} = \begin{bmatrix} \boldsymbol{\phi}_{FE\varepsilon am} \\ \boldsymbol{\phi}_{FE\varepsilon dm} \end{bmatrix} \breve{\boldsymbol{T}}_{mm}\, \breve{\boldsymbol{T}}^{+}_{mm}\, \boldsymbol{\phi}_{FEam}\, \boldsymbol{u}_{xa} \tag{4.29}$$

Following the same approach to estimate stresses, Eq. (4.30) is proposed:

$$\boldsymbol{\sigma_1} = \begin{bmatrix} \boldsymbol{\phi}_{FE\sigma am} \\ \boldsymbol{\phi}_{FE\sigma dm} \end{bmatrix} \breve{\boldsymbol{T}}_{mm}\, \widehat{\boldsymbol{q}}_{xm} = \boldsymbol{\phi}_{FE\sigma m}\, \breve{\boldsymbol{T}}_{mm}\, \boldsymbol{\phi}^{+}_{xam}\, \boldsymbol{u}_{xa} \tag{4.30}$$

or alternatively:

$$\boldsymbol{\sigma_1} = \begin{bmatrix} \boldsymbol{\phi}_{FE\sigma am} \\ \boldsymbol{\phi}_{FE\sigma dm} \end{bmatrix} \breve{\boldsymbol{T}}_{mm}\, \breve{\boldsymbol{T}}^{+}_{mm}\, \boldsymbol{\phi}_{FEam}\, \boldsymbol{u}_{xa} \tag{4.31}$$

As a summary, the information needed to apply this method (*Method 1*) has been summarized in Table 4.1. The assumptions, and the calculations needed to estimate strains and stresses at the locations of interests are also shown in Table 4.1.

Table 4.1: Summary of the input data, assumptions and equations for *Method 1.*

INPUTS	PREVIOUS DATA	EXPERIMENTAL MODEL	$\boldsymbol{\phi}_{xam}$
		NUMERICAL MODEL	$\boldsymbol{\phi}_{FEam}$ $\boldsymbol{\phi}_{FE\varepsilon m}$ or $\boldsymbol{\phi}_{FE\sigma m}$
	REAL TIME MEASUREMENTS		$\boldsymbol{u}_{xa}$
PRELIMINARY CALCULATIONS			$\breve{\boldsymbol{T}}_{mm} = \boldsymbol{\phi}^{+}_{FEam}\,\boldsymbol{\phi}_{xam}$
ASSUMPTIONS			$\breve{\boldsymbol{T}}_{mm} = \breve{\boldsymbol{T}}_{\sigma mm} = \breve{\boldsymbol{T}}_{\varepsilon mm}$
ESTIMATED STRAIN AND STRESS *At any point of the structure*			$\boldsymbol{\varepsilon}_{1} = \boldsymbol{\phi}_{FE\varepsilon m}\,\breve{\boldsymbol{T}}_{mm}\,\boldsymbol{\phi}^{+}_{xam}\,\boldsymbol{u}_{xa}$ $\boldsymbol{\sigma}_{1} = \boldsymbol{\phi}_{FE\sigma m}\,\breve{\boldsymbol{T}}_{mm}\,\boldsymbol{\phi}^{+}_{xam}\,\boldsymbol{u}_{xa}$
ESTIMATED STRAIN AND STRESS *At any point of the structure*			$\boldsymbol{\varepsilon}_{1} = \boldsymbol{\phi}_{FE\varepsilon m}\,\breve{\boldsymbol{T}}_{mm}\,\breve{\boldsymbol{T}}^{+}_{mm}\,\boldsymbol{\phi}^{+}_{FEam}\,\boldsymbol{u}_{xa}$ $\boldsymbol{\sigma}_{1} = \boldsymbol{\phi}_{FE\sigma m}\,\breve{\boldsymbol{T}}_{mm}\breve{\boldsymbol{T}}^{+}_{mm}\,\boldsymbol{\phi}^{+}_{FEam}\,\boldsymbol{u}_{xa}$

The main advantage of this methodology (*Method 1*) is the avoidance of strain gauges, significantly simplifying the stress estimation process due to the installation procedure and eliminating errors cause by noise in the strain measurements.

4.3.2 Method 2

If the strains are measured at the active DOFs of the structure, a new methodology to estimate strains and stresses at the unmeasured points can be proposed (denoted as *Method 2*). Again, an updated numerical model is needed, together with the following information from the experimental structure:

- Strain mode shapes $\boldsymbol{\phi}_{x\varepsilon am}$ (estimated with modal analysis).
- Strains $\boldsymbol{\varepsilon}_{xa}$ (measured with strain sensors).

If strain sensors are installed in a structure, the strain mode shapes can be estimated by modal analysis. If strain responses ($\boldsymbol{\varepsilon}_{xa}$) are projected in the subspace spanned by the experimental strain mode shapes ($\boldsymbol{\phi}_{x\varepsilon am}$), modal coordinates ($\widehat{\boldsymbol{q}}_{\varepsilon xm}$) can be estimated with Eq. (4.23).

If expanded strain mode shapes ($\widetilde{\boldsymbol{\phi}}_{\boldsymbol{x\varepsilon m}}$) are obtained from Eq. (4.17), the strains at the unmeasured points can be estimated with the expanded strain mode shapes ($\widetilde{\boldsymbol{\phi}}_{\boldsymbol{x\varepsilon m}}$) and the modal coordinates $\widehat{\boldsymbol{q}}_{\boldsymbol{\varepsilon xm}}$, as follows:

$$\boldsymbol{\varepsilon}_{\mathbf{2}} = \begin{bmatrix} \boldsymbol{\phi}_{\boldsymbol{FE\varepsilon am}} \\ \boldsymbol{\phi}_{\boldsymbol{FE\varepsilon dm}} \end{bmatrix} \breve{\boldsymbol{T}}_{\boldsymbol{\varepsilon mm}}\, \widehat{\boldsymbol{q}}_{\boldsymbol{\varepsilon xm}} = \begin{bmatrix} \boldsymbol{\phi}_{\boldsymbol{FE\varepsilon am}} \\ \boldsymbol{\phi}_{\boldsymbol{FE\varepsilon dm}} \end{bmatrix} \breve{\boldsymbol{T}}_{\boldsymbol{\varepsilon mm}}\, \boldsymbol{\phi}^{+}_{\boldsymbol{x\varepsilon am}}\, \boldsymbol{\varepsilon}_{\boldsymbol{xa}} \tag{4.32}$$

Or alternatively as:

$$\boldsymbol{\varepsilon}_{\mathbf{2}} = \begin{bmatrix} \boldsymbol{\phi}_{\boldsymbol{FE\varepsilon am}} \\ \boldsymbol{\phi}_{\boldsymbol{FE\varepsilon dm}} \end{bmatrix} \breve{\boldsymbol{T}}_{\boldsymbol{\varepsilon mm}}\, \breve{\boldsymbol{T}}^{+}_{\boldsymbol{\varepsilon mm}}\, \boldsymbol{\phi}^{+}_{\boldsymbol{FE\varepsilon am}}\, \boldsymbol{\varepsilon}_{\boldsymbol{xa}} = \begin{bmatrix} I \\ \boldsymbol{\phi}_{\boldsymbol{FE\varepsilon dm}} \end{bmatrix} \boldsymbol{\phi}^{+}_{\boldsymbol{FE\varepsilon am}}\, \boldsymbol{\varepsilon}_{\boldsymbol{xa}} \tag{4.33}$$

Stresses can be estimated with *Method 2* as:

$$\boldsymbol{\sigma}_{\mathbf{2}} = \begin{bmatrix} \boldsymbol{\phi}_{\boldsymbol{FE\sigma am}} \\ \boldsymbol{\phi}_{\boldsymbol{FE\sigma dm}} \end{bmatrix} \breve{\boldsymbol{T}}_{\boldsymbol{\sigma mm}}\, \widehat{\boldsymbol{q}}_{\boldsymbol{\varepsilon xm}} = \begin{bmatrix} \boldsymbol{\phi}_{\boldsymbol{FE\sigma am}} \\ \boldsymbol{\phi}_{\boldsymbol{FE\sigma dm}} \end{bmatrix} \breve{\boldsymbol{T}}_{\boldsymbol{\sigma mm}}\, \boldsymbol{\phi}^{+}_{\boldsymbol{x\varepsilon am}}\, \boldsymbol{\varepsilon}_{\boldsymbol{xa}} \tag{4.34}$$

and if it assumed that $\breve{\boldsymbol{T}}_{\boldsymbol{\sigma mm}} = \breve{\boldsymbol{T}}_{\boldsymbol{\varepsilon mm}}$, Eq. (4.34) can be rewritten as:

$$\boldsymbol{\sigma}_{\mathbf{2}} = \begin{bmatrix} I \\ \boldsymbol{\phi}_{\boldsymbol{FE\sigma dm}} \end{bmatrix} \boldsymbol{\phi}^{+}_{\boldsymbol{FE\varepsilon am}}\, \boldsymbol{\varepsilon}_{\boldsymbol{xa}} \tag{4.35}$$

As a summary, the information needed to apply this method (*Method 2*) has been summarized in Table 4.2. The assumptions, and the calculations needed to estimate strains and stresses at the locations of interests are also shown in Table 4.2.

Table 4.2: Summary of the input data, assumptions and equations for *Method 2.*

INPUTS	PREVIOUS DATA	EXPERIMENTAL MODEL	$\boldsymbol{\phi}_{x\varepsilon am}$
		NUMERICAL MODEL	$\boldsymbol{\phi}_{FE\varepsilon m}$ or $\boldsymbol{\phi}_{FE\sigma m}$
	REAL TIME MEASUREMENTS		$\boldsymbol{\varepsilon}_{xa}$
PRELIMINARY CALCULATIONS			$\breve{\boldsymbol{T}}_{\varepsilon mm} = \boldsymbol{\phi}^{+}_{FE\varepsilon am}\,\boldsymbol{\phi}_{x\varepsilon am}$
ASSUMPTIONS			$\breve{\boldsymbol{T}}_{\sigma mm} = \breve{\boldsymbol{T}}_{\varepsilon mm}$
ESTIMATED STRAIN AND STRESS *At any point of the structure*			$\boldsymbol{\varepsilon}_2 = \boldsymbol{\phi}_{FE\varepsilon m}\,\breve{\boldsymbol{T}}_{\varepsilon mm}\,\boldsymbol{\phi}^{+}_{x\varepsilon am}\,\boldsymbol{\varepsilon}_{xa}$ $\boldsymbol{\sigma}_2 = \boldsymbol{\phi}_{FE\sigma m}\,\breve{\boldsymbol{T}}_{\varepsilon mm}\,\boldsymbol{\phi}^{+}_{x\varepsilon am}\,\boldsymbol{\varepsilon}_{xa}$
ESTIMATED STRAIN AND STRESS *At any point of the structure*			$\boldsymbol{\varepsilon}_2 = \boldsymbol{\phi}_{FE\varepsilon m}\,\boldsymbol{\phi}^{+}_{FE\varepsilon am}\,\boldsymbol{\varepsilon}_{xa}$ $\boldsymbol{\sigma}_2 = \boldsymbol{\phi}_{FE\sigma m}\,\boldsymbol{\phi}^{+}_{FE\varepsilon am}\,\boldsymbol{\varepsilon}_{xa}$

It is worth noting that strain gages present some drawbacks compared to accelerometers, such as signal noise or more complicated installation processes [124]. However, extensive research has been conducted in recent years on the utilization of fiber-Bragg gratings (FBG) sensors due to their cost-effectiveness in comparison to DOFs they offer and their insensitivity to temperature variations [118].

4.3.3 Method 3

Method 3 is proposed to estimate strains and stresses when both displacements and strains are measured. An updated numerical model, together with the following information from the experimental structure are needed:

- Mode shapes $\boldsymbol{\phi}_{xam}$.
- Strain mode shapes $\boldsymbol{\phi}_{x\varepsilon am}$.
- Displacements $\boldsymbol{u}_{xa}$ (measured with displacement sensors)

The experimental mode shapes and strain mode shapes have to be previously estimated by modal analysis.

In *Method* 3, the modal coordinates ($\widehat{\boldsymbol{q}}_{\boldsymbol{xm}}$) are estimated with Eq. (4.21) and then, the experimental strain mode shapes are expanded to the unmeasured DOFs with Eq. (4.17). Therefore, strains can be estimated by means of the expression:

$$\boldsymbol{\varepsilon}_{\mathbf{3}} = \begin{bmatrix} \boldsymbol{\phi}_{\boldsymbol{FE\varepsilon am}} \\ \boldsymbol{\phi}_{\boldsymbol{FE\varepsilon dm}} \end{bmatrix} \breve{\boldsymbol{T}}_{\boldsymbol{\varepsilon mm}}\, \widehat{\boldsymbol{q}}_{\boldsymbol{xm}} = \begin{bmatrix} \boldsymbol{\phi}_{\boldsymbol{FE\varepsilon am}} \\ \boldsymbol{\phi}_{\boldsymbol{FE\varepsilon dm}} \end{bmatrix} \breve{\boldsymbol{T}}_{\boldsymbol{\varepsilon mm}}\, \boldsymbol{\phi}_{\boldsymbol{xam}}^{+}\, \boldsymbol{u}_{\boldsymbol{xa}} \tag{4.36}$$

or alternatively:

$$\boldsymbol{\varepsilon}_{\mathbf{3}} = \begin{bmatrix} \boldsymbol{\phi}_{\boldsymbol{FE\varepsilon am}} \\ \boldsymbol{\phi}_{\boldsymbol{FE\varepsilon dm}} \end{bmatrix} \breve{\boldsymbol{T}}_{\boldsymbol{\varepsilon mm}}\, \breve{\boldsymbol{T}}_{\boldsymbol{mm}}^{+}\, \boldsymbol{\phi}_{\boldsymbol{FEam}}^{+}\, \boldsymbol{u}_{\boldsymbol{xa}} \tag{4.37}$$

Similarly, stresses are estimated as:

$$\boldsymbol{\sigma}_{\mathbf{3}} = \begin{bmatrix} \boldsymbol{\phi}_{\boldsymbol{FE\sigma am}} \\ \boldsymbol{\phi}_{\boldsymbol{FE\sigma dm}} \end{bmatrix} \breve{\boldsymbol{T}}_{\boldsymbol{\sigma mm}}\, \widehat{\boldsymbol{q}}_{\boldsymbol{xm}} = \begin{bmatrix} \boldsymbol{\phi}_{\boldsymbol{FE\sigma am}} \\ \boldsymbol{\phi}_{\boldsymbol{FE\sigma dm}} \end{bmatrix} \breve{\boldsymbol{T}}_{\boldsymbol{\sigma mm}}\, \boldsymbol{\phi}_{\boldsymbol{xam}}^{+}\, \boldsymbol{u}_{\boldsymbol{xa}} \tag{4.38}$$

or alternatively:

$$\boldsymbol{\sigma}_{\mathbf{3}} = \begin{bmatrix} \boldsymbol{\phi}_{\boldsymbol{FE\sigma am}} \\ \boldsymbol{\phi}_{\boldsymbol{FE\sigma dm}} \end{bmatrix} \breve{\boldsymbol{T}}_{\boldsymbol{\sigma mm}}\, \breve{\boldsymbol{T}}_{\boldsymbol{mm}}^{+}\, \boldsymbol{\phi}_{\boldsymbol{FEam}}^{+}\, \boldsymbol{u}_{\boldsymbol{xa}} \tag{4.39}$$

The information needed to apply this method (*Method 3*) as well as the assumptions, and the calculations needed to estimate strains and stresses at the locations of interests are also shown in Table 4.3.

Table 4.3: Summary of the input data, assumptions and equations for *Method 3*.

INPUTS	PREVIOUS DATA	EXPERIMENTAL MODEL	$\boldsymbol{\phi}_{xam}$ $\boldsymbol{\phi}_{x\varepsilon am}$
		NUMERICAL MODEL	$\boldsymbol{\phi}_{FE\varepsilon}$ or $\boldsymbol{\phi}_{FE\sigma}$
	REAL TIME MEASUREMENTS		$\boldsymbol{u}_{xa}$
PRELIMINARY CALCULATIONS			$\breve{\boldsymbol{T}}_{\varepsilon mm} = \boldsymbol{\phi}_{FE\varepsilon a}^{+}\, \boldsymbol{\phi}_{x\varepsilon am}$
ASSUMPTIONS			$\breve{\boldsymbol{T}}_{\sigma mm} = \breve{\boldsymbol{T}}_{\varepsilon mm}$
ESTIMATED STRAIN AND STRESS *At any point of the structure*			$\boldsymbol{\varepsilon}_3 = \boldsymbol{\phi}_{FE\varepsilon}\, \breve{\boldsymbol{T}}_{\varepsilon mm}\, \boldsymbol{\phi}_{xam}^{+}\, \boldsymbol{u}_{xa}$ $\boldsymbol{\sigma}_3 = \boldsymbol{\phi}_{FE\varepsilon}\, \breve{\boldsymbol{T}}_{\sigma mm}\, \boldsymbol{\phi}_{xam}^{+}\, \boldsymbol{u}_{xa}$
ESTIMATED STRAIN AND STRESS *At any point of the structure*			$\boldsymbol{\varepsilon}_3 = \boldsymbol{\phi}_{FE\varepsilon}\, \breve{\boldsymbol{T}}_{\varepsilon mm}\, \breve{\boldsymbol{T}}_{mm}^{+}\, \boldsymbol{\phi}_{FEa}^{+}\, \boldsymbol{u}_{xa}$ $\boldsymbol{\sigma}_3 = \boldsymbol{\phi}_{FE\varepsilon}\, \breve{\boldsymbol{T}}_{\sigma mm}\, \breve{\boldsymbol{T}}_{mm}^{+}\, \boldsymbol{\phi}_{FEa}^{+}\, \boldsymbol{u}_{xa}$

4.3.4 Method 4

When both displacements and stress are measured, *Method 4* is also proposed to estimate strains and stresses. An updated numerical model and the following information from the experimental structure are needed:

- Mode shapes $\boldsymbol{\phi}_{xam}$.
- Strain mode shapes $\boldsymbol{\phi}_{x\varepsilon am}$.
- Displacements $\boldsymbol{u}_{xa}$ (measured with displacement sensors)
- Strains $\boldsymbol{\varepsilon}_{xa}$ (measured with strain sensors).

In this method, modal coordinates ($\widehat{\boldsymbol{q}}_{txm}$) are estimated with Eq. (4.25). A new transformation matrix $\breve{\boldsymbol{T}}_{tmm}$ is estimated with the expression:

$$\breve{\boldsymbol{T}}_{t\varepsilon mm} = \begin{bmatrix} \boldsymbol{\phi}_{FE\varepsilon am} \\ \boldsymbol{\phi}_{FEam} \end{bmatrix}^{+} \begin{bmatrix} \boldsymbol{\phi}_{x\varepsilon am} \\ \boldsymbol{\phi}_{xam} \end{bmatrix} \tag{4.40}$$

which can also be used to expand strain mode shapes as:

$$\widetilde{\boldsymbol{\phi}}_{\boldsymbol{x\varepsilon m_4}} = \boldsymbol{\phi}_{\boldsymbol{FE\varepsilon m}}\, \breve{\boldsymbol{T}}_{\boldsymbol{t\varepsilon mm}} \tag{4.41}$$

Therefore, in *Method 4*, strains are estimated as:

$$\boldsymbol{\varepsilon_4} = \boldsymbol{\phi}_{\boldsymbol{FE\varepsilon m}}\, \breve{\boldsymbol{T}}_{\boldsymbol{t\varepsilon mm}}\, \widehat{\boldsymbol{q}}_{\boldsymbol{txm}} = \boldsymbol{\phi}_{\boldsymbol{FE\varepsilon m}}\, \breve{\boldsymbol{T}}_{\boldsymbol{t\varepsilon mm}} \begin{bmatrix} \boldsymbol{\phi}_{\boldsymbol{x\varepsilon am}} \\ \boldsymbol{\phi}_{\boldsymbol{xam}} \end{bmatrix}^{+} \begin{bmatrix} \boldsymbol{\varepsilon}_{\boldsymbol{xa}} \\ \boldsymbol{u}_{\boldsymbol{xa}} \end{bmatrix} \tag{4.42}$$

or alternatively:

$$\boldsymbol{\varepsilon_4} = \boldsymbol{\phi}_{\boldsymbol{FE\varepsilon m}} \begin{bmatrix} \boldsymbol{\phi}_{\boldsymbol{FE\varepsilon am}} \\ \boldsymbol{\phi}_{\boldsymbol{FEam}} \end{bmatrix}^{+} \begin{bmatrix} \boldsymbol{\varepsilon}_{\boldsymbol{xa}} \\ \boldsymbol{u}_{\boldsymbol{xa}} \end{bmatrix} \tag{4.43}$$

Similarly, stresses are estimated as:

$$\boldsymbol{\sigma_4} = \boldsymbol{\phi}_{\boldsymbol{FE\sigma m}}\, \breve{\boldsymbol{T}}_{\boldsymbol{t\sigma mm}}\, \widehat{\boldsymbol{q}}_{\boldsymbol{txm}} = \boldsymbol{\phi}_{\boldsymbol{FE\sigma m}}\, \breve{\boldsymbol{T}}_{\boldsymbol{t\sigma mm}} \begin{bmatrix} \boldsymbol{\phi}_{\boldsymbol{x\varepsilon am}} \\ \boldsymbol{\phi}_{\boldsymbol{xam}} \end{bmatrix}^{+} \begin{bmatrix} \boldsymbol{\varepsilon}_{\boldsymbol{xa}} \\ \boldsymbol{u}_{\boldsymbol{xa}} \end{bmatrix} \tag{4.44}$$

where it has been assumed that $\breve{\boldsymbol{T}}_{\boldsymbol{t\sigma mm}} = \breve{\boldsymbol{T}}_{\boldsymbol{t\varepsilon mm}}$. Stresses can also be expressed as:

$$\boldsymbol{\sigma_4} = \boldsymbol{\phi}_{\boldsymbol{FE\sigma m}} \begin{bmatrix} \boldsymbol{\phi}_{\boldsymbol{FE\varepsilon am}} \\ \boldsymbol{\phi}_{\boldsymbol{FEam}} \end{bmatrix} \begin{bmatrix} \boldsymbol{\varepsilon}_{\boldsymbol{xa}} \\ \boldsymbol{u}_{\boldsymbol{xa}} \end{bmatrix} \tag{4.45}$$

The information needed to apply this method (*Method 4*) as well as the assumptions, and the calculations needed to estimate strains and stresses at the locations of interests are also shown in Table 4.4.

Table 4.4: Summary of the input data, assumptions and equations for *Method 4.*

INPUTS	PREVIOUS DATA	EXPERIMENTAL MODEL	$\boldsymbol{\phi}_{xam}$ $\boldsymbol{\phi}_{x\varepsilon am}$
		NUMERICAL MODEL	$\boldsymbol{\phi}_{FEam}$ $\boldsymbol{\phi}_{FE\varepsilon m}$ or $\boldsymbol{\phi}_{FE\sigma m}$
	REAL TIME MEASUREMENTS		$\boldsymbol{u}_{xa}$ $\boldsymbol{\varepsilon}_{xa}$
PRELIMINARY CALCULATIONS			$\breve{\boldsymbol{T}}_{tmm} = \begin{bmatrix} \boldsymbol{\phi}_{FE\varepsilon am} \\ \boldsymbol{\phi}_{FEam} \end{bmatrix}^{+} \begin{bmatrix} \boldsymbol{\phi}_{x\varepsilon am} \\ \boldsymbol{\phi}_{xam} \end{bmatrix}$
ASSUMPTIONS			$\breve{\boldsymbol{T}}_{t\sigma mm} = \breve{\boldsymbol{T}}_{t\varepsilon mm}$
ESTIMATED STRAIN AND STRESS *At any point of the structure*			$\boldsymbol{\varepsilon}_4 = \boldsymbol{\phi}_{FE\varepsilon m}\, \breve{\boldsymbol{T}}_{tmm} \begin{bmatrix} \boldsymbol{\phi}_{x\varepsilon am} \\ \boldsymbol{\phi}_{xam} \end{bmatrix}^{+} \begin{bmatrix} \boldsymbol{\varepsilon}_{x_a} \\ \boldsymbol{u}_{xa} \end{bmatrix}$ $\boldsymbol{\sigma}_4 = \boldsymbol{\phi}_{FE\sigma m}\, \breve{\boldsymbol{T}}_{tmm} \begin{bmatrix} \boldsymbol{\phi}_{x\varepsilon am} \\ \boldsymbol{\phi}_{xam} \end{bmatrix}^{+} \begin{bmatrix} \boldsymbol{\varepsilon}_{x_a} \\ \boldsymbol{u}_{xa} \end{bmatrix}$
ESTIMATED STRAIN AND STRESS *At any point of the structure*			$\boldsymbol{\varepsilon}_4 = \boldsymbol{\phi}_{FE\varepsilon m} \begin{bmatrix} \boldsymbol{\phi}_{FE\varepsilon am} \\ \boldsymbol{\phi}_{FEam} \end{bmatrix}^{+} \begin{bmatrix} \boldsymbol{\varepsilon}_{xa} \\ \boldsymbol{u}_{xa} \end{bmatrix}$ $\boldsymbol{\sigma}_4 = \boldsymbol{\phi}_{FE\sigma m} \begin{bmatrix} \boldsymbol{\phi}_{x\varepsilon am} \\ \boldsymbol{\phi}_{xam} \end{bmatrix}^{+} \begin{bmatrix} \boldsymbol{\varepsilon}_{x_a} \\ \boldsymbol{u}_{xa} \end{bmatrix}$

Variation of Method 4

Following with the same approach of measuring both, displacements and strains, an alternative method to estimate strains can be proposed. In this case, a FE model is not required, and strain gauges at que locations of interest must be temporarily installed.

Due to the fact that both the strains and the displacements are measured, the following relationship exists between them:

$$\boldsymbol{\varepsilon}_{xa} = \boldsymbol{C}_x\, \boldsymbol{u}_{xa} \tag{4.46}$$

And an estimate of matrix $\widehat{\boldsymbol{C}}_x$ can be obtained from:

$$\widehat{\boldsymbol{C}}_x = \boldsymbol{\varepsilon}_{xa}\, \boldsymbol{u}_{xa}^{+} \tag{4.47}$$

Therefore, if matrix $\widehat{\boldsymbol{C}}_{\boldsymbol{x}}$ is known from Eq. (4.46), the displacements $\boldsymbol{u}_{\boldsymbol{xa}}$ can be used to estimate the strains $\boldsymbol{\varepsilon}_{\boldsymbol{xa}}$ (at the active DOFs) i.e. the strain gauges can be removed (or disconnected) from the real structure and strains at active DOFs can be estimated with Eq. (4.46). Thus, in the real time calculations, only the displacement measurements are needed.

As an alternative to Eq. (4.47) the matrix $\widehat{\boldsymbol{C}}_{\boldsymbol{x}}$ can also be estimated as:

$$\widehat{\boldsymbol{C}}_{\boldsymbol{x}} = \boldsymbol{\phi}_{\boldsymbol{x\varepsilon a}} \boldsymbol{\phi}_{\boldsymbol{xam}}^{+} \tag{4.48}$$

Tarpo et al [124] proposed a similar technique to estimate $\widehat{\boldsymbol{C}}_{\boldsymbol{x}}$ using the principal component analysis (PCA). With this technique, firstly the measured strains and displacements are stacked in a vector $\boldsymbol{y}_{\boldsymbol{c}}(\boldsymbol{t})$. Then, the singular value decomposition is applied to the covariance matrix $\boldsymbol{C}_{\boldsymbol{y}_{\boldsymbol{c}}}$ of vector $\boldsymbol{y}_{\boldsymbol{c}}(\boldsymbol{t})$, where the singular vectors contain both the strain and displacement components, i.e.:

$$V = \begin{bmatrix} \boldsymbol{\phi}_{\boldsymbol{xam}} \\ \boldsymbol{\phi}_{\boldsymbol{x\varepsilon a}} \end{bmatrix} \tag{4.49}$$

The main advantage of this method is that the expansion is not needed and, consequently, a finite element model is not required, which saves time and eliminates correlation discrepancies that may lead to errors in the estimated stresses.

A significant drawback of this method is the necessity of installing strain gauges at the locations of interest, which may be impossible in certain situations, such as when these points are inaccessible (e.g., underwater) [116], [122]. Nevertheless, since strain measurements are temporary, the reliability issues associated with long term measurements are mitigated [124]. Additionally, as mentioned earlier, the use of fiber-optic sensors allows for obtaining modal strains at a relatively low cost [117], [118]

4.3.5 Method 5

Up to this point, the proposed methods (*Methods 1* to *4*) calculate modal coordinates by projecting the experimental responses onto an experimental subspace. However, from this point forward, the methods (*Methods 5* to *8*) calculate modal coordinates by projecting the experimental responses onto a numerical subspace.

In this section, a methodology to estimate strains and stresses in structures, denoted as *Method 5*, is described in detail. A numerical model is needed, which must be updated if the experimental-numerical correlation is not satisfactory. Moreover, the following information from the experimental structure is required:

- Mode shapes $\boldsymbol{\phi}_{\boldsymbol{xam}}$ (estimated with modal analysis).
- Displacements $\boldsymbol{u}_{\boldsymbol{xa}}$ (measured with displacement sensors or obtained by double integration of accelerations).

In this method, the modal coordinates ($\widetilde{\boldsymbol{q}}_{\boldsymbol{xm}}$) are estimated with Eq. (4.22).

The strain mode shapes are expanded in the same way as in *Method 1*, thus, using the transformation matrix $\breve{\boldsymbol{T}}_{\boldsymbol{mm}}$. Assuming that $\breve{\boldsymbol{T}}_{\boldsymbol{mm}} = \breve{\boldsymbol{T}}_{\boldsymbol{\sigma mm}} = \breve{\boldsymbol{T}}_{\boldsymbol{\varepsilon mm}}$, strain mode shapes are expanded with Eq. (4.27).

Due to the fact that $\widetilde{\boldsymbol{q}}_{\boldsymbol{xm}}$ are estimated using the numerical mode shapes $\boldsymbol{\phi}_{\boldsymbol{FEam}}$, and matrix $\breve{\boldsymbol{T}}_{\boldsymbol{mm}}$ is estimated with the experimental mode shapes $\boldsymbol{\phi}_{\boldsymbol{xam}}$, it is important to ensure that the mode shapes $\boldsymbol{\phi}_{\boldsymbol{FEam}}$ are normalized with the same sign/direction as the experimental ones. A diagonal matrix $\boldsymbol{s}$, with ones or negative ones along the diagonal, is used to overcome this issue.

Therefore, strains are estimated with *Method 5* as:

$$\boldsymbol{\varepsilon}_5 = \begin{bmatrix} \boldsymbol{\phi}_{\boldsymbol{FE\varepsilon am}} \\ \boldsymbol{\phi}_{\boldsymbol{FE\varepsilon dm}} \end{bmatrix} \breve{\boldsymbol{T}}_{\boldsymbol{mm}}\, \boldsymbol{s}\, \widetilde{\boldsymbol{q}}_{\boldsymbol{xm}} = \begin{bmatrix} \boldsymbol{\phi}_{\boldsymbol{FE\varepsilon am}} \\ \boldsymbol{\phi}_{\boldsymbol{FE\varepsilon dm}} \end{bmatrix} \breve{\boldsymbol{T}}_{\boldsymbol{mm}}\, \boldsymbol{s}\, \boldsymbol{\phi}^{+}_{\boldsymbol{FEam}}\, \boldsymbol{u}_{\boldsymbol{xa}} \tag{4.50}$$

Similarly, stresses are expressed as:

$$\boldsymbol{\sigma}_5 = \begin{bmatrix} \boldsymbol{\phi}_{\boldsymbol{FE\sigma am}} \\ \boldsymbol{\phi}_{\boldsymbol{FE\sigma dm}} \end{bmatrix} \breve{\boldsymbol{T}}_{\boldsymbol{mm}}\, \boldsymbol{s}\, \widetilde{\boldsymbol{q}}_{\boldsymbol{xm}} = \begin{bmatrix} \boldsymbol{\phi}_{\boldsymbol{FE\sigma am}} \\ \boldsymbol{\phi}_{\boldsymbol{FE\sigma dm}} \end{bmatrix} \breve{\boldsymbol{T}}_{\boldsymbol{mm}}\, \boldsymbol{s}\, \boldsymbol{\phi}^{+}_{\boldsymbol{FEam}}\, \boldsymbol{u}_{\boldsymbol{xa}} \tag{4.51}$$

The information needed to apply *Method 5*, as well as the assumptions and calculations needed to estimate strains and stresses at the locations of interests are show in Table 4.5

Table 4.5: Summary of the input data, assumptions and equations for *Method 5*.

INPUTS	PREVIOUS DATA	EXPERIMENTAL MODEL	$\boldsymbol{\phi}_{xam}$
		NUMERICAL MODEL	$\boldsymbol{\phi}_{FEam}$ $\boldsymbol{\phi}_{FE\varepsilon m}$ or $\boldsymbol{\phi}_{FE\sigma m}$
	REAL TIME MEASUREMENTS		$\boldsymbol{u}_{xa}$
PRELIMINARY CALCULATIONS			$\breve{\boldsymbol{T}}_{mm} = \boldsymbol{\phi}_{FEam}^{+}\,\boldsymbol{\phi}_{xam}$
ASSUMPTIONS			$\breve{\boldsymbol{T}}_{mm} = \breve{\boldsymbol{T}}_{\sigma mm} = \breve{\boldsymbol{T}}_{\varepsilon mm}$
ESTIMATED STRAIN AND STRESS *At any point of the structure*			$\boldsymbol{\varepsilon}_5 = \boldsymbol{\phi}_{FE\varepsilon m}\,\breve{\boldsymbol{T}}_{mm}\,\boldsymbol{s}\,\boldsymbol{\phi}_{FEam}^{+}\,\boldsymbol{u}_{xa}$ $\boldsymbol{\sigma}_5 = \boldsymbol{\phi}_{FE\sigma m}\,\breve{\boldsymbol{T}}_{mm}\,\boldsymbol{s}\,\boldsymbol{\phi}_{FEam}^{+}\,\boldsymbol{u}_{xa}$

4.3.6 Method 6

In *Method 6*, in addition to a numerical model, the following information from the experimental structure is needed:

- Strain mode shape $\boldsymbol{\phi}_{x\varepsilon am}$ (estimated with modal analysis).
- Strain response of the structure $\boldsymbol{\varepsilon}_{xa}$ (measured with strain sensors)

Modal coordinates $\tilde{\boldsymbol{q}}_{\varepsilon xm}$ are estimated with Eq. (4.24), and the expanded strain mode shapes are obtained as in *Method 2* (Eq. (4.17)) using $\breve{\boldsymbol{T}}_{\varepsilon mm}$. Thus, a diagonal matrix $\boldsymbol{s}_{\varepsilon}$ with ones or negative ones along the diagonal, must be used to ensure that the mode shapes $\boldsymbol{\phi}_{FE\varepsilon am}$ are normalized with the same sign/direction as the experimental ones $\boldsymbol{\phi}_{x\varepsilon am}$.

Consequently, strains are estimated as:

$$\boldsymbol{\varepsilon}_6 = \begin{bmatrix} \boldsymbol{\phi}_{FE\varepsilon am} \\ \boldsymbol{\phi}_{FE\varepsilon dm} \end{bmatrix} \breve{\boldsymbol{T}}_{\varepsilon mm}\,\boldsymbol{s}_{\varepsilon}\,\tilde{\boldsymbol{q}}_{\varepsilon xm} = \begin{bmatrix} \boldsymbol{\phi}_{FE\varepsilon am} \\ \boldsymbol{\phi}_{FE\varepsilon dm} \end{bmatrix} \breve{\boldsymbol{T}}_{\varepsilon mm}\,\boldsymbol{s}_{\varepsilon}\,\boldsymbol{\phi}_{FE\varepsilon am}^{+}\,\boldsymbol{\varepsilon}_{xa} \tag{4.52}$$

Assuming that $\breve{\boldsymbol{T}}_{\sigma mm} = \breve{\boldsymbol{T}}_{\varepsilon mm}$, stresses can be obtained as:

$$\boldsymbol{\sigma}_6 = \begin{bmatrix} \boldsymbol{\phi}_{FE\sigma am} \\ \boldsymbol{\phi}_{FE\sigma dm} \end{bmatrix} \breve{\boldsymbol{T}}_{\varepsilon mm}\,\boldsymbol{s}_{\varepsilon}\,\tilde{\boldsymbol{q}}_{\varepsilon xm} = \begin{bmatrix} \boldsymbol{\phi}_{FE\sigma am} \\ \boldsymbol{\phi}_{FE\sigma dm} \end{bmatrix} \breve{\boldsymbol{T}}_{\varepsilon mm}\,\boldsymbol{s}_{\varepsilon}\,\boldsymbol{\phi}_{FE\varepsilon am}^{+}\,\boldsymbol{\varepsilon}_{xa} \tag{4.53}$$

A summary of *Method 6* is presented in Table 4.6.

Table 4.6: Summary of the input data, assumptions and equations for *Method 6.*

INPUTS	PREVIOUS DATA	EXPERIMENTAL MODEL	$\boldsymbol{\phi}_{xam}$
		NUMERICAL MODEL	$\boldsymbol{\phi}_{FE\varepsilon m}$ or $\boldsymbol{\phi}_{FE\sigma m}$
	REAL TIME MEASUREMENTS		$\boldsymbol{\varepsilon}_{xa}$
PRELIMINARY CALCULATIONS			$\breve{\boldsymbol{T}}_{\varepsilon mm} = \boldsymbol{\phi}_{FE\varepsilon am}^{+}\,\boldsymbol{\phi}_{x\varepsilon am}$
ASSUMPTIONS			$\breve{\boldsymbol{T}}_{\sigma mm} = \breve{\boldsymbol{T}}_{\varepsilon mm}$
ESTIMATED STRAIN AND STRESS *At any point of the structure*			$\boldsymbol{\varepsilon}_6 = \boldsymbol{\phi}_{FE\varepsilon m}\,\breve{\boldsymbol{T}}_{\varepsilon mm}\,\boldsymbol{s}_{\varepsilon}\,\boldsymbol{\phi}_{FE\varepsilon am}^{+}\,\boldsymbol{\varepsilon}_{xa}$ $\boldsymbol{\sigma}_6 = \boldsymbol{\phi}_{FE\sigma m}\,\breve{\boldsymbol{T}}_{\varepsilon mm}\,\boldsymbol{s}_{\varepsilon}\,\boldsymbol{\phi}_{FE\varepsilon am}^{+}\,\boldsymbol{\varepsilon}_{xa}$

4.3.7 Method 7

In *Method 7*, in addition to a numerical model, the following information from the experimental structure is needed:

- Mode shapes $\boldsymbol{\phi}_{xam}$ (estimated with modal analysis).
- Strain mode shapes $\boldsymbol{\phi}_{x\varepsilon am}$ (estimated with modal analysis).
- Displacements $\boldsymbol{u}_{xa}$ (measured with displacement sensors or by double integration of accelerations).

In this method, modal coordinates ($\widetilde{\boldsymbol{q}}_{xm}$) are estimated with Eq. (4.22), and strain mode shapes are expanded using $\breve{\boldsymbol{T}}_{\varepsilon mm}$, as shown in with Eq. (4.17).

Strains can be estimated with the expression as:

$$\boldsymbol{\varepsilon}_7 = \begin{bmatrix}\boldsymbol{\phi}_{FE\varepsilon am}\\ \boldsymbol{\phi}_{FE\varepsilon dm}\end{bmatrix}\breve{\boldsymbol{T}}_{\varepsilon mm}\,\boldsymbol{s}\,\widetilde{\boldsymbol{q}}_{xm} = \begin{bmatrix}\boldsymbol{\phi}_{FE\varepsilon am}\\ \boldsymbol{\phi}_{FE\varepsilon dm}\end{bmatrix}\breve{\boldsymbol{T}}_{\varepsilon mm}\,\boldsymbol{s}\,\boldsymbol{\phi}_{FEam}^{+}\,\boldsymbol{u}_{xa} \tag{4.54}$$

Assuming that $\breve{\boldsymbol{T}}_{\sigma mm} = \breve{\boldsymbol{T}}_{\varepsilon mm}$, stresses are estimated as:

$$\boldsymbol{\sigma}_7 = \begin{bmatrix}\boldsymbol{\phi}_{FE\sigma am}\\ \boldsymbol{\phi}_{FE\sigma dm}\end{bmatrix}\breve{\boldsymbol{T}}_{\varepsilon mm}\,\boldsymbol{s}\,\widetilde{\boldsymbol{q}}_{xm} = \begin{bmatrix}\boldsymbol{\phi}_{FE\sigma am}\\ \boldsymbol{\phi}_{FE\sigma dm}\end{bmatrix}\breve{\boldsymbol{T}}_{\varepsilon mm}\,\boldsymbol{s}\,\boldsymbol{\phi}_{FEam}^{+}\,\boldsymbol{u}_{xa} \tag{4.55}$$

As a summary, the information needed to apply *Method 7*, the assumptions and the calculations needed to estimate strains and stresses at the locations of interests are shown in Table 4.7

Table 4.7: Summary of the input data, assumptions and equations for *Method 7.*

INPUTS	PREVIOUS DATA	EXPERIMENTAL MODEL	$\boldsymbol{\phi}_{x\varepsilon am}$
		NUMERICAL MODEL	$\boldsymbol{\phi}_{FEam}$ $\boldsymbol{\phi}_{FE\varepsilon m}$ or $\boldsymbol{\phi}_{FE\sigma m}$
	REAL TIME MEASUREMENTS		$\boldsymbol{u}_{xa}$
PRELIMINARY CALCULATIONS			$\breve{\boldsymbol{T}}_{\varepsilon mm} = \boldsymbol{\phi}^{+}_{FE\varepsilon am}\, \boldsymbol{\phi}_{x\varepsilon am}$
ASSUMPTIONS			$\breve{\boldsymbol{T}}_{\sigma mm} = \breve{\boldsymbol{T}}_{\varepsilon mm}$
ESTIMATED STRAIN AND STRESS *At any point of the structure*			$\boldsymbol{\varepsilon}_7 = \boldsymbol{\phi}_{FE\varepsilon m}\, \breve{\boldsymbol{T}}_{\varepsilon mm}\, \boldsymbol{s}\, \boldsymbol{\phi}^{+}_{FEam}\, \boldsymbol{u}_{xa}$ $\boldsymbol{\sigma}_7 = \boldsymbol{\phi}_{FE\sigma m}\, \breve{\boldsymbol{T}}_{\varepsilon mm}\, \boldsymbol{s}\, \boldsymbol{\phi}^{+}_{FEam}\, \boldsymbol{u}_{xa}$

4.3.8 Method 8

With the techniques presented in the previous sections, experimental mode shapes and experimental strain mode shapes are used to estimate matrices $\breve{\boldsymbol{T}}_{mm}$, $\breve{\boldsymbol{T}}_{\varepsilon mm}$ and $\breve{\boldsymbol{T}}_{\sigma mm}$ which are then utilized to expand the experimental mode shapes and strain mode shapes to the unmeasured DOFs. In this case, *Method 8* only uses the modal parameters of a numerical model, i.e., the experimental modal parameters are not required. However, it must be noticed that the experimental modal parameters are needed in a preliminary phase to study the correlation between the numerical and the experimental models, and proceed with the updating of the numerical model, if needed.

Using modal coordinates $\widetilde{\boldsymbol{q}}_{xm}$ estimated with Eq. (4.22) and numerical strain mode shapes, strains can be estimated as:

$$\boldsymbol{\varepsilon}_8 = \boldsymbol{\phi}_{FE\varepsilon m}\, \widetilde{\boldsymbol{q}}_{xm} = \begin{bmatrix} \boldsymbol{\phi}_{FE\varepsilon am} \\ \boldsymbol{\phi}_{FE\varepsilon dm} \end{bmatrix} \boldsymbol{\phi}^{+}_{FEam}\, \boldsymbol{u}_{xa} \tag{4.56}$$

Similarly, stresses are estimated as:

$$\boldsymbol{\sigma}_{\mathbf{8}} = \boldsymbol{\phi}_{\boldsymbol{FE\sigma m}}\, \widetilde{\boldsymbol{q}}_{\boldsymbol{xm}} = \begin{bmatrix} \boldsymbol{\phi}_{\boldsymbol{FE\sigma am}} \\ \boldsymbol{\phi}_{\boldsymbol{FE\sigma dm}} \end{bmatrix} \boldsymbol{\phi}_{\boldsymbol{FEam}}^{+}\, \boldsymbol{u}_{\boldsymbol{xa}} \tag{4.57}$$

The information needed to apply *Method 8*, as well as the assumptions and calculations needed are show in Table 4.8

Table 4.8: Summary of the input data, assumptions and equations for *Method 8*.

INPUTS	PREVIOUS DATA	EXPERIMENTAL MODEL	
		NUMERICAL MODEL	$\boldsymbol{\phi}_{\boldsymbol{FEam}}$ $\boldsymbol{\phi}_{\boldsymbol{FE\varepsilon m}}$ or $\boldsymbol{\phi}_{\boldsymbol{FE\sigma m}}$
	REAL TIME MEASUREMENTS		$\boldsymbol{u}_{\boldsymbol{xa}}$
PRELIMINARY CALCULATIONS			
ASSUMPTIONS			$\breve{\boldsymbol{T}}_{\boldsymbol{mm}} = \breve{\boldsymbol{T}}_{\boldsymbol{\sigma mm}} = \breve{\boldsymbol{T}}_{\boldsymbol{\varepsilon mm}}$
ESTIMATED STRAIN AND STRESS *At any point of the structure*			$\boldsymbol{\varepsilon}_{\mathbf{8}} = \boldsymbol{\phi}_{\boldsymbol{FE\varepsilon m}}\, \boldsymbol{\phi}_{\boldsymbol{FEam}}^{+}\, \boldsymbol{u}_{\boldsymbol{xa}}$ $\boldsymbol{\sigma}_{\mathbf{8}} = \boldsymbol{\phi}_{\boldsymbol{FE\sigma m}}\, \boldsymbol{\phi}_{\boldsymbol{FEam}}^{+}\, \boldsymbol{u}_{\boldsymbol{xa}}$

This methodology presents significant advantages. Modal expansion is not required, and consequently, the calculation of transformation matrices is not needed, either. Moreover, issues related to closely spaced modes, mode pairing, overfitting of mode shapes, etc., are prevented, and a number of modes higher than the experimental modes can be used.

It is interesting to note that the expressions obtained with *Method 1* coincide with those derived with *Method 8*, i.e.:

$$\boldsymbol{\varepsilon}_{\mathbf{1}} = \begin{bmatrix} \boldsymbol{\phi}_{\boldsymbol{FE\varepsilon am}} \\ \boldsymbol{\phi}_{\boldsymbol{FE\varepsilon dm}} \end{bmatrix} \breve{\boldsymbol{T}}_{\boldsymbol{mm}}\, \breve{\boldsymbol{T}}_{\boldsymbol{mm}}^{+}\, \boldsymbol{\phi}_{\boldsymbol{FEam}}\, \boldsymbol{u}_{\boldsymbol{xa}} = \begin{bmatrix} \boldsymbol{\phi}_{\boldsymbol{FE\varepsilon am}} \\ \boldsymbol{\phi}_{\boldsymbol{FE\varepsilon dm}} \end{bmatrix} \boldsymbol{\phi}_{\boldsymbol{FEam}}\, \boldsymbol{u}_{\boldsymbol{xa}} = \boldsymbol{\varepsilon}_{\mathbf{8}} \tag{4.58}$$

And the same is inferred for stresses:

$$\boldsymbol{\sigma}_{\mathbf{1}} = \begin{bmatrix} \boldsymbol{\phi}_{\boldsymbol{FE\sigma am}} \\ \boldsymbol{\phi}_{\boldsymbol{FE\sigma dm}} \end{bmatrix} \breve{\boldsymbol{T}}_{\boldsymbol{mm}}\, \breve{\boldsymbol{T}}_{\boldsymbol{mm}}^{+}\, \boldsymbol{\phi}_{\boldsymbol{FEam}}\, \boldsymbol{u}_{\boldsymbol{xa}} = \begin{bmatrix} \boldsymbol{\phi}_{\boldsymbol{FE\sigma am}} \\ \boldsymbol{\phi}_{\boldsymbol{FE\sigma dm}} \end{bmatrix} \boldsymbol{\phi}_{\boldsymbol{FEam}}\, \boldsymbol{u}_{\boldsymbol{xa}} = \boldsymbol{\sigma}_{\mathbf{8}} \tag{4.59}$$

Therefore, the projection of the experimental response on the subspace spanned by the experimental mode shapes and the subsequent expansion to the unmeasured DOFs, does not represent any kind of benefit when it is assumed that $\breve{\boldsymbol{T}}_{\boldsymbol{\sigma mm}} = \breve{\boldsymbol{T}}_{\boldsymbol{\varepsilon mm}} = \breve{\boldsymbol{T}}_{\boldsymbol{mm}}$; on the contrary, extra work is needed to obtain the same results.

Some authors [114]–[116], [121], [123], [127] seem to have already used equations similar to Eq. (4.56) and (4.57) to calculate stresses, thus, using numerical stress mode shapes to calculate stresses and not using a transformation matrix. Stresses were estimated in offshore monopile wind turbines [114], [116], [127], a small scale vehicle-like frame structure [121] and in a numerical model of a truss [123]. However, this approach was supposedly based on the hypothesis of a perfect correlation between the experimental and the numerical models, and no further theoretical explanations were developed.

Variations of Method 8

Alternative equations could be proposed using modal coordinates $\widetilde{\boldsymbol{q}}_{\boldsymbol{\varepsilon xm}}$ obtained from Eq.(4.24). Strains would be estimated as:

$$\boldsymbol{\varepsilon}_{\boldsymbol{8b}} = \boldsymbol{\phi}_{\boldsymbol{FE\varepsilon m}}\, \widetilde{\boldsymbol{q}}_{\boldsymbol{\varepsilon xm}} = \begin{bmatrix} \boldsymbol{\phi}_{\boldsymbol{FE\varepsilon am}} \\ \boldsymbol{\phi}_{\boldsymbol{FE\varepsilon dm}} \end{bmatrix} \boldsymbol{\phi}^{+}_{\boldsymbol{FE\varepsilon am}}\, \boldsymbol{\varepsilon}_{\boldsymbol{xa}} \tag{4.60}$$

and stresses as follows:

$$\boldsymbol{\sigma}_{\boldsymbol{8b}} = \boldsymbol{\phi}_{\boldsymbol{FE\sigma m}}\, \widetilde{\boldsymbol{q}}_{\boldsymbol{\varepsilon xm}} = \begin{bmatrix} \boldsymbol{\phi}_{\boldsymbol{FE\sigma am}} \\ \boldsymbol{\phi}_{\boldsymbol{FE\sigma dm}} \end{bmatrix} \boldsymbol{\phi}^{+}_{\boldsymbol{FE\varepsilon am}}\, \boldsymbol{\varepsilon}_{\boldsymbol{xa}} \tag{4.61}$$

Alternatively, if modal coordinates $\widetilde{\boldsymbol{q}}_{\boldsymbol{txm}}$ are calculated with Eq. (4.26), strains are estimated as:

$$\boldsymbol{\varepsilon}_{\boldsymbol{8c}} = \boldsymbol{\phi}_{\boldsymbol{FE\varepsilon m}}\, \widetilde{\boldsymbol{q}}_{\boldsymbol{txm}} = \begin{bmatrix} \boldsymbol{\phi}_{\boldsymbol{FE\varepsilon am}} \\ \boldsymbol{\phi}_{\boldsymbol{FE\varepsilon dm}} \end{bmatrix} \begin{bmatrix} \boldsymbol{\phi}_{\boldsymbol{FE\varepsilon am}} \\ \boldsymbol{\phi}_{\boldsymbol{FEam}} \end{bmatrix}^{+} \begin{bmatrix} \boldsymbol{\varepsilon}_{\boldsymbol{xa}} \\ \boldsymbol{u}_{\boldsymbol{xa}} \end{bmatrix} \tag{4.62}$$

Similarly, stresses can be expressed as:

$$\boldsymbol{\sigma}_{\boldsymbol{8c}} = \boldsymbol{\phi}_{\boldsymbol{FE\sigma m}}\, \widetilde{\boldsymbol{q}}_{\boldsymbol{txm}} = \begin{bmatrix} \boldsymbol{\phi}_{\boldsymbol{FE\sigma am}} \\ \boldsymbol{\phi}_{\boldsymbol{FE\sigma dm}} \end{bmatrix} \begin{bmatrix} \boldsymbol{\phi}_{\boldsymbol{FE\varepsilon am}} \\ \boldsymbol{\phi}_{\boldsymbol{FEam}} \end{bmatrix}^{+} \begin{bmatrix} \boldsymbol{\varepsilon}_{\boldsymbol{xa}} \\ \boldsymbol{u}_{\boldsymbol{xa}} \end{bmatrix} \tag{4.63}$$

4.3.9 Summary

In this section a summary of the main characteristics and requirements of each of the methods presented is provided.

Firstly, Table 4.9 presets the requirements of each methodology in terms of sensors needed and if a numerical model is required. It is assumed that displacements ($\boldsymbol{u}_{xa}$) are estimated from acceleration measurements.

Table 4.9: Required sensors and/or numerical models in the studied methodologies.

Method	**Accelerometers**	**Strain gauges**	**FEM**
Method 1	Required	Not required	Required
Method 2	Not Required	Required	Required
Method 3	Required	Required	Required
Method 4	Required	Required	Required
Method 5	Required	Not required	Required
Method 6	Not Required	Required	Required
Method 7	Required	Required	Required
Method 8	Required	Not required	Required

In Table 4.10, the strain estimation equations for each method are summarize. The initial equations based on modal superposition are presented, along with the final equations expressed in terms of modal parameters and experimental responses.

Table 4.10: Summary of the strain estimation equations for each method.

Method	**Initial equation**	**Final equation**
Method 1	$\boldsymbol{\varepsilon_1 = \widetilde{\phi}_{x\varepsilon m_1}\, \widehat{q}_{xm}}$	$\boldsymbol{\varepsilon_1 = \phi_{FE\varepsilon m}\, \breve{T}_{mm}\, \phi^{+}_{xam}\, u_{xa}}$
Method 2	$\boldsymbol{\varepsilon_2 = \widetilde{\phi}_{x\varepsilon m_2}\, \widehat{q}_{\varepsilon xm}}$	$\boldsymbol{\varepsilon_2 = \phi_{FE\varepsilon m}\, \breve{T}_{\varepsilon mm}\, \phi^{+}_{x\varepsilon am}\, \varepsilon_{xa}}$
Method 3	$\boldsymbol{\varepsilon_3 = \widetilde{\phi}_{x\varepsilon m_3}\, \widehat{q}_{xm}}$	$\boldsymbol{\varepsilon_3 = \phi_{FE\varepsilon m}\, \breve{T}_{\varepsilon mm}\, \phi^{+}_{xam}\, u_{xa}}$
Method 4	$\boldsymbol{\varepsilon_4 = \widetilde{\phi}_{x\varepsilon m_4}\, \widehat{q}_{txm}}$	$\boldsymbol{\varepsilon_4 = \phi_{FE\varepsilon m}\, \breve{T}_{tmm} \begin{bmatrix} \phi_{x\varepsilon} \\ \phi_x \end{bmatrix}^{+} \begin{bmatrix} \varepsilon_{x_a} \\ u_{xa} \end{bmatrix}}$
Method 5	$\boldsymbol{\varepsilon_5 = \widetilde{\phi}_{x\varepsilon m_5}\, \widetilde{q}_{xm}}$	$\boldsymbol{\varepsilon_5 = \phi_{FE\varepsilon m}\, \breve{T}_{mm}\, s\, \phi^{+}_{FEam}\, u_{xa}}$
Method 6	$\boldsymbol{\varepsilon_6 = \widetilde{\phi}_{x\varepsilon m_6}\, \widetilde{q}_{\varepsilon xm}}$	$\boldsymbol{\varepsilon_6 = \phi_{FE\varepsilon m}\, \breve{T}_{\varepsilon mm}\, s_{\varepsilon}\, \phi^{+}_{FE\varepsilon am}\, \varepsilon_{xa}}$
Method 7	$\boldsymbol{\varepsilon_7 = \widetilde{\phi}_{x\varepsilon m_7}\, \widetilde{q}_{xm}}$	$\boldsymbol{\varepsilon_7 = \phi_{FE\varepsilon m}\, \breve{T}_{\varepsilon mm}\, s\, \phi^{+}_{FEam}\, u_{xa}}$
Method 8	$\boldsymbol{\varepsilon_8 = \phi_{FE\varepsilon m_8}\, \widetilde{q}_{xm}}$	$\boldsymbol{\varepsilon_8 = \phi_{FE\varepsilon m}\, \phi^{+}_{FEam}\, u_{xa}}$

Considering that:

- $\widetilde{\boldsymbol{\phi}}_{x\varepsilon m_2} = \widetilde{\boldsymbol{\phi}}_{x\varepsilon m_3} = \widetilde{\boldsymbol{\phi}}_{x\varepsilon m6} = \widetilde{\boldsymbol{\phi}}_{x\varepsilon m7}$
- $\widetilde{\boldsymbol{\phi}}_{x\varepsilon m_1} = \widetilde{\boldsymbol{\phi}}_{x\varepsilon m_5}$

4.4 Uncertainty analysis

In this section, all the sources of error that could potentially affect the methods proposed to estimate stresses, as well as their effects in the precision obtained with these methodologies are investigated.

4.4.1 Factors influencing modal coordinates $\widehat{\boldsymbol{q}}_{xm}$

In this section, the impact of mode shape truncation, signal noise, errors in mode shape estimation, and modes complexity on the modal coordinates $\widehat{\boldsymbol{q}}_{xm}$ is studied.

Truncation

The exact modal decomposition of the experimental response vector $\boldsymbol{u}_{xa}$ is given by:

$$\boldsymbol{u}_{xa} = [\boldsymbol{\phi}_{xam} \quad \boldsymbol{\phi}_{xar}] \begin{bmatrix} \boldsymbol{q}_{xm} \\ \boldsymbol{q}_{xr} \end{bmatrix} = \boldsymbol{\phi}_{xam}\, \boldsymbol{q}_{xm} + \boldsymbol{\phi}_{xar}\, \boldsymbol{q}_{xr} \tag{4.64}$$

where subscript *'r'* indicates truncated modes (not measured). As seen previously, due to modal truncation, an approximation of the experimental modal coordinates ($\widehat{\boldsymbol{q}}_{xm}$) can be obtained Eq. (4.21). Substituting Eq. (4.64) in Eq. (4.21), it is inferred that:

$$\widehat{\boldsymbol{q}}_{xm} = \boldsymbol{\phi}_{xam}^{+}\, (\boldsymbol{\phi}_{xam}\, \boldsymbol{q}_{xm} + \boldsymbol{\phi}_{xar}\, \boldsymbol{q}_{xr}) = \boldsymbol{q}_{xm} + \boldsymbol{\phi}_{xam}^{+} \boldsymbol{\phi}_{xar}\, \boldsymbol{q}_{xr} \tag{4.65}$$

where the term $\boldsymbol{\phi}_{xam}^{+} \boldsymbol{\phi}_{xar}\, \boldsymbol{q}_{xr}$ gives the contribution of the truncated modes to the measured experimental coordinates. If the modal coordinates $\widehat{\boldsymbol{q}}_{xm}$ are plotted in the frequency domain, the effect of the truncated modes appears as small peaks at each natural frequency corresponding to the truncated modes. The effect of the truncated modes is easily removed if the experimental responses are filtered.

This phenomenon is illustrated in Figure 4.3, which considers a system with five modes. In Figure 4.3 (a), the five modal coordinates are plotted, while in Figure 4.3 (b), the effect of truncation is illustrated by estimating only three modal coordinates with the first three mode shapes.

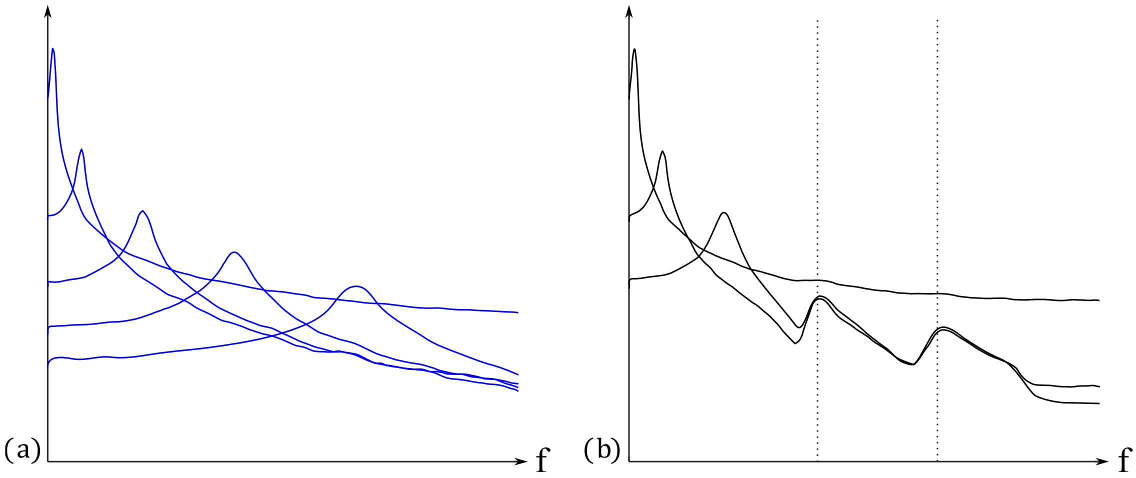

Figure 4.3: Effects of truncation in the experimental modal coordinates: (a) no truncation effects and (b) truncation effects.

If some mode is missing in the modal matrix (for example, if it was not identified), some peaks corresponding to this mode will appear, mainly in the neighbour modal coordinates. This phenomenon is also illustrated in Figure 4.4. In Figure 4.4 (b), for instance, modes 2 and 5 are missing, which is why only three modal coordinates are displayed. It can be observed that modal coordinates show more peaks than the principal one.

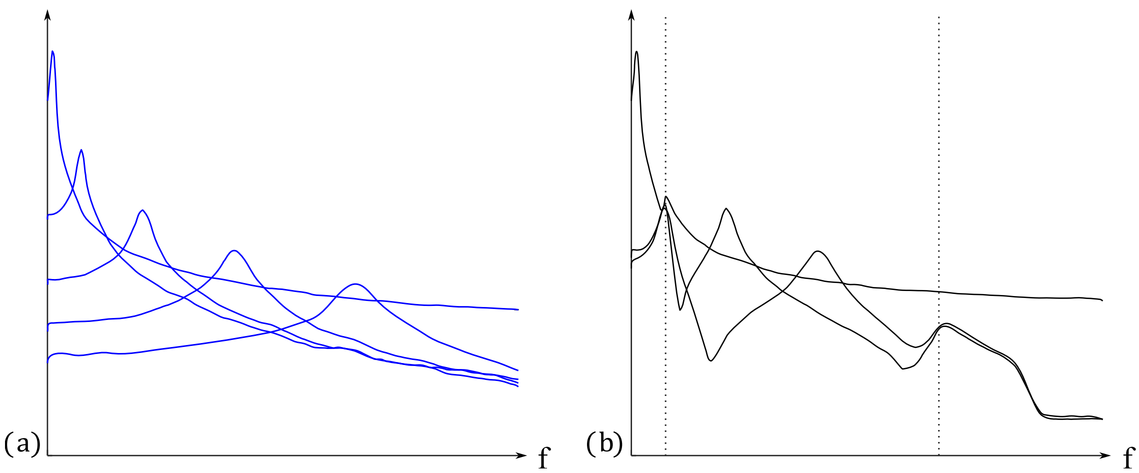

Figure 4.4: Effects of missing modes in the experimental modal coordinates: (a) all modes are considered and (b) mode two is missing.

Errors in the mode shapes

If the experimental mode shapes are estimated with modal analysis and some errors are present in the components of the mode shapes, the modal coordinates ($\widehat{\boldsymbol{q}}_{xm}$) are obtained with the expression:

$$\widehat{\boldsymbol{q}}_{xm} = \widehat{\boldsymbol{\phi}}_{xam}^{+}\, \boldsymbol{u}_{xa} \tag{4.66}$$

where $\widehat{\boldsymbol{\phi}}_{xam}$ is the estimated experimental modal matrix. Substitution of Eq. (4.64) in Eq. (4.66) gives:

$$\widehat{\boldsymbol{q}}_{xm} = \widehat{\boldsymbol{\phi}}_{xam}^{+}\boldsymbol{\phi}_{xam}\boldsymbol{q}_{xm} + \widehat{\boldsymbol{\phi}}_{xam}^{+}\boldsymbol{\phi}_{xar}\boldsymbol{q}_{xr} \tag{4.67}$$

Defining the error in the mode shapes $\boldsymbol{\Delta\phi}_{xam}$ as:

$$\boldsymbol{\Delta\phi}_{xam} = \boldsymbol{\phi}_{xam} - \widehat{\boldsymbol{\phi}}_{xam} \tag{4.68}$$

Eq. (4.67) can be rewritten as:

$$\widehat{\boldsymbol{q}}_{xm} = \boldsymbol{q}_{xm} + \widehat{\boldsymbol{\phi}}_{xam}^{+}\, \boldsymbol{\Delta\phi}_{x}\boldsymbol{q}_{xm} + \widehat{\boldsymbol{\phi}}_{xam}^{+}\boldsymbol{\phi}_{xar}\boldsymbol{q}_{xr} \tag{4.69}$$

From which can be inferred that some peaks at both (measured and not measured natural frequencies) can appear in the modal coordinates when the experimental mode shapes are not estimated with accuracy.

The effect of errors in the mode shapes is illustrated in Figure 4.5, which compares the modal coordinates estimated of a system with four modes without errors (Figure 4.5 (b)) and the modal coordinates obtained after inducing a random error of 5% in the components of the mode shapes (Figure 4.5 (b)). The errors follow a normal distribution from -5% to 5% of each mode shape component.

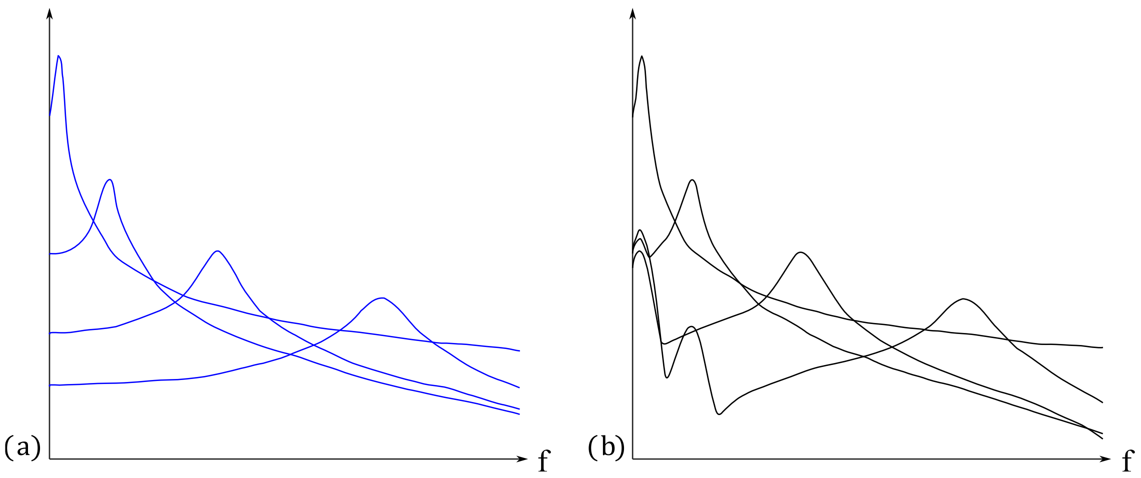

Figure 4.5: Effect of mode shape errors in the experimental modal coordinates: (a) no mode shape errors and (b) errors in the mode shape components around 5%.

Noise in the experimental responses

Assuming that some noise is present in the experimental response of the structure, and the noise in the signals is defined by the vector $\boldsymbol{n}_{xa}$, then the measured signal is given by $\boldsymbol{u}_{xa} + \boldsymbol{n}_{xa}$, and Eq. (4.65) becomes:

$$\widehat{\boldsymbol{q}}_{xm} = \boldsymbol{q}_{xm} + \boldsymbol{\phi}_{xam}^{+}\, \boldsymbol{\phi}_{xar}\, \boldsymbol{q}_{xr} + \boldsymbol{\phi}_{xam}^{+}\, \boldsymbol{n}_{xa} \qquad (4.70)$$

From which is inferred that contribution of the noise to the modal coordinates is given by the term $\boldsymbol{\phi}_{xam}^{+}\boldsymbol{n}_{xa}$.

This effect is illustrated in Figure 4.6, where a system with only four mode shapes is considered. When white noise is present in the measured displacements of all DOFs, the modal coordinates exhibit a higher level of noise (Figure 4.6 (b)).

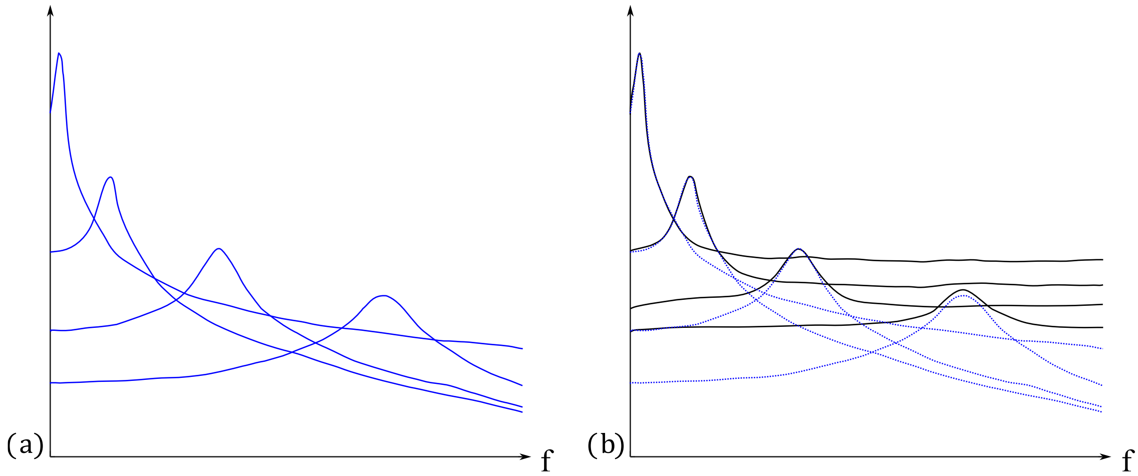

Figure 4.6: Effect of response noise in the modal coordinates: (a) without noise and (b) noise in the measure displacements.

Complexity

If the mode shapes are complex, the decomposition of $\boldsymbol{u}_{xa}$ in modal coordinates is given by:

$$\boldsymbol{u}_{xa} = [\boldsymbol{\phi}_{xam} \quad \boldsymbol{\phi}_{xar}] \begin{bmatrix} \boldsymbol{q}_{xm} \\ \boldsymbol{q}_{xr} \end{bmatrix} + [\boldsymbol{\phi}^*_{xam} \quad \boldsymbol{\phi}^*_{xar}] \begin{bmatrix} \boldsymbol{q}^*_{xm} \\ \boldsymbol{q}^*_{xr} \end{bmatrix} \tag{4.71}$$

where the superscript '*' indicates complex conjugate. If the experimental modal coordinates $\widehat{\boldsymbol{q}}_{xm}$ are approximated with Eq. (4.21), the following relationship between the exact and the approximate solution is obtained:

$$\widehat{\boldsymbol{q}}_{xm} = \boldsymbol{q}_{xm} + \boldsymbol{\phi}^+_{xam}\boldsymbol{\phi}_{xar}\,\boldsymbol{q}_{xr} + \boldsymbol{\phi}^+_{xam}\boldsymbol{\phi}^*_{xam}\,\boldsymbol{q}^*_{xm} + \boldsymbol{\phi}^+_{xam}\,\boldsymbol{\phi}^*_{xar}\,\boldsymbol{q}^*_{xr} \tag{4.72}$$

From which it is inferred that, in the frequency domain, apart to the main peak corresponding to $\boldsymbol{q}_{xm}$, three additional set of peaks will be obtained:

- $\boldsymbol{\phi}^+_{xam}\,\boldsymbol{\phi}_{xar}\,\boldsymbol{q}_{xr}$: Contribution of the truncated modes (as small peaks at each natural frequency corresponding to the truncated modes).
- $\boldsymbol{\phi}^+_{xam}\,\boldsymbol{\phi}^*_{xam}\,\boldsymbol{q}^*_{xm}$: Contribution of the conjugate modal coordinates in the measured frequency range (small peaks at the measured natural frequencies).
- $\boldsymbol{\phi}^+_{xam}\,\boldsymbol{\phi}^*_{xar}\,\boldsymbol{q}^*_{xr}$: Contribution of the truncated conjugate modal coordinates out of the measured frequency range (small peaks at each natural frequency corresponding to the truncated modes).

4.4.2 Factors influencing modal coordinates $\widetilde{\boldsymbol{q}}_{\boldsymbol{xm}}$

In this section, the impact of mode shape truncation, signal noise, and errors in mode shape estimation on the modal coordinates $\widetilde{\boldsymbol{q}}_{\boldsymbol{xm}}$ is studied.

Truncation

If Eq. (4.64) is substituted in Eq. (4.22), the modal coordinates $\widetilde{\boldsymbol{q}}_{\boldsymbol{xm}}$ can be expressed as:

$$\widetilde{\boldsymbol{q}}_{\boldsymbol{xm}} = \boldsymbol{\phi}^{+}_{\boldsymbol{FEam}} \left(\boldsymbol{\phi}_{\boldsymbol{xam}}\, \boldsymbol{q}_{\boldsymbol{xm}} + \boldsymbol{\phi}_{\boldsymbol{xar}}\, \boldsymbol{q}_{\boldsymbol{xr}}\right) \tag{4.73}$$

Eq. (4.73) can be rewritten as:

$$\widetilde{\boldsymbol{q}}_{\boldsymbol{xm}} = \boldsymbol{\phi}^{+}_{\boldsymbol{FEam}}\, \boldsymbol{\phi}_{\boldsymbol{xam}}\, \boldsymbol{q}_{\boldsymbol{xm}} + \boldsymbol{\phi}^{+}_{\boldsymbol{FEam}}\, \boldsymbol{\phi}_{\boldsymbol{xar}}\, \boldsymbol{q}_{\boldsymbol{xr}} \tag{4.74}$$

where the term $\boldsymbol{\phi}^{+}_{\boldsymbol{FEam}}\, \boldsymbol{\phi}_{\boldsymbol{xar}}\, \boldsymbol{q}_{\boldsymbol{xr}}$ gives the contribution of the residual modes to the measured experimental coordinates and $\boldsymbol{\phi}^{+}_{\boldsymbol{FEam}}\, \boldsymbol{\phi}_{\boldsymbol{xam}}\, \boldsymbol{q}_{\boldsymbol{xm}}$ the contribution of the measured modes. If the modal coordinates $\widetilde{\boldsymbol{q}}_{\boldsymbol{xm}}$ are plotted in the frequency domain, this effect appears as small peaks at each natural frequency corresponding to the residual modes.

This effect is illustrated in Figure 4.7, where a system with five mode shapes is considered. Truncation of different modes is illustrated as well as missing modes. Figure 4.7 (a) shows the expected modal coordinates $\boldsymbol{q}_{\boldsymbol{xm}}$, Figure 4.7 (b) illustrates $\widetilde{\boldsymbol{q}}_{\boldsymbol{xm}}$ when the last mode is truncated, Figure 4.7 (c) when modes three and five are truncated and Figure 4.7 (d) when the third mode is missing and the last mode is truncated. As expected, small peaks at each natural frequency corresponding to the truncated or missing mode appear, however, other peaks due to errors in the mode shapes also appear (see section: Error in the mode shapes).

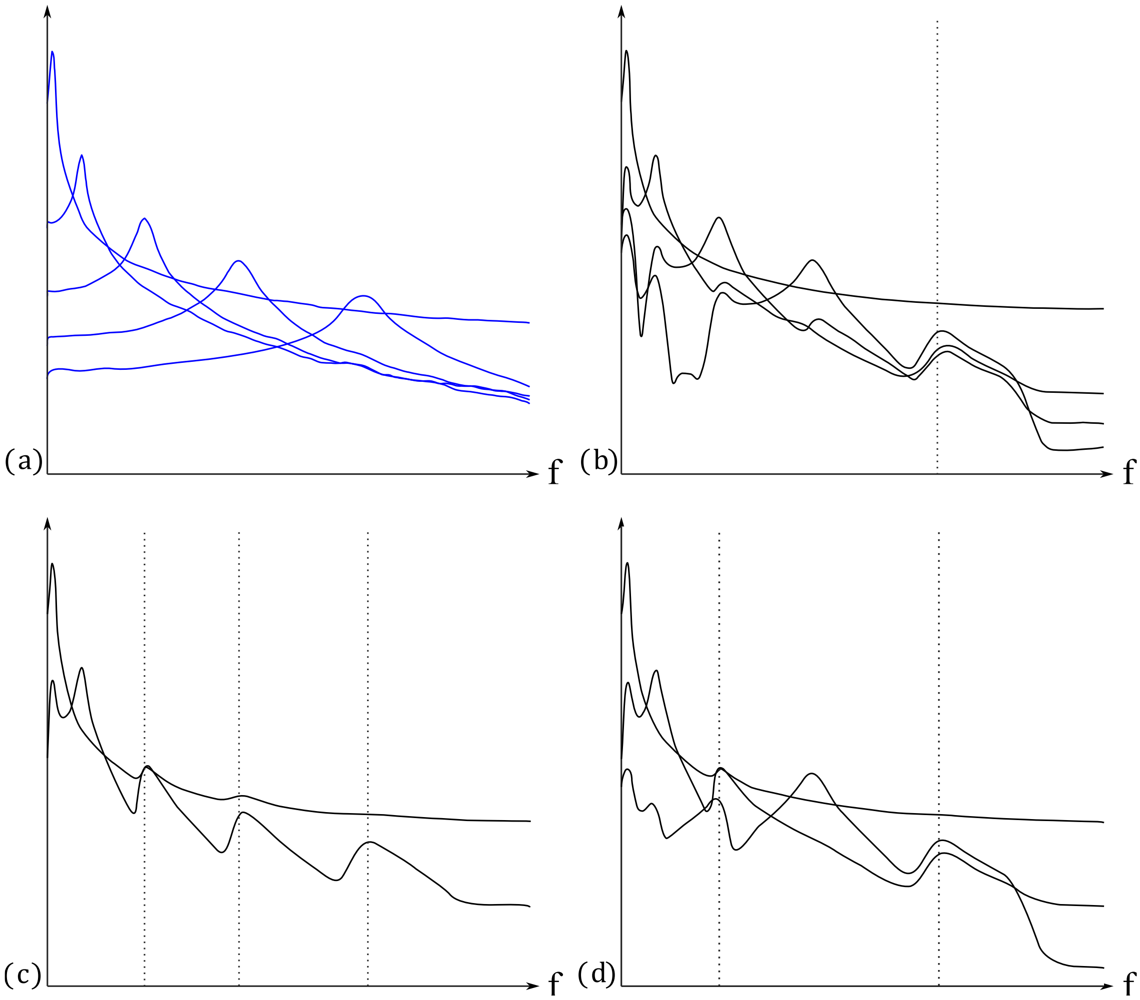

Figure 4.7: Effects of truncation and missing modes in the modal coordinates $\widetilde{\boldsymbol{q}}_{\boldsymbol{xm}}$: (a) exact modal coordinates, (b) truncation of mode 5, (c) truncation of modes 3, 4 and 5 and (d) truncation of mode 5 and third mode missing.

Error in the mode shapes

If the discrepancies between the experimental and the numerical mode shapes ($\boldsymbol{\Delta\phi_{xFE}}$) are defined as:

$$\boldsymbol{\Delta\phi_{xFE}} = \boldsymbol{\phi_{xam}} - \boldsymbol{\phi_{FEam}} \tag{4.75}$$

Substitution of Eq. (4.75) in Eq. (4.74), leads to:

$$\widetilde{\boldsymbol{q}}_{\boldsymbol{xm}} = \boldsymbol{q_{xm}} + \boldsymbol{\phi^{+}_{FEam}}\,\boldsymbol{\Delta\phi_{xFE}}\,\boldsymbol{q_{xm}} + \boldsymbol{\phi^{+}_{FEam}}\,\boldsymbol{\phi_{xar}}\,\boldsymbol{q_{xr}} \tag{4.76}$$

where the term $\boldsymbol{\phi}_{FEam}^{+}\,\boldsymbol{\Delta\phi}_{xFE}\,\boldsymbol{q}_{xm}$ gives the effect of errors in the mode shapes. If the modal coordinates $\widetilde{\boldsymbol{q}}_{xm}$ are plotted in the frequency domain, the effect of the term $\boldsymbol{\phi}_{FEam}^{+}\,\boldsymbol{\Delta\phi}_{xFE}\,\boldsymbol{q}_{xm}$ appears as peaks at the natural frequencies of the measured modes, the magnitude of the peaks being dependent on $\boldsymbol{\Delta\phi}_{xFE}$.

Figure 4.8 illustrates this effect, with peaks appearing at the frequencies of the measured modes. No truncation effects are considered in this illustration.

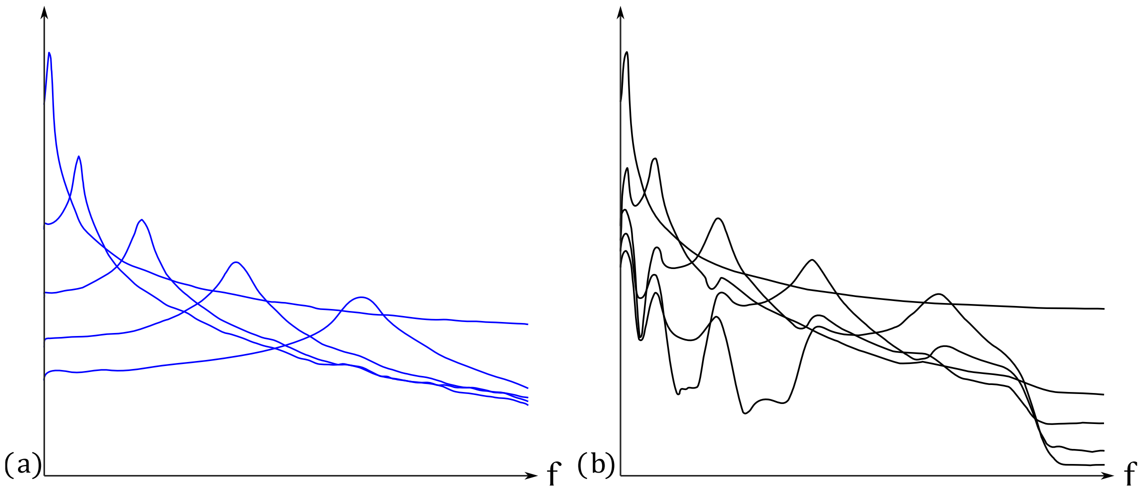

Figure 4.8: Effect of error in the mode shapes in the modal coordinates: (a) no errors in the mode shapes and (b) errors between the experimental and numerical modes.

Noise

If the effect of noise in the experimental responses is considered and defined by the vector $\boldsymbol{n}_{xa}$, the measured signal is given by $\boldsymbol{u}_{xa} + \boldsymbol{n}_{xa}$, Eq. (4.76) becomes:

$$\widetilde{\boldsymbol{q}}_{xm} = \boldsymbol{q}_{xm} + \boldsymbol{\phi}_{FEam}^{+}\,\boldsymbol{\Delta\phi}_{xE}\,\boldsymbol{q}_{xm} + \boldsymbol{\phi}_{FEam}^{+}\boldsymbol{\phi}_{xar}\,\boldsymbol{q}_{xr} + \boldsymbol{\phi}_{FEam}^{+}\,\boldsymbol{n}_{xa} \tag{4.77}$$

where the effect of noise is given by the term $\boldsymbol{\phi}_{FEam}^{+}\boldsymbol{n}_{xa}$.

This effect is illustrated in Figure 4.9 where a system with only four mode shapes is considered. When white noise is present in the measured displacements at all DOFs, the modal coordinates exhibit a higher level of noise (Figure 4.9 (b)).

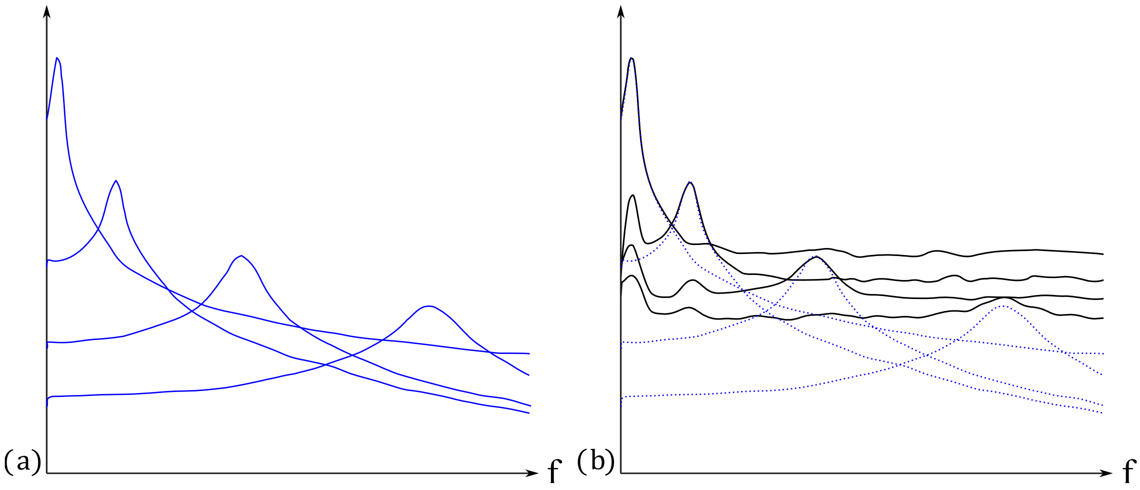

Figure 4.9: Effect of response noise in the modal coordinates: (a) without noise and (b) noise in the measured displacements.

4.4.3 Uncertainty in the strain estimation methods

The exact solution given by Eq. (4.3) can also be expressed as:

$$\boldsymbol{\varepsilon}_{x} = \boldsymbol{\phi}_{x\varepsilon}\,\boldsymbol{q}_{x} = \boldsymbol{\phi}_{x\varepsilon m}\,\boldsymbol{q}_{xm} + \boldsymbol{\phi}_{x\varepsilon r}\,\boldsymbol{q}_{xr} \tag{4.78}$$

Method 1

The following expression for the strains estimated with *Method 1* can be obtained substituting Eq. (4.65) in Eq. (4.28):

$$\boldsymbol{\varepsilon}_{1} = \boldsymbol{\phi}_{FE\varepsilon m}\,\breve{\boldsymbol{T}}_{mm}\,\widehat{\boldsymbol{q}}_{xm} = \boldsymbol{\phi}_{FE\varepsilon}\,\breve{\boldsymbol{T}}_{mm}\,(\boldsymbol{q}_{xm} + \boldsymbol{\phi}^{+}_{xam}\boldsymbol{\phi}_{xar}\,\boldsymbol{q}_{xr}) \tag{4.79}$$

Combining Eq. (4.78) and Eq. (4.79), the error in the estimated strains with *Method 1* ($\boldsymbol{\Delta\varepsilon_1} = \boldsymbol{\varepsilon}_{x} - \boldsymbol{\varepsilon}_{1}$), can be expressed as:

$$\boldsymbol{\Delta\varepsilon_1} = \left(\boldsymbol{\phi}_{x\varepsilon m} - \boldsymbol{\phi}_{FE\varepsilon m}\,\breve{\boldsymbol{T}}_{mm}\right)\boldsymbol{q}_{xm} + \left(\boldsymbol{\phi}_{x\varepsilon r} - \boldsymbol{\phi}_{FE\varepsilon m}\,\breve{\boldsymbol{T}}_{mm}\boldsymbol{\phi}^{+}_{xam}\boldsymbol{\phi}_{xar}\right)\boldsymbol{q}_{xr} \tag{4.80}$$

Method 2

In the case of *Method 2*, the effects of truncation in the estimated modal coordinates $\widehat{\boldsymbol{q}}_{x\varepsilon m}$ can be expressed as:

$$\widehat{\boldsymbol{q}}_{x\varepsilon m} = \boldsymbol{q}_{x\varepsilon m} + \boldsymbol{\phi}_{x\varepsilon am}^{+}\boldsymbol{\phi}_{x\varepsilon ar}\,\boldsymbol{q}_{x\varepsilon r} = \boldsymbol{q}_{xm} + \boldsymbol{\phi}_{x\varepsilon am}^{+}\boldsymbol{\phi}_{x\varepsilon ar}\,\boldsymbol{q}_{xr} \tag{4.81}$$

where $\boldsymbol{q}_{x\varepsilon m} = \boldsymbol{q}_{xm}$ and $\boldsymbol{q}_{x\varepsilon r} = \boldsymbol{q}_{xr}$. The strains estimated with *Method 2* can be rewritten as:

$$\boldsymbol{\varepsilon}_2 = \widetilde{\boldsymbol{\phi}}_{x\varepsilon m_2}\,(\boldsymbol{q}_{xm} + \boldsymbol{\phi}_{x\varepsilon am}^{+}\boldsymbol{\phi}_{x\varepsilon ar}\,\boldsymbol{q}_{xr}) \tag{4.82}$$

Combining Eq. (4.78) and Eq. (4.82), the error of *Method 2* ($\boldsymbol{\Delta\varepsilon_2} = \boldsymbol{\varepsilon}_x - \boldsymbol{\varepsilon}_2$) can be expressed as:

$$\boldsymbol{\Delta\varepsilon_2} = \left(\boldsymbol{\phi}_{x\varepsilon m} - \widetilde{\boldsymbol{\phi}}_{x\varepsilon m_2}\right)\boldsymbol{q}_{xm} + \left(\boldsymbol{\phi}_{x\varepsilon r} - \widetilde{\boldsymbol{\phi}}_{x\varepsilon m_2}\boldsymbol{\phi}_{x\varepsilon am}^{+}\boldsymbol{\phi}_{x\varepsilon ar}\right)\boldsymbol{q}_{xr} \tag{4.83}$$

or alternatively:

$$\boldsymbol{\Delta\varepsilon_2} = \left(\boldsymbol{\phi}_{x\varepsilon m} - \boldsymbol{\phi}_{FE\varepsilon m}\,\breve{\boldsymbol{T}}_{\varepsilon mm}\right)\boldsymbol{q}_{xm} + \left(\boldsymbol{\phi}_{x\varepsilon r} - \boldsymbol{\phi}_{FE\varepsilon m}\breve{\boldsymbol{T}}_{\varepsilon mm}\boldsymbol{\phi}_{x\varepsilon am}^{+}\boldsymbol{\phi}_{x\varepsilon ar}\right)\boldsymbol{q}_{xr} \tag{4.84}$$

Method 3

The equation to estimated strains with *Method 3* are rewritten as:

$$\boldsymbol{\varepsilon}_3 = \boldsymbol{\phi}_{FE\varepsilon}\,\breve{\boldsymbol{T}}_{\varepsilon mm}\,\widehat{\boldsymbol{q}}_{xm} = \boldsymbol{\phi}_{FE\varepsilon}\,\breve{\boldsymbol{T}}_{\varepsilon mm}\,(\boldsymbol{q}_{xm} + \boldsymbol{\phi}_{x\varepsilon am}^{+}\boldsymbol{\phi}_{x\varepsilon ar}\,\boldsymbol{q}_{xr}) \tag{4.85}$$

And the following expression for error $\boldsymbol{\Delta\varepsilon_3} = \boldsymbol{\varepsilon}_x - \boldsymbol{\varepsilon}_3$ can be obtained combining Eq. (4.78) and Eq. (4.85):

$$\boldsymbol{\Delta\varepsilon_3} = \left(\boldsymbol{\phi}_{x\varepsilon m} - \widetilde{\boldsymbol{\phi}}_{x\varepsilon m_3}\right)\boldsymbol{q}_{xm} + \left(\boldsymbol{\phi}_{x\varepsilon r} - \widetilde{\boldsymbol{\phi}}_{x\varepsilon m_3}\boldsymbol{\phi}_{xam}^{+}\boldsymbol{\phi}_{xar}\right)\boldsymbol{q}_{xr} \tag{4.86}$$

or:

$$\boldsymbol{\Delta\varepsilon_3} = \left(\boldsymbol{\phi}_{x\varepsilon m} - \boldsymbol{\phi}_{FE\varepsilon m}\breve{\boldsymbol{T}}_{\varepsilon mm}\right)\boldsymbol{q}_{xm} + \left(\boldsymbol{\phi}_{x\varepsilon r} - \boldsymbol{\phi}_{FE\varepsilon m}\breve{\boldsymbol{T}}_{\varepsilon mm}\boldsymbol{\phi}_{xam}^{+}\boldsymbol{\phi}_{xar}\right)\boldsymbol{q}_{xr} \tag{4.87}$$

Method 4

Regarding *Method 4,* Eq. (4.43) can be expressed as:

$$\boldsymbol{\varepsilon}_4 = \boldsymbol{\phi}_{FE\varepsilon}\,\breve{\boldsymbol{T}}_{tmm}\,\widehat{\boldsymbol{q}}_{txm} \tag{4.88}$$

Therefore, the error $\boldsymbol{\Delta\varepsilon_4} = \boldsymbol{\varepsilon_x} - \boldsymbol{\varepsilon_4}$ is expressed as follows:

$$\boldsymbol{\Delta\varepsilon_4} = \left[\boldsymbol{\phi_{x\varepsilon m}} - \boldsymbol{\widetilde{\phi}_{x\varepsilon m_4}}\right] \boldsymbol{q_{xm}} + \left[\boldsymbol{\phi_{x\varepsilon r}} - \boldsymbol{\widetilde{\phi}_{x\varepsilon m_4}} \begin{pmatrix} \boldsymbol{\phi_{x\varepsilon am}} \\ \boldsymbol{\phi_{xam}} \end{pmatrix}^+ \begin{pmatrix} \boldsymbol{\phi_{x\varepsilon ar}} \\ \boldsymbol{\phi_{xar}} \end{pmatrix}\right] \boldsymbol{q_{xm}} \tag{4.89}$$

or:

$$\begin{aligned} \boldsymbol{\Delta\varepsilon_4} &= \left[\boldsymbol{\phi_{x\varepsilon m}} - \boldsymbol{\phi_{FE\varepsilon m}}\,\boldsymbol{\breve{T}_{t\varepsilon mm}}\right] \boldsymbol{q_{xm}} \\ &\quad + \left[\boldsymbol{\phi_{x\varepsilon r}} - \boldsymbol{\phi_{FE\varepsilon m}}\,\boldsymbol{\breve{T}_{t\varepsilon mm}} \begin{pmatrix} \boldsymbol{\phi_{x\varepsilon am}} \\ \boldsymbol{\phi_{xam}} \end{pmatrix}^+ \begin{pmatrix} \boldsymbol{\phi_{x\varepsilon ar}} \\ \boldsymbol{\phi_{xar}} \end{pmatrix}\right] \boldsymbol{q_{xm}} \end{aligned} \tag{4.90}$$

Method 5

In the case of *Method 5*, the errors are given by the expression:

$$\boldsymbol{\Delta\varepsilon_5} = \boldsymbol{\varepsilon_x} - \boldsymbol{\varepsilon_5} = \boldsymbol{\phi_{x\varepsilon m}}\,\boldsymbol{q_{xm}} + \boldsymbol{\phi_{x\varepsilon r}}\,\boldsymbol{q_{xr}} - \boldsymbol{\widetilde{\phi}_{x\varepsilon m}}\,\boldsymbol{\widetilde{q}_{xm}} \tag{4.91}$$

Denoting the discrepancies between the experimental strain mode shapes $\boldsymbol{\phi_{x\varepsilon m}}$ and the expanded strain mode shapes $\boldsymbol{\widetilde{\phi}_{x\varepsilon m_5}}$ as $\boldsymbol{\Delta\phi_{x\varepsilon m}}$, i.e:

$$\boldsymbol{\Delta\phi_{x\varepsilon m_5}} = \boldsymbol{\phi_{x\varepsilon m}} - \boldsymbol{\widetilde{\phi}_{x\varepsilon m_5}} = \boldsymbol{\phi_{x\varepsilon m}} - \boldsymbol{\phi_{FE\varepsilon m}}\boldsymbol{\breve{T}_{mm}} \tag{4.92}$$

Considering $\boldsymbol{\Delta\widetilde{q}_{xm}}$ the difference between the experimental modal coordinates $\boldsymbol{q_{xm}}$ and the modal coordinates $\boldsymbol{\widetilde{q}_{xm}}$, thus:

$$\boldsymbol{\Delta\widetilde{q}_{xm}} = \boldsymbol{q_{xm}} - \boldsymbol{\widetilde{q}_{xm}} \tag{4.93}$$

where

$$\boldsymbol{\widetilde{q}_{xm}} = \left(\boldsymbol{\breve{T}_{mm}} + \boldsymbol{\phi^+_{FEam}}\boldsymbol{\phi_{FEar}}\boldsymbol{\breve{T}_{mm}}\right)\boldsymbol{q_{xm}} + \left(\boldsymbol{\breve{T}_{mr}} + \boldsymbol{\phi^+_{FEam}}\boldsymbol{\phi_{FEar}}\boldsymbol{\breve{T}_{rr}}\right)\boldsymbol{q_{xr}} \tag{4.94}$$

Eq. (4.91) can be rewritten as:

$$\boldsymbol{\Delta\varepsilon_5} = \boldsymbol{\phi_{x\varepsilon r}}\,\boldsymbol{q_{xr}} + \boldsymbol{\phi_{x\varepsilon m}}\,\boldsymbol{\Delta\widetilde{q}_{xm}} + \boldsymbol{\Delta\phi_{x\varepsilon m_5}}\boldsymbol{q_{xm}} - \boldsymbol{\Delta\phi_{x\varepsilon m_5}}\,\boldsymbol{\Delta\widetilde{q}_{xm}} \tag{4.95}$$

Method 6

In a similar way, the errors obtained with *Method 6* are given by:

$$\boldsymbol{\Delta\varepsilon_6} = \boldsymbol{\phi_{x\varepsilon r}}\, \boldsymbol{q_{xr}} + \boldsymbol{\phi_{x\varepsilon m}}\, \boldsymbol{\Delta\tilde{q}_{\varepsilon xm}} + \boldsymbol{\Delta\phi_{x\varepsilon m_6}}\, \boldsymbol{q_{xm}} - \boldsymbol{\Delta\phi_{x\varepsilon m_6}}\, \boldsymbol{\Delta\tilde{q}_{\varepsilon xm}} \tag{4.96}$$

where $\boldsymbol{\Delta\phi_{x\varepsilon m_6}}$ is here obtained with the expression:

$$\boldsymbol{\Delta\phi_{x\varepsilon m_6}} = \boldsymbol{\phi_{x\varepsilon m}} - \boldsymbol{\tilde{\phi}_{x\varepsilon m_6}} = \boldsymbol{\phi_{x\varepsilon m}} - \boldsymbol{\phi_{FE\varepsilon m}}\boldsymbol{\breve{T}_{\varepsilon mm}} \tag{4.97}$$

And $\boldsymbol{\Delta\tilde{q}_{x\varepsilon m}}$ is expressed as:

$$\boldsymbol{\Delta\tilde{q}_{x\varepsilon m}} = \boldsymbol{q_{xm}} - \boldsymbol{\tilde{q}_{x\varepsilon m}} \tag{4.98}$$

Method 7

The error of *Method 7* is again expressed as:

$$\boldsymbol{\Delta\varepsilon_7} = \boldsymbol{\phi_{x\varepsilon r}}\, \boldsymbol{q_{xr}} + \boldsymbol{\phi_{x\varepsilon m}}\, \boldsymbol{\Delta\tilde{q}_{xm}} + \boldsymbol{\Delta\phi_{x\varepsilon m_6}}\, \boldsymbol{q_{xm}} - \boldsymbol{\Delta\phi_{x\varepsilon m_6}}\, \boldsymbol{\Delta\tilde{q}_{xm}} \tag{4.99}$$

Method 8

Finally, the error of *Method 8* is expressed as:

$$\boldsymbol{\Delta\varepsilon_8} = \boldsymbol{\phi_{x\varepsilon m}}\, \boldsymbol{q_{xm}} + \boldsymbol{\phi_{x\varepsilon r}}\, \boldsymbol{q_{xr}} - \boldsymbol{\phi_{FE\varepsilon m}}\, \boldsymbol{\tilde{q}_{xm}} \tag{4.100}$$

Substitution of Eq. (4.94) in Eq.(4.100), gives:

$$\boldsymbol{\Delta\varepsilon_8} = \boldsymbol{\phi_{x\varepsilon r}}\, \boldsymbol{q_{xr}} + (\boldsymbol{\phi_{x\varepsilon m}} - \boldsymbol{\phi_{FE\varepsilon m}})\boldsymbol{q_{xm}} + \boldsymbol{\phi_{FE\varepsilon m}}\, \boldsymbol{\Delta\tilde{q}_{xm}} \tag{4.101}$$

4.4.4 Errors in the strain mode shapes. Assumption $\boldsymbol{\breve{T}_{\varepsilon mm}} = \boldsymbol{\breve{T}_{mm}}$

As previously commented, the experimental mode shapes $\boldsymbol{\tilde{\phi}_{xam}}$ can be expressed as a linear combination of the numerical ones $\boldsymbol{\phi_{FEam}}$ through the transformation matrix $\boldsymbol{\breve{T}_{mm}}$. Moreover, the modal matrix $\boldsymbol{\phi_{xam}}$ can be expressed as:

$$\boldsymbol{\phi_{xam}} = \boldsymbol{\tilde{\phi}_{xam}} + \boldsymbol{\Delta\phi_{xam}} \tag{4.102}$$

where matrix $\boldsymbol{\Delta\phi_{xam}}$ is the error between experimental mode shapes $\boldsymbol{\phi_{xam}}$ and expanded mode shapes $\boldsymbol{\widetilde{\phi}_{xam}}$.

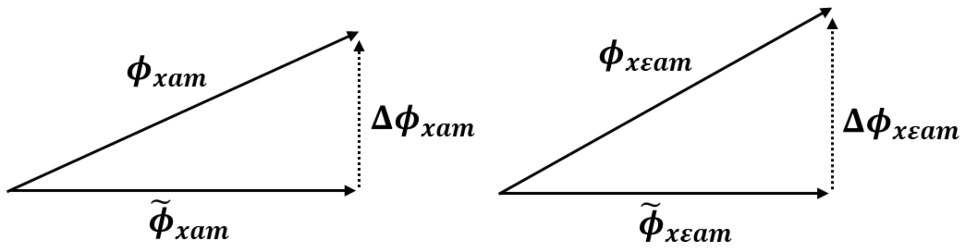

Figure 4.10: Notation of errors between experimental mode shapes and expanded mode shapes.

Eq. (4.102) can be rewritten as:

$$\boldsymbol{\phi_{xam}} = \boldsymbol{\phi_{FEam}\breve{T}_{mm}} + \boldsymbol{\Delta\phi_{xam}} \tag{4.103}$$

In the same manner, strain mode shapes can be expressed as:

$$\boldsymbol{\phi_{x\varepsilon am}} = \boldsymbol{\widetilde{\phi}_{x\varepsilon am}} + \boldsymbol{\Delta\phi_{x\varepsilon am}} \tag{4.104}$$

where the experimental strain mode shapes $\boldsymbol{\widetilde{\phi}_{x\varepsilon am}}$ can be expressed as a linear combination of the numerical ones $\boldsymbol{\phi_{FE\varepsilon am}}$ through the transformation matrix $\boldsymbol{\breve{T}_{\varepsilon mm}}$.

If a planar beam in bending is considered, the strain mode shapes are related with the mode shapes trough the expression:

$$\boldsymbol{\phi_{x\varepsilon am}} = y\, \boldsymbol{\phi''_{xam}} \tag{4.105}$$

where y is the distance to the neutral axis. Substitution of Eq. (4.103) in Eq. (4.105) gives:

$$\boldsymbol{\phi_{x\varepsilon am}} = y\left(\boldsymbol{\phi_{FEam}\breve{T}_{mm}} + \boldsymbol{\Delta\phi''_{xam}}\right) = \boldsymbol{\phi_{FE\varepsilon am}\breve{T}_{mm}} + y\, \boldsymbol{\Delta\phi''_{xam}} \tag{4.106}$$

From Eq. (4.104) and (4.106) the following relationship between $\boldsymbol{\breve{T}_{\varepsilon mm}}$ and $\boldsymbol{\breve{T}_{mm}}$ is obtained:

$$\boldsymbol{\breve{T}_{\varepsilon mm}} = \boldsymbol{\breve{T}_{mm}} + \boldsymbol{\phi^{+}_{FE\varepsilon am}}(y\boldsymbol{\Delta\phi''_{xam}} - \boldsymbol{\Delta\phi_{\varepsilon xam}}) \tag{4.107}$$

which demonstrates that $\boldsymbol{T_{\varepsilon mm}} \neq \boldsymbol{\breve{T}_{mm}}$ and the difference depends on $\boldsymbol{\Delta\phi''_{xam}}$ and $\boldsymbol{\Delta\phi_{x\varepsilon am}}$.

4.4.5 Scale of mode shapes

If the experimental mode shapes are unscaled ($\boldsymbol{\psi}_{\boldsymbol{x}}$) the modal decomposition is given by:

$$\boldsymbol{u}_{\boldsymbol{xa}} \cong \boldsymbol{\psi}_{\boldsymbol{xam}}\, \widehat{\boldsymbol{q}}_{\boldsymbol{\psi xm}} \tag{4.108}$$

The scaled and unscaled mode shapes are related by:

$$\boldsymbol{\phi}_{\boldsymbol{xam}} = \boldsymbol{\psi}_{\boldsymbol{xam}}\, \boldsymbol{\alpha}_{\boldsymbol{xm}} \tag{4.109}$$

where $\boldsymbol{\alpha}_{\boldsymbol{xm}}$ is a diagonal matrix containing the scaling factors. From Eqs. (4.21), (4.108) and (4.109), the following relationship between $\boldsymbol{q}_{\boldsymbol{\psi xm}}$ and $\boldsymbol{q}_{\boldsymbol{xm}}$ is obtained.

$$\widehat{\boldsymbol{q}}_{\boldsymbol{\psi xm}} = \boldsymbol{\alpha}_{\boldsymbol{xm}}\, \widehat{\boldsymbol{q}}_{\boldsymbol{xm}} \tag{4.110}$$

The scaled and unscaled strain mode shapes are also related by:

$$\boldsymbol{\phi}_{\boldsymbol{\varepsilon xam}} = \boldsymbol{\psi}_{\boldsymbol{\varepsilon xam}}\, \boldsymbol{\alpha}_{\boldsymbol{\varepsilon xm}} \tag{4.111}$$

where $\boldsymbol{\alpha}_{\boldsymbol{\varepsilon xm}}$ is also a diagonal matrix containing the scaling factors of the strain mode shapes. If $\boldsymbol{\psi}_{\boldsymbol{xam}}$ and $\boldsymbol{\psi}_{\boldsymbol{\varepsilon xam}}$ are used, the strains can be obtained as:

$$\boldsymbol{\varepsilon}_{\boldsymbol{x}} \cong \boldsymbol{\phi}_{\boldsymbol{\varepsilon xam}} \widehat{\boldsymbol{q}}_{\boldsymbol{xm}} = \boldsymbol{\psi}_{\boldsymbol{\varepsilon xam}}\, \boldsymbol{\alpha}_{\boldsymbol{\varepsilon xm}}\, \boldsymbol{\alpha}_{\boldsymbol{xm}}^{-1}\, \widehat{\boldsymbol{q}}_{\boldsymbol{\psi xm}} \tag{4.112}$$

where it can be observed that the scaling factors of both the mode shapes $\boldsymbol{\alpha}_{\boldsymbol{xm}}$ and the strain mode shapes $\boldsymbol{\alpha}_{\boldsymbol{\varepsilon xm}}$ are needed. Using the structural dynamic modification, the mode shapes $\boldsymbol{\psi}_{\boldsymbol{xam}}$ and the strain mode shapes $\boldsymbol{\psi}_{\boldsymbol{\varepsilon xam}}$ can be expressed as:

$$\boldsymbol{\psi}_{\boldsymbol{xam}}\, \boldsymbol{\alpha}_{\boldsymbol{xm}} \cong \boldsymbol{\phi}_{\boldsymbol{FEa}} \breve{\boldsymbol{T}}_{\boldsymbol{mm}} \tag{4.113}$$

and

$$\boldsymbol{\psi}_{\boldsymbol{\varepsilon xam}}\, \boldsymbol{\alpha}_{\boldsymbol{\varepsilon xm}} \cong \boldsymbol{\phi}_{\boldsymbol{FE\varepsilon a}} \breve{\boldsymbol{T}}_{\boldsymbol{\varepsilon mm}} \tag{4.114}$$

Respectively, if it is assumed that $\breve{\boldsymbol{T}}_{\boldsymbol{mm}} = \breve{\boldsymbol{T}}_{\boldsymbol{\varepsilon mm}}$ the product $\boldsymbol{\alpha}_{\boldsymbol{x\varepsilon m}} \boldsymbol{\alpha}_{\boldsymbol{xm}}^{-1}$ can be isolated from Eqs. (4.113) and (4.114) as:

$$\boldsymbol{\alpha}_{\boldsymbol{\varepsilon x m}}\boldsymbol{\alpha}_{\boldsymbol{x m}}^{-1} \cong \boldsymbol{\psi}_{\boldsymbol{\varepsilon x a m}}^{+}\boldsymbol{\phi}_{\boldsymbol{F E \varepsilon a m}}\boldsymbol{\phi}_{\boldsymbol{F E a m}}^{+}\boldsymbol{\psi}_{\boldsymbol{x a m}} \tag{4.115}$$

If Eq. (4.115) is substituted in Eq. (4.11), the strains at any point of the structure can be obtained with the expression:

$$\boldsymbol{\varepsilon}_{\boldsymbol{x}} \cong \boldsymbol{\phi}_{\boldsymbol{F E \varepsilon m}}\boldsymbol{\phi}_{\boldsymbol{F E a m}}^{+}\boldsymbol{\psi}_{\boldsymbol{x a m}}\widehat{\boldsymbol{q}}_{\boldsymbol{\psi x m}} = \boldsymbol{\phi}_{\boldsymbol{F E \varepsilon m}}\boldsymbol{\phi}_{\boldsymbol{F E a m}}^{+}\boldsymbol{u}_{\boldsymbol{x a}} \tag{4.116}$$

From which is inferred that the scaling factors $\boldsymbol{\alpha}_{\boldsymbol{x m}}$ and $\boldsymbol{\alpha}_{\boldsymbol{\varepsilon x m}}$ are not needed if it is assumed that $\breve{\boldsymbol{T}}_{\boldsymbol{m m}} = \breve{\boldsymbol{T}}_{\boldsymbol{\varepsilon m m}}$.

5

Application cases

This chapter aims to apply, validate and compare the stress/strain estimation methods proposed in Chapter 4. To do this, three examples are studied: a numerical example of a cantilever beam, an experimental example of a simply monolithic glass beam and an experimental example of a lab-scale steel cantilever beam. Additionally, some of the proposed correlation indicators of Chapter 3 will also be applied to study discrepancies between structures.

5.1 Numerical example: a cantilever beam

As previously commented, when applying modal expansion techniques to estimate strains, a finite element model (*Model B / FEM*) of the real structure (*Model A / Experimental*) is required. In this section, both models (*Models A* and *B*), are simulated through FEM in order to analyse the accuracy of the results, avoiding all the sources of error related to experimental measurements.

In this application case, a steel cantilever beam was modelled with the finite element software Abaqus. Model B, which is required to apply the proposed methods, was modelled with a fixed support (Figure 5.1). In Model A, an elastic foundation was modelled as boundary condition, instead of the fixed support considered in Model *B*. To obtain different levels of correlation, two values of stiffness (K_1 and K_2) were modelled for the elastic foundation (Figure 5.1), thus, two experimental models were considered (hereafter Model A1 and Model A2).

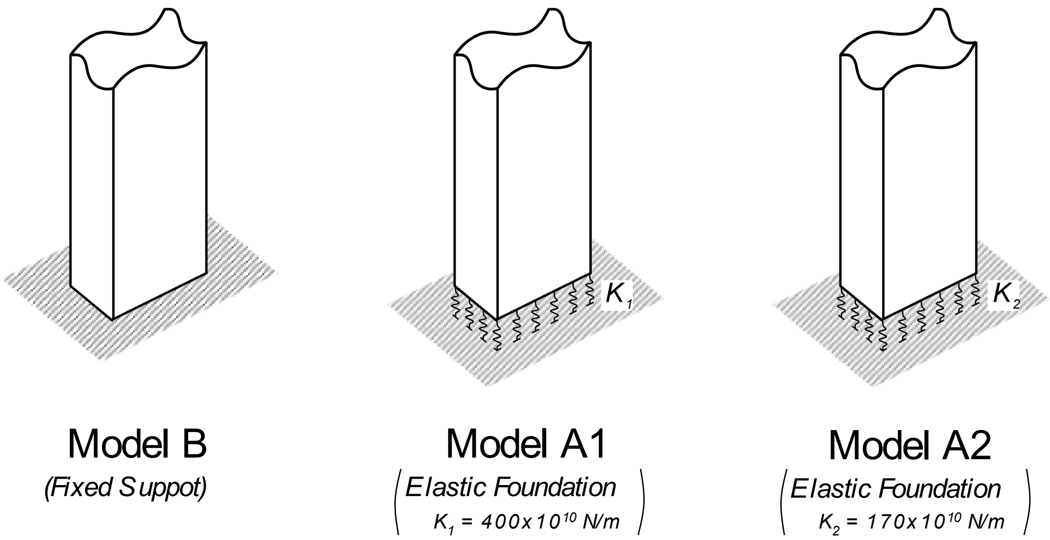

Figure 5.1: Boundary conditions of Models B, A1 and A2.

The following geometrical and material properties were considered in the finite element models of the cantilever beam: length 1.8 m, rectangular section of 40 mm x 80 mm, linear elastic material with E=200 GPa, Poisson's ratio = 0.3, and mass-density of 7850 kg/m^3. The models were meshed with 1920 quadratic brick elements with reduced integration (C3D20R). A damping ratio of 5% was considered for all modes.

Two cases, with different active DOFs, were considered. In the first simulation case, presented in section 5.1.1, the structure's responses were only measured in one direction, thereby considering only bending modes in one direction. In the second simulation, detailed in section 5.1.2, the responses were measured in two directions, thus bending modes in two directions, and torsional modes, were considered.

5.1.1 First simulation case. Only bending modes

Firstly, it was assumed that the external force acting on the experimental structure only excites the bending modes in the x direction (Figure 5.2).

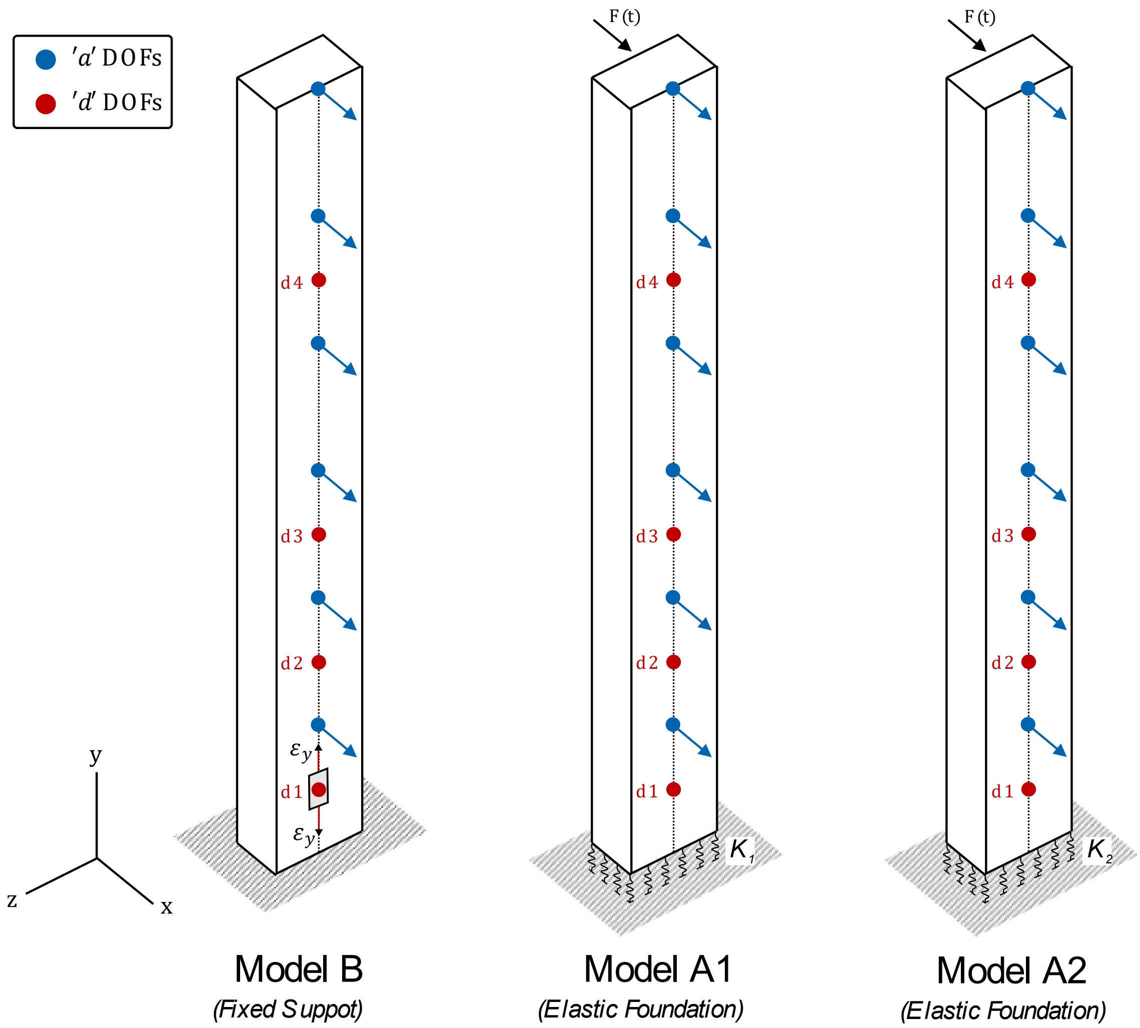

Figure 5.2: Models B, A1 and A2 of the cantilever beam and DOFs when only bending modes are considered.

Models A1 and A2 were loaded with a concentrated load F(t) generated from a spectral density of constant magnitude in the frequency range 0-1600 Hz, that is to say, this load excites five bending modes in the x direction in that frequency range. It was assumed that both the strain and the displacement response of models A1 and A2 were measured in 6 degrees of freedom ('a' DOF's), uniformly distributed as it is shown in Figure 5.2, and in the frequency range 0-800 Hz.

The natural frequencies, mode shapes, and strain mode shapes, corresponding to the first four bending modes in the x direction, were extracted with a frequency analysis for the three models (B, A1 and A2), and they are presented in Table 5.1, Figure 5.3 and Figure 5.4, respectively, where the locations of the active DOFs are plotted with dots. Although there are five bending modes in the frequency range 0-800 Hz, only four modes were considered in this application case.

Table 5.1: Natural frequencies [Hz] and errors [%].

Mode shape	$f_B\ [Hz]$	$f_{A1}\ [Hz]$	Error B-A1 [%]	$f_{A2}\ [Hz]$	Error B-A2 [%]
Mode 1	10.07	9.55	5.43	8.96	12.39
Mode 2	62.94	59.98	4.94	57.16	10.11
Mode 3	175.61	167.98	4.54	161.78	8.55
Mode 4	342.33	328.68	4.15	319.06	7.29

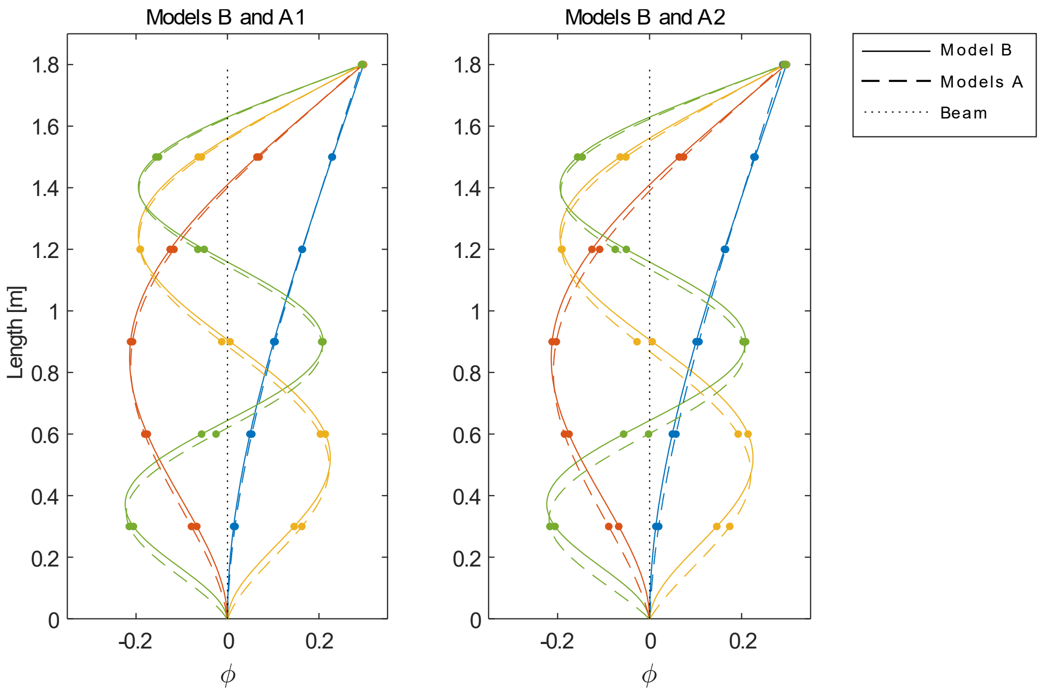

Figure 5.3: First four bending mode shapes of Models B, A1 and A2.

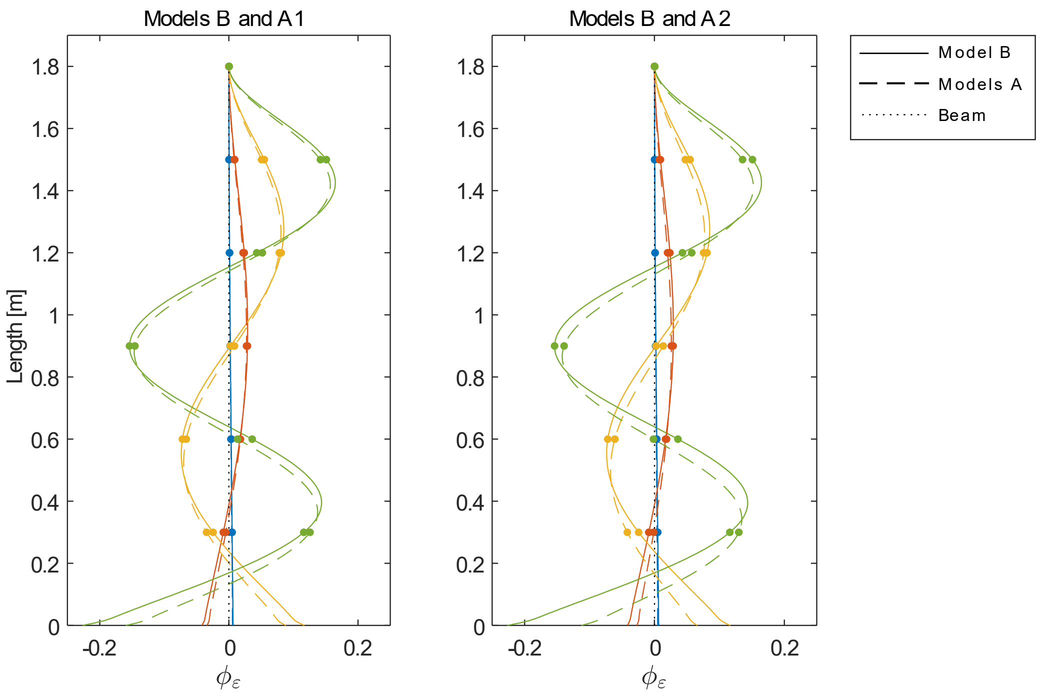

Figure 5.4: First four bending strain mode shapes of Models B, A1 and A2.

The maximum error between the natural frequencies of models B and A1 is 5.43%, while that between models B and A2 of 12.39% (Table 5.1). With respect to the mode shapes, a good correlation is obtained between models B and A1 and A2, as it can be seen in the MAC (Table 5.2). The MAC between the strain mode shapes is presented in Table 5.3, where it can be seen that the correlation is worst when compared with the results obtained for the mode shapes (Table 5.2).

Table 5.2: MAC between modal matrices of models B and A1 and models B and A2.

MAC (ϕ_B, ϕ_{A1})				MAC (ϕ_B, ϕ_{A2})			
0.9997	0.0708	0.0881	0.0922	0.9988	0.0626	0.0888	0.0888
0.0841	0.9985	0.0787	0.1112	0.0908	0.9944	0.0653	0.1171
0.0836	0.1109	0.9960	0.0846	0.0808	0.1271	0.9872	0.0682
0.0948	0.0967	0.1362	0.9935	0.0951	0.0910	0.1603	0.9814

Table 5.3: MAC between strain modal matrices of models B and A1 and models B and A2.

MAC ($\phi_{B\varepsilon}, \phi_{A1\varepsilon}$)				MAC ($\phi_{B\varepsilon}, \phi_{A2\varepsilon}$)			
1.0000	0.1444	0.1087	0.0772	1.0000	0.1427	0.1093	0.0778
0.2211	0.9905	0.0501	0.0360	0.3060	0.9626	0.0286	0.0230
0.1341	0.1153	0.9876	0.0118	0.1524	0.1500	0.9605	0.0019
0.0782	0.0584	0.0623	0.9872	0.0760	0.0618	0.0849	0.9647

Moreover, the ***T-Mass*** y ***T-Stiffness*** indicators are calculated for both models A1 and A2. ***T-Mass*** (Table 5.4) shows values close to 90°, indicating almost perfect mass correlation, whereas ***T-Stiffness*** (Table 5.5) presents significantly low values, indicating discrepancies in terms of stiffness.

Table 5.4: ***T-Mass*** indicator for models A1 and A2

T-Mass (A1)				***T-Mass*** (A2)			
---	89.95	89.81	89.53	---	89.91	89.69	89.28
89.95	---	89.88	89.40	89.91	---	89.75	88.90
89.81	89.88	---	89.75	89.69	89.75	---	89.89
89.53	89.40	89.75	---	89.28	88.90	89.89	0.00

Table 5.5: ***T-Stiffness*** indicator for models A1 and A2

T-Stiffness (A1)				***T-Stiffness*** (A2)			
---	89.06	89.64	89.85	---	88.25	89.24	89.69
78.94	---	87.95	89.14	77.00	---	86.04	88.41
59.48	75.68	---	87.67	56.92	67.28	---	86.08
36.98	67.37	81.28	---	37.61	56.25	75.80	---

With these models, the objective is to estimate the strain time histories at points d1, d2, d3 and d4 (deleted DOFs) (Figure 5.2), for both models A1 and A2, using the eight methods proposed in Chapter 4. Normal strains are estimated in 'y' direction, as it is illustrated in Figure 5.2. The strains estimated are compared with those obtained directly from the Abaqus simulation (denoted as ε_{FEM}). The strains at the four 'd' DOFs of Model A1 estimated with filtered modal coordinates are plotted in: Figure 5.5 at 'd1', Figure 5.6 at 'd2', Figure 5.7 at 'd3' and Figure 5.8 at 'd4'. For Model A2, the strain time histories calculated with filtered modal coordinates are also show in: Figure 5.9 at 'd1', Figure 5.10 at 'd2', Figure 5.11 at 'd3' and Figure 5.12 at 'd4'.

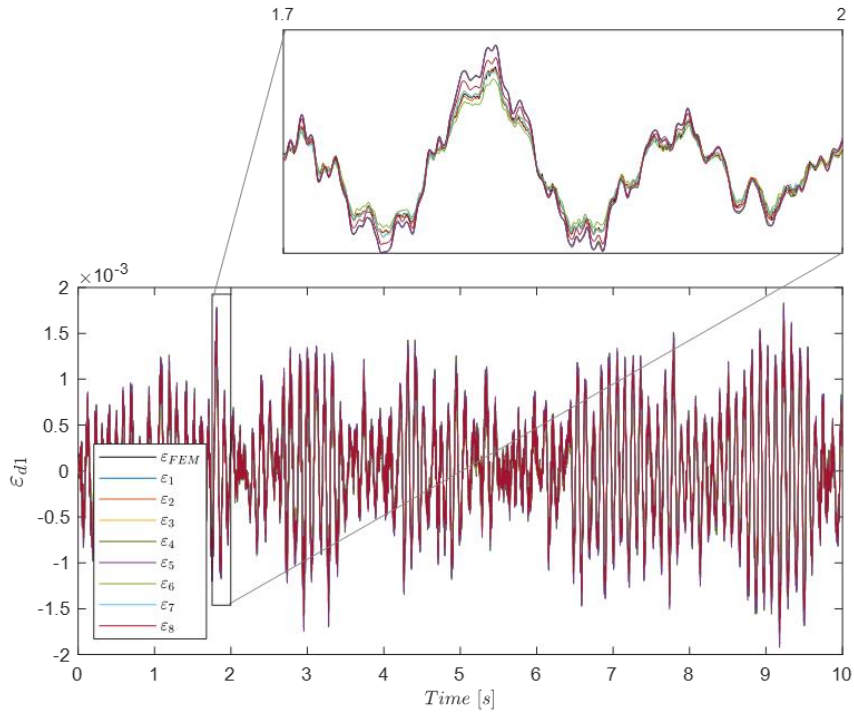

Figure 5.5: Estimated strains with all methods compared with the expected strains for Model A1 at ‘d1’ DOF.

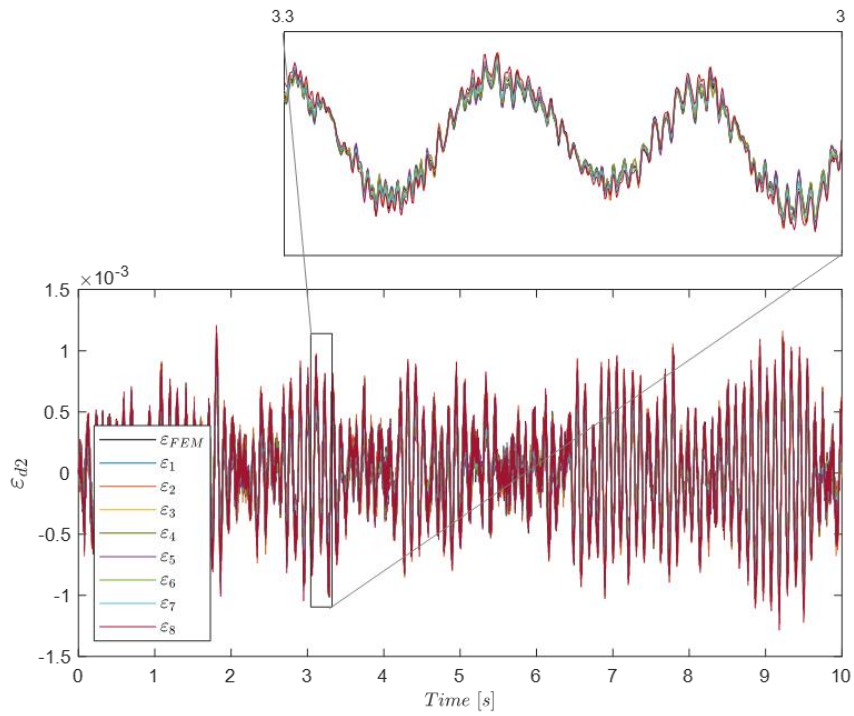

Figure 5.6: Estimated strains with all methods compared with the expected strains for Model A1 at ‘d2’ DOF.

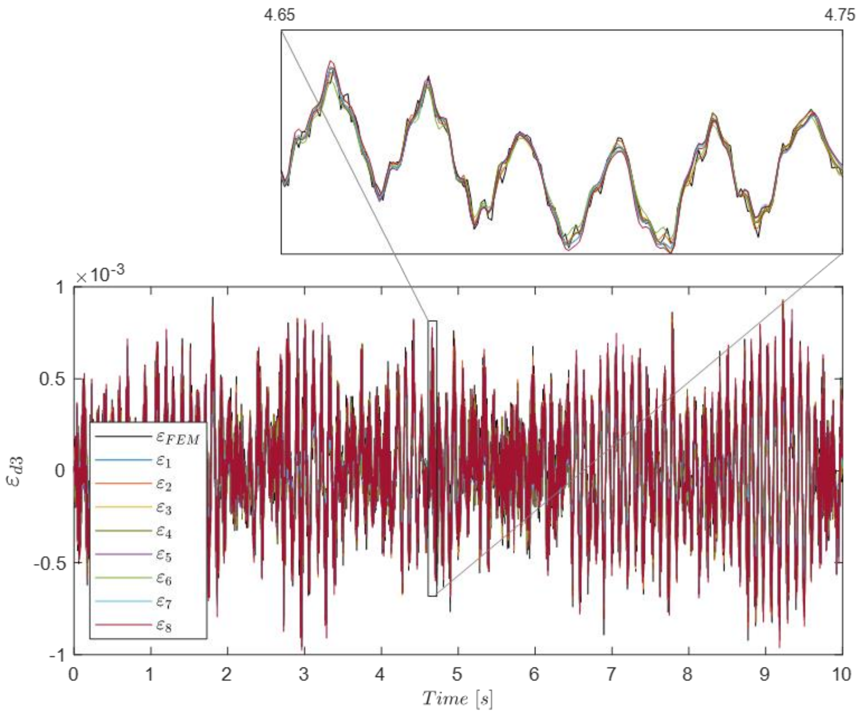

Figure 5.7: Estimated strains with all methods compared with the expected strains for Model A1 at ‘d3’ DOF.

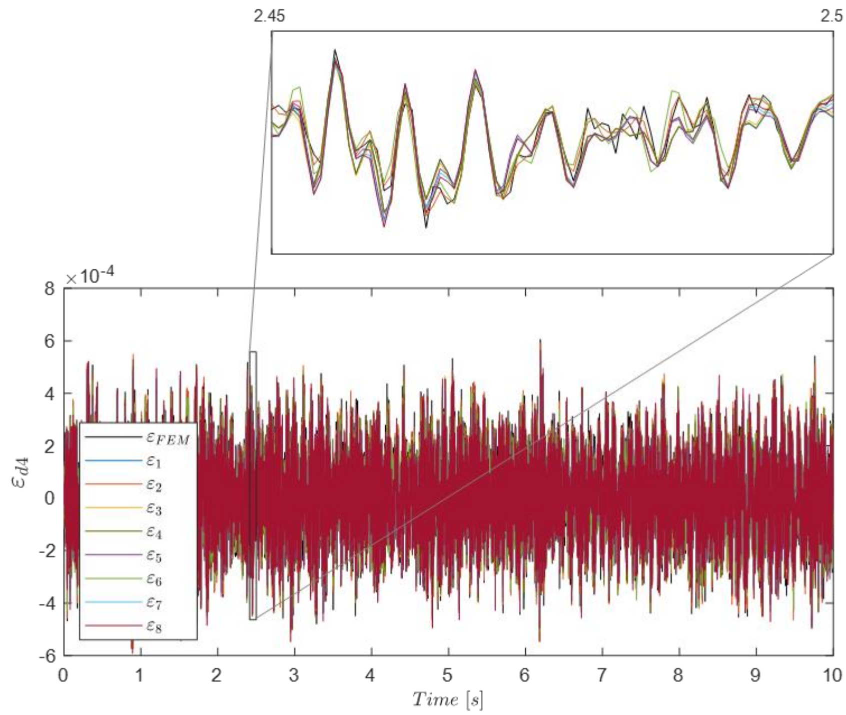

Figure 5.8: Estimated strains with all methods compared with the expected strains for Model A1 at ‘d4’ DOF.

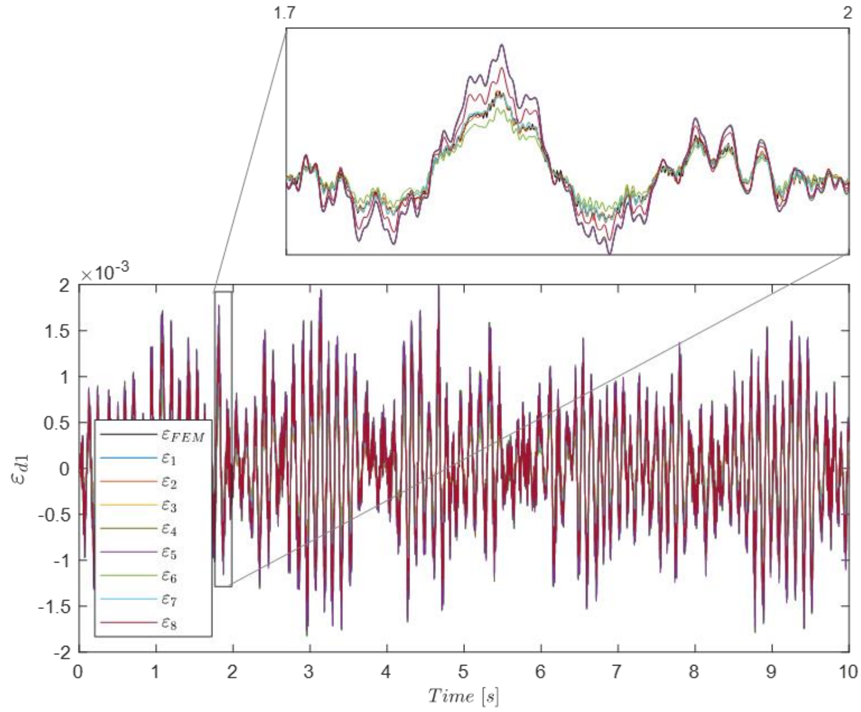

Figure 5.9: Estimated strains with all methods compared with the expected strains for Model A2 at ‘d1’ DOF.

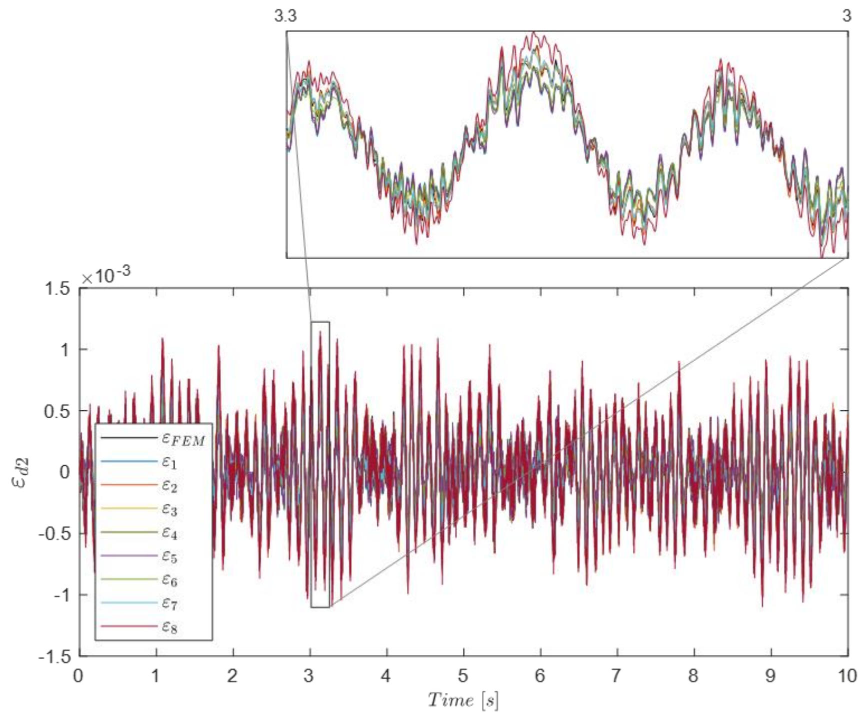

Figure 5.10: Estimated strains with all methods compared with the expected strains for Model A2 at ‘d2’ DOF.

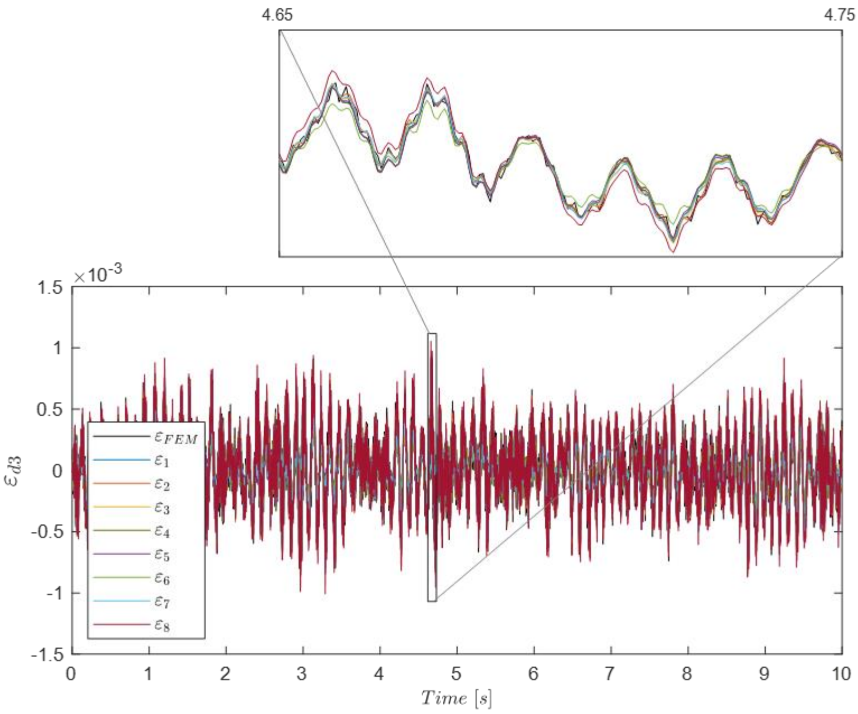

Figure 5.11 Estimated strains with all methods compared with the expected strains for Model A2 at 'd3' DOF.

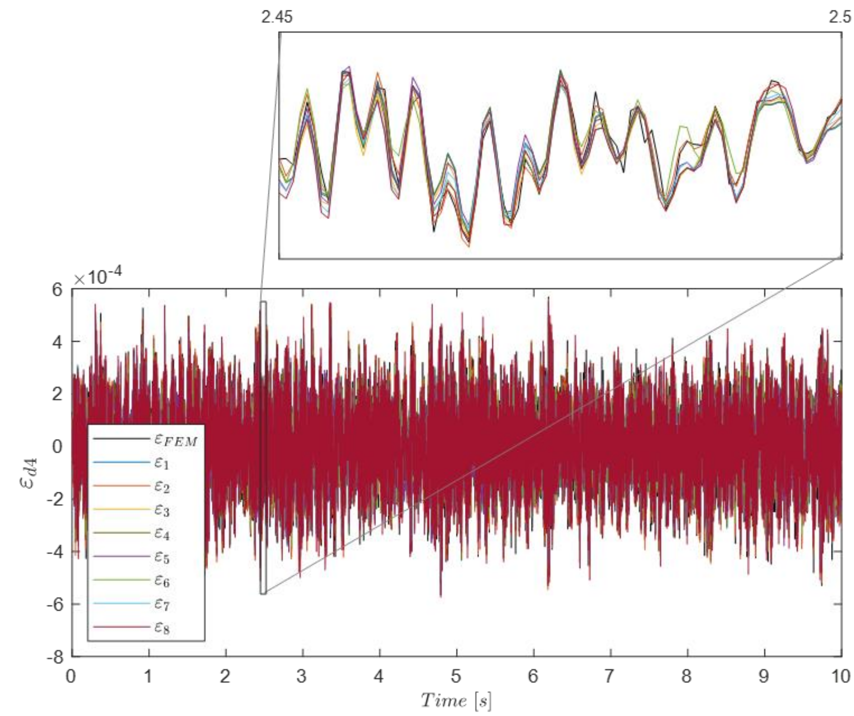

Figure 5.12: Estimated strains with all methods compared with the expected strains for Model A2 at 'd4' DOF.

From the estimated strain time histories (Figure 5.5 to Figure 5.12), it can be inferred that the quality of the estimated strain depends on the selected method, the 'd' point at which the strains are estimated, and the correlation of the system (Model A1 vs Model A2). To analyse the accuracy in depth, the quality of the estimated strains for each method is measured by using three criteria widely applied in the literature, both in time and frequency domains: the Time Response Assurance Criterion (TRAC), the Frequency Response Assurance Criterion (FRAC) and the coefficient of determination (R^2) (see Table 5.6 and Table 5.7). Whereas the strain time histories previously plotted are those estimated with filtered modal coordinates, the quality indicators are calculated for both assumptions: filtered modal coordinates and with no-filtered modal coordinates. Modal coordinates are analysed in the following subsection (*Modal coordinates analysis*).

Table 5.6: Quality measurements of the estimated strains for Model A1.

		Using modal coordinates without filtering					Using filtered modal coordinates		
		TRAC	FRAC	R^2			TRAC	FRAC	R^2
Method 1	d1	0.996	1.000	0.931	*Method 1*	d1	0.992	1.000	0.927
	d2	0.993	1.000	0.986		d2	0.984	1.000	0.976
	d3	0.974	0.999	0.974		d3	0.949	0.998	0.948
	d4	0.976	0.964	0.976		d4	0.848	0.915	0.847
Method 2	d1	0.897	0.999	0.883	*Method 2*	d1	0.996	1.000	0.996
	d2	0.985	1.000	0.985		d2	0.991	1.000	0.991
	d3	0.991	1.000	0.991		d3	0.976	1.000	0.976
	d4	0.987	0.997	0.987		d4	0.949	0.996	0.949
Method 3	d1	0.997	1.000	0.997	*Method 3*	d1	0.993	1.000	0.993
	d2	0.999	1.000	0.999		d2	0.989	1.000	0.989
	d3	0.975	1.000	0.975		d3	0.950	0.999	0.950
	d4	0.983	0.998	0.983		d4	0.855	0.963	0.855
Method 4	d1	0.996	1.000	0.933	*Method 4*	d1	0.992	1.000	0.929
	d2	0.994	1.000	0.989		d2	0.985	1.000	0.979
	d3	0.974	0.999	0.974		d3	0.948	0.997	0.947
	d4	0.977	0.974	0.977		d4	0.850	0.928	0.850
Method 5	d1	0.997	1.000	0.846	*Method 5*	d1	0.990	1.000	0.926
	d2	0.924	0.992	0.867		d2	0.981	1.000	0.974
	d3	0.962	0.988	0.948		d3	0.938	0.997	0.937
	d4	0.933	0.846	0.930		d4	0.843	0.918	0.843
Method 6	d1	0.934	1.000	0.933	*Method 6*	d1	0.997	1.000	0.987
	d2	0.975	1.000	0.969		d2	0.992	1.000	0.982
	d3	0.985	0.999	0.978		d3	0.969	1.000	0.960
	d4	0.985	0.995	0.982		d4	0.899	0.988	0.897
Method 7	d1	0.997	1.000	0.994	*Method 7*	d1	0.991	1.000	0.991
	d2	0.980	0.999	0.950		d2	0.987	1.000	0.987
	d3	0.970	0.997	0.961		d3	0.939	0.998	0.939
	d4	0.971	0.949	0.967		d4	0.850	0.964	0.850
Method 8	d1	0.996	1.000	0.932	*Method 8*	d1	0.989	1.000	0.974
	d2	0.992	1.000	0.985		d2	0.985	1.000	0.974
	d3	0.973	0.999	0.972		d3	0.937	0.998	0.929
	d4	0.977	0.964	0.977		d4	0.850	0.966	0.846

Table 5.7: Quality measurements of the estimated strains for Model A2.

Using modal coordinates without filtering					Using filtered modal coordinates				
		TRAC	FRAC	R^2			TRAC	FRAC	R^2
Method 1	d1	0.986	1.000	0.629	*Method 1*	d1	0.983	1.000	0.629
	d2	0.956	0.994	0.931		d2	0.948	0.994	0.919
	d3	0.965	0.990	0.963		d3	0.932	0.987	0.929
	d4	0.949	0.906	0.949		d4	0.796	0.839	0.796
Method 2	d1	0.872	0.997	0.845	*Method 2*	d1	0.991	1.000	0.991
	d2	0.982	1.000	0.982		d2	0.990	1.000	0.990
	d3	0.990	1.000	0.990		d3	0.970	1.000	0.970
	d4	0.988	0.997	0.987		d4	0.935	0.993	0.934
Method 3	d1	0.992	1.000	0.992	*Method 3*	d1	0.990	1.000	0.990
	d2	0.999	1.000	0.999		d2	0.985	1.000	0.985
	d3	0.972	1.000	0.972		d3	0.939	0.997	0.939
	d4	0.980	0.998	0.980		d4	0.828	0.952	0.828
Method 4	d1	0.986	1.000	0.638	*Method 4*	d1	0.983	1.000	0.637
	d2	0.967	0.996	0.946		d2	0.957	0.996	0.933
	d3	0.964	0.987	0.962		d3	0.930	0.983	0.927
	d4	0.958	0.928	0.958		d4	0.806	0.862	0.806
Method 5	d1	0.989	1.000	0.142	*Method 5*	d1	0.983	1.000	0.630
	d2	0.229	0.014	0.219		d2	0.944	0.994	0.915
	d3	0.892	0.811	0.852		d3	0.924	0.987	0.921
	d4	0.726	0.857	0.720		d4	0.811	0.845	0.811
Method 6	d1	0.941	1.000	0.918	*Method 6*	d1	0.991	1.000	0.950
	d2	0.944	0.999	0.923		d2	0.990	1.000	0.949
	d3	0.973	0.990	0.948		d3	0.965	0.999	0.927
	d4	0.981	0.988	0.969		d4	0.892	0.981	0.876
Method 7	d1	0.989	1.000	0.989	*Method 7*	d1	0.989	1.000	0.989
	d2	0.822	0.929	0.751		d2	0.983	1.000	0.983
	d3	0.951	0.977	0.924		d3	0.931	0.997	0.931
	d4	0.920	0.873	0.912		d4	0.841	0.957	0.841
Method 8	d1	0.986	1.000	0.630	*Method 8*	d1	0.977	0.999	0.895
	d2	0.955	0.994	0.931		d2	0.973	1.000	0.916
	d3	0.963	0.990	0.961		d3	0.922	0.991	0.880
	d4	0.951	0.906	0.951		d4	0.838	0.955	0.823

Based on the information presented in Table 5.6 and Table 5.7, the following comments can be drawn. When a good correlation exists between models A and B, as demonstrated in the case of Model

A1, high accurate results are consistently obtained across all methods, even in the absence of filtering in the modal coordinates. For methods based on modal coordinates derived from projections onto an experimental subspace (*Methods 1* to *4*), no significant differences are observed whether the modal coordinates are filtered or not, except in the case of *Method 2* (based on strain modal coordinates) where filtered modal coordinates results in a slight improvement. In the context of modal coordinates $\widetilde{\boldsymbol{q}}_{\boldsymbol{xm}}$, filtering is essential for *Method 5*. Furthermore, it is noteworthy that in the case of *Method 8*, if modal coordinates are not filtered, the precision achieved is the same as in *Method 1*, thereby validating the equivalence of *Methods 1* and *8*. Moreover, when *Method 8* is applied with filtered modal coordinates, the quality of the results significantly improves (Figure 5.13). In light of the high-quality indicator values achieved with *Method 8* when using filtered modal coordinates, and considering its ease of use, this method shows strong potential as an effective approach for practical applications.

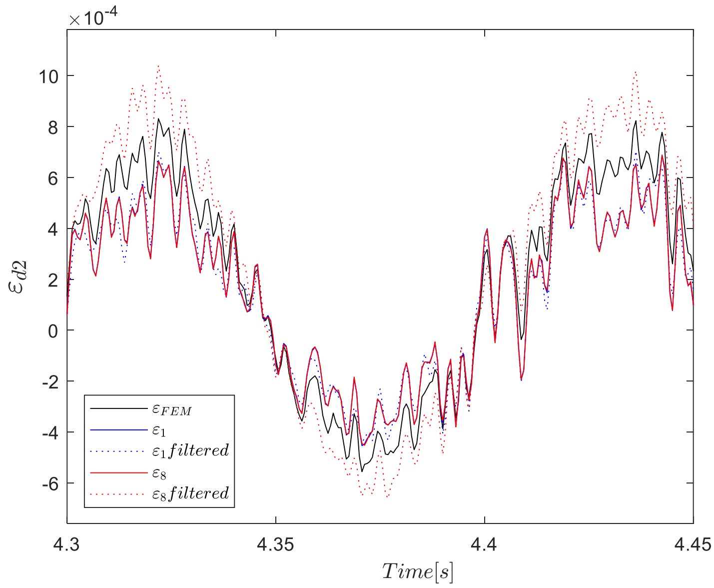

Figure 5.13 Comparison of estimated strains with *Method 1* and *8* for Model A2 at 'd2' DOF.

Modal coordinates analysis

In this section, a comparison of modal coordinates is conducted in order to study the effects of projecting responses into an experimental or a numerical subspace.

Firstly, the exact modal coordinates $\boldsymbol{q}_{\boldsymbol{xm}}$ obtained directly from the FE models A1 or A2 are compared with the modal coordinates $\widehat{\boldsymbol{q}}_{\boldsymbol{xm}}$ and $\widetilde{\boldsymbol{q}}_{\boldsymbol{xm}}$. In Figure 5.14 (a), the modal coordinates ($\boldsymbol{q}_{\boldsymbol{xm}}$, $\widehat{\boldsymbol{q}}_{\boldsymbol{xm}}$, and $\widetilde{\boldsymbol{q}}_{\boldsymbol{xm}}$) of Model A1 are compared. It can be observed that the modal coordinates $\widetilde{\boldsymbol{q}}_{\boldsymbol{xm}}$ present some peaks at low frequencies, due to errors in the mode shapes. A possible solution to this problem is to filter the modal coordinates with a band-pass filter. Figure 5.14 (b) shows the estimated modal coordinates ($\widehat{\boldsymbol{q}}_{\boldsymbol{xm}}$ and $\widetilde{\boldsymbol{q}}_{\boldsymbol{xm}}$) band-pass filtered. The same is show in Figure 5.15 for Model A2.

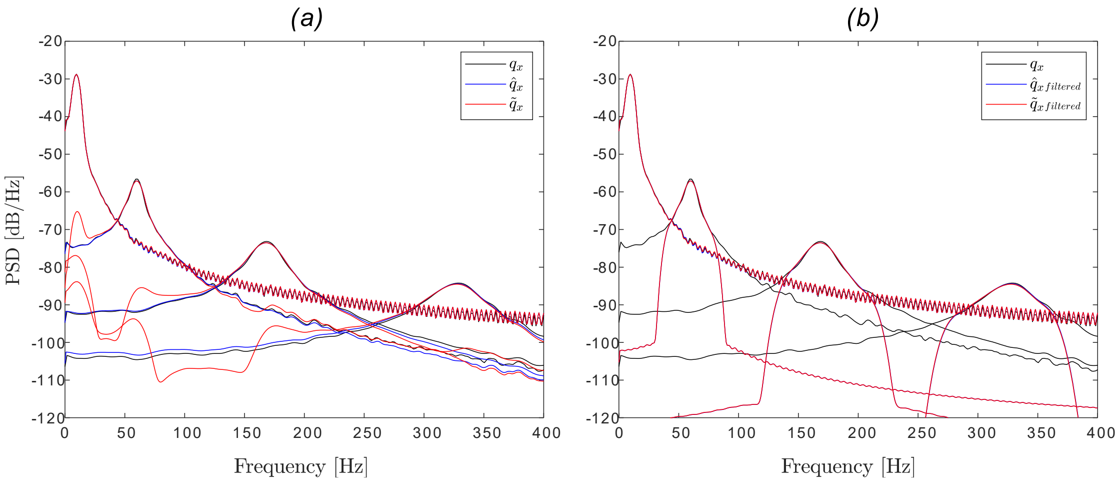

Figure 5.14: Comparison of modal coordinates: $\boldsymbol{q}_{\boldsymbol{xm}}$, $\widehat{\boldsymbol{q}}_{\boldsymbol{xm}}$ and $\widetilde{\boldsymbol{q}}_{\boldsymbol{xm}}$ of Model A1: (a) without filtering and (b) filtered.

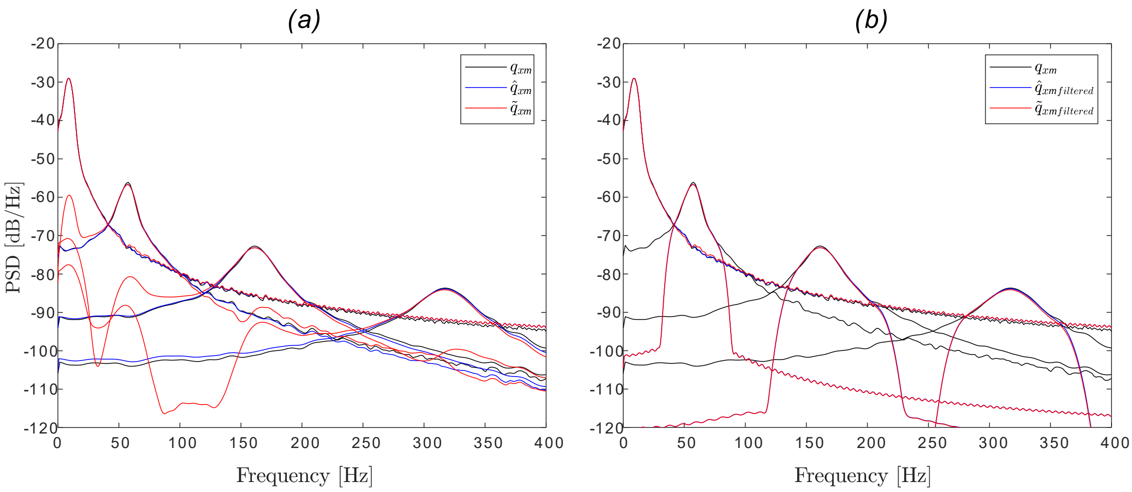

Figure 5.15: Comparison of modal coordinates: $\boldsymbol{q}_{\boldsymbol{xm}}$, $\widehat{\boldsymbol{q}}_{\boldsymbol{xm}}$ and $\widetilde{\boldsymbol{q}}_{\boldsymbol{xm}}$ of Model A2: (a) without filtering and (b) filtered.

Similarly, strain modal coordinates $\widehat{\boldsymbol{q}}_{\boldsymbol{x\varepsilon m}}$ and $\widetilde{\boldsymbol{q}}_{\boldsymbol{x\varepsilon m}}$ are study and compared with the exact modal coordinates ($\boldsymbol{q}_{\boldsymbol{xm}} = \boldsymbol{q}_{\boldsymbol{\varepsilon xm}}$). Figure 5.16 shows strain modal coordinates of Model A1 and Figure 5.17 of Model A2. As can be observed in Figure 5.16 (a) and Figure 5.17 (a), non-filtered modal coordinates present significant errors (and some peaks) at high frequencies. Low-pass filtered modal coordinates $\widehat{\boldsymbol{q}}_{\boldsymbol{x\varepsilon m}}$ and $\widetilde{\boldsymbol{q}}_{\boldsymbol{x\varepsilon m}}$ are plotted in Figure 5.16 (b) and Figure 5.17 (b).

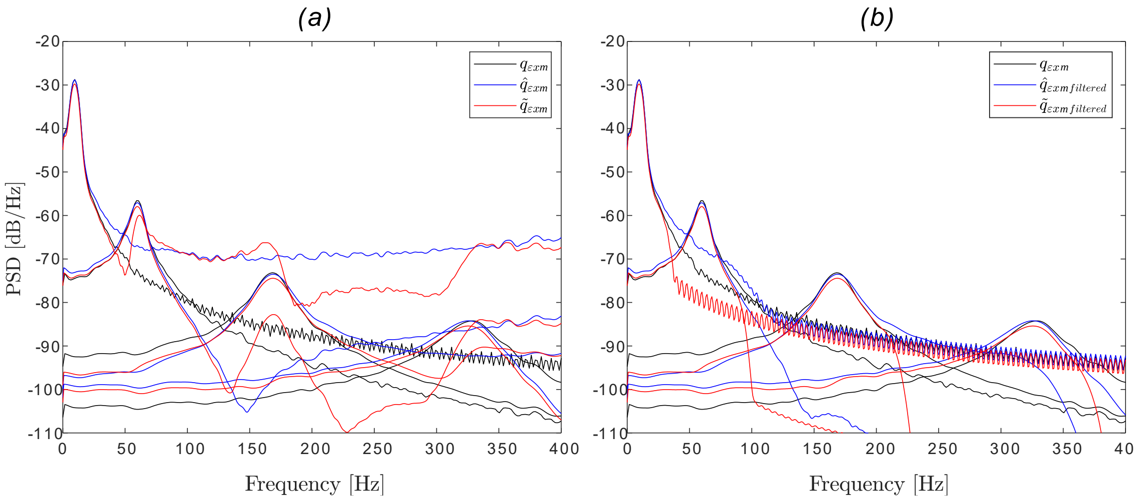

Figure 5.16: Comparison of modal coordinates: $\boldsymbol{q}_{xm}$, $\widehat{\boldsymbol{q}}_{x\varepsilon m}$ and $\widetilde{\boldsymbol{q}}_{x\varepsilon m}$ of Model A1: (a) without filtering and (b) filtered.

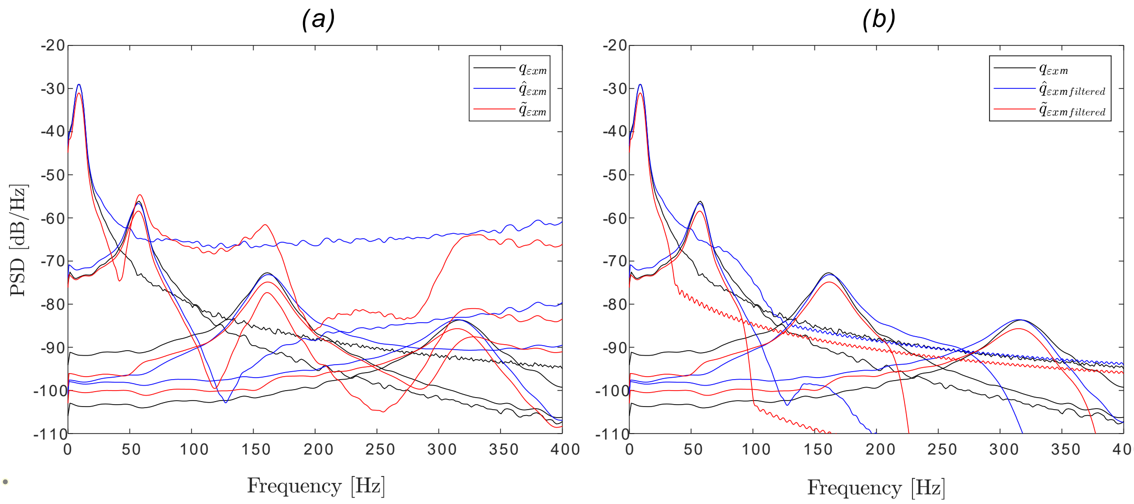

Figure 5.17: Comparison of modal coordinates: $\boldsymbol{q}_{xm}$, $\widehat{\boldsymbol{q}}_{x\varepsilon m}$ and $\widetilde{\boldsymbol{q}}_{x\varepsilon m}$ of Model A2: (a) without filtering and (b) filtered.

As shown in section 4.4.1, the effects of truncation and error in the mode shapes in the $\widehat{\boldsymbol{q}}_{xm}$ modal coordinates (in blue in Figure 5.14 and Figure 5.15) are expressed by means of:

$$\widehat{\boldsymbol{q}}_{xm} = \boldsymbol{q}_{xm} + \widehat{\boldsymbol{\phi}}^{+}_{xam}\,\Delta\boldsymbol{\phi}_{x}\boldsymbol{q}_{xm} + \widehat{\boldsymbol{\phi}}^{+}_{xam}\boldsymbol{\phi}_{xar}\boldsymbol{q}_{xr} \tag{5.1}$$

where the product $\widehat{\boldsymbol{\phi}}^{+}_{xam}\,\Delta\boldsymbol{\phi}_{x}\boldsymbol{q}_{xm}$ gives the contribution of the errors in the estimation of the mode shapes. In this section, since numerical models are used, no errors are considered in the mode shapes. Therefore, Eq. (5.1) can be expressed as:

$$\hat{\boldsymbol{q}}_{xm} = \boldsymbol{q}_{xm} + \boldsymbol{\phi}_{xam}^{+}\boldsymbol{\phi}_{xar}\ \boldsymbol{q}_{xr} \tag{5.2}$$

where the product $\boldsymbol{\phi}_{xam}^{+}\boldsymbol{\phi}_{xar}$ gives the contribution of truncated modes. Considering four measured modes (1 to 4) and four unmeasured 'r' modes (5 to 8) are considered, the results shown in Table 5.8 are obtained for models A1 and A2. For example, the term -0.174 (shaded) gives the contribution of mode 5 to the first modal coordinate $\hat{\boldsymbol{q}}_{xm1}$

The effect of modal truncation in the strain modal coordinates $\hat{\boldsymbol{q}}_{\varepsilon xm}$, is given by the product $\boldsymbol{\phi}_{x\varepsilon am}^{+}\boldsymbol{\phi}_{x\varepsilon ar}$ (Table 5.8). In this case, the term -8.419 (shaded) gives the contribution of mode 5 to the first modal coordinate $\hat{\boldsymbol{q}}_{\varepsilon xm1}$. This demonstrates that the effect of the truncated modes in the strain modal coordinates is significantly higher than that corresponding to the modal coordinates, and explain the differences between Figure 5.14 and Figure 5.16.

Table 5.8: Effects of truncation in the modal coordinates $\hat{\boldsymbol{q}}_{xm}$ and $\hat{\boldsymbol{q}}_{\varepsilon xm}$.

	Model A1				*Model A2*			
$\boldsymbol{\phi}_{xam}^{+}\boldsymbol{\phi}_{xar}$	-0.174	-0.175	-0.196	-0.162	-0.172	0.175	-0.194	0.171
	0.178	0.192	0.197	0.202	-0.177	0.193	-0.196	0.208
	0.204	0.180	0.257	0.157	-0.202	0.184	-0.248	0.179
	-0.181	-0.250	-0.188	-0.462	0.185	-0.242	0.203	-0.408
$\boldsymbol{\phi}_{x\varepsilon am}^{+}\boldsymbol{\phi}_{x\varepsilon ar}$	-8.419	12.789	-20.378	23.606	-6.688	-11.144	-19.087	-26.040
	-1.264	2.013	-2.910	4.046	0.898	1.564	2.367	3.826
	0.481	-0.610	1.278	-0.864	-0.329	-0.414	-0.984	-0.658
	0.199	-0.441	0.355	-1.757	-0.118	-0.316	-0.181	-1.401

In the case of modal coordinates $\tilde{\boldsymbol{q}}_{xm}$ (in red), the effects of errors and modal truncation can be expressed as:

$$\tilde{\boldsymbol{q}}_{xm} = \boldsymbol{q}_{xm} + \boldsymbol{\phi}_{FEam}^{+}\,\Delta\boldsymbol{\phi}_{xFE}\ \boldsymbol{q}_{xm} + \boldsymbol{\phi}_{FEam}^{+}\ \boldsymbol{\phi}_{xar}\ \boldsymbol{q}_{xr} \tag{5.3}$$

where, as in the previous case, the product $\boldsymbol{\phi}_{FEam}^{+}\ \boldsymbol{\phi}_{xar}\ \boldsymbol{q}_{xr}$ gives the contribution of the modal truncation. Therefore, the product $\boldsymbol{\phi}_{FEam}^{+}\ \boldsymbol{\phi}_{xar}$ quantifies the effect of modal truncation in $\tilde{\boldsymbol{q}}_{xm}$, and the product $\boldsymbol{\phi}_{FE\varepsilon am}^{+}\ \boldsymbol{\phi}_{x\varepsilon ar}$ the effects in $\tilde{\boldsymbol{q}}_{\varepsilon xm}$ (Table 5.9). Again, higher values have been obtained for $\boldsymbol{\phi}_{FE\varepsilon am}^{+}\ \boldsymbol{\phi}_{x\varepsilon ar}$.

Table 5.9: Effects of truncation in the modal coordinates $\tilde{\boldsymbol{q}}_{xm}$ and $\tilde{\boldsymbol{q}}_{x\varepsilon m}$.

	Model A1				Model A2			
$\boldsymbol{\phi}_{FEam}^{+}\,\boldsymbol{\phi}_{xar}$	-0.162	-0.179	-0.194	-0.156	-0.154	0.181	-0.192	0.161
	-0.177	-0.189	-0.198	-0.194	-0.174	0.189	-0.198	0.197
	0.166	0.197	0.247	0.151	0.140	-0.208	0.239	-0.161
	-0.245	-0.223	-0.199	-0.489	-0.291	0.203	-0.210	0.460
$\boldsymbol{\phi}_{FE\varepsilon am}^{+}\,\boldsymbol{\phi}_{x\varepsilon ar}$	-6.299	8.688	-14.146	12.491	-4.021	-5.180	-9.474	-7.505
	1.039	-1.538	2.201	-2.624	0.666	0.950	1.410	1.697
	0.412	-0.480	1.109	-0.457	0.258	0.258	0.789	0.104
	0.118	-0.379	0.299	-1.714	-0.004	0.239	0.130	1.390

Moreover, the product $\boldsymbol{\phi}_{FEam}^{+}\,\Delta\boldsymbol{\phi}_{xFE}$ gives the contribution of the discrepancies between the numerical and the estimated experimental mode shapes in modal coordinates $\tilde{\boldsymbol{q}}_{xm}$ (Table 5.10). Similarly, the product $\boldsymbol{\phi}_{FE\varepsilon am}^{+}\,\Delta\boldsymbol{\phi}_{\varepsilon xFE}$ gives the contribution of the discrepancies between the numerical and the estimated experimental mode shapes in modal coordinates $\tilde{\boldsymbol{q}}_{\varepsilon xm}$. It can be observed in Table 5.10 (shaded), that the contribution of errors in strain mode shapes two, three and four, to the first strain modal coordinate $\tilde{\boldsymbol{q}}_{\varepsilon xm}$ is negligible.

Table 5.10: Effects of errors in mode shapes on the modal coordinates $\tilde{\boldsymbol{q}}_{xm}$ and $\tilde{\boldsymbol{q}}_{\varepsilon xm}$.

	Model A1				Model A2			
$\boldsymbol{\phi}_{FEam}^{+}\,\Delta\boldsymbol{\phi}_{xFE}$	0.000	0.016	0.002	-0.006	0.000	0.033	0.005	-0.009
	-0.016	-0.002	-0.042	-0.025	-0.034	-0.006	-0.080	-0.042
	-0.006	0.039	0.001	-0.05	-0.012	0.072	-0.003	-0.093
	-0.003	0.016	0.054	-0.013	-0.006	0.031	0.094	-0.029
$\boldsymbol{\phi}_{FE\varepsilon am}^{+}\,\Delta\boldsymbol{\phi}_{\varepsilon xFE}$	-0.106	0.619	1.498	2.287	-0.215	1.153	2.600	3.772
	0.000	-0.097	-0.276	-0.379	0.000	-0.182	-0.487	-0.629
	0.000	0.003	-0.087	-0.189	0.000	0.006	-0.157	-0.322
	0.000	0.000	0.014	-0.071	0.000	0.000	0.024	-0.126

5.1.2 Second simulation case. Bending and torsional modes.

The same models B, A1 and A2 are also considered in this section. In this case, models A1 and A2 were excited with two loads (F_X and F_Z) as shown in Figure 5.18 in the x and z directions, so that both torsional modes and bending modes were excited. The loads were generated from a spectral density of constant magnitude in the frequency range 0-1600 Hz. The purpose of this application case is to validate the methodology when modes in different directions are excited.

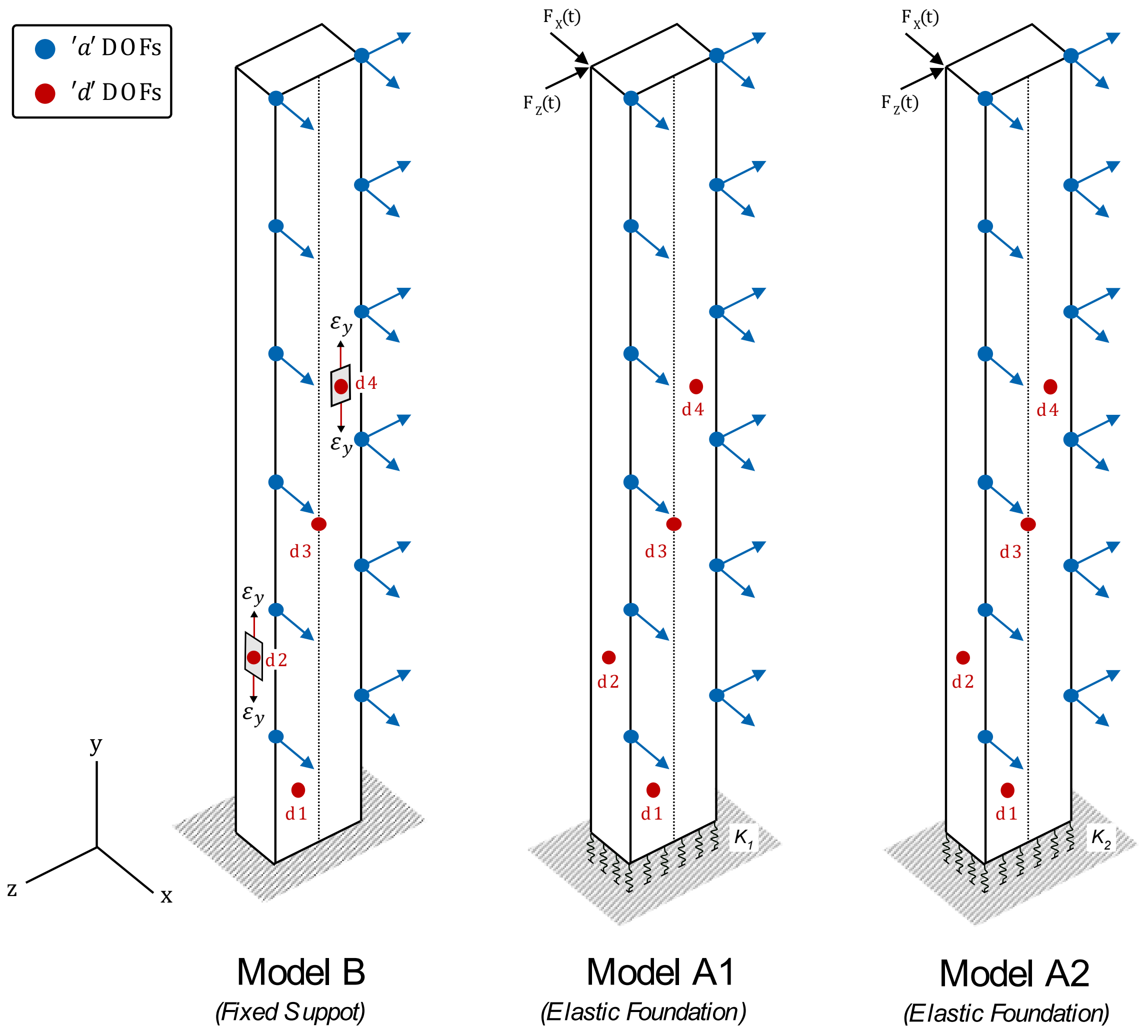

Figure 5.18: Models B, A1 and A2 of the cantilever beam and DOFs when considering modes in several directions.

It was assumed that the displacement response of the structure was measured with 18 DOFs (active DOFs), indicated with blue arrows in Figure 5.18, and in the frequency range 0-800 Hz.

The natural frequencies extracted with a frequency analysis are presented in Table 5.11. In this case, 4 bending modes in the x direction, 4 bending modes in the z direction and one torsional mode were considered (all the modes in the frequency range 0-400 Hz). The maximum error in natural frequencies is 5.43% between models B and A1, and 12.39% between models B and A2 (Table 5.11).

Table 5.11: Natural frequencies [Hz] and errors [%].

Mode shape	f_B $[Hz]$	f_{A1} $[Hz]$	Error B-A1 [%]	f_{A2} $[Hz]$	Error B-A2 [%]
Mode Bx	10.07	9.55	5.43	8.96	12.39
Mode By	20.10	19.07	5.41	17.89	12.36
Mode Bx	62.94	59.98	4.94	57.16	10.11
Mode By	124.74	118.98	4.84	113.50	9.91
Mode Bx	175.61	167.98	4.54	161.78	8.55
Mode T	322.09	320.65	0.45	320.27	0.57
Mode Bx	342.33	328.68	4.15	319.06	7.29
Mode By	344.08	329.83	4.32	318.17	8.14

Regarding the correlation between mode shapes, the MAC values are shown in Figure 5.19. Between Model B and Model A1 all mode shapes have a MAC value higher than 0.99, and between Model B and A2 all the MAC values are higher than 0.98.

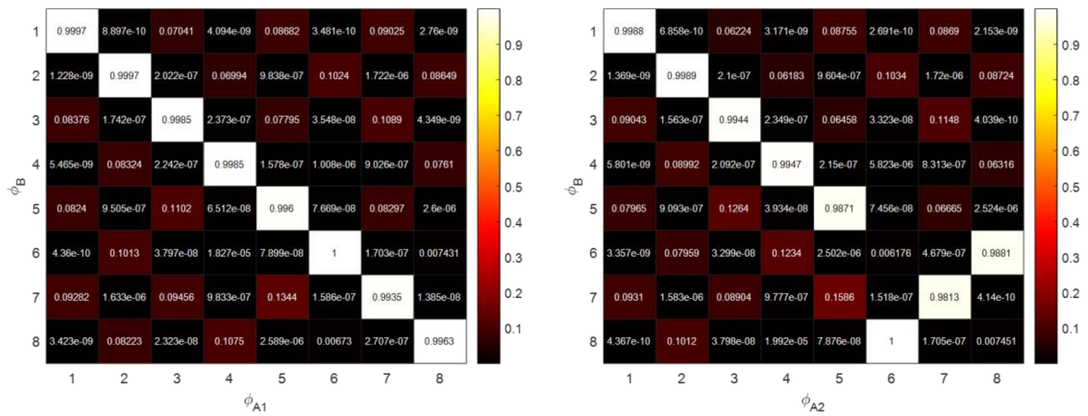

Figure 5.19: MAC between mode shapes of models B and A1 and models B and A2.

Moreover, the ***T-Mass*** and ***T-Stiffness*** indicators are shown in Figure 5.20, where values close to 90° are observed in the ***T-Mass*** for both models, indicating an almost perfect mass correlation. Regarding the ***T-Stiffness***, significantly low angles are obtained, detecting stiffness discrepancies as expected. The ***T-Mass*** and ***T-Stiffness*** matrices are included in Appendix A in Table A 3 and Table A 4 for Model A1 and in Table A 5 and Table A 6 for Model A2.

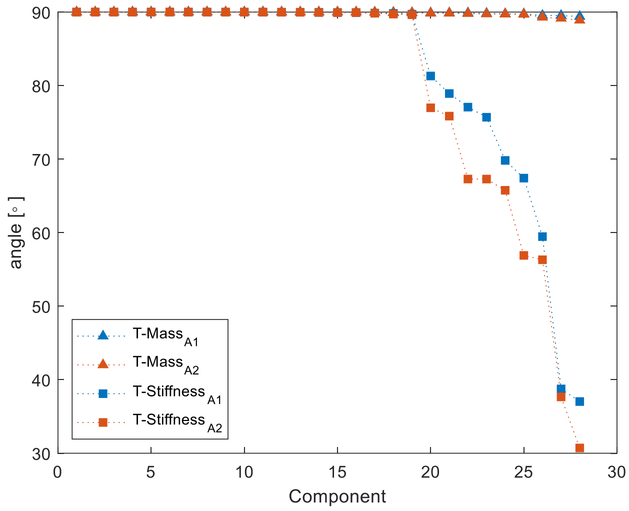

Figure 5.20: ***T-Mass*** and ***T-Stiffness*** of models A1 and A2.

In this example, strains are estimated with *Methods 1, 5* and *8*. These methods do not require strain measurements, i.e. they are easier to be applied when modes in different directions are involved. As previously mentioned, all the proposed methodologies allow to estimate whichever component of the strain or stress matrix, in this case the component $\boldsymbol{\varepsilon_y}$. An illustration of the strain measurements direction is show in Figure 5.18 (illustrated in Model B at d2 and d4). Strains are estimated for the four 'd' DOFs (Figure 5.21 and Figure 5.22).

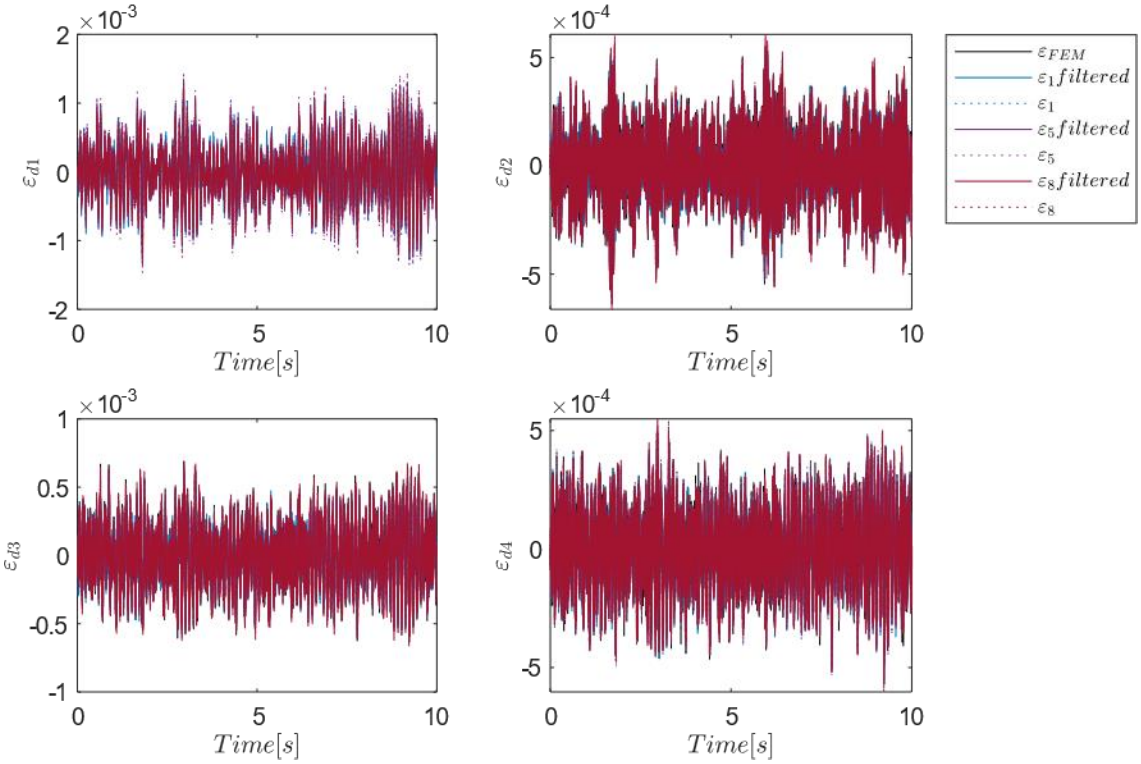

Figure 5.21: Estimated strains at locations ‘d1’, ‘d2’, ‘d3’ and ‘d4’.

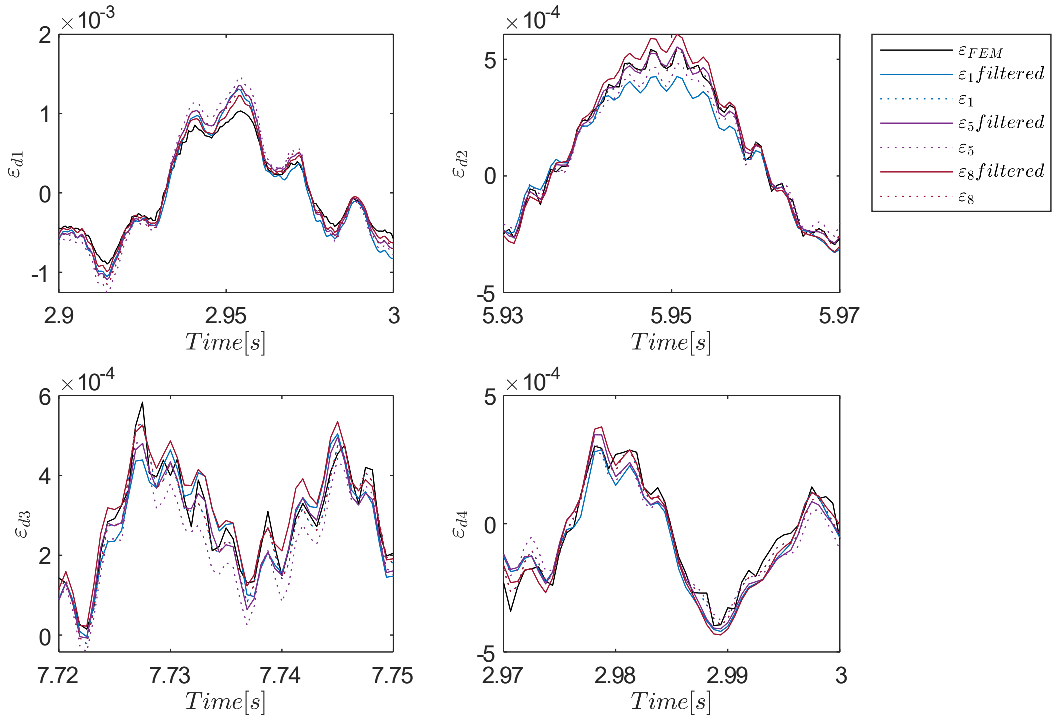

Figure 5.22: Estimated strains zoom in the time scale at locations ‘d1’, ‘d2’, ‘d3’ and ‘d4’.

Again, the quality indicators used in the previous section are calculated in Table 5.12 for Model A1 and in Table 5.13 for Model A2.

Table 5.12: Quality measurements of the estimated strains for Model A1.

Using modal coordinates without filtering					Using filtered modal coordinates				
		TRAC	FRAC	R^2			TRAC	FRAC	R^2
Method 1	d1	0.996	1.000	0.931	*Method 1*	d1	0.949	0.998	0.885
	d2	0.984	1.000	0.984		d2	0.908	0.997	0.908
	d3	0.977	0.999	0.976		d3	0.876	0.982	0.875
	d4	0.946	0.964	0.941		d4	0.842	0.953	0.838
Method 5	d1	0.997	1.000	0.848	*Method 5*	d1	0.994	1.000	0.931
	d2	0.979	1.000	0.968		d2	0.974	1.000	0.974
	d3	0.957	0.987	0.943		d3	0.952	0.996	0.952
	d4	0.911	0.886	0.900		d4	0.902	0.958	0.898
Method 8	d1	0.996	1.000	0.932	*Method 8*	d1	0.993	1.000	0.978
	d2	0.983	1.000	0.983		d2	0.971	1.000	0.961
	d3	0.976	0.999	0.975		d3	0.955	0.997	0.947
	d4	0.950	0.964	0.945		d4	0.912	0.991	0.906

Table 5.13: Quality measurements of the estimated strains for Model A2.

Using modal coordinates without filtering					Using filtered modal coordinates				
		TRAC	FRAC	R^2			TRAC	FRAC	R^2
Method 1	d1	0.984	1.000	0.631	*Method 1*	d1	0.933	0.997	0.599
	d2	0.984	1.000	0.984		d2	0.905	0.997	0.905
	d3	0.963	0.988	0.961		d3	0.846	0.955	0.843
	d4	0.900	0.847	0.872		d4	0.785	0.835	0.760
Method 5	d1	0.990	0.999	0.195	*Mehod 5*	d1	0.988	0.999	0.644
	d2	0.765	1.000	0.727		d2	0.779	1.000	0.770
	d3	0.879	0.817	0.831		d3	0.915	0.982	0.910
	d4	0.750	0.654	0.614		d4	0.851	0.838	0.824
Method 8	d1	0.984	1.000	0.632	*Method 8*	d1	0.978	0.999	0.895
	d2	0.982	1.000	0.982		d2	0.959	1.000	0.904
	d3	0.961	0.988	0.959		d3	0.940	0.990	0.900
	d4	0.905	0.847	0.879		d4	0.892	0.978	0.863

It can be observed that in *Method 5*, filtering of modal coordinates significantly improves the quality of the results. *Methods 1* and *8*, when using unfiltered modal coordinates, show similar error levels. However, *Method 8* improves significantly when using filtered modal coordinates, whereas no significant changes are observed with *Method 1*.

The quality indicators showed in Table 5.13 present values very close to those obtained in the previous section 5.1.1, where only bending modes where considered. Therefore, if a structure with modes in different directions is to be considered, the proposed methods can also be applied to estimate strains and stresses.

5.2 Experimental case: a monolithic glass beam

In this section an experimental case is presented. Strains are estimated on a simply supported monolithic glass beam using some of the methods proposed in Chapter 4, and validated with the experimental strains measured with strain gauges.

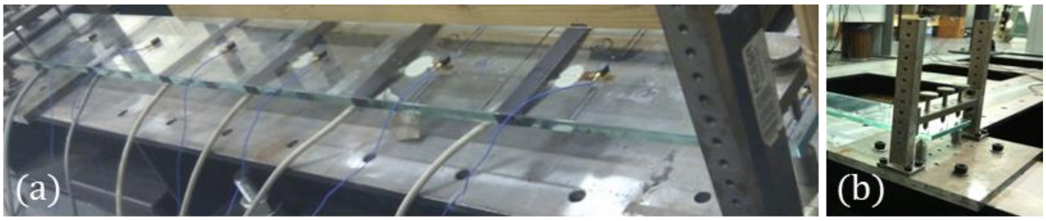

Figure 5.23: Monolithic glass beam: (a) Experimental setup, and (b) detail of the support.

The glass beam had rectangular section of 100 x 10 mm^2 and a length of 1 m (Figure 5.23). In order to estimate the experimental modal parameters, the structural response was measured with seven accelerometers uniformly distributed (Figure 5.24), with sensitivity of 100 mV/g, and seven unidirectional strain gauges (350 Ω) were attached to the beam The measurements were recorded for approximately 5 minutes using a sampling frequency of 2132 Hz. The experimental modal parameters (Model A) were estimated through operational modal analysis (OMA) using the FDD technique in the Artemis Modal software. The modal identification was performed using both the acceleration response and the strain response. The experimental natural frequencies are shown in Table 5.14.

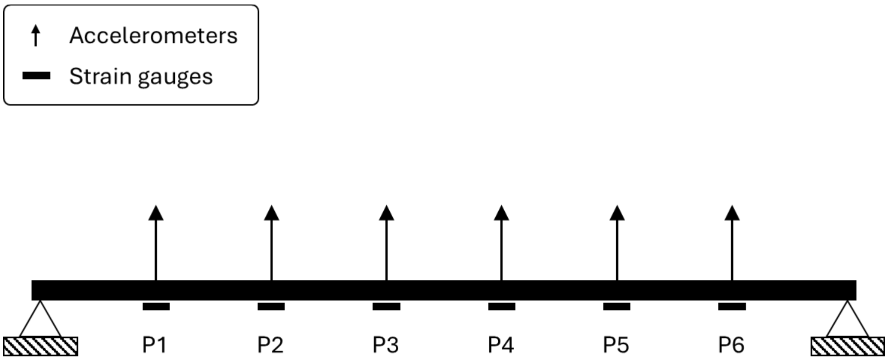

Figure 5.24: Experimental setup. Locations of accelerometers and strain gauges.

Table 5.14: Natural frequencies of the experimental and numerical models.

Mode	f_{Exp} $[Hz]$	f_{FEM} $[Hz]$	Error [%]
Mode 1	25.8	25.3	1.80
Mode 2	99.4	101.3	1.90
Mode 3	222.1	227.7	2.50
Mode 4	399.3	404.3	1.20
Mode 5	618.6	630.7	2.00

A finite element model (*Model B*) of the structure was assembled in Abaqus and meshed with 1D quadratic beam elements 20 mm long. Regarding the material properties of the glass, a mass-density of 2500 kg/m^3 and a Young's modulus of 72 GPa were considered. The numerical natural frequencies are shown in in Table 5.14, the numerical and experimental mode shapes in Figure 5.26 and the numerical and experimental strain mode shapes in Figure 5.26. Figure 5.26 (a) shows the first three experimental and numerical mode, whereas modes four and five are show in Figure 5.26 (b). Similarly, Figure 5.26. (a) shows the first three experimental and numerical strain mode shapes, whereas modes four and five are show in Figure 5.26. (b).

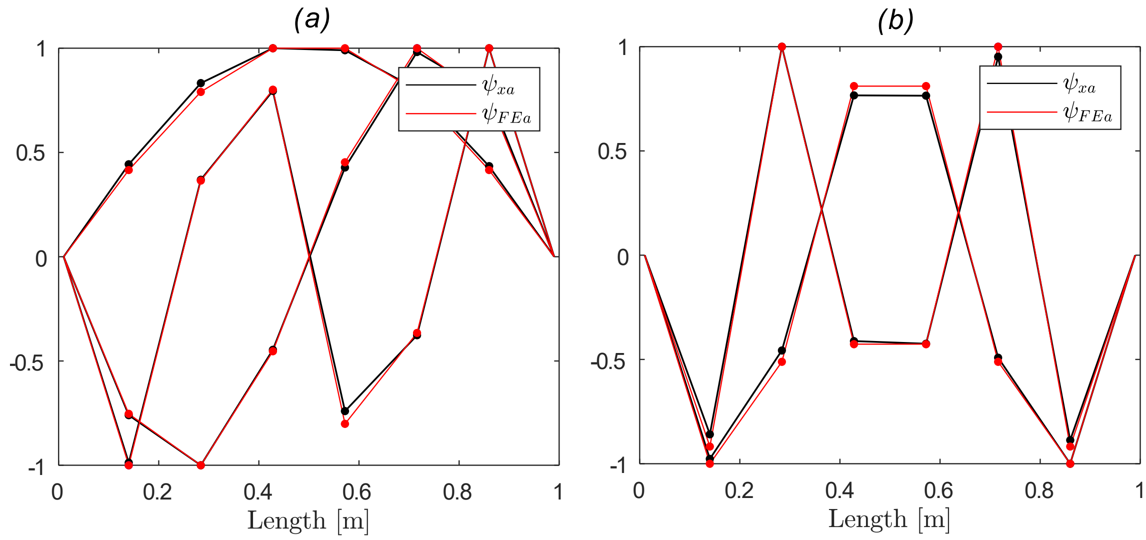

Figure 5.25 Experimental and numerical mode shapes: (a) modes one to three, and (b) modes four and five.

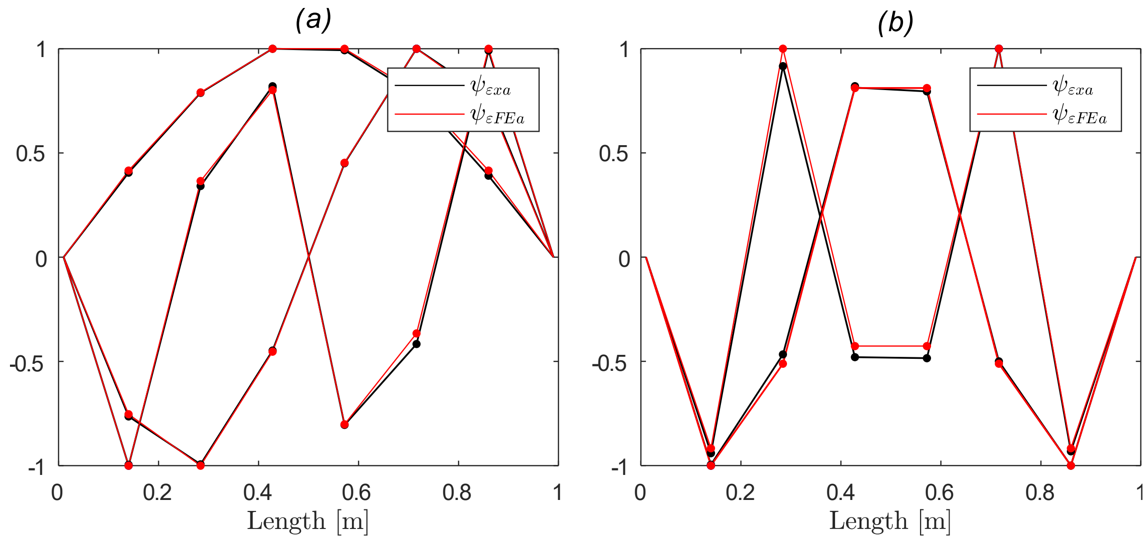

Figure 5.26: Experimental and numerical strain mode shapes: (a) modes one to three, and (b) modes four and five.

A good correlation between the numerical and experimental models is obtained, as it can be observed in Table 5.14, where the errors in the natural frequencies are less than a 2.5%. Moreover, a good MAC is obtained for both the mode shapes and the strain mode shapes, with all diagonal values above 0.99 (Figure 5.27). Regarding the ***T-Mass*** and ***T-Stiffness*** (Table 5.15), a very good correlation in term of mass is obtained, whereas stiffness discrepancies are detected.

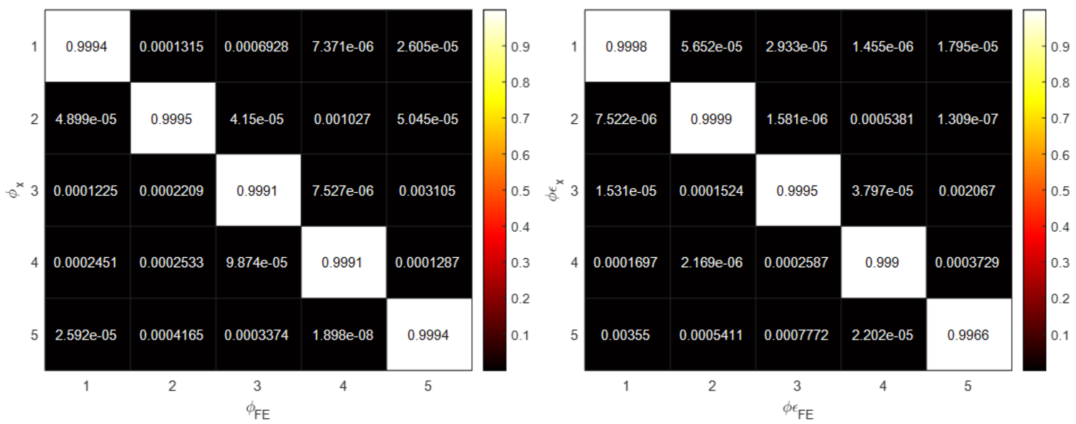

Figure 5.27: Modal assurance criteria of mode shapes and strain mode shapes.

Table 5.15: ***T-Mass*** and ***T-Stiffness*** indicators

T-Mass					***T-Stiffness***				
---	88.94	88.43	88.95	89.47	---	89.38	88.83	89.85	89.74
88.94	---	88.78	88.87	88.41	86.99	---	89.40	88.96	89.58
88.43	88.78	---	89.57	89.31	61.71	87.14	---	89.99	88.70
88.95	88.87	89.57	---	89.35	78.81	74.39	89.98	---	89.35
89.47	88.41	89.31	89.35	---	36.46	74.70	80.11	88.43	---

In this section, the strains at the locations of sensors (P1 to P6 in Figure 5.24) are estimated projecting the experimental responses onto the experimental subspace, i.e. using methods 1 to 4. Due to the fact that the experimental mode shapes and strain mode shapes are obtained through OMA, they are unscaled (not mass-normalized). The unscaled mode shapes and strain mode shapes are denoted as $\boldsymbol{\psi}_{\boldsymbol{xam}}$ and $\boldsymbol{\psi}_{\boldsymbol{\varepsilon xam}}$, respectively. When using unscaled experimental mode shapes, *Method 3* leads to expressions equal to those developed for *Method 1*. On the other hand, *Method 4* cannot be applied when only unscaled mode shapes are available. Therefore, the strains in the glass beam at locations P1 to P6 (Figure 5.24) are estimated with *Methods 1* and *2*. Mass-normalized numerical mode shapes $\boldsymbol{\phi}_{\boldsymbol{FEam}}$ and numerical strain mode shapes $\boldsymbol{\phi}_{\boldsymbol{FE\varepsilon am}}$ are used in the strain estimation process.

To record the structural response, it was excited randomly with a plastic-headed hammer for 5 minutes, using the same sensors as those used in the OMA (Figure 5.24). Firstly, both acceleration and strain signals are filtered using a high-pass filter with a cut-off frequency of 15 Hz. Moreover, accelerations are integrated in the frequency domain to obtain displacements. Unscaled modal coordinates $\widehat{\boldsymbol{q}}_{\boldsymbol{\psi xm}}$ and $\widehat{\boldsymbol{q}}_{\boldsymbol{\psi \varepsilon xm}}$ are estimated with the following expressions:

$$\widehat{\boldsymbol{q}}_{\boldsymbol{\psi xm}} = \boldsymbol{\psi}_{\boldsymbol{xam}}^{+} \, \boldsymbol{u}_{\boldsymbol{xa}} \tag{5.4}$$

and:

$$\widehat{\boldsymbol{q}}_{\boldsymbol{\psi \varepsilon xm}} = \boldsymbol{\psi}_{\boldsymbol{x\varepsilon am}}^{+} \, \boldsymbol{\varepsilon}_{\boldsymbol{xa}} \tag{5.5}$$

The estimated modal coordinates $\widehat{\boldsymbol{q}}_{\boldsymbol{\psi xm}}$ and $\widehat{\boldsymbol{q}}_{\boldsymbol{\psi \varepsilon xm}}$ are shown in Figure 5.28. In order to minimize inaccuracies, the modal coordinates $\widehat{\boldsymbol{q}}_{\boldsymbol{\psi xm}}$ are filtered with band-pass filters (Figure 5.28 (b)) in order to minimize errors in the mode shape estimation, truncation and response noise. The effect of this filtering in the estimation of strain time histories is very small, as it has been proven in section 5.1.

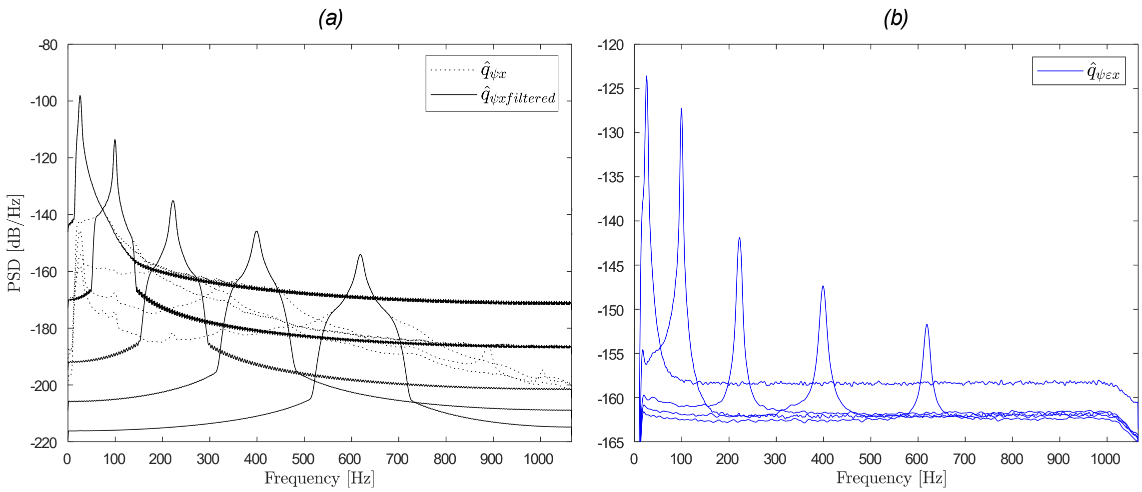

Figure 5.28: Spectral density of modal coordinates: (a) displacement modal coordinates $\widehat{\boldsymbol{q}}_{\boldsymbol{\psi xm}}$ and (b) strain modal coordinates $\widehat{\boldsymbol{q}}_{\boldsymbol{\psi \varepsilon xm}}$.

Since the experimental mode shapes and strain mode shapes are unscaled, the following equations are used to estimate the transformation matrices $\breve{\boldsymbol{T}}_{\boldsymbol{Umm}}$.

$$\breve{\boldsymbol{T}}_{\boldsymbol{Umm}} = \boldsymbol{\phi}_{\boldsymbol{FEam}}^{+} \, \boldsymbol{\psi}_{\boldsymbol{xam}}^{+} \tag{5.6}$$

and $\breve{\boldsymbol{T}}_{\boldsymbol{U\varepsilon mm}}$.

$$\breve{\boldsymbol{T}}_{\boldsymbol{U\varepsilon mm}} = \boldsymbol{\phi}_{\boldsymbol{FE\varepsilon am}}^{+} \, \boldsymbol{\psi}_{\boldsymbol{x\varepsilon am}}^{+} \tag{5.7}$$

Consistently, the equations to estimated strains with *Method 1* and *2* are now rewritten as:

$$\boldsymbol{\varepsilon_1} = \boldsymbol{\phi_{FE\varepsilon d}}\, \boldsymbol{\breve{T}_{Umm}}\, \boldsymbol{\hat{q}_{\psi xm}} \tag{5.8}$$

and

$$\boldsymbol{\varepsilon_2} = \boldsymbol{\phi_{FE\varepsilon d}}\, \boldsymbol{\breve{T}_{U\varepsilon mm}}\, \boldsymbol{\hat{q}_{\psi\varepsilon xm}} \tag{5.9}$$

The estimated strains obtained with *Method 1* and *Method 2*, together with the experimental strain measurements (also high-pass filtered at 15 Hz) are presented in Figure 5.29 at P1, Figure 5.30 at P2, Figure 5.31 at P3, Figure 5.32 at P4, Figure 5.33 at P5 and Figure 5.34 at P6.

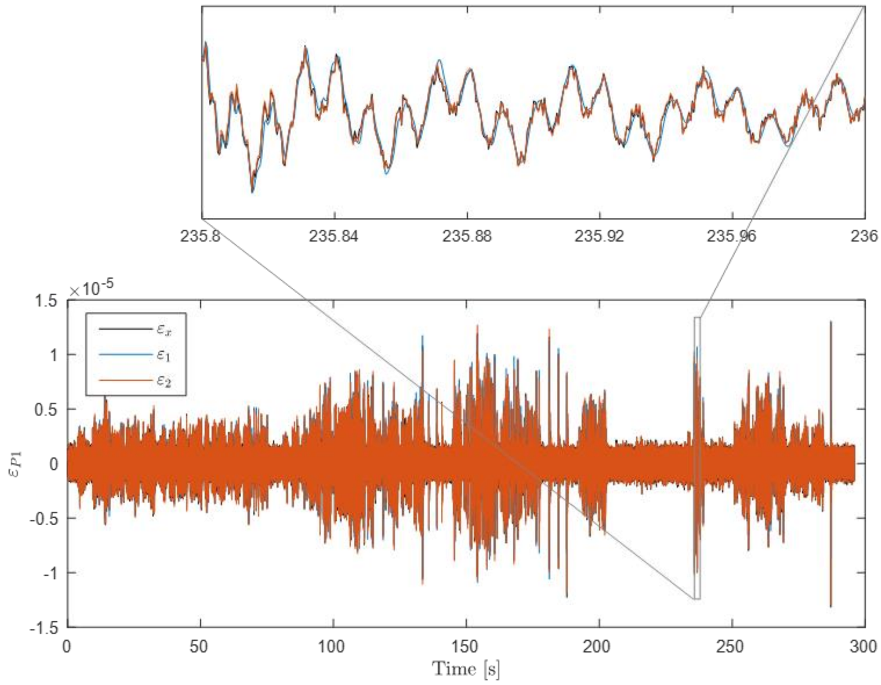

Figure 5.29: Estimated and measured strains at P1.

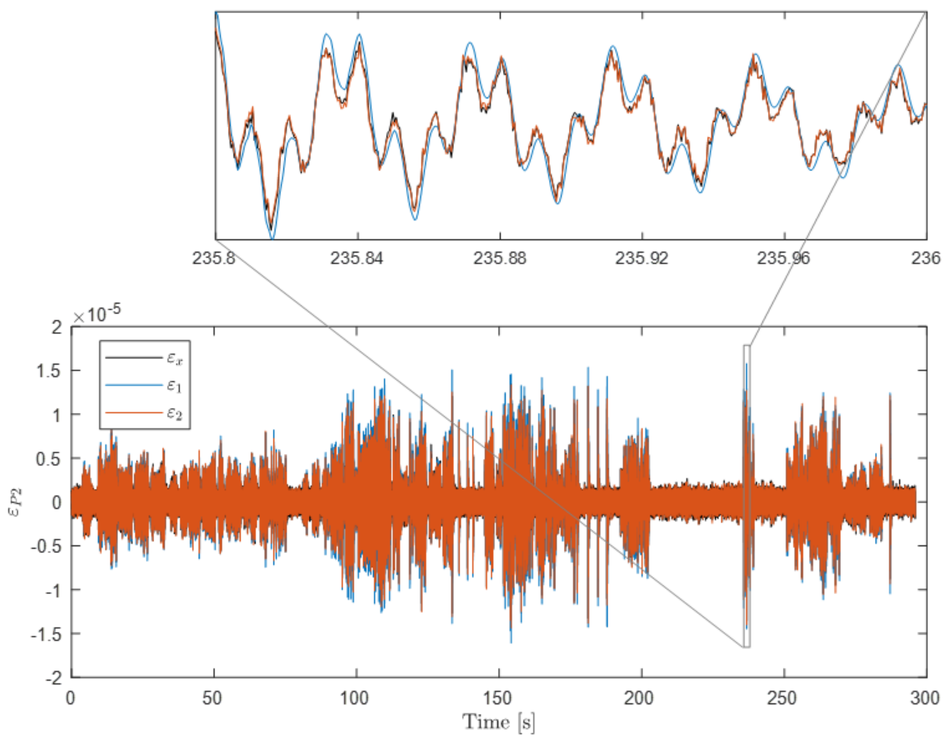

Figure 5.30: Estimated and measured strains at P2.

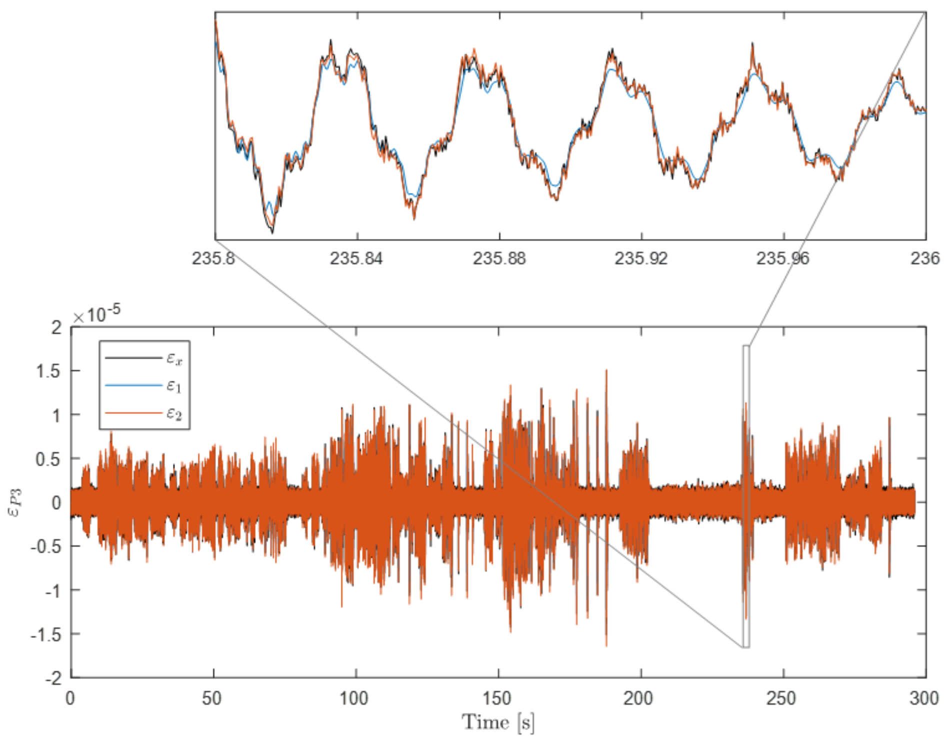

Figure 5.31: Estimated and measured strains at P3.

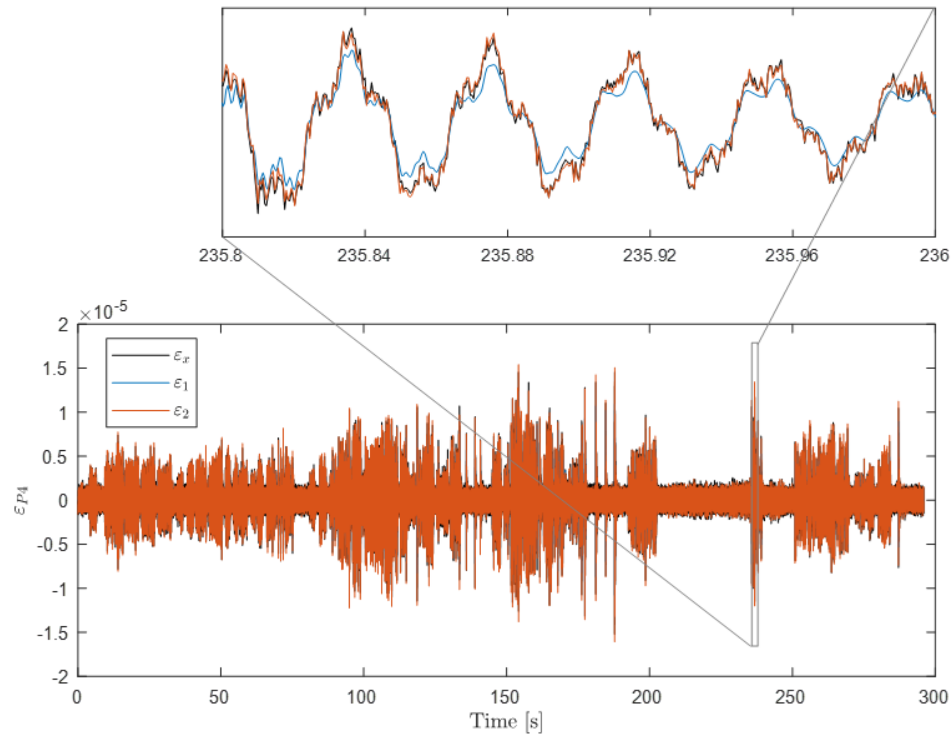

Figure 5.32: Estimated and measured strains at P4.

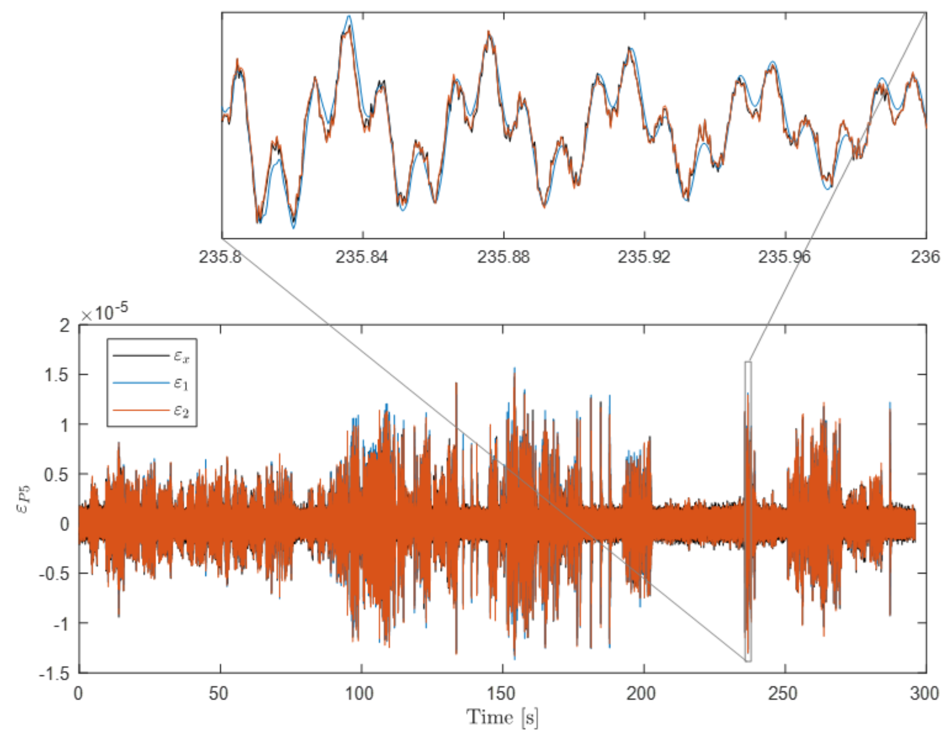

Figure 5.33 Estimated and measured strains at P5.

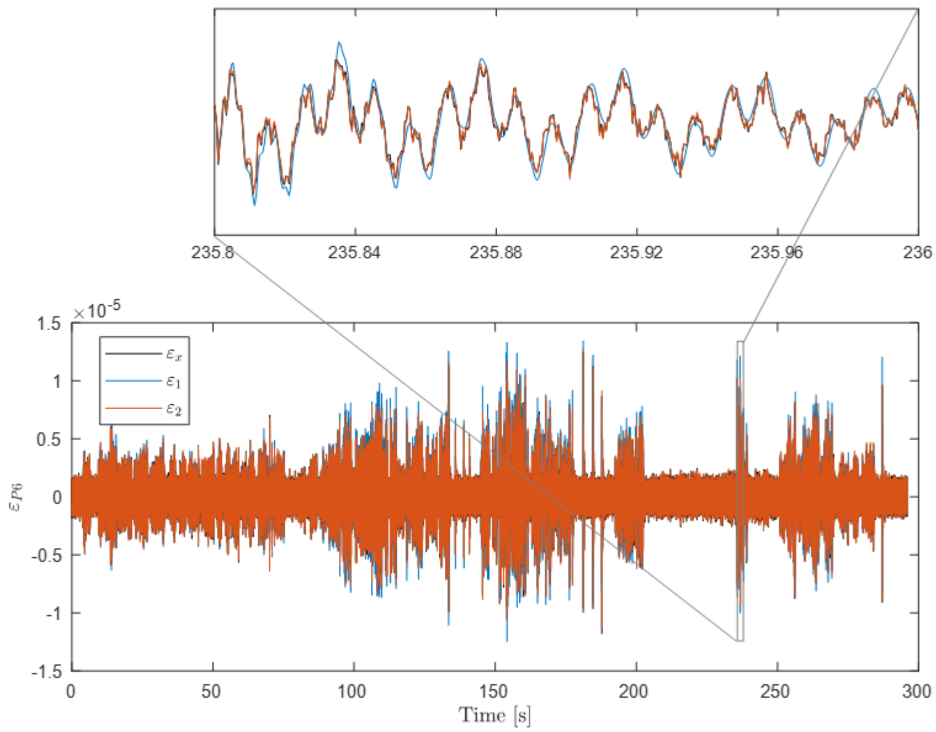

Figure 5.34: Estimated and measured strains at P6.

Table 5.16: Quality measurements of the estimated strains.

		TRAC	FRAC	R^2
Method 1	P1	0.735	0.971	0.726
	P2	0.858	0.950	0.814
	P3	0.882	1.000	0.864
	P4	0.876	0.998	0.827
	P5	0.851	0.959	0.842
	P6	0.719	0.983	0.686
Method 2	P1	0.982	1.000	0.982
	P2	0.973	1.000	0.973
	P3	0.962	0.999	0.962
	P4	0.962	0.999	0.962
	P5	0.974	0.999	0.974
	P6	0.983	1.000	0.983

Moreover, quality measurements are presented in Table 5.16. The quality indicators show that both *Method 1* and *Method 2* allow for accurate strain estimation, although the results from *Method 1* could be improved at locations ‘P1’ and ‘P6’. *Method 2* shows better results at all locations, even though the integration of the modal coordinates is not required. However, it is worth noting that experimental strain measurements on glass material typically present low noise levels, so these results could be worse for other materials. Moreover, considering that *Method 2* uses strain measurements to estimate the strain modal coordinates and to validate the results, the same level of noise is present in both signals, whereas *Method 1* show smoother results. If only strain measurements and estimated strains with *Method 1* are compared, this effect is observed in Figure 5.35. These differences explain the lower TRAC, FRAC and R^2 values for *Method 1*, since accelerometers present low noise in the signals.

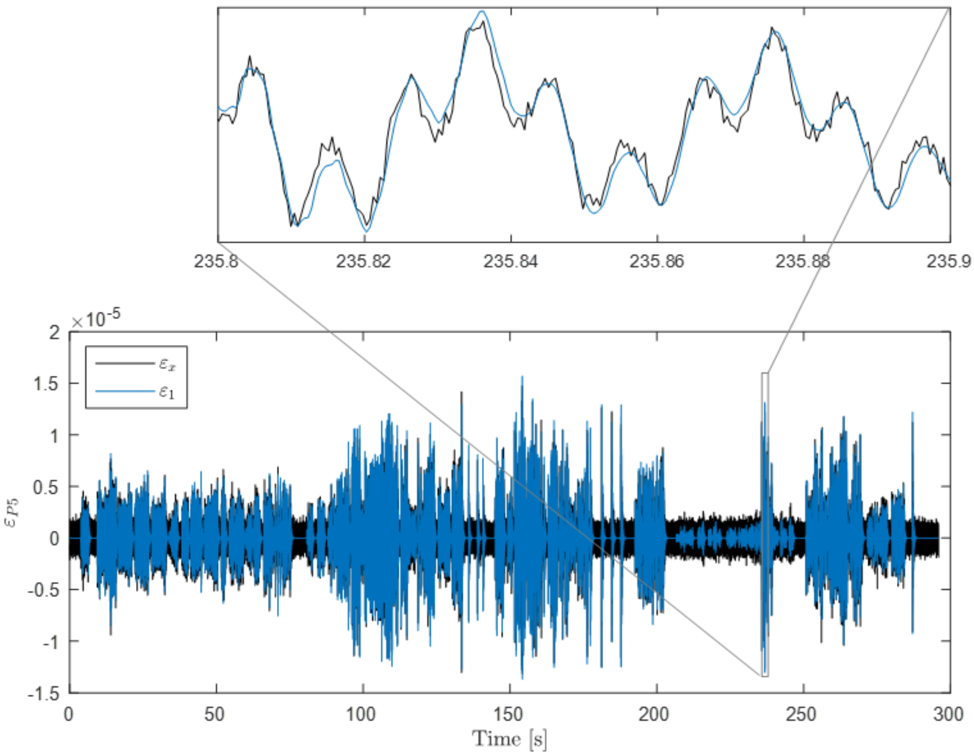

Figure 5.35: Estimated strains with *Method 1* and measured strains at P5.

5.3 Experimental case: a lab-scaled steel beam structure

In this section only *Method 8*, due to its simplicity and promising potential applicability, is used to estimate strains on a lab-scaled steel cantilever structure. The estimated strains are compared with those measured with strain gauges.

A steel beam, fixed supported on the base and with a rectangular hollow section of 100 x 40 x 4 mm^2 and length of 1.750 m, was used in the experiments. The modal parameters were estimated by operational modal analysis using the frequency domain decomposition technique. The test was carried out using a sampling frequency of 1828 Hz over a period of approximately one minute, exciting the structure by hitting it with hands in the direction of the measurements. The experimental response was measured with seven accelerometers of 100 mV/g of sensitivity and equally spaced along the beam (Figure 5.36: 'a' DOFs). The experimental natural frequencies are shown in Table 5.17.

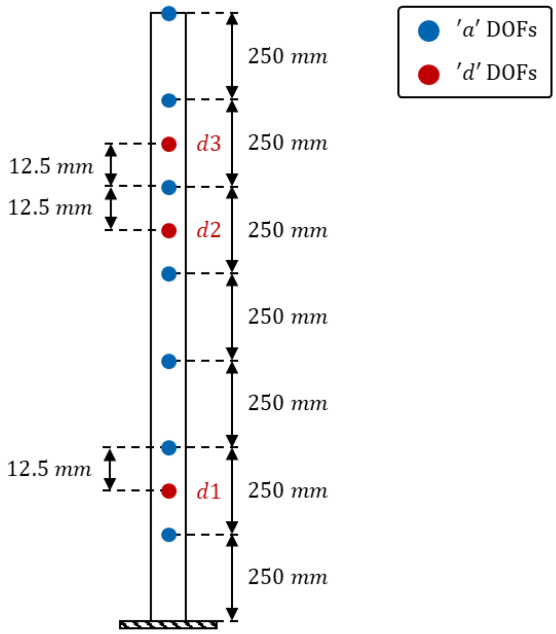

Figure 5.36: Experimental setup. Active and deleted DOFs of the cantilever steel beam.

A finite element model (*Numerical model* or *Model B*) of the structure was assembled in Abaqus. The cantilever beam was modelled with 2D shell elements, and the steel was modelled as a linear elastic material, with a Poisson's ratio equal to 0.3, a mass-density of 7850 kg/m^3 and a Young's modulus of 210 GPa. The numerical natural frequencies were extracted using a frequency modal analysis and they are presented in Table 5.17 (f_{FEM_0}). Due to the discrepancies in the natural frequencies (Table 5.17) and considering that this type of support is typically not perfectly fixed, it is assumed that there is no perfect clamping to the ground.

Table 5.17: Experimental and numerical natural frequencies [Hz] and error [%].

Mode	f_{Exp} $[Hz]$	f_{FEM_0} $[Hz]$	Error_0 [%]	f_{FEM} $[Hz]$	Error [%]
Mode 1	11.34	15.30	34.91	11.25	0.75
Mode 2	76.39	94.14	23.24	77.16	1.01
Mode 3	216.84	255.81	17.97	221.57	2.18
Mode 4	417.56	478.38	14.56	430.15	3.01
Mode 5	647.60	740.52	14.35	683.61	5.56

In order to achieve a better correlation, the fixed support was modified in Model B locating vertical springs and fixing the edges in the rest of directions. Model B was updated to improve the correlation with Model A. The objective of this updating procedure was to minimize the error between experimental and numerical natural frequencies and mode shapes. The model parameters scope of the updating process were: the stiffness of the springs (K) and the Young's modulus (E). The values obtained after the model updating process are shown in Table 5.18.

Table 5.18: Updated parameters of *Model B.*

Modal parameters	Updated value
Springs stiffness K	1.3 x 10^{8} N/m
Young's modulus E	200 GPa

The numerical natural frequencies of the updated model are also shown in Table 5.17. The mode shapes at the active 'a' DOFs were also extracted from the frequency analysis and the MAC between mode shapes of Model A and B is show in Figure 5.37.

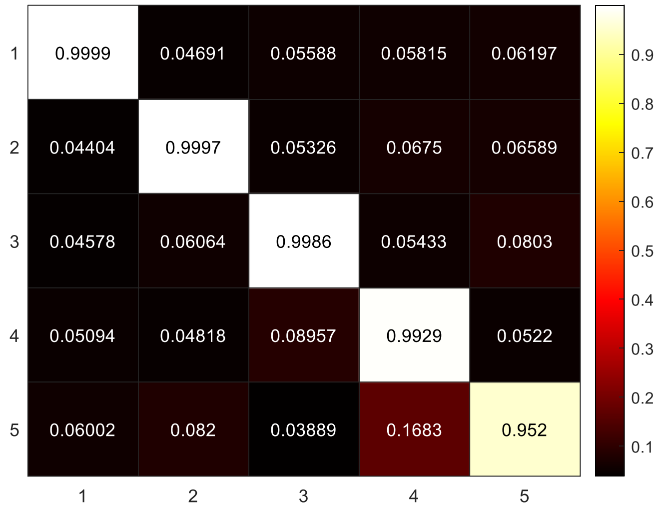

Figure 5.37: MAC between experimental and numerical mode shapes.

The ***T-Mass*** and ***T-Stiffness*** indicators (Table 5.19) show some low angles at the last row, which may be due to modal truncation effects. Excluding the last row, some stiffness discrepancies are still present.

Table 5.19: ***T-Mass*** and ***T-Stiffness*** indicators

T-Mass					***T-Stiffness***				
---	89.12	89.30	89.58	89.31	---	89.70	89.67	89.92	89.86
89.12	---	89.61	88.26	88.09	88.43	---	89.20	89.55	89.84
89.30	89.61	---	88.07	83.59	75.79	83.60	---	89.15	89.80
89.58	88.26	88.07	---	82.00	78.07	76.48	86.87	---	88.16
89.31	88.09	83.59	82.00	---	22.45	78.43	88.21	85.47	---

In order to estimate the strains of the cantilever structure, the same test setup was used (Figure 5.36). The test was carried out using a sampling frequency of 1828 Hz and the beam was excited hitting it with hands in the direction of the measurements. Accelerations were registered at the ‘a’ DOFs and strains were measured with three strains gauges located in ‘d’ DOFs (d1, d2, d3 and d4) to validate the estimated strains.

To estimate strains at locations d1, d2 and d3 *Method 8* is applied. As the modal parameters are obtained from Model B, the number of modes considered in the estimation can be higher than the number of experimental modes. In this case, six bending modes are employed in the modal decomposition.

Accelerations are integrated twice and filtered (high-pass filter to avoid amplifications due to the integration and band-pass filter at 50 Hz to remove noise from the power supply) in the frequency domain to obtain the required displacements. The estimated modal coordinates $\widetilde{\boldsymbol{q}}_{\boldsymbol{xm}}$ are shown in Figure 5.38 (a). It can be observed that many peaks appear outside the main frequency of each modal coordinate due to errors in the mode shapes (discrepancies between $\boldsymbol{\phi}_{\boldsymbol{xam}}$ and $\boldsymbol{\phi}_{\boldsymbol{FEam}}$). As explained in section 4.4.2, these errors can be expressed as the contribution of the product $\boldsymbol{\phi}_{\boldsymbol{FEam}}^{+}\ \boldsymbol{\Delta\phi}_{\boldsymbol{xFE}}\ \boldsymbol{q}_{\boldsymbol{xm}}$. A possible solution to this problem is to apply a band-pass filter to each modal coordinate around its natural frequency. The modal coordinates $\widetilde{\boldsymbol{q}}_{\boldsymbol{xm}}$ after the filtering process are shown in Figure 5.38 (b).

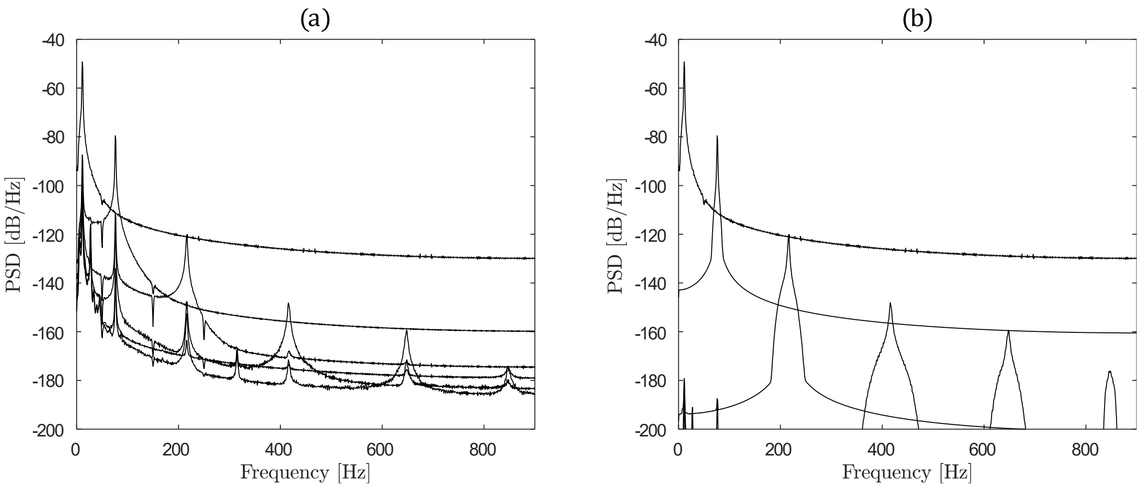

Figure 5.38: Modal coordinates $\widetilde{\boldsymbol{q}}_{\boldsymbol{xm}}$: (a) without filtering and (b) filtered.

Considering that the estimated strains are validated by comparing them with the strain measurements, the experimental strain responses are processed as follows:

- Detrending and mean value removal: to eliminate the linear increase of the signals and to ensure a zero mean.
- Filtering: high-pass filtered to eliminate low-frequency high values and band-pass filtered to remove noise from the power supply.
- Decimation (by a factor of 4): to reduce high-frequency noise signal components.

The signals before and after the processing are shown in Figure 5.39 and Figure 5.40.

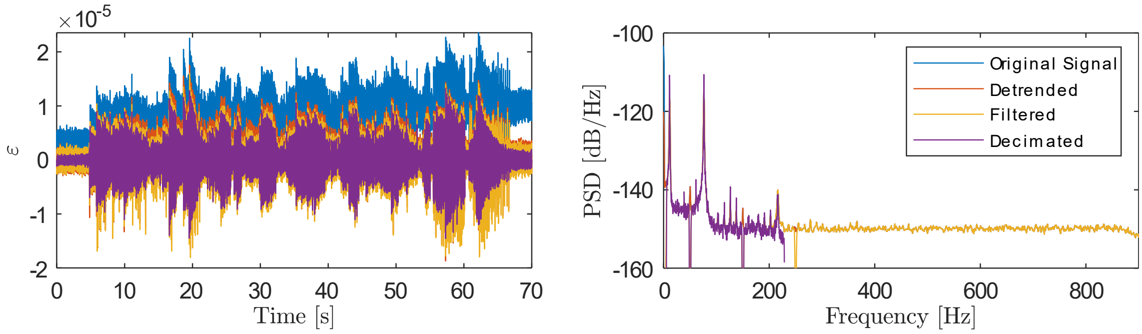

Figure 5.39: Signal processing of the measured strains at ‘d3’: (a) time domain and (b) frequency domain.

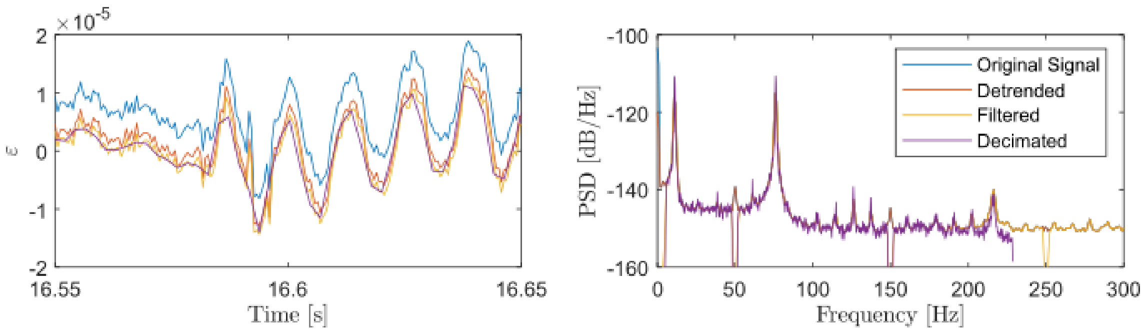

Figure 5.40: Signal processing details for measured strains at ‘d3’: (a) zoomed view in the time domain and (b) zoomed view in the frequency domain.

The estimated strains at points d1, d2 and d3 are shown in Figure 5.41. A detailed view of the strains presented in Figure 5.41 are shown in Figure 5.42, from which is inferred that strains are estimated with a good accuracy.

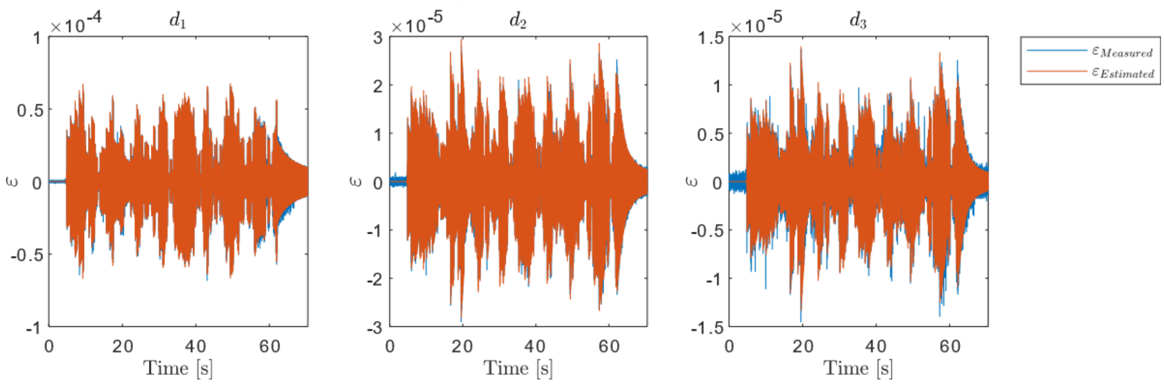

Figure 5.41: Measured and estimated strains with *Method 8* at ‘d1’, ‘d2’ and ‘d3’.

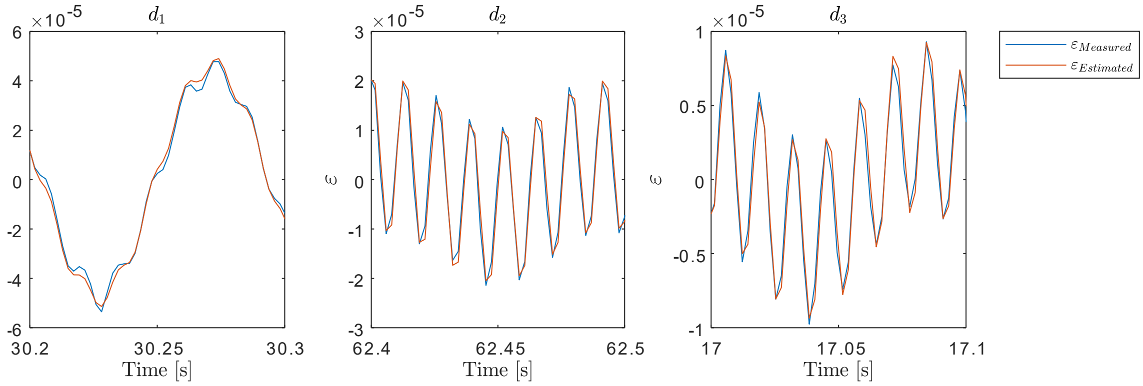

Figure 5.42: Measured and estimated strains with *Method 8* at ‘d1’, ‘d2’ and ‘d3’. Zoom in the time scale.

Moreover, the quality measurements (TRAC, FRAC and R^2) are shown in Table 5.20. High values of the three indicators are obtained at the three locations of interest (d1, d2 and d3) indicating an accurate estimation. The best quality factors are obtained at location ‘d1’ (values of the quality indicators close to 1), whereas the worst results correspond to point ‘d3’ (values of the quality indicators higher that 0.945). However, it must be noticed that lower level of strains is achieved at point ‘d3’ and, consequently, higher errors are expected. On the other hand, the higher levels of strain are achieved at point ‘d1’.

Table 5.20: Quality measurements of the estimated strains at ‘d’ DOFs.

		TRAC	FRAC	R^2
Method 8	d1	0.995	1.000	0.995
	d2	0.975	0.997	0.974
	d3	0.945	0.997	0.945

6

Conclusions and future work

6.1 Conclusions

This PhD thesis proposes a fatigue monitoring methodology to calculate the real-time accumulated fatigue damage based on the estimated stresses at specific points of interest. To accurately estimate stresses, a well-calibrated numerical model of the structure is essential, consequently, correlation methods were extensively studied. New correlation indicators were developed to detect discrepancies in mass, stiffness, or both. Additionally, a novel variation of the MAC, named ROTMAC was introduced. In terms of stress estimation techniques, eight methods based on modal superposition, using expanded mode shapes, were presented.

The following conclusions are drawn and grouped in line with the objectives of this thesis.

1. *To develop a methodology for fatigue monitoring of structures, combining a numerical model and the experimental response of the structure measured at discrete points.*

   - The most frequently used SHM techniques are modal-based methods; therefore, automated modal identification techniques are required. Damage detection techniques are widely spread in the literature and in real applications, while localization presents challenges, and damage assessment and prediction are still being explored. Thus, fatigue monitoring is essential for predicting the remaining life of structures and prevent future catastrophes.

- A methodology for fatigue monitoring of structures is proposed, which allows for the calculation of real time accumulated fatigue damage from estimated stresses at locations of interest or hot spots (previously identified). This methodology employs a numerical model of the structure together with the experimental responses measured at discrete points, which facilitates the combination with other vibration-based SHM techniques.

- Stress time histories at critical points of interest can be directly measured with strain sensors installed at those same locations or by employing stress estimation techniques. These techniques involve real time measurement of experimental displacements, velocities, accelerations, or strain responses using a limited number of sensors. Among these methods, modal expansion and Kalman filter techniques are the most commonly utilized.

- The most common practice in time domain fatigue analysis is to assume a Basquin linear S–N field, cycle counting using the rainflow algorithm, and the use of Miner's rule to estimate the accumulated fatigue damage. In the frequency domain fatigue analysis, the Miner's rule is also commonly used, but the fatigue stress spectrum is obtained from the moments of the stress PSDs.

2. *To propose and validate novel indicators for correlation of numerical and experimental models.*

- New correlation indicators to detect mass discrepancies between models were proposed. In the absence of stiffness discrepancies, ***T-Mass*** off-diagonal entries must be 90°, ***T-Mass-norm*** off-diagonal entries must be 1, and the AUTOMAC of matrix $\boldsymbol{T}$ should show off-diagonal terms equal to zero. In cases where mass-normalized mode shapes are available for both models, the diagonal terms of the inner product $\boldsymbol{T}^{\boldsymbol{T}}\boldsymbol{T}$ also serve as an effective mass correlation indicator.

- New correlation indicators to detect stiffness discrepancies between models were proposed. In the absence of stiffness discrepancies, ***T-Stiffness*** off-diagonal entries must be 90°, ***T-Stiffness-norm*** off-diagonal values must be 1 and the MAC between matrix $\boldsymbol{T}$ and $\boldsymbol{\omega}_{\boldsymbol{B}}^{\boldsymbol{2}}\boldsymbol{T}$ should have off-diagonal terms equal to zero. In cases where mass-normalized mode shapes are available for both models the diagonal terms of the product $\boldsymbol{T}^{\boldsymbol{T}}\boldsymbol{\omega}_{\boldsymbol{B}}^{\boldsymbol{2}}\boldsymbol{T}$ also serve as an effective stiffness correlation indicator.

- A novel version of the MAC, named ROTMAC, was proposed to address challenges in models with closely spaced or repeated modes. These modes mainly rotate in their local subspace, leading to low MAC values despite strong model correlation. The ROTMAC overcomes this issue by detecting only shear effects, thus providing a more accurate assessment of model correlation in cases where modes are closely spaced or repeated.

- All the proposed indicators were applied and validated in a simulated symmetric structure with repeated modes, where a mass change was introduced. Since mass-normalized modes were considered, the indicators provided extensive information and the mass discrepancies were successfully detected.
- Different levels of mass or stiffness discrepancies were simulated in a numerical two-span simply supported beam. The proposed indicators effectively distinguished between mass and stiffness discrepancies, even when errors were induced in the mode shapes. A variation of the ***T-Stiffness*** indicator was proposed to better address errors in the mode shapes.
- In an experimental glass plate with repeated modes, the ROTMAC demonstrated strong correlation with the numerical model, while the standard MAC showed significant discrepancies.
- Truncation effects were examined in the discussed examples, which represent one of the main limitations of the use of ***T*** matrix as a correlation indicator.

3. *To propose, compare and validate real time stress estimation techniques based on modal superposition and on the expansion of experimental mode shapes and/or strain mode shapes.*

Conclusions related to the theory:

- A comprehensive review of stress estimation methods based on modal expansion techniques, along with the most commonly used quality indicators, was conducted.
- The theory to perform modal expansion and feasible alternatives was developed. Additionally, the estimation of modal coordinates is also developed, which can be achieved by projecting structural responses onto either an experimental or a numerical subspace. Moreover, the structural response can be measure with accelerometers, strain sensors or both. Therefore, six alternatives to estimate modal coordinates are proposed.
- Eight methods to estimate strains and stresses were proposed, with four of them projecting responses onto an experimental subspace and four onto a numerical subspace. The requirements and limitations of each method are discussed. *Method 8*, which avoids the use of a transformation matrix, is introduced as a novel and promising technique.

- The main sources of errors impacting modal coordinates—such as truncation, response noise, mode shape errors, and complexity—are theoretically quantified and illustrated. To reduce these errors and improve accuracy in estimated strains, filtering the modal coordinates is proposed as an effective solution.

- The expected uncertainties in estimated strains for each method were mathematically developed. The results indicate that discrepancies due to the assumption $\boldsymbol{T}_{\boldsymbol{\varepsilon mm}} \neq \breve{\boldsymbol{T}}_{\boldsymbol{mm}}$ depend on the differences $\boldsymbol{\Delta\phi}''_{\boldsymbol{xam}}$ and $\boldsymbol{\Delta\phi}_{\boldsymbol{x\varepsilon am}}$. Scaling issues were also addressed, noting that *Method 3* converges to *Method 1*, while *Method 4* is not applicable when experimental modes are not mass-normalized.

- Three application cases were proposed in this thesis to validate the proposed stress estimation techniques. Model correlation was studied, as the accuracy in the stress estimation depends on the level of correlation between the numerical and the experimental models. A numerical case was used to avoid potential error sources from the experimental measurements or signal processing, while in two experimental cases, the estimation methods were applied under real conditions, including inherent errors such as noise and mode shape inaccuracies, as well as the presence of unscaled mode shapes.

Conclusions related to the quality obtained with the methods:

- When a good correlation exists between models, all proposed methods yield highly accurate results. In such cases, the selection of methods can be based primarily on the availability of required sensors.

- Among the methods that project the experimental responses onto the experimental subspace (*Methods 1* to *4*), *Methods 2* and *3* consistently deliver excellent results, even without filtering modal coordinates. Conversely, *Methods 1* and *4* exhibit lower quality indicator values, but both of them demonstrate similar levels of accuracy.

- It is important to note that in real applications, strain gauges often produce higher noise levels than accelerometer signals, which can introduce errors when using *Method 2*. However, since strain gauges are also utilized for validation, the same noise levels are present, potentially compromising the reliability of the high-quality values obtained.

- For methods that project onto the numerical subspace (*Methods 5* to *8*), filtering of modal coordinates becomes almost mandatory to achieve reliable results. *Method 5*, when using filtered modal coordinates, attains precision levels comparable to those of *Methods 1* and *4*. *Methods 6* and *7* also demonstrate high quality. In the case of *Method 8*, using unfiltered modal coordinates results in precision similar to *Method 1*; however, with filtered modal coordinates, it yields significantly higher quality results.

<u>Conclusions related to the advantages and disadvantages of each method and general comments:</u>

- Although *Method 1* is not as effective as *Methods 2* and *3*, it has the advantage of not requiring the use of strain gauges, making it simpler to apply. This method can be implemented using only accelerometers, which are widely used in Structural Health Monitoring (SHM), representing a significant advantage.
- *Methods 2, 3, 6,* and *7* require the use of strain gauges. The growing interest in strain gauge applications within SHM is likely to encourage the adoption of these methods, particularly *Methods 2* and *6*, which rely exclusively on strain sensors. However, special attention must be given to the interpretation of strain mode shapes, which can be more complex to analyse than traditional mode shapes.
- *Methods 3* and *7* involve a slightly more complex application as both the strain and the displacement experimental responses must be measured. When utilizing experimental and strain mode shapes, it is essential to pay attention to their signs (directions). Specifically, strain mode shapes should correspond to the second derivative of the mode shapes. While finite element models inherently satisfy this condition, it must be manually verified when numerical mode shapes and strain mode shapes are used together with experimental mode shapes and strain mode shapes estimated with Operational Modal Analysis (OMA).
- The formulations developed for *Method 3* with unscaled mode shapes yield expressions that are equivalent to those developed for *Method 1*.
- *Method 4* cannot be applied with unscaled mode shapes. Additionally, the quality of its results, in relation to the sensor requirements and calculation process, suggests that *Method 4* is not particularly advantageous.
- *Methods 5* to 8 do not require automated OMA since the necessary modal parameters are obtained from numerical models. These models only need to be updated when changes occur in the experimental structure and the correlation with the numerical model deteriorates.

- *Method 8* shows high-quality results in experimental cases, obtaining quality indicators higher than 0.94, even at locations where the strain magnitude was quite small. This technique seems to have promising potential due to several factors: it does not require experimental modal parameters, it is easy to use, and it delivers high-quality results. *Variation b* of *Method 8*, which incorporates strain measurements, is likely to be equally promising, particularly as the use of fiber-optic sensors becomes more widespread and well-established.
- It is well known that modal parameters, particularly damping ratios and natural frequencies, are influenced by environmental conditions. However, since the proposed methods rely solely on mode shapes, the estimated stress histories are minimally affected by these variations, because the information corresponding to natural frequencies and damping ratios are contained in the modal coordinates.

Conclusions related to the modal coordinates

- In numerical simulations, the filtering of modal coordinates in *Methods 1* to *4* does not provide substantial advantages. However, filtering becomes important in experimental scenarios where mode shape estimation errors and measurement noise (often associated with strain gauges).
- For *Methods 5* to *8*, filtering of modal coordinates is mandatory to ensure accurate results.
- For the numerical and experimental cases addressed in this thesis, strain modal coordinates (both, projecting onto an experimental or numerical subspace) are more sensitive to truncation effects, leading to significant errors at higher frequencies.
- Errors in mode shapes can induce inaccuracies in displacement coordinates across all frequencies. In the case of strain modal coordinates, errors in mode shapes primarily affect the higher frequencies.

6.2 Future work

Based on the conclusions presented above, the correlation techniques and stress estimation methods can be extended and improved to enhance the acquired knowledge. The planned future work can be summarized as follows:

Future work related to model correlation

- Using unscaled mode shapes in one of the models, the scaling discrepancies cannot be studied. This implies a significant loss of information, especially in the case of repeated modes perturbed by a mass change, when shear does not appear. Therefore, it is essential to investigate whether scaling the mode shapes is worthwhile, despite the errors introduced, to determine if scaling ultimately leads to a more accurate and informative representation
- To develop or modify existing correlation techniques to address the correlation between two systems with unscaled mode shapes. This is a common scenario in modal-based SHM, where the modal parameters of the structure in its 'healthy' state are compared with its current modal parameters; consequently, both mode shapes are usually unscaled. This approach is aimed at facilitating effective damage detection purposes.
- To study and propose modifications to correlation techniques when complex mode shapes are considered.
- To propose an approach for selecting which modes to use in the calculation of the matrix $\boldsymbol{T}$, ensuring that the estimated matrix is accurate and provides reliable information

Future work related to stress estimation

- Continue to explore *Method 8*, given its promising results and ease of application, by extending its use to more complex, multiaxial, and real-world scenarios.
- To apply *Variation b* of *Method 8* by measuring strain responses, as advancements in fiber-optic sensor research are likely to increase the popularity of this method.
- To determine when it is necessary to update the numerical model in *Method 8* applications, as the accuracy of the results is directly related to the correlation between the numerical and experimental models.

6

Conclusiones y trabajo futuro

6.1 Conclusiones

Esta tesis doctoral propone y desarrolla una nueva metodología de monitorización a fatiga de estructuras que permite calcular el daño acumulado a fatiga en tiempo real a partir de las tensiones estimadas en ciertos puntos de interés. Para estimar con precisión estas tensiones, se hace indispensable disponer de un modelo numérico bien calibrado de la estructura. En consecuencia, en primer lugar, se estudiaron y analizaron en profundidad los métodos de correlación más utilizados en la actualidad. Posteriormente, se propusieron y analizaron nuevos indicadores de correlación entre dos modelos, los cuales permiten identificar si existen discrepancias en términos de masa, rigidez, o ambas. Adicionalmente, se propuso una nueva técnica de correlación de modos derivadas del MAC, denominada ROTMAC, que permite identificar si existe una adecuada correlación en aquellos casos donde los modos son cercanos o repetidos. Finalmente, en cuanto a las técnicas de estimación de tensiones que se han desarrollado, se presentaron ocho metodologías diferentes para tal fin basadas en técnicas de superposición modal y utilizando métodos de expansión modal.

En esta sección se presentan las conclusiones obtenidas, organizadas de acuerdo con los objetivos establecidos en esta tesis:

1. *Desarrollar una metodología para la monitorización a fatiga de estructuras, combinando un modelo numérico y la respuesta experimental de la estructura medida en puntos discretos.*

   - Las técnicas de monitorización más utilizadas son aquellas basadas en parámetros modales; por lo tanto, se requieren técnicas de identificación modal automatizadas. A partir de dichas identificaciones, existen diferentes técnicas ampliamente desarrolladas tanto a nivel teórico en la literatura como en aplicaciones reales, que permiten la detección de daño. Sin embargo, si bien la detección de daño es ya una técnica ampliamente utilizada, la localización del daño, así como la evaluación y predicción del mismo requieren de técnicas adicionales que han de ser mejoradas, desarrolladas y exploradas. Por lo tanto, la propuesta de monitorización a fatiga que se presenta en esta tesis es esencial para predecir la vida remanente de las estructuras y prevenir futuras catástrofes.
   - Se propone una metodología para la monitorización a fatiga de estructuras, que permite el cálculo en tiempo real del daño por fatiga acumulado a partir de las tensiones estimadas en las ubicaciones de interés o puntos críticos (previamente identificados). Esta metodología emplea un modelo numérico de la estructura junto con las respuestas experimentales medidas en puntos discretos, lo que facilita su combinación con otras técnicas de monitorización basadas en vibraciones (vibration-based SHM).
   - Las tensiones en los puntos críticos de interés se pueden medir directamente con sensores de deformación instalados en esos mismos lugares o mediante técnicas de estimación de tensiones. Estas técnicas implican la medición experimental en tiempo real de desplazamientos, velocidades, aceleraciones o deformaciones utilizando un número limitado de sensores. Entre estos métodos, la expansión modal y las técnicas de filtro de Kalman son las más comúnmente utilizadas.
   - La práctica más común en el análisis de fatiga en el dominio del tiempo es asumir un campo lineal S–N de Basquin, el conteo de ciclos utilizando el rainflow y el uso de la regla de Miner para estimar el daño acumulado. En el análisis de fatiga en el dominio de la frecuencia, la regla de Miner también se utiliza comúnmente, pero el espectro de tensiones de fatiga se obtiene a partir de los momentos de las densidades espectrales de las tensiones.

2. *Proponer y validar nuevos indicadores de correlación entre modelos numéricos y experimentales.*

   - Se propusieron nuevos indicadores de correlación para detectar discrepancias de masa entre dos modelos. En ausencia de discrepancias de rigidez, los elementos fuera de la diagonal de

T-Mass deben ser de 90°, mientras que en el caso de ***T-Mass-norm*** los elementos fuera de la diagonal deben ser 1. Adicionalmente, el AUTOMAC de la matriz $\boldsymbol{T}$ debe mostrar términos fuera de la diagonal iguales a cero. En casos donde los modos están normalizados a la masa para ambos modelos, la diagonal del producto $\boldsymbol{T}^{\boldsymbol{T}}\boldsymbol{T}$ también sirve como un indicador de correlación en términos masa.

- Se propusieron nuevos indicadores de correlación para detectar discrepancias de rigidez entre dos modelos. En ausencia de discrepancias de masa, los elementos fuera de la diagonal de ***T-Stiffness*** deben ser de 90°, mientras que en el caso de ***T-Stiffness-norm*** los elementos fuera de la diagonal deben ser 1. Adicionalmente, el MAC entre la matriz $\boldsymbol{T}$ y $\boldsymbol{\omega}_{\boldsymbol{B}}^{\boldsymbol{2}}\boldsymbol{T}$ debe mostrar términos fuera de la diagonal iguales a cero. En casos donde los modos están normalizados a la masa para ambos modelos, la diagonal del producto $\boldsymbol{T}^{\boldsymbol{T}}\boldsymbol{\omega}_{\boldsymbol{B}}^{\boldsymbol{2}}\boldsymbol{T}$ también sirve como un indicador de correlación en términos de rigidez.

- Se propuso una versión novedosa del MAC, llamada ROTMAC, para abordar desafíos en la correlación entre modelos con modos cercanos o repetidos. Estos modos rotan principalmente en su subespacio local, lo que da lugar a valores bajos de MAC a pesar de una buena correlación entre modelos. El ROTMAC soluciona este problema al detectar solo efectos de *shear*, proporcionando así una evaluación más precisa de la correlación en casos donde hay modos cercanos o repetidos.

- Todos los indicadores de correlación se aplicaron y validaron en una estructura simétrica simulada con modos repetidos mediante un modelo de elementos finitos. Como perturbación del sistema se introdujo un cambio de masa. Dado que se consideraron modos normalizados a la masa, los indicadores proporcionaron información extensa y muy buenos resultados, detectando de manera exitosa las discrepancias de masa.

- Se simularon diferentes niveles de discrepancias en términos de masa y rigidez en una viga de dos vanos simplemente apoyada. Los indicadores propuestos pudieron diferenciar si las discrepancias eran debidas a cambios de masa o rigidez, incluso cuando se introdujeron errores en los modos de vibración. Adicionalmente se propuso una variación del indicador ***T-Stiffness*** para abordar mejor estos errores en los modos.

- Se analizó experimentalmente el caso de una placa de vidrio con modos repetidos mediante el ROTMAC. La técnica demostró una buena correlación con el modelo numérico, mientras que el MAC mostraba discrepancias significativas en algunos modos.

- Se examinaron los efectos del truncado del número de modos de vibración en los ejemplos presentados. Como se pudo demostrar, el efecto del truncado es significativo y representa una de las principales limitaciones del uso de la matriz $\boldsymbol{T}$ como indicador de correlación.

3. *Proponer, comparar y validar técnicas de estimación de tensiones en tiempo real basadas en la superposición modal y en la expansión de modos experimentales.*

<u>*Conclusiones relacionadas con la teoría:*</u>

- Se llevó a cabo una revisión exhaustiva de los métodos de estimación de tensiones basados en técnicas de expansión modal, así como de los indicadores de calidad más comúnmente utilizados para evaluar la precisión de las tensiones estimadas.

- Se desarrolló la teoría para llevar a cabo la expansión modal y se presentaron las alternativas existentes. También se desarrollaron las ecuaciones necesarias para la estimación de coordenadas modales, la cual se puede realizar proyectando las respuestas estructurales o bien en un subespacio experimental o bien en un subespacio numérico. Además, dado que la respuesta estructural se puede medir con acelerómetros, sensores de deformación o ambos, se proponen seis alternativas para estimar las coordenadas modales.

- Se propusieron ocho métodos para estimar deformaciones (y tensiones), cuatro de los cuales proyectan las respuestas en un subespacio experimental y cuatro en un subespacio numérico. Además, se discutieron los requisitos y limitaciones de cada método. Cabe resaltar que el *Método 8*, que evita el uso de una matriz de transformación, se presenta como una técnica novedosa y prometedora.

- Se cuantificaron e ilustraron teóricamente las principales fuentes de error que afectan a las coordenadas modales, tales como el truncado de los modos, el contenido en ruido de la respuesta, los posibles errores en los modos de vibración, así como la aparición de modos complejos. Para reducir estos errores y mejorar la precisión en la estimación de las deformaciones, se propone el filtrado de las coordenadas modales como una solución efectiva.

- Se desarrollaron matemáticamente las ecuaciones de la incertidumbre esperada en las deformaciones estimadas con cada método. Los resultados indican que las discrepancias debidas a la suposición $\boldsymbol{T}_{\boldsymbol{\varepsilon mm}} \neq \breve{\boldsymbol{T}}_{\boldsymbol{mm}}$ dependen de las diferencias $\boldsymbol{\Delta\phi}''_{\boldsymbol{xam}}$ y $\boldsymbol{\Delta\phi}_{\boldsymbol{x\varepsilon am}}$. También se abordó el problema del tipo de escalado de los modos, señalando que el *Método*

3 converge al *Método 1*, mientras que el *Método 4* no es aplicable cuando los modos experimentales no están normalizados a la masa.

- En esta tesis se utilizaron tres casos prácticos para validar las técnicas de estimación de tensiones propuestas. Además, se estudió la correlación entre modelos, ya que la precisión en la estimación de tensiones depende del nivel de correlación entre el modelo numérico y experimental utilizados. Dichas técnicas se analizaron a través del estudio con casos de modelización numérica con el fin de evitar posibles fuentes de error derivadas tanto del proceso de adquisición de las mediciones experimentales así, como, por ejemplo, del tratamiento de las señales. Los métodos también se aplicaron a dos estructuras de laboratorio, utilizando en estos casos datos experimentales, incluyendo así errores inherentes como el ruido presente en las señales o las imprecisiones en la identificación de los modos de vibración. También, al utilizar OMA como método de identificación modal, se analizó la opción de disponer únicamente en el caso experimental de modos sin escalar a la masa.

Conclusiones relacionadas con la calidad de los métodos propuestos:

- Cuando existe una buena correlación entre el modelo experimental y el modelo numérico, todos los métodos propuestos ofrecen resultados con errores muy bajos. En dichos casos, la selección de los métodos puede basarse principalmente en la disponibilidad de sensores de medida.
- Entre los métodos que proyectan las respuestas experimentales en el subespacio experimental (*Métodos 1* a *4*), los *Métodos 2* y *3* ofrecen excelentes resultados, incluso cuando las coordenadas modales no se filtran. Por el contrario, los *Métodos 1* y *4* arrojan valores más bajos en los indicadores de calidad aplicados, demostrando niveles similares de precisión entre ellos (*Métodos 1 y 4*). En aplicaciones reales, las medidas con galgas extensométricas suelen contener niveles más altos de ruido en comparación con las medidas de los acelerómetros, lo que puede introducir errores al utilizar el *Método 2*. Sin embargo, dado que las galgas extensométricas también se utilizan para la validación, los mismos niveles de ruido están presentes en la señal estimada y en la de referencia, lo cual podría comprometer la fiabilidad de los buenos valores obtenidos en los indicadores de calidad.
- Para los métodos que se basan en proyectar en el subespacio de los modos numéricos (*Métodos 5* a *8*), se ha comprobado como el filtrado de las coordenadas modales se vuelve un paso necesario para lograr resultados precisos en la estimación de las deformaciones. El

Método 5, al utilizar coordenadas modales filtradas, alcanza niveles de precisión comparables a los de los *Métodos 1* y *4*. Los *Métodos 6* y *7* muestran valores muy altos en los indicadores de calidad. En el caso del *Método 8*, el uso de coordenadas modales sin filtrar da lugar a niveles de precisión similares a los del *Método 1*; sin embargo, con coordenadas modales filtradas, ofrece resultados significativamente mejores.

Conclusiones relacionadas con las ventajas y desventajas de cada método y comentarios generales:

- Aunque el *Método 1* no es tan efectivo como los *Métodos 2* y *3*, tiene la ventaja de evitar el uso de galgas extensométricas, lo que facilita su aplicación. Este método se puede implementar utilizando solo acelerómetros, los cuales son ampliamente utilizados en la monitorización de estructuras lo que supone un beneficio significativo.

- Los *Métodos 2, 3, 6* y *7* requieren el uso de galgas extensométricas. El creciente interés en utilizar también sensores de deformaciones en los procesos de monitorización estructural (SHM), favorecerá la potencial utilización de estos métodos, en particular los *Métodos 2* y *6*, que utilizan únicamente sensores de deformación. Sin embargo, se debe prestar especial atención a la interpretación de los modos de vibración de deformaciones, ya que puede resultar un proceso más complejo en comparación con la interpretación de los modos de vibración tradicionales.

- La aplicación de los *Métodos 3* y *7* resulta aplicación ligeramente más compleja, al requerir tanto la respuesta experimental en desplazamientos como en deformaciones. Al utilizar modos de vibración experimentales de desplazamiento y de deformación, es crucial prestar atención a sus signos (direcciones). Teniendo en cuenta que, las formas modales de deformación se deben corresponder con la segunda derivada de los modos de desplazamiento. Mientras que los modos obtenidos a través de modelos numéricos cumplen inherentemente con esta condición, debe verificarse manualmente cuando se usan conjuntamente modos de desplazamiento y deformación, numéricos y experimentales.

- Las ecuaciones desarrolladas para el *Método 3* con modos sin escalar producen expresiones equivalentes a las desarrolladas para el *Método 1*.

- El *Método 4* no puede aplicarse con modos sin escalar. Además, los indicadores de calidad de sus resultados, en relación con los requisitos de los sensores y el proceso de cálculo, sugieren que el *Método 4* no es particularmente ventajoso.

- Los *Métodos 5* a *8* no requieren OMA automatizado, ya que los parámetros modales necesarios se obtienen de modelos numéricos. Estos modelos solo necesitan ser calibrados cuando ocurren cambios en la estructura experimental y, por lo tanto, la correlación con el modelo numérico disminuye.

- El *Método 8* muestra muy buenos resultados en casos experimentales, obteniendo indicadores de calidad superiores a 0.94, incluso en ubicaciones desfavorables donde la magnitud de la deformación era considerablemente pequeña. Esta técnica parece tener un potencial prometedor debido a varios factores: no requiere parámetros modales experimentales, es fácil de utilizar y proporciona resultados de gran calidad. La *Variación 2* del *Método 8*, que utiliza mediciones experimentales de deformaciones, tiene un alto potencial, especialmente a medida que el uso de sensores de fibra óptica se vuelva una técnica más común y se consolide.

- Se sabe que los parámetros modales, en particular el amortiguamiento y las frecuencias naturales, están influenciados por las condiciones ambientales. Sin embargo, dado que los métodos de estimación de tensiones propuestos se basan únicamente en los modos de vibración, las tensiones estimadas se ven mínimamente afectadas por estas variaciones, ya que la información correspondiente a las frecuencias naturales y el amortiguamiento se encuentra en las coordenadas modales.

Conclusiones relacionadas con las coordenadas modales:

- En las simulaciones numéricas, el filtrado de las coordenadas modales en los *Métodos 1* a *4* no ofrece ventajas sustanciales. Sin embargo, el filtrado se vuelve importante en escenarios experimentales donde existen errores en la estimación de los modos de vibración, así como se tenga presenta ruido en las mediciones.

- Para los *Métodos 5* a *8*, el filtrado de las coordenadas modales es necesario para garantizar resultados precisos.

- En los casos numéricos y experimentales abordados en esta tesis, las coordenadas modales de deformación (tanto proyectadas en un subespacio experimental como en uno numérico) son más sensibles a los efectos del truncado, lo que resulta en errores significativos a frecuencias más altas.

- Los errores en los modos de vibración pueden inducir inexactitudes en las coordenadas de desplazamiento en todas las frecuencias. Con respecto a las coordenadas modales de deformación, los cálculos con errores en los modos de vibración afectan principalmente a frecuencias altas.

6.2 Trabajo futuro

A partir de las conclusiones presentadas anteriormente, los estudios relativos a las técnicas de correlación y los métodos de estimación de tensiones pueden ampliarse y mejorarse para profundizar en el conocimiento adquirido. El trabajo futuro planificado se resume en los siguientes puntos:

Trabajo futuro relacionado con métodos de correlación:

- El uso de modos sin escalar en uno de los modelos impide el estudio de las discrepancias de escalado. Esto implica una pérdida significativa de información, especialmente en el caso de modos repetidos afectados por un cambio de masa, donde no aparece *shear*. Por ello, es esencial investigar si vale la pena escalar las formas modales, a pesar de los errores introducidos, para poder obtener una representación más fiel de la correlación.
- Desarrollar o modificar las técnicas de correlación existentes para abordar la correlación entre dos sistemas con modos sin escalar. Este es un escenario común en la monitorización basada en modos, donde los parámetros modales de la estructura en su estado 'sano' se comparan con sus parámetros modales actuales; en consecuencia, ambos modos suelen estar sin escalar. Esta mejora permitiría mejorar en la detección efectiva de daño.
- Estudiar y proponer modificaciones a las técnicas de correlación para los casos en los que se consideran modos complejos.
- Proponer un enfoque para seleccionar qué modos se deben utilizar en el cálculo de la matriz $\boldsymbol{T}$, garantizando que dicha matriz estimada sea precisa y proporcione información fiable.

Trabajo futuro relacionado con estimación de tensiones:

- Continuar explorando el *Método 8*, dado los resultados prometedores y la facilidad de aplicación, extendiendo su uso a escenarios más complejos, multiaxiales y/o reales.
- Aplicar la *Variación 2* del *Método 8* midiendo respuestas de deformaciones, ya que los avances en la investigación de sensores de fibra óptica probablemente aumentarán la popularidad de este método.

- Determinar cuándo es necesario calibrar el modelo numérico durante la utilización del *Método 8*, ya que la precisión de los resultados está directamente relacionada con la correlación entre los modelos numéricos y experimentales.

A

Appendix

This appendix includes some correlation matrices that were not reproduced in the main text for clarity.

A two-spanned steel beam

In this section, the diagonal values of the product $\boldsymbol{T^T}\,\boldsymbol{\omega_B^2}\,\boldsymbol{T}$ compared to $\boldsymbol{\omega_A^2}$ are showed in Table A 1 for models A1 and in Table A 2 for models A2 of the two-spanned beam presented in section 3.4.

Table A 1: Diagonal values of the product $\boldsymbol{T^T \omega_B^2\, T}$ compared to $\boldsymbol{\omega_A^2}$ for models A1

A1									
$\Delta M1$		$\Delta M2$		$\Delta M3$		$\Delta M4$		$\Delta M5$	
$\sqrt{T^T\omega_B^2 T}$	ω_A	$\sqrt{T^T\omega_B^2 T}$	ω_A	$\sqrt{T^T\omega_B^2 T}$	ω_A	$\sqrt{T^T\omega_B^2 T}$	ω_A	$\sqrt{T^T\omega_B^2 T}$	ω_A
41.7	41.7	42.7	42.7	43.7	43.7	45.4	45.4	46.5	46.5
71.6	71.6	72.2	72.2	72.9	72.9	74.1	74.1	75.1	75.1
154.8	154.8	158.1	158.1	161.9	161.9	168.6	168.6	173.9	173.9
206.6	206.6	207.7	207.8	209.2	209.2	212.4	212.4	216.0	216.0
338.8	338.8	345.8	345.9	352.9	353.0	363.5	363.8	370.3	370.9
412.7	412.6	415.7	415.5	419.4	419.3	426.9	427.0	433.7	434.4
592.6	593.0	605.4	605.5	621.3	618.9	649.1	639.2	664.0	650.5
682.8	687.8	675.4	692.2	666.6	698.8	653.0	716.4	650.3	737.6

Table A 2: Diagonal values of the product $\boldsymbol{T^T \omega_B^2\, T}$ compared to $\boldsymbol{\omega_A^2}$ for models A2

A2									
$\Delta K1$		$\Delta K2$		$\Delta K3$		$\Delta K4$		$\Delta K5$	
$\sqrt{T^T\omega_B^2 T}$	ω_A	$\sqrt{T^T\omega_B^2 T}$	ω_A	$\sqrt{T^T\omega_B^2 T}$	ω_A	$\sqrt{T^T\omega_B^2 T}$	ω_A	$\sqrt{T^T\omega_B^2 T}$	ω_A
41.3	41.1	41.5	40.8	43.7	39.8	49.3	38.4	57.1	36.9
71.5	70.1	72.4	68.5	77.7	63.9	83.7	60.0	87.5	57.1
153.5	152.6	154.2	151.6	159.2	148.5	166.7	145.5	173.3	143.1
206.6	202.8	208.1	198.6	213.5	189.6	216.3	183.9	216.7	180.6
335.8	333.9	337.0	331.8	343.1	326.4	349.2	322.2	353.2	319.4
411.8	405.0	412.9	397.7	414.0	384.5	412.3	377.8	410.2	374.3
587.4	584.6	588.4	581.3	592.5	573.6	595.2	568.6	596.5	565.5
691.2	675.8	693.8	665.1	690.1	648.5	684.3	641.1	680.3	637.6

A cantilever beam

In this section, the ***T-Mass*** and ***T-Stiffness*** matrices for the numerical cantilever beam presented in section 5.1.2 are presented. The ***T-Mass*** and ***T-Stiffness*** indicators for model A1 are shown in Table A 3 and Table A 4, while those for model A2 are shown in Table A 5 and Table A 6.

Table A 3: ***T-Mass*** for model A1.

---	90.000	89.951	90.000	89.817	90.000	89.538	89.998
90.000	---	89.999	89.894	89.999	89.973	89.997	89.530
89.951	89.999	---	89.999	89.876	90.000	89.393	89.996
90.000	89.894	89.999	---	89.999	89.881	89.999	89.746
89.817	89.999	89.876	89.999	---	90.000	89.766	89.998
90.000	89.973	90.000	89.881	90.000	---	90.000	89.882
89.538	89.997	89.393	89.999	89.766	90.000	---	89.998
89.998	89.530	89.996	89.746	89.998	89.882	89.998	---

Table A 4: ***T-Stiffness*** for model A1.

---	90.000	89.057	90.000	89.638	90.000	89.848	90.000
90.000	---	90.000	89.022	90.000	89.998	90.000	89.700
78.923	89.999	---	89.999	87.948	90.000	89.144	89.999
89.996	69.825	89.997	---	90.000	89.972	89.998	88.259
59.466	89.998	75.700	90.000	---	90.000	87.676	89.997
90.000	89.715	90.000	89.818	90.000	---	90.000	89.883
37.032	89.934	67.420	89.982	81.310	90.000	---	89.999
89.928	38.749	89.962	77.073	89.988	89.866	89.999	---

Table A 5: ***T-Mass*** for model A2.

---	90.000	89.914	89.999	89.690	89.997	89.289	90.000
90.000	---	89.999	89.797	89.998	89.156	89.996	89.970
89.914	89.999	---	89.997	89.744	89.992	88.893	90.000
89.999	89.797	89.997	---	89.999	89.722	89.998	89.840
89.690	89.998	89.744	89.999	---	89.997	89.923	90.000
89.997	89.156	89.992	89.722	89.997	---	89.996	89.841
89.289	89.996	88.893	89.998	89.923	89.996	---	90.000
90.000	89.970	90.000	89.840	90.000	89.841	90.000	---

Table A 6: ***T-Stiffness*** for model A2.

---	90.000	88.248	90.000	89.241	90.000	89.693	90.000
90.000	---	90.000	87.989	90.000	89.384	89.999	89.995
76.986	89.999	---	89.999	86.045	89.997	88.417	90.000
89.996	65.764	89.996	---	90.000	86.761	89.996	89.955
56.909	89.997	67.294	90.000	---	89.995	86.094	90.000
89.933	30.718	89.949	67.290	89.982	---	89.997	89.818
37.661	89.932	56.316	89.971	75.853	89.997	---	90.000
90.000	89.642	90.000	89.730	90.000	89.841	90.000	---

References

[1] B. Barros, B. Conde, M. Cabaleiro, and B. Riveiro, “Deterministic and probabilistic-based model updating of aging steel bridges,” *Structures*, vol. 54, pp. 89–105, Aug. 2023, doi: 10.1016/j.istruc.2023.05.020.

[2] ASCE, “2021 Report Card for America’s Infrastructure,” 2021.

[3] R. Woodward *et al.*, “Bridge Management in Europe (BRIME)-Deliverable D14-Final Report,” 2001.

[4] C. Du, S. Dutta, P. Kurup, T. Yu, and X. Wang, “A review of railway infrastructure monitoring using fiber optic sensors,” *Sensors Actuators A Phys.*, vol. 303, p. 111728, Mar. 2020, doi: 10.1016/j.sna.2019.111728.

[5] J. C. Sánchez-Quesada, A. Romero, P. Galvín, E. Moliner, and M. D. Martínez-Rodrigo, “3D analysis of railway induced vibrations on skew girder bridges including ballast track–bridge interaction effects,” *Eng. Struct.*, vol. 279, p. 115546, Mar. 2023, doi: 10.1016/j.engstruct.2022.115546.

[6] Wind Europe, “Wind energy in Europe in 2018 - Trends and statistics,” 2019.

[7] J. Pacheco, S. Guimarães, C. Moutinho, M. Marques, J. C. Matos, and F. Magalhães, “New strategies for optimized structural monitoring of wind farms: experimental campaign,” *Wind Energy Sci.*, vol. 5, no. 3, pp. 983–996, Aug. 2020, doi: 10.5194/wes-5-983-2020.

[8] J. Pacheco, F. Pimenta, S. Pereira, Á. Cunha, and F. Magalhães, “Fatigue Assessment of Wind Turbine Towers: Review of Processing Strategies with Illustrative Case Study,” *Energies*, vol. 15, no. 13, p. 4782, Jun. 2022, doi: 10.3390/en15134782.

[9] European Commission, “EU Solar Energy Strategy,” Brussels, 2022. [Online]. Available: https://eur-lex.europa.eu/legal-content/EN/TXT/?uri=COM%3A2022%3A221%3AFIN&qid=1653034500503.

[10] E. Martínez-García, E. Marigorta, J. Navarro-Manso, P. Antonio, and A. Navarro-Manso, “Experimental determination of the resistance of a single-axis solar tracker to torsional galloping,” *Struct. Eng. Mech.*, vol. 78, no. 5, pp. 519–528, 2021, doi: 10.12989/sem.2021.78.5.519.

[11] D. Valentín, C. Valero, M. Egusquiza, and A. Presas, “Failure investigation of a solar tracker due to wind-induced torsional galloping,” *Eng. Fail. Anal.*, vol. 135, p. 106137, May 2022, doi: 10.1016/j.engfailanal.2022.106137.

[12] R. Claus and M. López, “Key issues in the design of floating photovoltaic structures for the marine environment,” *Renew. Sustain. Energy Rev.*, vol. 164, p. 112502, Aug. 2022, doi: 10.1016/j.rser.2022.112502.

[13] DNVGL, “DNVGL-RP-0584 Design, development and operation of floating solar photovoltaic systems,” 2021.

[14] H. N. Li, T. H. Yi, L. Ren, D. S. Li, and L. S. Huo, “Reviews on innovations and applications

in structural health monitoring for infrastructures," *Struct. Monit. Maint.*, vol. 1, no. 1, pp. 1–45, 2014, doi: 10.12989/smm.2014.1.1.001.

[15] X. W. Ye, C. Z. Dong, and T. Liu, "A Review of Machine Vision-Based Structural Health Monitoring: Methodologies and Applications," *J. Sensors*, vol. 2016, p. 10, 2016, doi: 10.1155/2016/7103039.

[16] D. A. M. Amafabia, D. Montalvão, O. David-West, and G. Haritos, "A review of structural health monitoring techniques as applied to composite structures," *SDHM Struct. Durab. Heal. Monit.*, vol. 11, no. 2, pp. 91–147, 2017, doi: 10.3970/sdhm.2017.011.091.

[17] D. Montalvão, N. M. M. Maia, and A. M. R. Ribeiro, "A review of vibration-based structural health monitoring with special emphasis on composite materials," *Shock Vib. Dig.*, vol. 38, no. 4, p. 295, 2006, doi: 10.1177/0583102406065898.

[18] C. Kralovec and M. Schagerl, "Review of Structural Health Monitoring Methods Regarding a Multi-Sensor Approach for Damage Assessment of Metal and Composite Structures," *Sensors*, vol. 20, no. 3, p. 826, Feb. 2020, doi: 10.3390/s20030826.

[19] A. Rytter and P. H. P. Kirkegaard, "Vibration based inspection of civil engineering structures," Aalborg University, 1994.

[20] I. Farreras-Alcover, M. K. Chryssanthopoulos, and J. E. Andersen, "Data-based models for fatigue reliability of orthotropic steel bridge decks based on temperature, traffic and strain monitoring," *Int. J. Fatigue*, vol. 95, pp. 104–119, Feb. 2017, doi: 10.1016/j.ijfatigue.2016.09.019.

[21] J. Di, X. Ruan, X. Zhou, J. Wang, and X. Peng, "Fatigue assessment of orthotropic steel bridge decks based on strain monitoring data," *Eng. Struct.*, vol. 228, p. 111437, Feb. 2021, doi: 10.1016/j.engstruct.2020.111437.

[22] N. Dervilis, "A machine learning approach to Structural HealthMonitoring with a view towards wind turbines," University of Sheffield, 2013.

[23] C. L. Wilson, K. Lonkar, S. Roy, F. Kopsaftopoulos, and F.-K. Chang, "7.20 Structural Health Monitoring of Composites," in *Comprehensive Composite Materials II*, Elsevier, 2018, pp. 382–407.

[24] P. Cawley, "Structural health monitoring: Closing the gap between research and industrial deployment," *Struct. Heal. Monit.*, vol. 17, no. 5, pp. 1225–1244, 2018, doi: 10.1177/1475921717750047.

[25] C. P. Fritzen, "Vibration-Based Structural Health Monitoring – Concepts and Applications," *Key Eng. Mater.*, vol. 293–294, pp. 3–20, 2005, doi: 10.4028/www.scientific.net/kem.293-294.3.

[26] N. García-Fernández, M. Aenlle, A. Álvarez-Vázquez, M. Muniz-Calvente, and P. Fernández, "A review on fatigue monitoring of structures," *Int. J. Struct. Integr.*, vol. 14, no. 2, pp. 133–165, Mar. 2023, doi: 10.1108/IJSI-09-2022-0117.

[27] A. Saisi, C. Gentile, and A. Ruccolo, "Pre-diagnostic prompt investigation and static monitoring of a historic bell-tower," *Constr. Build. Mater.*, vol. 122, pp. 833–844, Sep. 2016, doi: 10.1016/j.conbuildmat.2016.04.016.

[28] Y. J. Lee and S. Cho, "Shm-based probabilistic fatigue life prediction for bridges based on fe model updating," *Sensors (Switzerland)*, vol. 16, no. 3, p. 317, 2016, doi: 10.3390/s16030317.

[29] P. Gardner, "On novel approaches to model-based structural health monitoring," University

of Sheffield, 2018.

[30] D. Goyal and B. S. Pabla, "The Vibration Monitoring Methods and Signal Processing Techniques for Structural Health Monitoring: A Review," *Arch. Comput. Methods Eng.*, vol. 23, pp. 585–594, 2016, doi: 10.1007/s11831-015-9145-0.

[31] H. Khodabandehlou, G. Pekcan, and M. S. Fadali, "Vibration-based structural condition assessment using convolution neural networks," *Struct. Control Heal. Monit.*, vol. 26, no. 2, pp. 1545–2255, 2019, doi: 10.1002/stc.2308.

[32] F. Ubertini, G. Comanducci, and N. Cavalagli, "Vibration-based structural health monitoring of a historic bell-tower using output-only measurements and multivariate statistical analysis," *Struct. Heal. Monit.*, vol. 15, no. 4, pp. 438–457, 2016, doi: 10.1177/1475921716643948.

[33] D. J. Ewins, *Modal Testing: Theory, Practice and Application*. Wiley, 2000.

[34] R. Brincker and C. E. Ventura, *Introduction to Operational Modal Analysis*. Chichester, UK: John Wiley & Sons, Ltd, 2015.

[35] S. D. Fassois and F. P. Kopsaftopoulos, "Statistical Time Series Methods for Vibration Based Structural Health Monitoring," in *New Trends in Structural Health Monitoring*, 2013, pp. 209–264.

[36] O. Avci, O. Abdeljaber, S. Kiranyaz, M. Hussein, M. Gabbouj, and D. J. Inman, "A review of vibration-based damage detection in civil structures: From traditional methods to Machine Learning and Deep Learning applications," *Mech. Syst. Signal Process.*, vol. 147, p. 107077, Jan. 2021, doi: 10.1016/j.ymssp.2020.107077.

[37] C. Rainieri, F. Magalhaes, and F. Ubertini, "Automated Operational Modal Analysis and Its Applications in Structural Health Monitoring," *Shock Vib.*, vol. 2019, pp. 1–3, Nov. 2019, doi: 10.1155/2019/5497065.

[38] C. Rainieri and G. Fabbrocino, *Operational Modal Analysis of Civil Engineering Structures*. New York, NY: Springer New York, 2014.

[39] P. Guillaume, T. De Troyer, C. Devriendt, and G. De Sitter, "OMAX - A combined experimental-operational modal analysis approach," 2006.

[40] A. Brandt, M. Berardengo, S. Manzoni, M. Vanali, and A. Cigada, "Overview of the New OMAH Technique for Scaling OMA Mode Shapes.," *Sound&Vibration*, vol. 52, no. 3, pp. 1–5, 2018, doi: 10.32604/sv.2018.03872.

[41] P. Andersen, R. Brincker, M. Goursat, and L. Mevel, "Automated modal parameter estimation for operational modal analysis of large systems," 2007.

[42] C. Rainieri, G. Fabbrocino, and E. Cosenza, "Automated Operational Modal Analysis as structural health monitoring tool: Theoretical and applicative aspects," *Key Eng. Mater.*, vol. 347, pp. 479–484, 2007, doi: 10.4028/0-87849-444-8.479.

[43] S. S. Christensen and A. Brandt, "Parameter study of statistics of modal parameter estimates using automated operational modal analysis," in *Dynamics of Civil Structures - Conference Proceedings of the Society for Experimental Mechanics Series*, vol. 2, Springer, Cham, 2020, pp. 243–254.

[44] E. Reynders, J. Houbrechts, and G. De Roeck, "Fully automated (operational) modal analysis," *Mech. Syst. Signal Process.*, vol. 29, pp. 228–250, May 2012, doi: 10.1016/j.ymssp.2012.01.007.

[45] J. Li, T. Bao, and C. E. Ventura, “An automated operational modal analysis algorithm and its application to concrete dams,” *Mech. Syst. Signal Process.*, vol. 168, p. 108707, Apr. 2022, doi: 10.1016/j.ymssp.2021.108707.

[46] S. S. Christensen, “Vibration and Strain Monitoring of an Offshore Structure,” University of Southern Denmark, Faculty of Engineering, 2020.

[47] F. Ubertini, G. Comanducci, N. Cavalagli, A. Laura Pisello, A. Luigi Materazzi, and F. Cotana, “Environmental effects on natural frequencies of the San Pietro bell tower in Perugia, Italy, and their removal for structural performance assessment,” *Mech. Syst. Signal Process.*, vol. 82, pp. 307–322, Jan. 2017, doi: 10.1016/j.ymssp.2016.05.025.

[48] R. J. Allemang and D. Brown, “Correlation Coefficient for Modal Vector Analysis,” in *Proceedings of the 1st International Modal Analysis Conference*, 1982, pp. 110–116.

[49] R. J. Allemang, “The modal assurance criterion - Twenty years of use and abuse.,” *Sound Vib.*, 2003.

[50] F. Frigui, J. P. Faye, C. Martin, O. Dalverny, F. Peres, and S. Judenherc, “Global methodology for damage detection and localization in civil engineering structures,” *Eng. Struct.*, vol. 171, pp. 686–695, 2018, doi: 10.1016/j.engstruct.2018.06.026.

[51] A. K. Pandey and M. Biswas, “Damage Detection in Structures Using Changes in Flexibility,” *J. Sound Vib.*, vol. 169, no. 1, pp. 3–17, Jan. 1994, doi: 10.1006/jsvi.1994.1002.

[52] M. M. Abdel Wahab and G. De Roeck, “Damage detection in bridges using modal curvatures: application to a real damage scenario,” *J. Sound Vib.*, vol. 226, no. 2, pp. 217–235, Sep. 1999, doi: 10.1006/jsvi.1999.2295.

[53] F. Bjørheim, S. C. Siriwardane, and D. Pavlou, “A review of fatigue damage detection and measurement techniques,” *Int. J. Fatigue*, vol. 154, p. 106556, Jan. 2022, doi: 10.1016/j.ijfatigue.2021.106556.

[54] H. Wei and Y. Liu, “An energy-based model to assess multiaxial fatigue damage under tension-torsion and tension-tension loadings,” *Int. J. Fatigue*, vol. 141, p. 105858, Dec. 2020, doi: 10.1016/j.ijfatigue.2020.105858.

[55] D. Leonetti, J. Maljaars, and H. H. (Bert) Snijder, “Fracture mechanics based fatigue life prediction for a weld toe crack under constant and variable amplitude random block loading—Modeling and uncertainty estimation,” *Eng. Fract. Mech.*, vol. 242, p. 107487, Feb. 2021, doi: 10.1016/j.engfracmech.2020.107487.

[56] M. Matsuishi and T. Endo, “Fatigue of metals subject to varying stress,” in *Proc. Kyushu District Meeting*, 1968, pp. 37–40.

[57] A. Palmgren, “Die lebensdauer von kugellagern,” *VDI-Zetischrift*, vol. 68, pp. 339–341, 1924.

[58] M. A. Miner, “Cumulative Damage in Fatigue,” *J. Appl. Mech.*, vol. 12, no. 3, pp. A159–A164, Sep. 1945, doi: 10.1115/1.4009458.

[59] Y. Kondo, “Fatigue under Variable Amplitude Loading,” *Compr. Struct. Integr.*, vol. 4 — Cyclic, pp. 253–280, 2003.

[60] S. S. Manson and G. R. Halford, “Re-examination of cumulative fatigue damage analysis—an engineering perspective,” *Eng. Fract. Mech.*, vol. 25, no. 5–6, pp. 539–571, Jan. 1986, doi: 10.1016/0013-7944(86)90022-6.

[61] B. F. Langer, “Fatigue Failure From Stress Cycles of Varying Amplitude,” *J. Appl. Mech.*,

vol. 4, no. 4, pp. A160–A162, Dec. 1937, doi: 10.1115/1.4008807.

[62] H. J. Grover, "An observation concerning the cycle ratio in cumulative damage," 1960.

[63] F. E. Richart and N. M. Newmark, "A hypothesis for the determination of cumulative damage in fatigue," *Proc., Am. Soc. Test. Mater*, vol. 48, pp. 767–800, 1948.

[64] S. M. Marco and W. L. Starkey, "A concept of fatigue damage," *Trans. ASME*, vol. 76, pp. 627–632, 1954.

[65] P. Watson, K. N. Smith, and T. H. Topper, "A stress-strain function for the fatigue of metals," *J Mater*, vol. 5, no. 4, pp. 767–778, 1970.

[66] J. L. Chaboche and P. M. Lesne, "A non-linear continuous fatigue damage model," *Fatigue Fract. Eng. Mater. Struct.*, vol. 11, no. 1, pp. 1–17, Jan. 1988, doi: 10.1111/j.1460-2695.1988.tb01216.x.

[67] E. Castillo and A. Fernández-Canteli, *A Unified Statistical Methodology for Modeling Fatigue Damage*. Springer Netherlands, 2009.

[68] P. H. Wirsching, T. L. Paez, and K. Ortiz, *Random Vibrations. Theory and Practice*, 1st ed. New York: John Wiley & Sons, 1995.

[69] D. Benasciutti and R. Tovo, "Comparison of spectral methods for fatigue analysis of broad-band Gaussian random processes," *Probabilistic Eng. Mech.*, vol. 21, no. 4, pp. 287–299, Oct. 2006, doi: 10.1016/j.probengmech.2005.10.003.

[70] T. Dirlik, "Application of computers in fatigue analysis," University of Warwick, 1985.

[71] T. Dirlik and D. Benasciutti, "Spectral Methods in Vibration Fatigue: A Review with a Historical Perspective," *Metals (Basel).*, vol. 11, no. 9, p. 1333, Aug. 2021, doi: 10.3390/met11091333.

[72] W. Zhao and M. J. Baker, "On the probability density function of rainflow stress range for stationary Gaussian processes," *Int. J. Fatigue*, vol. 14, no. 2, pp. 121–135, Mar. 1992, doi: 10.1016/0142-1123(92)90088-T.

[73] R. Tovo, "Cycle distribution and fatigue damage under broad-band random loading," *Int. J. Fatigue*, vol. 24, no. 11, pp. 1137–1147, Nov. 2002, doi: 10.1016/S0142-1123(02)00032-4.

[74] I. Rychlik, "Note on cycle counts in irregular loads," *Fatigue Fract. Eng. Mater. Struct.*, vol. 16, no. 4, pp. 377–390, Apr. 1993, doi: 10.1111/j.1460-2695.1993.tb00094.x.

[75] R. Brincker, L. Zhang, and P. Andersen, "Modal identification of output-only systems using frequency domain decomposition," *Smart Mater. Struct.*, vol. 10, no. 3, pp. 441–445, Jun. 2001, doi: 10.1088/0964-1726/10/3/303.

[76] F. Magalhães, Á. Cunha, and E. Caetano, "Online automatic identification of the modal parameters of a long span arch bridge," *Mech. Syst. Signal Process.*, vol. 23, no. 2, pp. 316–329, Feb. 2009, doi: 10.1016/j.ymssp.2008.05.003.

[77] A. Romanazzi, D. Scocciolini, M. Savoia, and N. Buratti, "Iterative hierarchical clustering algorithm for automated operational modal analysis," *Autom. Constr.*, vol. 156, p. 105137, Dec. 2023, doi: 10.1016/j.autcon.2023.105137.

[78] G. Zini, M. Betti, and G. Bartoli, "A quality-based automated procedure for operational modal analysis," *Mech. Syst. Signal Process.*, vol. 164, p. 108173, Feb. 2022, doi: 10.1016/j.ymssp.2021.108173.

[79] G. De Roeck, B. Peeters, and J. Maeck, "Dynamic Monitoring of Civil Engineering Structures," 2000.

[80] M. I. Friswell and J. E. Mottershead, *Finite Element Model Updating in Structural Dynamics*, vol. 38. Dordrecht: Springer Netherlands, 1995.

[81] P. Avitabile and M. Mains, "Finite Element Model Correlation," in *Handbook of Experimental Structural Dynamics*, New York, NY: Springer New York, 2020, pp. 1–39.

[82] J. E. Mottershead, M. Link, and M. I. Friswell, "The sensitivity method in finite element model updating: A tutorial," *Mech. Syst. Signal Process.*, vol. 25, no. 7, pp. 2275–2296, Oct. 2011, doi: 10.1016/j.ymssp.2010.10.012.

[83] K. Abasi, M. Asayesh, and M. Nikravesh, "Comparing of Direct and Sensitivity-Base Model Updating Methods in Structural Dynamics and Its Application for Updating of Cantilever Model," in *Volume 14: New Developments in Simulation Methods and Software for Engineering Applications*, Jan. 2008, pp. 157–164, doi: 10.1115/IMECE2008-68507.

[84] S. Ereiz, I. Duvnjak, and J. Fernando Jiménez-Alonso, "Review of finite element model updating methods for structural applications," *Structures*, vol. 41, pp. 684–723, Jul. 2022, doi: 10.1016/j.istruc.2022.05.041.

[85] N. Mendes Maia and J. Montalvão Silva, *Theoretical and Experimental Modal Analysis.* Research Studies Press, 1997.

[86] W. Heylen, S. Lammens, and P. Sas, *Modal analysis theory and testing*. Belgium: Katholieke Universiteit Leuven, 2007.

[87] C. Lein and M. Beitelschmidt, "Comparative study of model correlation methods with application to model order reduction," 2014.

[88] L. Rigner, J. Golinval, and M. Razeto, "Modal assurance criteria value for two orthogonal modal vectors.," 1998.

[89] D. J. Ewins, "Model validation: Correlation for updating," *Sadhana*, vol. 25, no. 3, pp. 221–234, Jun. 2000, doi: 10.1007/BF02703541.

[90] D. Fotsch and D. J. Ewins, "Application of MAC in the frequency domain.," *Proc Int Modal Anal Conf - IMAC*, 2000.

[91] N. Lieven and D. J. Ewins, "Spatial correlation of mode shapes: the coordinate modal assurance criterion (COMAC)," 1988.

[92] W. D'Ambrogio and A. Fregolent, "Higher-order MAC factor for the correlation of close and multiple modes," *Mech. Syst. Signal Process.*, vol. 17, no. 3, pp. 599–610, May 2003, doi: 10.1006/mssp.2002.1468.

[93] W. D'Ambrogio and A. Fregolent, "Correlation of close modes using S2MAC," 2002.

[94] M. I. Friswell, "The Derivatives of Repeated Eigenvalues and Their Associated Eigenvectors," *J. Vib. Acoust.*, vol. 118, no. 3, pp. 390–397, Jul. 1996, doi: 10.1115/1.2888195.

[95] M. Aenlle, N. García-Fernández, and F. Pelayo, "Rotation of mode shapes in structural dynamics due to mass and stiffness perturbations," *Mech. Syst. Signal Process.*, vol. 212, p. 111269, Apr. 2024, doi: 10.1016/j.ymssp.2024.111269.

[96] M. Aenlle, J. Pacheco-Chérrez, and R. Brincker, "Sensitivity analysis of a system with two closely spaced modes using structural dynamic modification," *Mech. Syst. Signal Process.*,

vol. 206, p. 110894, Jan. 2024, doi: 10.1016/j.ymssp.2023.110894.

[97] R. Brincker, C. E. Ventura, and P. Andersen, “Why Output-Only Modal Testing is a Desirable Tool for a Wide Range of Practical Applications,” 2003.

[98] H. P. Hjelm, R. Brincker, J. Graugaard-Jensen, and K. Munch, “Determination of Stress Histories in Structures by Natural Input Modal Analysis,” 2005.

[99] P. Fernández, M. L. Aenlle, R. Brincker, and A. F. Canteli, “Stress estimation in structures using operational modal analysis,” 2009.

[100] M. L. Aenlle, A. Skafte, P. Fernández, and R. Brincker, “Strain Estimation in a Glass Beam Using Operational Modal Analysis,” in *Conference Proceedings of the Society for Experimental Mechanics Series*, 2013, pp. 375–382.

[101] M. López-Aenlle, L. Hermanns, F. Pelayo, and A. Fraile, “Stress Estimation in a Scale Model of a Symetric Two Story Building,” 2013.

[102] F. Pelayo, A. Skafte, M. L. Aenlle, and R. Brincker, “Modal Analysis Based Stress Estimation for Structural Elements Subjected to Operational Dynamic Loadings,” *Exp. Mech.*, vol. 55, no. 9, pp. 1791–1802, 2015, doi: 10.1007/s11340-015-0073-6.

[103] M. Tarpø *et al.*, “Operational modal analysis based prediction of actual stress in an offshore structural model,” *Procedia Eng.*, vol. 199, pp. 2262–2267, 2017, doi: 10.1016/j.proeng.2017.09.234.

[104] B. Nabuco, M. Tarpø, U. T. Tygesen, and R. Brincker, “Fatigue Stress Estimation of an Offshore Jacket Structure Based on Operational Modal Analysis,” *Shock Vib.*, vol. 2020, pp. 1–12, May 2020, doi: 10.1155/2020/7890247.

[105] R. J. GUYAN, “Reduction of stiffness and mass matrices,” *AIAA J.*, vol. 3, no. 2, pp. 380–380, Feb. 1965, doi: 10.2514/3.2874.

[106] M. Paz, “Dynamic Condensation,” *AIAA J.*, vol. 22, no. 5, pp. 724–727, May 1984, doi: 10.2514/3.48498.

[107] J. C. O’Callahan, P. Avitabile, and R. Riemer, “System Equivalent Reduction Expansion Process,” 1989.

[108] D. C. Kammer, “A Hybrid Approach to Test-Analysis-Model Development for Large Space Structures,” *J. Vib. Acoust.*, vol. 113, no. 3, pp. 325–332, Jul. 1991, doi: 10.1115/1.2930188.

[109] P. Avitabile and P. Pingle, “Prediction of full field dynamic strain from limited sets of measured data,” *Shock Vib.*, vol. 19, no. 5, pp. 765–785, 2012, doi: 10.3233/SAV-2012-0686.

[110] J. Baqersad, C. Niezrecki, and P. Avitabile, “Extracting full-field dynamic strain on a wind turbine rotor subjected to arbitrary excitations using 3D point tracking and a modal expansion technique,” *J. Sound Vib.*, vol. 352, pp. 16–29, Sep. 2015, doi: 10.1016/j.jsv.2015.04.026.

[111] R. Brincker, A. Skafte, M. López-Aenlle, A. Sestieri, W. D’Ambrogio, and A. Canteli, “A local correspondence principle for mode shapes in structural dynamics,” *Mech. Syst. Signal Process.*, vol. 45, no. 1, pp. 91–104, Mar. 2014, doi: 10.1016/j.ymssp.2013.10.025.

[112] P. Avitabile, “Proper Projection Vectors for the Expansion of Measured Experimental Modal Data,” *J. Eng. Mech.*, vol. 144, no. 5, May 2018, doi: 10.1061/(ASCE)EM.1943-7889.0001431.

[113] M. Tarpø, B. Nabuco, C. Georgakis, and R. Brincker, “Expansion of experimental mode shape from operational modal analysis and virtual sensing for fatigue analysis using the modal

expansion method,” *Int. J. Fatigue*, vol. 130, p. 105280, Jan. 2020, doi: 10.1016/j.ijfatigue.2019.105280.

[114] A. Iliopoulos, W. Weijtjens, D. Van Hemelrijck, and C. Devriendt, “Full-field strain prediction applied to an offshorewind turbine,” in *Conference Proceedings of the Society for Experimental Mechanics Series*, 2016, vol. 3, pp. 349–357, doi: 10.1007/978-3-319-29754-5_34.

[115] M. Henkel, J. Häfele, W. Weijtjens, C. Devriendt, C. G. Gebhardt, and R. Rolfes, “Strain estimation for offshore wind turbines with jacket substructures using dual-band modal expansion,” *Mar. Struct.*, vol. 71, p. 102731, May 2020, doi: 10.1016/j.marstruc.2020.102731.

[116] M. Henkel, W. Weijtjens, and C. Devriendt, “Fatigue Stress Estimation for Submerged and Sub-Soil Welds of Offshore Wind Turbines on Monopiles Using Modal Expansion,” *Energies*, vol. 14, no. 22, p. 7576, Nov. 2021, doi: 10.3390/en14227576.

[117] D. Anastasopoulos and E. P. B. Reynders, “Modal strain monitoring of the old Nieuwebrugstraat Bridge: Local damage versus temperature effects,” *Eng. Struct.*, vol. 296, p. 116854, Dec. 2023, doi: 10.1016/j.engstruct.2023.116854.

[118] D. Anastasopoulos, K. Maes, G. De Roeck, G. Lombaert, and E. P. B. Reynders, “Influence of frost and local stiffness variations on the strain mode shapes of a steel arch bridge,” *Eng. Struct.*, vol. 273, p. 115097, Dec. 2022, doi: 10.1016/j.engstruct.2022.115097.

[119] J. Baqersad, K. Bharadwaj, and P. Poozesh, “Modal Expansion using Strain Mode Shapes,” in *Shock & Vibration, Aircraft/Aerospace, Energy Harvesting, Acoustics & Optics, Volume 9*, 2017, pp. 219–226, doi: 10.1007/978-3-319-54735-0_23.

[120] C. Robertrs, S. Isbister, C. Murphy, C. Nisbet, P. Sweeney, and D. Garcia, “Strain estimation using modal expansion approach via virtual sensing for structural asset management,” 2018.

[121] D. C. Papadioti, D. Giagopoulos, and C. Papadimitriou, “Fatigue monitoring in metallic structures using vibration measurements,” *Conf. Proc. Soc. Exp. Mech. Ser.*, vol. 3, pp. 33–40, 2014, doi: 10.1007/978-3-319-04552-8_4.

[122] B. Mora, J. Basurko, I. Sabahi, U. Leturiondo, and J. Albizuri, “Strain Virtual Sensing for Structural Health Monitoring under Variable Loads,” *Sensors*, vol. 23, no. 10, p. 4706, May 2023, doi: 10.3390/s23104706.

[123] P. Ren and Z. Zhou, “Strain estimation of truss structures based on augmented Kalman filtering and modal expansion,” *Adv. Mech. Eng.*, vol. 9, no. 11, pp. 1–10, 2017, doi: 10.1177/1687814017735788.

[124] M. Tarpø, S. Amador, E. Katsanos, M. Skog, J. Gjødvad, and R. Brincker, “Data-driven virtual sensing and dynamic strain estimation for fatigue analysis of offshore wind turbine using principal component analysis,” *Wind Energy*, vol. 25, no. 3, pp. 505–516, Mar. 2022, doi: 10.1002/we.2683.

[125] P. Hansen, V. Pereyra, and G. Scherer, *Least Squares Data Fitting with Applications*. Baltimore, MD, USA: Johns Hopkins University Press, 2012.

[126] W. Heylen, S. Lammens, M. I. Friswell, and J. E. Mottershead, “FRAC: A Consistent Way of Comparing Frequency Response Functions,” 1996.

[127] K. Maes, A. Iliopoulos, W. Weijtjens, C. Devriendt, and G. Lombaert, “Dynamic strain estimation for fatigue assessment of an offshore monopile wind turbine using filtering and modal expansion algorithms,” *Mech. Syst. Signal Process.*, vol. 76–77, pp. 592–611, Aug. 2016, doi: 10.1016/j.ymssp.2016.01.004.

[128] A. Sestieri and W. D'Ambrogio, "Structural dynamic modifications," in *Encyclopedia of Vibration*, Elsevier, 2001, pp. 1253–1264.

Dissemination of Results

Journal Publications

During the course of this doctoral program, six articles related to the topic of this thesis have been published in journals indexed in the JCR.

1. Title: Mass and Stiffness Correlation Using a Transformation Matrix
   Authors: N. García-Fernández, F. Pelayo, R. Brincker and M. Aenlle*
   Journal: Infrastructures 2024, 9(6), 96
   DOI: 10.3390/infrastructures9060096

2. Title: Rotation of mode shapes in structural dynamics due to mass and stiffness perturbations
   Authors: M. Aenlle, N. García-Fernández* and F. Pelayo
   Journal Mechanical Systems and Signal Processing 2024, 212, 111269
   DOI: 10.1016/j.ymssp.2024.111269

3. Title: Cross-length of mode shapes in structural dynamics: concept and applications
   Authors: M. Aenlle, R. Stufano, N. García-Fernández*, F. Pelayo and R. Brincker
   Journal Shock and Vibration 2023, 2023, 2745671
   DOI: 10.1155/2023/2745671

4. Title: A review on fatigue monitoring of structures
   Authors: N. García-Fernández*, M. Aenlle, A. Álvarez-Vázquez, M. Muñiz-Calvente and F. Pelayo
   Journal Shock and Vibration 2023, 2023, 2745671
   DOI: 10.1108/IJSI-09-2022-011

5. Title: A comparative review of time- and frequency-domain methods for fatigue damage assessment.

Authors: M. Muñiz-Calvente*, A. Álvarez-Vázquez, F. Pelayo, M. Aenlle, N. García-Fernández and M.J. Lamela-Rey

Journal International Journal of Fatigue. Elsevier. 163.

DOI: 10.1016/j.ijfatigue.2022.107069

6. Title: Response of laminated glass elements subject to dynamic loadings using a monolithic model and a stress effective Young's modulus

Authors: M. Aenlle, F. Pelayo, A. Álvarez-Vázquez, N. García-Fernández and M. Muñiz-Calvente.

Journal Journal of Sandwich Structures and Materials, 2022, 24(4), pp. 1771–1789

DOI: 10.1177/10996362221084636

Conference publications

During these years, the research has also been presented at both national and international conferences. The corresponding publications are shown below, with the author responsible for the oral presentation underlined.

1. Title: Application of T-Mass and T-Stiffness correlation techniques on a bridge model.

Authors: N. García-Fernández, F. Pelayo, C. Gentile and M. Aenlle

Conference: III Congreso de dinámica estructural (DinEst 2024)

Place and date: Sevilla (Spain), Sept 2024

Publication: Proceedings of the DinEst 2024 (pp.: 308-311)

2. Title: Model updating method based on T-Mass and T-Stiffness correlation techniques.

Authors: N. García-Fernández, M. Aenlle and F. Pelayo

Conference: III Congreso de dinámica estructural (DinEst 2024)

Place and date: Sevilla (Spain), Sept 2024

Publication: Proceedings of the DinEst 2024 (pp.: 313-330)

3. Title: The concept of ROTMAC in structural dynamics

Authors: N. García-Fernández, F. Pelayo and M. Aenlle

Conference: III Congreso de dinámica estructural (DinEst 2024)

Place and date: Sevilla (Spain), Sept 2024

Publication: Proceedings of the DinEst 2024 (pp.: 343-355)

4. Title: Dynamic analysis of a 7th floor concrete prefabricated building.
Authors: B. Istegün, F. Pelayo, N. García-Fernández and M. Aenlle
Conference: III Congreso de dinámica estructural (DinEst 2024)
Place and date: Sevilla (Spain), Sept 2024
Publication: Proceedings of the DinEst 2024 (pp.: 244-247)

5. Title: Fatigue monitoring of structures as a SHM technique.
Authors: F. Pelayo, N. García-Fernández, M. Muñiz-Calvente and M. Aenlle
Conference: III Congreso de dinámica estructural (DinEst 2024)
Place and date: Sevilla (Spain), Sept 2024
Publication: Proceedings of the DinEst 2024 (pp.: 361-364)

6. Title: Vibration testing and finite element modelling of a steel-concrete composite bridge.
Authors: N. García-Fernández, M. Aenlle and C.Gentile
Conference: 10th International Operational Modal Analysis Conference (IOMAC 2024)
Place and date: Naples (Italy), May 2024.
Publication: Lecture of Notes in Civil Engineering. Proceedings of the 10th International Operational Modal Analysis Conference (ISSN 2366-2557) (vol. 2 pp.: 137-144)

7. Title: Real time fatigue monitoring using OMA.
Authors: F. Pelayo, N. García-Fernández and M. Aenlle
Conference: 10th International Operational Modal Analysis Conference (IOMAC 2024)
Place and date: Naples (Italy), May 2024.
Publication: Lecture of Notes in Civil Engineering. Proceedings of the 10th International Operational Modal Analysis Conference (ISSN 2366-2557) (vol. 2 pp.: 79-86)

8. Title: Monitorización de estructuras a fatiga en tiempo real.
Authors: N. García-Fernández, F. Pelayo, and M. Aenlle

	Conference:	I Jornadas de difusión del departamento de construcción e ingeniería de fabricación (DCIF 2023).
	Place and date:	Gijón (Spain), July 2023.
	Contribution	Poster
9.	Title:	Metodología para el uso de agitadores electrodinámicos en la caracterización y predicción de vida a fatiga en materiales metálicos.
	Authors:	D. Díaz-Salamanca, N. García-Fernández, M. Muñiz and M. Aenlle
	Conference:	Congreso del Grupo Español de Fractura (GEF 2024).
	Place and date:	Mallorca (Spain), March 2023.
	Publication:	Revista de Mecánica de la Fractura (In Press)
10.	Title:	Monitorización de estructuras a fatiga en tiempo real.
	Authors:	N. García-Fernández, F. Pelayo and M. Aenlle
	Conference:	Congreso del Grupo Español de Fractura (GEF 2023).
	Place and date:	Gijón (Spain), March 2023.
	Publication:	Revista de Mecánica de la Fractura (ISSN: 2792-4246) (Vol. 5 pp.: 199-204)
11.	Title:	A physical interpretation of modal mass in structural dynamics.
	Authors:	M. Aenlle, R. Brincker, N. García-Fernández and F. Pelayo
	Conference:	9th International Operational Modal Analysis Conference (IOMAC 2022).
	Place and date:	Vancouver (Canada), July 2022.
	Publication:	Proceedings of the 9th International Operational Modal Analysis Conference (ISBN 978-840944336-9)
12.	Title:	Dynamic response of laminated glass elements in time domain.
	Authors:	M. Aenlle, F. Pelayo, N. García-Fernández, M. Muñiz-Calvente and M.J. Lamela-Rey
	Conference:	9th International Operational Modal Analysis Conference (IOMAC 2022).
	Place and date:	Vancouver (Canada), July 2022.
	Publication:	Proceedings of the 9th International Operational Modal Analysis Conference (ISBN 978-840944336-9)

13. Title: Examples of model correlation with closely spaced modes.
Authors: N. García-Fernández, F. Pelayo and M. Aenlle.
Conference: 9th International Operational Modal Analysis Conference (IOMAC 2022).
Place and date: Vancouver (Canada), July 2022.
Publication: Proceedings of the 9th International Operational Modal Analysis Conference (ISBN 978-840944336-9)

14. Title: Finite element modelling and OMA of the 'Laboral city of culture' tower.
Authors: N. García-Fernández, F. Pelayo and M. Aenlle.
Conference: 9th International Operational Modal Analysis Conference (IOMAC 2022).
Place and date: Vancouver (Canada), July 2022.
Publication: Proceedings of the 9th International Operational Modal Analysis Conference (ISBN 978-840944336-9)

15. Title: Length of mode shapes in numerical and experimental models.
Authors: N. García-Fernández, F. Pelayo and R. Brincker.
Conference: 9th International Operational Modal Analysis Conference (IOMAC 2022).
Place and date: Vancouver (Canada), July 2022.
Publication: Proceedings of the 9th International Operational Modal Analysis Conference (ISBN 978-840944336-9)

16. Title: Operational modal analysis and numerical modelling of a footbridge gallery linking two buildings.
Authors: N. García-Fernández, F. Pelayo and M. Aenlle.
Conference: 9th International Operational Modal Analysis Conference (IOMAC 2022).
Place and date: Vancouver (Canada), July 2022.
Publication: Proceedings of the 9th International Operational Modal Analysis Conference (ISBN 978-840944336-9)

17. Title: Fatigue damage assessment and detection in notched components based on phenomenological models and operational modal analysis.

Authors: N. García-Fernández, A. Álvarez-Vázquez, M. Muñiz-Calvente, F. Pelayo and M. Aenlle.
Conference: 5th Iberian Conference on Structural Integrity
Place and date: Coimbra (Portugal), April 2022.
Publication: Revista de Mecánica de la Fractura (ISSN: 2792-4246) (Vol. 4 pp.: 83-88)

18. Title: Estimation and validation of modal masses in constant mass-density systems.
Authors: N. García-Fernández, R. Stufano, M. Aenlle and F. Pelayo.
Conference: 6th International conference on mechanical models in structural engineering (CMMoST 2021)
Place and date: Valladolid (Spain), Dec. 2021.
Publication: CMMOST 2021. Full Papers (ISBN: 978-84-09-39323-7) (pp.: 246-258)

19. Title: Study of the reinforcement in a footbridge with vibration problems.
Authors: N. García-Fernández, F. Pelayo, M. Aenlle, M. Muñiz-Calvente and A. Álvarez-Vazquez
Conference: 6th International conference on mechanical models in structural engineering (CMMoST 2021)
Place and date: Valladolid (Spain), Dec. 2021.
Publication: CMMOST 2021. Full Papers (ISBN: 978-84-09-39323-7) (pp.: 259-271)

20. Title: Numerical modelling and modal analysis of the pedestrian footbridge at the Milan's campus.
Authors: N. García-Fernández, M.R. Quintana-Camporro, F. Pelayo and M. Aenlle.
Conference: II Congreso de Dinámica Estructural. Universidad de Oviedo (DinEst 2021)
Place and date: Gijón (Spain), July. 2021.
Publication: Proceedings of the DinEst 2021 (pp.: 240-245)

21. Title: Modelización numérica y análisis modal de la pasarela peatonal del campus del Milán

Authors: M.R. Quintana-Camporro, N. García-Fernández, F. Pelayo and M. Aenlle.

Conference: 3as Jornadas de Investigación, Desarrollo e Innovación en Ingeniería Civil. Escuela Politécnica de Mieres

Place and date: Online, Nov. 2020.

Publication: ---